Search for the Standard Model Higgs boson decaying to tau leptons with the CMS experiment at LHC

Lorenzo Bianchini

ÉCOLE POLYTECHNIQUE

Thèse présentée pour obtenir le grade de

DOCTEUR EN SCIENCES

Search for the Standard Model Higgs boson decaying to tau leptons with the CMS experiment at LHC

Recherche du boson de Higgs du modèle standard dans la voie de désintégration en leptons taus avec l'expérience CMS au LHC

Candidat:

Lorenzo BIANCHINI

Commission d'examen:

G. BERNARDI *Rapporteur*
A. DE ROECK *Examinateur*
P. FAYET *Président du jury*
A. NISATI *Rapporteur*
L. ROLANDI *Examinateur*
Y. SIROIS *Directeur de thèse*

Soutenue le 18 Septembre 2012

Abstract

In this thesis, I present my work in the CMS experiment on a search for the standard model Higgs boson decaying into a pair of tau leptons. The original goal and the final aim of this research is a contribution to the discovery of the Higgs boson at the LHC.

After a summary of the theoretical framework and of the experimental apparatus, I will describe the particle–flow technique developed for the offline CMS event reconstruction, which I contributed to commission with the first LHC collisions delivered at 900 GeV and 7 TeV center–of–mass energy. The particle–flow reconstruction gives optimal performances for the measurement of jets, missing transverse energy and taus, and is therefore ideally suited for the search of the Higgs boson decaying to tau leptons.

Tau reconstruction and identification in CMS are described. Particular emphasis is devoted to the discrimination between the electrons and tau leptons decaying semi–leptonically (giving hadrons and neutrinos), an aspect of the tau identification where I brought original improvements.

A crucial and challenging aspect in the search for the Higgs boson decaying into tau leptons is the reconstruction of the di–tau mass, given that an unknown fraction of the tau momenta is carried away by the undetected neutrinos. Existing and novel di–tau mass reconstruction techniques are described. On this subject, I have provided original contributions in the development of a new likelihood–based technique, called SVfit, which is then used for the analysis.

Finally, a search for the Standard Model Higgs boson in the di–tau channel, based on 4.9 fb^{-1} of pp collisions at $\sqrt{s} = 7$ TeV, is presented. A first version of this analysis was completed for the CMS publications in Spring 2012. This analysis was then further improved and included in the combination using an additional 5.3 fb^{-1} collected at $\sqrt{s} = 8$ TeV in the first half of 2012. This 2012 version of the analysis is presented here. Events are selected where one tau decays semi–leptonically and the other decays fully–leptonically into neutrinos and lighter charged leptons (electrons or muons). The sensitivity of the analysis is enhanced by separating the events into exclusive categories with different signal purity. One of the category is optimized for the vector–boson fusion production mechanism, a process that is intimately related to the very nature of the spontaneous symmetry breaking.

No significant excess over the Standard Model backgrounds is observed. The statistical interpretation of the results is then translated into 95% CL upper limits on the signal cross–section.

Résumé

Dans cette thèse, je présente mon travail effectué au sein de l'expérience CMS, et consacré à la recherche du boson de Higgs du modèle standard dans sa voie de désintégration en une paire de leptons tau. L'objectif original et la finalité de cette recherche est une contribution à la découverte du boson de Higgs au LHC.

Après un résumé du cadre théorique et expérimental de ma thèse, j'expose la technique particle–flow développée pour la reconstruction des événements hors ligne enregistrés par CMS, et que j'ai contribué à mettre en place avec les premières collisions du LHC à 900 GeV et 7 TeV. L'algorithme particle–flow donne des performances optimales en termes de reconstruction des jets, énergie transverse manquante et taus, et il est idéalement adapté à l'étude du canal $H \to \tau\tau$.

La reconstruction et l'identification des leptons tau dans CMS sont décrites en détail dans la thèse. Une attention particulière est consacrée à la discrimination entre les électrons et les leptons taus qui se désintégrant en voie semi–leptoniques (donnant des neutrinos et des hadrons), à laquelle j'ai apporté des améliorations originales.

Un élément crucial dans l'étude $H \to \tau\tau$ est la reconstruction de la masse invariante, puisqu'une fraction de l'impulsion des leptons tau est emportée par les neutrinos. Sur ce sujet, j'ai apporté des contributions originales au développement d'un Dynamical Likelihood Model, appelé SVfit, pour estimer la masse totale de la paire des taus, et qui sera utilisé pour l'analyse.

Enfin, une recherche du boson de Higgs SM dans la voie $H \to \tau\tau$, basée sur 4.9 fb^{-1} de collisions pp à $\sqrt{s} = 7$ TeV, est présentée. Une première version de cette analyse a été complétée pour les publications CMS du printemps 2012. Cette analyse a ensuite été optimisée plus avant et inclue dans la combinaison utilisant 5.3 fb^{-1} de données additionnelles accumulées à $\sqrt{s} = 8$ TeV durant la première moitié de 2012. La version 2012 de l'analyse est présentée ici. Des événements avec une paire de taus sont sélectionnés où l'un se désintègre de façon semi–leptonique (i.e. en hadrons et neutrinos) et l'autre en façon leptonique (i.e. en muons ou électrons et en neutrinos). La sensibilité de l'analyse est renforcée par la séparation des événements dans des catégories exclusives conçues pour optimiser les limites d'exclusion. Une des catégories est optimisée pour le mécanisme de la production par fusion de bosons vecteurs (vector–boson fusion), un processus qui est intimement lié à la nature même de la brisure de symétrie. Aucun excès par dessus aux bruits de fond prédicts par le SM n'a été observé. L'interprétation statistique des résultats à été faite dans le cadre du SM et elle est finalement traduite en limites au 95% CL sur la section efficace du signal.

Acknowledgments

Contents

Chapter 1

Introduction

The Standard Model (SM) [1]–[3] of particle physics has been soundly confirmed by a variety of direct and indirect measurements. The only missing piece in the spectrum of the theory is the Higgs boson (H) , the quantum of the field believed to be responsible for the spontaneous breaking of the SM gauge symmetry. In this thesis, I describe my work in the CMS experiment concerned with the search for the SM Higgs boson decaying into tau leptons. The original goal and final aim is the discovery of the Higgs boson in a channel with manifest couplings to leptons, and where the production via vector–boson fusion (VBF) through WWH and ZZH couplings could play a major role. The di–tau channel can also contribute to the early Higgs boson discovery, which is expected to be first established in the $H \to \gamma\gamma$ and $H \to ZZ \to 4\ell$ channels.

Chapter 2 is devoted to the description of the theoretical framework. After a brief reminder of the building bricks of the SM, I introduce the scalar sector with one doublet of complex scalar fields, the so–called "Higgs doublet". With the presence of the Higgs doublet, masses to the gauge bosons, which in a gauge theory with unbroken symmetry are bound to be massless, can be generated via the Brout–Englert–Higgs (BEH) mechanism [4]–[9]. In addition, mass terms for the matter fields (fermions) can naturally arise via their Yukawa interactions with the Higgs doublet. In its minimal version, the BEH mechanism implies the existence of a new neutral degree of freedom with $J^{\mathrm{CP}} = 0^{++}$ (the so–called Higgs boson), the only elementary scalar particle in the SM spectrum.

The mass of this new hypothesized particle (M_H) is a free parameter of the theory. Constraints on M_H come from both theoretical arguments and from experiments. If the Higgs boson is too heavy, the theory eventually violates unitarity and becomes non–perturbative. This can be prevented if

M_H does not exceed about 700 GeV [18]. On the contrary, if the Higgs boson is too light, the electroweak vacuum on which the theory is built is no longer stable. Depending on the cut–off scale of the theory, i.e. when some new physics should eventually intervene to restore the stability, lower bounds on M_H can be set. In particular, if no new physics appears before the Planck scale, M_H should not be smaller than about 130 GeV [20].

Indirect constraints on M_H come from precision measurements of electroweak observables which, in the SM, receive quantum corrections proportional to $\log M_H$ [25]. The ensemble of electroweak precision tests highly disfavors an Higgs boson with mass larger than about 180 GeV [26]. These measurements are complemented by direct searches. The most stringent direct search results have been obtained from the experiments carried out at LEP2, Tevatron and, more recently, at LHC. The latter is briefly summarized in the last chapter. At first, I concentrate on the results on direct and indirect searches before the LHC had provided the bulk of the luminosity used in this thesis.

The phenomenology of the SM Higgs boson in high–energy hadron–hadron collisions depends significantly on its mass [10]. The main decay channels are described and leading order estimates of their decay widths are reported. Then, I summarize the characteristics of the four dominant production mechanisms in pp collisions, reporting for each one the cross–section with its state of the art theoretical accuracy [28].

Finally, I shortly describe a minimal extension of the scalar sector realized by adding a second doublet of scalar fields. The success of this model is owed to its application in the minimal supersymmetric extension of the SM (MSSM) [33]. Two–doublets models bring to a richer phenomenology, with up to five different scalar bosons, three neutral and two charged. The production cross–sections for the neutral Higgs bosons in pp collisions is finally reported for a specific MSSM scenario.

The search for the Higgs boson plays a main role in the physics programme of the Compact Muon Solenoid (CMS) [39] experiment at the CERN Large Hadron Collider (LHC). Chapter 3 is devoted to the description of CMS, a general purpose detector located at the Point–5 pit of the LHC tunnel. With its calorimeters extending up to $|\eta| = 5.0$, the CMS apparatus is, to all effects, a 4π detector, instrumented with subdetectors for micro–vertexing, tracking, muon reconstruction and calorimetric measurement of electrons, photons and jets. The distinguishing features of CMS are the fully silicon–based tracking system (pixel in the inner tracker, silicon strips elsewhere), an intense solenoidal magnetic field, which allows to meet the goals of momentum resolution for charged particles even for a compact experiment like CMS, and a fully active (so–called homogeneous), crystal–based, scintillat-

ing electromagnetic calorimeter, very granular and performing in terms of energy resolution. These outstanding characteristics also make CMS ideally suited for the deployment of the particle–flow algorithm [46], which is the main subject of Chapter 4.

Measuring the energy and direction of hadronic jets is a task traditionally assigned to calorimeters. In principle, the charged component of the jet could be measured with superior precision by tracking devices, leaving the detection of neutral particles to the calorimeters. However, the energy deposited by the charged and neutral particles eventually mixes in the calorimeter: the separation between the two becomes an involved procedure. An appealing solution is provided by the particle–flow algorithm, i.e. a method which aims at reconstructing all stable particles in the event, making the best use of the different subdetectors to determine their type and energy. After a brief introduction to the generic aspects, I then concentrate on the particle–flow algorithm implemented in the offline reconstruction of CMS collision events. The superior performances of the particle–flow reconstruction in terms of jets and missing transverse energy, when compared to a purely calorimetric approach, have been extensively validated with collision data. The building bricks of the algorithm [47] and the higher–level objects [48] have been promptly commissioned with the first collisions at $\sqrt{s} = 0.9$ and 7 TeV, a topic where I have brought an original contribution.

The particle–flow algorithm delivers a list of reconstructed particles, whose energy, type and direction have been determined by an optimal combination of all subdetectors. This list can be then passed as input to algorithms that build higher–level objects. This is the case, for example, for the reconstruction of the semi–leptonic decays of the tau lepton [67].

Tau reconstruction in CMS is seeded by the output of the particle–flow algorithm. Charged hadrons and photons are combined to reconstruct particular decays of the tau lepton. Chapter 5 is devoted to the description of the main algorithms for tau reconstruction in CMS, namely the HPS and TaNC algorithm [63]. I have contributed to their first commissioning with 7 TeV data, with particular emphasis on the optimization and validation of algorithms to discriminate semi–leptonic tau decays from electrons [64], whose signature, with a high–momentum track and large electromagnetic component, can resemble that of the semi–leptonic tau decay into a neutrino plus one charged and a few neutral pions.

In searches for a narrow resonance $\phi \to \tau\tau$ with mass $M_\phi \gtrsim M_Z$, the di–tau mass offers the single most sensitive observable that can discriminate the signal ($\phi \to \tau\tau$) from its irreducible and most prominent background ($Z \to \tau\tau$). The sensitivity to a small excess of di–tau events over this overwhelming background relies on how efficiently the Z and ϕ mass peaks can

be separated. Chapter 6 is dedicated to the description of existing and novel di–tau mass reconstruction techniques. A specific optimization for the CMS experiment [88], which I contributed to develop, is presented. This algorithm, called SVfit, belongs to the class of likelihood–based estimators known as Dynamical Likelihood Models (DLM) [85, 86]. Given the momenta of the visible tau decay products and the total imbalance of transverse momentum in the event, the so–called missing transverse energy, there are infinitely–many values of the tau lepton momenta that are consistent with that observation. Each value maps to a particular tau decay final state. The idea implemented by SVfit is to weight all possible final states by their probability of occurrence. This results in an *a posteriori* event–by–event likelihood for the di–tau mass, which is then used to derive an estimator of the true resonance mass. The superior performances of the SVfit mass reconstruction, compared to e.g. the visible mass, have driven to its deployment in the analysis presented in this thesis.

Finally, Chapter 7 describes a search for a light SM Higgs boson ($M_H \lesssim$ 145 GeV) decaying to tau leptons. The analysis is based on 4.9 fb^{-1} of pp collision data collected by CMS at $\sqrt{s} = 7$ TeV. Events are searched where one tau decays semi–leptonically into a neutrino plus hadrons and the other decays leptonically into lighter leptons, electrons or muons, and two neutrinos. The sensitivity of the analysis is enhanced by subdividing the events into mutually exclusive categories, characterized by a different signal purity. One category is specifically designed to enhance the contribution from an Higgs boson produced in VBF. The other categories are optimized for the gluon–gluon fusion (GGF) production mechanism. The observed exclusion limits on the production cross–section of a SM–like Higgs boson are compatible with the background–only hypothesis for all tested values of M_H. An Higgs boson with $M_H = 125$ GeV, produced at a rate 1.90 times larger than the SM prediction, is ruled out at 95% CL, compared to an expectation of 1.98 in the absence of a signal.

The core of the analysis presented in this thesis, which I had first developed for an early CMS publication using 2011 data, was re–optimized and improved in the course of 2012 and finally entered in the combination of the 2011 data with 5.3 fb^{-1} of data collected at $\sqrt{s} = 8$ TeV up to June 2012. The results using the combined data have been published for the di–tau channel in Ref. [95]. These results have contributed to the observation paper [96] from the CMS experiment and are summarized in the final chapter.

Chapter 2

Theoretical context: the Standard Model and the Higgs boson

The Standard Model (SM) [1, 2, 3] is the theory of the strong and electroweak interactions between elementary particles. It has been verified with considerable success in all high energy physics experiments to date. A cornerstone of the model, i.e. the symmetry, or invariance, of the theory under gauge transformations, manifestly clashes against the experimental evidence that some of the force–mediators (gauge bosons) are massive, whereas the gauge simmetry would bound them to be massless. In the mid–sixties a solution to this apparent inconsistency was proposed in analogy with symmetry–breaking phenomena occurring in condensed matter physics: the symmetry of the theory is spontaneously broken by the ground state (vacuum) being no longer invariant under an arbitrary gauge transformation. In the context of the SM, the spontaneous symmetry breaking can be achieved, after the introduction of a new scalar field, the so–called Higgs field, via the *Brout–Englert–Higgs mechanism* (BEH) [4, 5, 6, 7, 8, 9], which nicely accounts for the mass of the gauge bosons. The BEH mechanism also naturally allows to introduce mass terms for the fermions by interactions of the elementary chiral fermions with the Higgs field. A consequence of the introduction on the Higgs field and the BEH mechanism is the introduction of new scalar degree(s) of freedom: the physical *Higgs boson*(s). In its minimal version, only one neutral Higgs boson is predicted, whose mass (M_H) is a free parameter of the theory.

First, I will remind the structure of the SM with spontaneously broken symmetry. Constraints on M_H coming from theoretical arguments and from experiments are then presented. The phenomenology of the SM Higgs boson

produced at the LHC is then discussed, with a concise summary of production cross–section and decay widths. Finally, I will outline the Higgs boson phenomenology in a minimal, supersymmetry–oriented, extension of the Higgs sector.

2.1 The Standard Model of strong and electroweak interactions

2.1.1 The Standard Model Lagrangian

The Standard Model is a quantum field theory invariant under the gauge group:

$$G_{SM} = SU(3)_{\mathrm{C}} \times SU(2)_{\mathrm{L}} \times U(1)_{\mathrm{Y}}. \tag{2.1}$$

where $SU(3)_{\mathrm{C}}$ (*color*) is the symmetry group associated with the strong force, and $SU(2)_{\mathrm{L}} \times U(1)_{\mathrm{Y}}$ (*isospin* and *hypercharge*) is the symmetry related to the electroweak interactions.

In a gauge theory, each generator of the group is associated with a spin–1 particle (vector boson), which is the mediator of a fundamental force between the spin–$\frac{1}{2}$ matter particles. In the SM, there are $8 + 3 + 1$ vector bosons. Following the notation of Ref. [10], I denote the gauge fields associated to the three sub–groups of Eq. (2.1) as G_μ^a, $a = 1, ..., 8$, W_μ^a, $a = 1, 2, 3$ and B_μ, respectively. The Lagrangian density of the gauge fields can be expressed in a compact form in terms of the field strengths:

$$
\begin{aligned}
G_{\mu\nu}^a &= \partial_\mu G_\nu^a - \partial_\nu G_\mu^a + g_s f^{abc} G_\mu^b G_\nu^c \\
W_{\mu\nu}^a &= \partial_\mu W_\nu^a - \partial_\nu W_\mu^a + g_2 \epsilon^{abc} W_\mu^b W_\nu^c \\
B_{\mu\nu} &= \partial_\mu B_\nu - \partial_\nu B_\mu,
\end{aligned}
\tag{2.2}
$$

where f^{abc} and ϵ^{abc} are the structure constants of $SU(3)_{\mathrm{C}}$ and $SU(2)_{\mathrm{L}}$, and two of the three adimensional coupling constants of the theory (g_s and g_2) have been introduced. The third coupling (g_1), being associated to the abelian $U(1)_{\mathrm{Y}}$ sub-group, enters only through the interaction with matter fields.

In addition to the gauge bosons, the spectrum of the theory accommodates all the elementary matter particles observed in experiments: *quarks* and *leptons*. These come in three replicas, or *families*. One family is composed by fifteen independent degrees of freedom (Weil spinors):

- the up and down left–handed quarks (Q), with three different colors;

- the up and down right–handed quarks (u_R and d_R), with three different colors;

- the up and down left–handed leptons (L) ;

- the down right–handed lepton (e_R).

They can be conveniently arranged into a multiplet of fields [11]:

$$\{Q(\mathbf{3},\mathbf{2})_{1/3}, L(\mathbf{1},\mathbf{2})_{-1}, u_R(\mathbf{3},\mathbf{1})_{4/3}, d_R(\mathbf{3},\mathbf{1})_{-2/3}, e_R(\mathbf{1},\mathbf{1})_{-2}\} \qquad (2.3)$$

where the quantum numbers have been explicitated. The first (second) number in parenthesis indicates under which representation of the color (isospin) group the fields transform, while the subscript corresponds to the hypercharge. To this multiplet, one should possibly add a right–handed neutrino ($N_R(\mathbf{1},\mathbf{1})_0$) to accommodate massive neutrinos. The right–handed neutrino is however sterile because it does not couple with the gauge fields (it is a singlet under transformations of the group in Eq. (2.1)). Since its presence is irrelevant for the following discussion, all terms involving N_R will be dropped from the Lagrangian and it will not be considered further.

The SM is said to be a chiral theory since it treats left and right handed fermions on a different footing: the left–handed particles are charged under $SU(2)_{\mathrm{L}}$, whereas the right-handed fermions are singlet.

All fields are charged under $U(1)_{\mathrm{Y}}$, but only quarks feel the strong force. The representation in the multiplet basis of the group in Eq. (2.1) is therefore reducible to blocks.

The gauge symmetry dictates the structure of the Lagrangian: to achieve invariance under an arbitrary local transformation of Eq. (2.1), only a few combinations of the fields are allowed. For example, a local transformation of $SU(2)_{\mathrm{L}} \times U(1)_{\mathrm{Y}}$ acts on the left–handed (L), right–handed (R) fermions, and on the vector bosons in the following way [10]:

$$
\begin{aligned}
L(x) &\to e^{i\alpha(x)_a T^a + i\beta(x)Y} L(x), \\
R(x) &\to e^{i\beta(x)Y} R(x) \\
\vec{W}_\mu(x) &\to \vec{W}_\mu(x) - \frac{1}{g_2}\partial_\mu\vec{\alpha}(x) - \vec{\alpha}(x) \times \vec{W}_\mu(x), \\
B_\mu(x) &\to B_\mu(x) - \frac{1}{g_1}\partial_\mu\beta(x),
\end{aligned}
\qquad (2.4)
$$

where $\alpha(x)_a$ and $\beta(x)$ are arbitrary functions, while the T^a (Y) matrices are representations of the $SU(2)_{\mathrm{L}}$ ($U(1)_{\mathrm{Y}}$) generators. A Lagrangian density of

the gauge and of the matter fields of one–family, renormalizable and invariant under an arbitrary local transformation of Eq. (2.1), is provided by:

$$\mathcal{L}_{SM} = -\frac{1}{4}G^a_{\mu\nu}G^{\mu\nu}_a - \frac{1}{4}W^a_{\mu\nu}W^{\mu\nu}_a - \frac{1}{4}B_{\mu\nu}B^{\mu\nu} +$$
$$i\bar{L}D_\mu\gamma^\mu L + i\bar{e}_R D_\mu\gamma^\mu e_R + i\bar{Q}D_\mu\gamma^\mu Q +$$
$$i\bar{u}_R D_\mu\gamma^\mu u_R + i\bar{d}_R D_\mu\gamma^\mu d_R, \tag{2.5}$$

with the covariant derivative D_μ defined as

$$D_\mu\psi \equiv (\partial_\mu - ig_s T_a G^a_\mu - ig_2 \frac{\sigma_a}{2}W^a_\mu - ig_1 \frac{Y}{2}B_\mu)\psi. \tag{2.6}$$

The matrices T_a and σ_a are a particular representation of the generators of $SU(3)_{\rm C}$ and $SU(2)_{\rm L}$, respectively. In the basis where the left–handed neutrino and electron are the first and second element of the isospin doublet, σ_a are chosen to be the three Pauli matrices. The λ_a are taken to be the eight Gell–Mann matrices. The Y matrices are diagonal in the multiplet space.

The first row of Eq. (2.5) describes the dynamic of the gauge fields, with the kinetic, triple and quartic self–interaction terms (the latter two are present only for the non–abelian groups); the second and third rows contain the kinetic lagrangian of the fermions plus the interactions with the gauge fields.

2.1.2   The Brout–Englert–Higgs mechanism

In the attempt to write all allowed gauge–invariant and renormalizable combination of matter and gauge fields, any mass term is automatically excluded (see Eq. (2.5)). This is true both for the vector bosons and the fermions. Therefore, the spectrum of the theory described by the right–hand side of Eq. (2.5) consists of massless particles.

The inclusion of new scalar fields with the correct quantum numbers allows other gauge–invariant terms to come in. By injecting a $SU(2)_{\rm L}$ doublet of complex scalar fields:

$$\Phi = \begin{pmatrix} \phi^+ \\ \phi^0 \end{pmatrix} = \begin{pmatrix} \phi_1 + i\phi_2 \\ \phi_3 + i\phi_4 \end{pmatrix} \tag{2.7}$$

with $Y_\Phi = 1$, three (+three) more terms pop up:

$$\mathcal{L}_F = -\lambda_e \bar{L}\Phi e_R - \lambda_d \bar{Q}\Phi d_R - \lambda_u \bar{Q}(i\sigma_2)\Phi^* u_R + h.c. \tag{2.8}$$

where the λ_i are adimensional Yukawa couplings and become unitary matrices when more families are considered. By adding to the right–hand side of

Eq. (2.8) a kinetic Lagrangian for Φ, with the usual $\partial_\mu \leftrightarrow D_\mu$ replacement, the Φ fields propagate and interact with the gauge fields.

In even more generality, the scalar sector can be supplemented with a gauge–invariant potential $V(\Phi, \Phi^*)$. In order for the theory to be renormalizable, no operators with dimension larger than four should be present at tree–level, which singles out a limited number of possible terms in $V(\Phi, \Phi^*)$. The most general scalar Lagrangian is then given by:

$$\mathcal{L}_S = (D^\mu \Phi^\dagger)(D_\mu \Phi) - \mu^2 \Phi^\dagger \Phi - \lambda (\Phi^\dagger \Phi)^2 \tag{2.9}$$

where λ needs to be positive for the potential to be bounded from below and μ^2 is a mass term for the Φ field.

The ground state (vacuum) of the theory is defined as the state where the energy density is at a minimum. The minimum of the scalar potential in Eq. (2.9) depends on the sign of μ^2: if $\mu^2 > 0$, then the ground state $|0\rangle$ satisfies: $\langle 0| \Phi |0\rangle = (0, 0)$.
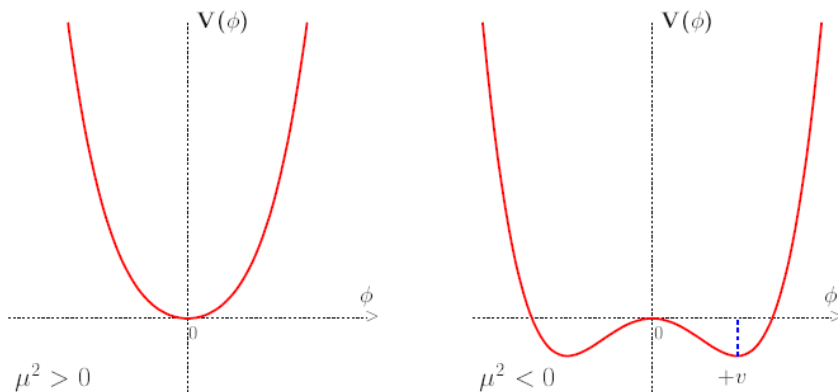
Figure 2.1: The one-dimensional potential $V(\phi)$ for different signs of μ^2

On the contrary, for negative values of μ^2, the vacuum state on which the expectation value of $V(\Phi, \Phi^*)$ is at a minimum satisfies $\langle 0| \Phi |0\rangle \neq (0, 0)$. This is illustrated in Fig. 2.1 for the simple case of a one–dimensional potential $V(\phi)$. By defining the *vacuum expectation value* of the Higgs doublet

$$v \equiv \left(\frac{-\mu^2}{\lambda} \right)^{1/2}, \tag{2.10}$$

all states on which the expectation value of Φ is related to

$$\begin{pmatrix} 0 \\ \frac{v}{\sqrt{2}} \end{pmatrix}$$

14

by a rotation of $SU(2)$, correspond to a minimum of $V(\Phi, \Phi^*)$. The ground state is clearly no longer invariant under an arbitrary transformation of the $SU(2)_\mathrm{L} \times U(1)_\mathrm{Y}$ sub–group. The $SU(2)_\mathrm{L} \times U(1)_\mathrm{Y}$ symmetry has been spontaneously broken.

The neutral component of the doublet is chosen to develop $v \neq 0$, so that the electric charge can be conserved. To see the effect of the minimum being displaced from zero, it is convenient to expand Φ around the new minimum by means of a clever parametrization:

$$\Phi(x) = e^{i\pi_a(x)\sigma_a/v} \begin{pmatrix} 0 \\ \frac{1}{\sqrt{2}}(v + H(x)) \end{pmatrix} \tag{2.11}$$

where the ϕ_i have been mixed into $\vec{\pi}(x)$ and $H(x)$. By a gauge transformation, the $\vec{\pi}(x)$ fields are reabsorbed and only H survives in the scalar potential. Terms proportional to $\partial_\mu \vec{\pi}(x)$ will stem from the kinetic Lagrangian $(D^\mu\Phi^\dagger)(D_\mu\Phi)$, but no mass terms $\propto \pi_i^2$: three massless bosons have appeared. At the same time, the transformation acts on the gauge fields as in Eq. (2.4), producing terms that exactly cancel the $\vec{\pi}(x)$ from the Lagrangian. These particles correspond to the would–be Goldstone bosons originating from the spontaneous breaking of the symmetry: indeed, the Goldstone theorem [12, 13, 14, 15] asserts that for every spontaneously broken continuous symmetry, massless spin–0 particles (Goldstone bosons) are generated in number equal to the generators of the symmetry group that have been broken. A generator T is said to be broken if the vacuum is not invariant under T:

$$T\,|0\rangle \neq |0\rangle$$

By the Brout–Englert–Higgs (BEH) mechanism [4]-[9], all generators of $SU(2)_\mathrm{L} \times U(1)_\mathrm{Y}$ *but* the combination $T_3 + Y/2$ are broken, and three Goldstone bosons appear in the spectrum. It is only in a gauge theory that these scalar bosons get re–absorbed by the gauge bosons as their longitudinal degrees of freedom.

By a proper rotation that diagonalizes the mass matrix of the gauge bosons, three combinations of mass–eigenstates are defined, together with

the fermion current they interact with:

$$W_\mu^\pm \equiv \frac{W_\mu^1 \mp iW_\mu^2}{\sqrt{2}}, \ M_W = \frac{1}{2}vg_2$$

$$\Rightarrow J_\mu^+ = \frac{1}{2}\bar{f}_u\gamma_\mu(1-\gamma_5)f_d$$

$$Z_\mu \equiv \frac{g_2W_\mu^3 - g_1B_\mu}{\sqrt{g_1^2 + g_2^2}}, \ M_Z = \frac{1}{2}v\sqrt{g_1^2 + g_2^2} \tag{2.12}$$

$$\Rightarrow J_\mu^Z = \frac{1}{4}\bar{f}\gamma_\mu[(2T_f^3 - 4Q_f\sin^2\theta_W) - 2T_f^3\gamma_5]f$$

$$A_\mu \equiv \frac{g_2W_\mu^3 + g_1B_\mu}{\sqrt{g_1^2 + g_2^2}}, \ M_A = 0$$

$$\Rightarrow J_\mu^A = Q_f\bar{f}\gamma_\mu f$$

with $\sin^2\theta_W \equiv 1 - \frac{M_W^2}{M_Z^2}$ and $Q_f \equiv T_f^3 - \frac{Y_f}{2}$. The interaction between the fermions and the W, Z and A fields are governed by the neutral- and charged-current Lagrangians:

$$\mathcal{L}_{NC} = g_2\sin\theta_W J_\mu^A A^\mu + \frac{g_2}{\cos\theta_W}J_\mu^Z Z^\mu$$

$$\mathcal{L}_{CC} = \frac{g_2}{\sqrt{2}}(J_\mu^+ W^{+\,\mu} + J_\mu^- W^{-\,\mu}) \tag{2.13}$$

The BEH mechanism has given mass to three of the gauge bosons ($W^\pm$, Z) and one (the photon, γ) has remained massless, It still remains to generate masses for the fermions. This happens by virtue of the Yukawa interactions in Eq. (2.8): by simply replacing Φ with $(0, 1/\sqrt{2}(v + H))$, a Dirac mass term $m_{f\,i}\bar{f}f$, with

$$m_{f\,i} \equiv \frac{\lambda_i v}{\sqrt{2}},$$

is generated for a fermion of type $i = e, u, d$. When the three families of leptons and quarks are added together, the λ_i couplings become unitary matrices in the family space. By means of a $SU(3)$ rotation, λ_e can be made diagonal. The same happens for either λ_u or λ_d, but not for both: in order to diagonalize all λ matrices, thus having canonical mass terms for the fermions, the up and down-type quarks of the three families will be mixed in the charged weak current by a unitary matrix, known as the Cabibbo–Kobaiashi–Maskawa (V_{CKM}) matrix [16, 17]. The individual quark flavors are no longer a symmetry of the theory, in agreement with the experiment.

2.1.3 The Higgs particle in the Standard Model

Expanding the Higgs doublet around the minimum, Eq. (2.9) becomes

$$\mathcal{L}_H = \frac{1}{2}(\partial_\mu H)(\partial^\mu H) - \lambda v^2 H^2 - \lambda v H^3 - \frac{\lambda}{4}H^4 \qquad (2.14)$$

which implies that the physical Higgs boson has a mass

$$M_H = \sqrt{2\lambda}v,$$

and a cubic and quartic self–interaction with a vertex

$$g_{H^3} = 3\frac{M_H^2}{v} \text{ and } g_{H^4} = 3\frac{M_H^2}{v^2}$$

The μ and λ parameters of the bare Lagrangian can be traded for the Higgs boson mass (M_H) and the vacuum expectation value (v). The latter can be put in relation with the W boson mass (M_W) and with an other experimental observable, the Fermi constant (G_μ). This is done by reinterpreting the effective Fermi Lagrangian describing the charged weak decay as the low–energy limit of the charged–current interaction of Eq. (2.12). By doing so, the dimensionful parameter G_μ, that can be very precisely measured in e.g. the $\mu^- \to e^- \nu_\mu \bar{\nu}_e$ decay, is identified with

$$G_\mu = \frac{g_2^2 \sqrt{2}}{8M_W^2}$$

By making use of Eq. (2.12), the above relation implies that

$$v = \frac{1}{(\sqrt{2}G_\mu)^{1/2}} \approx 246 \text{ GeV}.$$

The only unknown parameter of the Higgs sector is therefore the mass of the physical Higgs boson.

The Yukawa couplings in Eq. (2.8) determine the strength of the interaction between the Higgs boson and the fermions:

$$g_{Hff} = \frac{m_f}{v} \equiv (\sqrt{2}G_\mu)^{1/2}m_f, \qquad (2.15)$$

while the couplings of the Higgs boson to gauge vectors can be read from the covariant derivative:

$$g_{HVV} = -2\frac{M_V^2}{v} \equiv -2(\sqrt{2}G_\mu)^{1/2}M_V^2, \quad g_{HHVV} = -2\frac{M_V^2}{v^2} \equiv 2\sqrt{2}G_\mu M_V^2 \tag{2.16}$$

Equations (2.15) and (2.16) show that the Higgs boson couples to the SM particles with strength proportional to the particle mass, for fermions, and to the mass squared, for gauge bosons.

The Higgs boson in the SM is a definite CP = 1 eigenstate, and is assigned the quantum numbers $J^{CP} = 0^{++}$.

2.1.4 Theory predictions

The theory is not predictive of the fermion masses, because as many adimensional Yukawa couplings as fermion species were introduced.

The symmetry breaking mechanism predicts that the coupling of the fermions to the gauge bosons are non–trivial functions of the quantum numbers and of the fundamental couplings of the theory. From Eq. (2.12), the vector and axial couplings of the gauge bosons to a fermion f are derived to be

$$v_f = \frac{2T_f^3 - 4Q_f \sin^2 \theta_W}{4 \sin \theta_W \cos \theta_W}, \quad a_f = \frac{2T_f^3}{4 \sin \theta_W \cos \theta_W} \tag{2.17}$$

where $\sin \theta_W$ has already been introduced in Eq. (2.8). Likewise, the trilinear couplings between the electroweak gauge bosons are predicted to be

$$g_{WWA} = g_2 \sin \theta_W \equiv e, \quad g_{WWZ} = e \cos \theta_W / \sin \theta_W$$

where the electric charge e, that controls the strength of the neutral current interaction $J_\mu^A A^\mu$, has been introduced.

From the definition of $\sin \theta_W$, one obtains that

$$\frac{M_W^2}{\cos^2 \theta_W M_Z^2} \equiv \rho \tag{2.18}$$

is equal to one at tree–level. This is a non trivial implication of the Higgs potential structure: if the spontaneous breaking of the SM symmetry had been triggered by, for example, a triplet of scalar fields getting non–zero v, then this result wouldn't old anymore (see e.g. [11]).

2.2 Constraints on the Higgs boson mass

The Higgs boson mass M_H is the only parameter of the SM Lagrangian after spontaneous symmetry breaking that has not yet been measured. Constraints on M_H can however be set from both theoretical arguments and experiments.

2.2.1 Theory constraints: unitarity, triviality and vacuum stability

The request for mathematical consistency of the SM up to a given energy scale constrains the M_H parameter space. Indeed, unitarity will be eventually violated at very large energies if the Higgs boson is too heavy. This can be verified by studying the high–energy behavior of the scattering amplitude for two gauge bosons, e.g. $W^+W^- \to W^+W^-$. At leading order, this happens via the quartic-interaction term plus all diagrams where a Higgs boson is exchanged between the incoming bosons (Fig. 2.2).
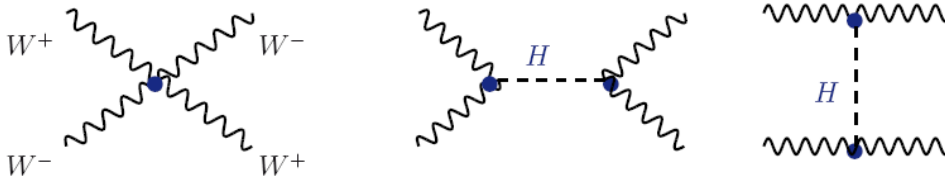
Figure 2.2: Some diagrams contributing at leading order to the WW scattering.

The amplitude is no longer growing with the energy of the incoming W bosons, as it is the case for the SM without Higgs boson: in the limit $s \gg M_W^2$ one has [18]

$$\mathcal{A}(W^+W^- \to W^+W^-) \to \frac{1}{v^2}\left[s + t - \frac{s^2}{s - M_H^2} - \frac{t^2}{t - M_H^2}\right] \qquad (2.19)$$

where s and t indicate the usual Mandelstan variables that parametrize the scattering. The amplitude in Eq. (2.19) is noticeably finite in the $s \to \infty$ limit. The Optical Theorem [19] states that for any scattering amplitude $\mathcal{A}$, the partial amplitudes a_l, defined such that

$$\mathcal{A} = 16\pi \sum_{l=0}^{\infty}(2l + 1)P_l(\cos\theta)a_l \qquad (2.20)$$

must satisfy the requirement

$$|a_l|^2 = \text{Im}(a_l) \Leftrightarrow |\text{Re}(a_l)| < \frac{1}{2} \qquad (2.21)$$

as imposed by the unitarity of the scattering matrix. By identifying the right–hand sides of Eq. (2.19) and (2.20), it can be shown that for the WW

scattering at high energy, the 0th partial amplitude, is equal to

$$a_0 \approx -\frac{M_H^2}{8\pi v^2}$$

which exceeds the unitarity bound (2.21) for $M_H \lesssim 870$ GeV. By imposing the same argument to the largest a_0 among all possible scattering processes between vectors and Higgs bosons, the upper bound can be tightened up to $M_H \lesssim 710$ GeV.

A consistent bound can be derived on purely theoretical arguments by requiring the theory to remain perturbative up to very large energies: the perturbativity gets jeopardized if the Higgs boson is too heavy because the coupling constant $\lambda = M_H^2/v^2$ becomes increasingly larger, thus ruining the convergence of the perturbative expansion.

The larger is the value of λ at the electroweak scale, the sooner it will reach the Landau pole, i.e. the scale Λ_C at which $\lambda(\Lambda_C^2) \to \infty$. The singular behavior in the running of λ can be proved by solving the related Renormalization Group Equation (RGE) [19]. At one–loop, and considering only the contributions from the Higgs boson self–couplings [10]:

$$\lambda(Q^2) = \lambda(v^2) \left[1 - \frac{3}{4\pi^2}\lambda(v^2)\log\frac{Q^2}{v^2} \right]^{-1}$$

which implies that the Landau pole is reached at a scale

$$\Lambda_C = v \exp\left(\frac{2\pi^2 v^2}{3M_H^2} \right).$$

This breakdown scale is interpreted as the limit of validity (cut–off) of the incomplete theory, i.e. where some new physics should show up and restore the perturbativity. For the theory to be valid up to $\Lambda_C \sim 10^{16}$ GeV (10^3 GeV), the Higgs mass should not exceed ~ 200 GeV (1 TeV).

On the other hand, if the coupling λ at the electroweak scale is too small ($\lambda \ll \lambda_t, g_1, g_2$), its running becomes sensitive to the contributions stemming from fermions (top) and gauge bosons. The top quark may eventually drive λ to negative values for energies larger than some cut–off Λ_C, which would make the potential V not bounded from below and the vacuum unstable ($V(Q^2) < V(v^2)$ for $Q^2 > \Lambda_C^2$). The cut–off scale depends on the value of M_H: the smaller M_H, the smaller $\lambda(v^2)$, hence the smaller Λ_C. For $\Lambda_C = 10^3$ (10^{16}) GeV, the lower Higgs mass bound is about 70 (130) GeV. The combined triviality and vacuum stability bounds on the M_H vs Λ_C plane, after including the known higher–order effects in the RGE equation, are shown in Fig. 2.3.
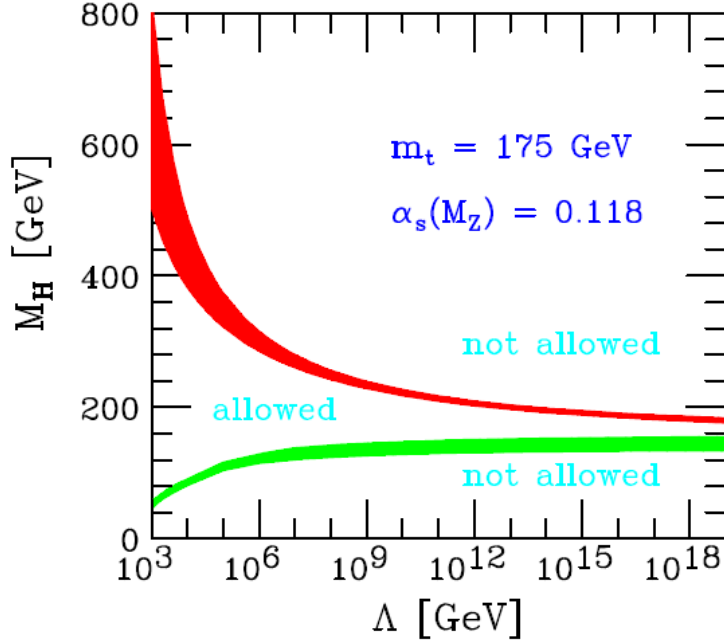
Figure 2.3: Triviality and vacuum stability bounds in the M_H vs Λ_C plane for $m_t = 175 \pm 6$ GeV and $\alpha_s(M_Z) = 0.118 \pm 0.002$ (from Ref. [20])

2.2.2 Experimental constraints

The four experiments operating at LEP2 have measured a lower bound on M_H [21]. The main production mechanism of the Higgs boson at a e^+e^- collider is shown in Fig. 2.4. The largest center–of–mass energy reached at LEP2 ($\sqrt{s} = 209$ GeV) made it possible to directly produce an Higgs boson in association with a Z, provided that $M_H \lesssim \sqrt{s} - M_Z \approx 117$ GeV.
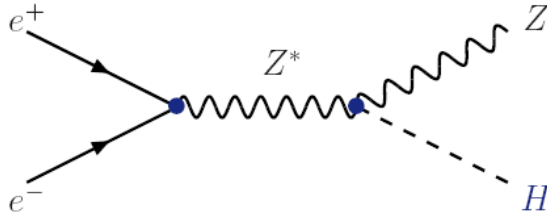
Figure 2.4: The main production mechanism of the Higgs boson at LEP2.

The leading order cross–section for this process is given by [10]

$$\sigma(e^+e^- \to ZH) = \frac{G_\mu^2 M_Z^4}{96\pi s}[1 + (1 - 4\sin^2\theta_W)^2]\lambda^{1/2}\frac{\lambda + 12M_Z^2/s}{(1 - M_Z^2/s)^2} \qquad (2.22)$$

21

with $\lambda = [(1 - M_H^2/s - M_Z^2/s)^2 - 4M_H^2 M_Z^2/s^2]$. For $M_H = 115$ GeV, the cross–section value is of order 100 nb at the LEP2 energy: with the total luminosity integrated at that energy ($\mathcal{L} = 0.1$ fb^{-1}), about 10 events were expected. In the absence of a positive observation, the exclusion limit $M_H > 114.4$ GeV at 95% CL was set, to be compared with an expectation of $M_H > 115.3$ in the absence of a signal (Fig. 2.5).
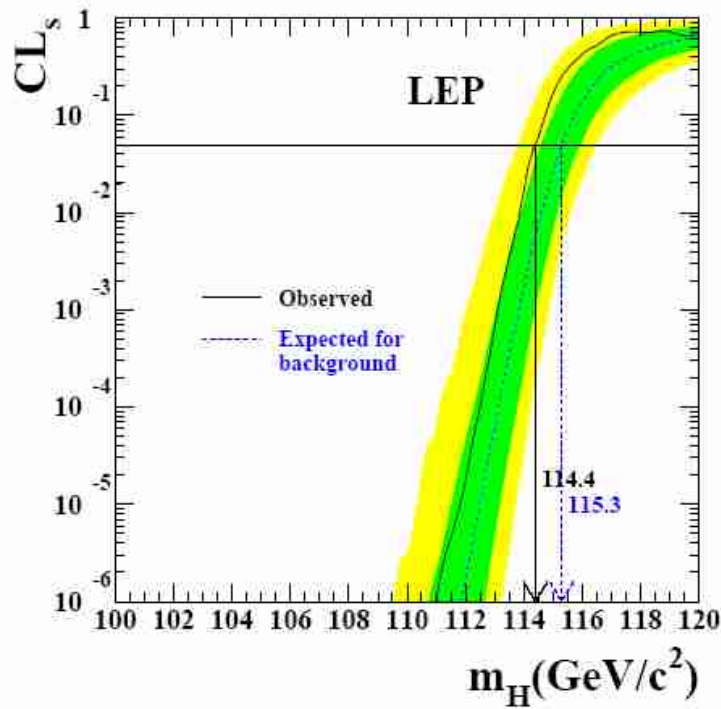
Figure 2.5: The expected and observed values of CLs on the exclusion of the SM Higgs at LEP2 as a function of M_H: all values below $M_H = 114.4$ GeV are excluded at more than 95% confidence level (from Ref. [21]).

More recently, experiments at hadron colliders have attained an unprecedented sensitivity to the SM Higgs boson. I will concentrate here on the TeVatron and LHC preliminary results made public following the EPS international conference in July 2011, thus before the LHC had provided the bulk of the luminosity used in this thesis. An overview of the current direct constraints and recent observations will be presented in Chapter 7.

The CDF and D0 combined results on the SM Higgs boson search, based on up to 8.6 fb^{-1} of $p\bar{p}$ collisions at $\sqrt{s} = 1.96$ TeV, are documented in Ref. [22]. The Higgs boson is searched in the $b\bar{b}$, W^+W^-, ZZ, $\tau^+\tau^-$, and $\gamma\gamma$ decay modes. The upper limits on Higgs boson production are factors of 1.17, 1.71,

and 0.48 times the values of the SM cross–section for Higgs bosons of mass $M_H = 115$, 140, and 165 GeV, respectively. The corresponding median upper limits expected in the absence of Higgs boson production are 1.16, 1.16, and 0.57. There is a 1σ excess of data events with respect to the background estimation in searches for the Higgs boson in the mass range $[125, 155]$ GeV. The SM Higgs boson is excluded at 95% CL in the region $[156, 177]$ GeV, compared with an expected exclusion region of $[148, 180]$ GeV (Fig. 2.6).

Figure 2.6: Observed and expected (median, for the background–only hypothesis) 95% CL upper limits on the ratios to the SM cross section, as functions of the Higgs boson mass for the combined CDF and D0 analyses (from Ref. [22]).

The ATLAS Collaboration has reported a combination of searches for the SM Higgs boson based on up to 1.21 fb^{-1} of pp collision data at $\sqrt{s} = 7$ TeV [23]. The following decay modes are considered: $H \to \gamma\gamma$, $H \to WW^{(*)} \to 2\ell 2\nu$, $H \to WW \to \ell\nu jj$, $H \to ZZ^{(*)} \to 4\ell$, $H \to ZZ \to 2\ell 2\nu$, $H \to ZZ \to 2\ell jj$, and $VH(\to b\bar{b})$, where $\ell = e, \mu$. The Higgs boson mass ranges $[155, 190]$ GeV and $[295, 450]$ GeV are excluded at the 95% CL, which is similar to the expected exclusion mass ranges in the absence of a signal of $[136, 196]$ GeV and $[327, 443]$ GeV (Fig. 2.7). In the low mass range (120–140 GeV) an excess of events with a significance of approximately 2.8σ above the background expectation is observed. The excess is driven mostly by the $H \to WW^{(*)} \to 2\ell 2\nu$ channel. The probability for such an excess to arise

from background, for the combination of all channels and in the range of Higgs boson mass hypotheses searched for, is estimated to be $\approx 8\%$.

Figure 2.7: Observed and expected (median, for the background–only hypothesis) 95% CL upper limits on the ratios to the SM cross section, as functions of the Higgs boson mass for the combined ATLAS analyses (from Ref. [23]).

The CMS Collaboration has presented results from a combination of six independent search analyses, namely $H \to \gamma\gamma$, $H \to \tau\tau$, $H \to WW^{(*)} \to 2\ell2\nu$, $H \to ZZ^{(*)} \to 4\ell$, $H \to ZZ \to 2\ell2\nu$, and $H \to ZZ \to 2\ell jj$. The analyses are based on up to 1.1 fb^{-1} of pp collision data at $\sqrt{s} = 7$ TeV [24]. The conclusion of this combination is that the SM Higgs boson is excluded at 95% CL in two mass ranges $[149, 206]$ and $[300, 440]$ GeV, as well as several narrower intervals in between (Fig. 2.8). The expected exclusion in the absence of a signal is $[127, 420]$ GeV. The observed CLs values are about 2σ larger than expectation in the mass range of $[130, 170]$ GeV, which is largely driven by a broad excess in the $H \to WW^{(*)} \to 2\ell2\nu$ channel.

Indirect constraints on the Higgs boson mass have been derived from electroweak precision measurements [25], coming mostly from LEP, SLC, and the TeVatron experiments. At leading–order, the Higgs boson contributes to the
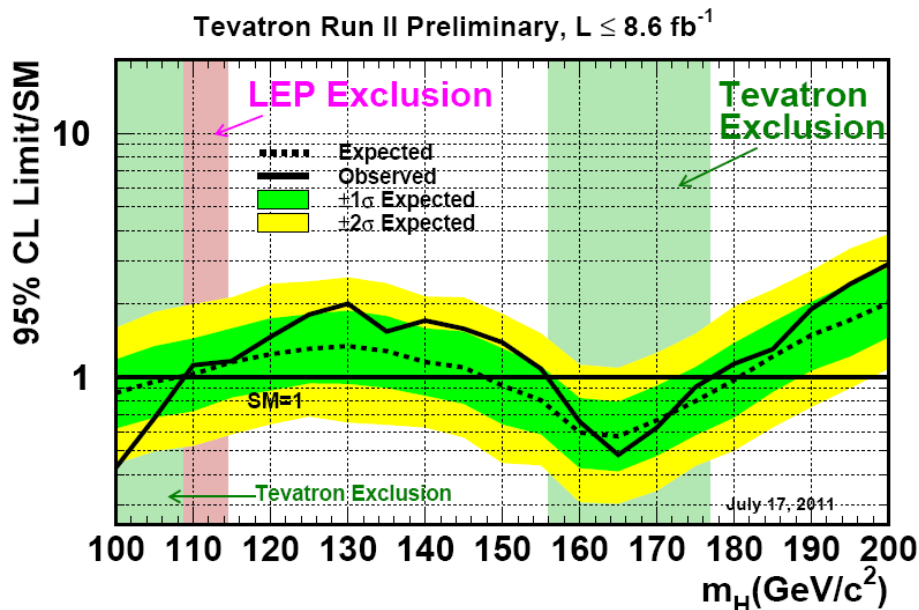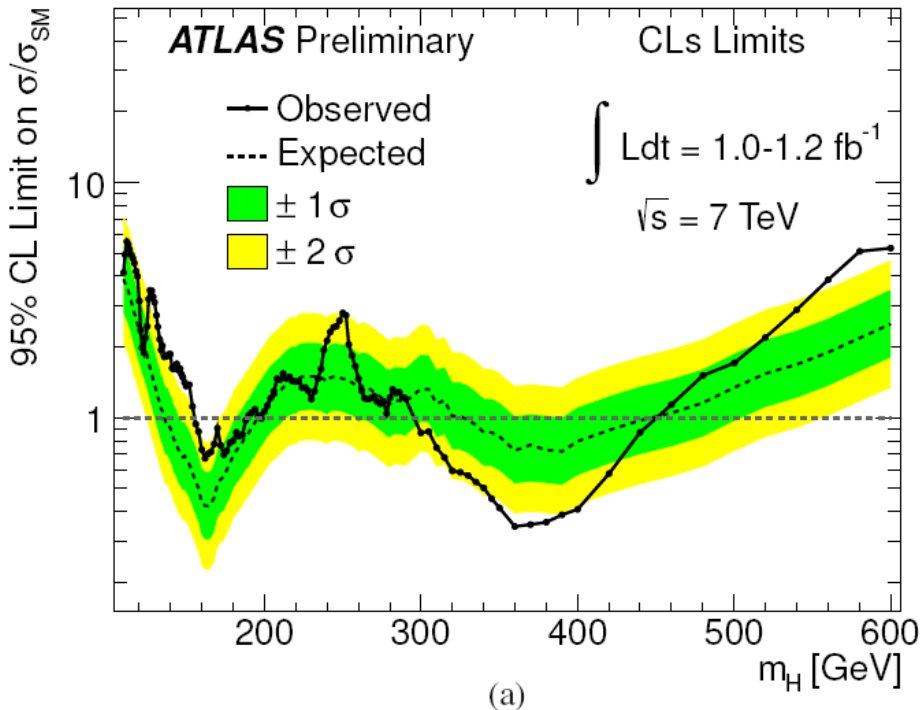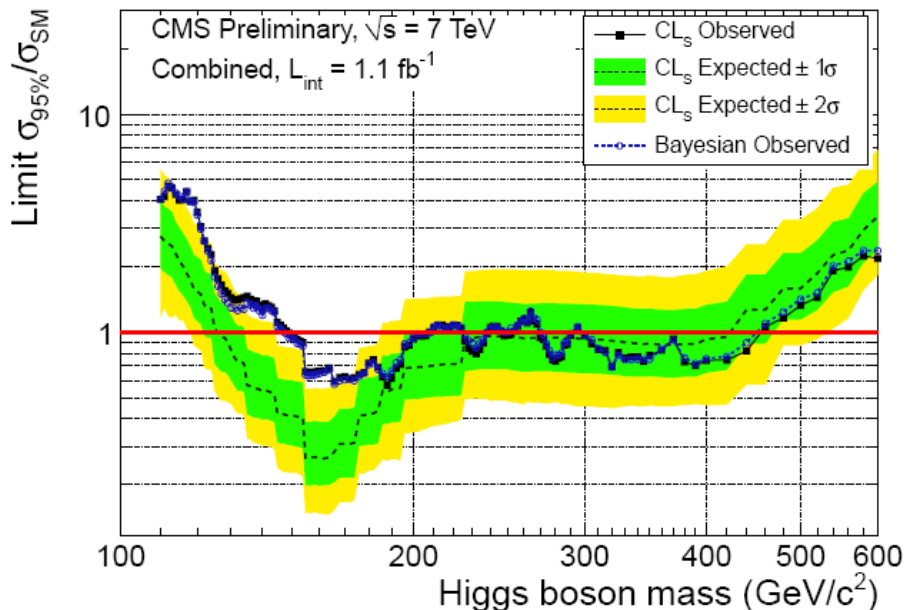
Figure 2.8: Observed and expected (median, for the background–only hypothesis) 95% CL upper limits on the ratios to the SM cross section, as functions of the Higgs boson mass for the combined CMS analyses (from Ref. [24]).

radiative correction of electroweak observables with terms proportional to $\log M_H$. By fitting the electroweak measurements to their theoretical prediction, expanded up to a suitable order in the perturbative series, constraints to the Higgs boson mass are obtained. The order to which calculations have to be expanded must be large enough to make the Higgs boson contributions appear and make the theoretical uncertainties due to the missing orders smaller than the experimental resolutions.

An update of the SM fit to electroweak observables has made public by the G–fitter Collaboration [26] following the EPS conference in July 2011. Based on these results, the departure of the χ^2 of the global fit from its minimum ($\Delta\chi^2$) is shown in Fig. 2.9 as a function of the Higgs boson mass under test. A best–fit value of $M_H = 96^{+31}_{-24}$ GeV is measured, with an upper limit $M_H < 169$ GeV at 95% CL. Shaded areas in the plot show the regions excluded at 95% CL by LEP2 and from the preliminary results of the TeVatron. Focusing here on the indirect constraints, the outcome of the fit indicates that values of M_H larger than about $2M_W$ are highly disfavored by precision data, and that the preferred value for M_H sits around 100 GeV.
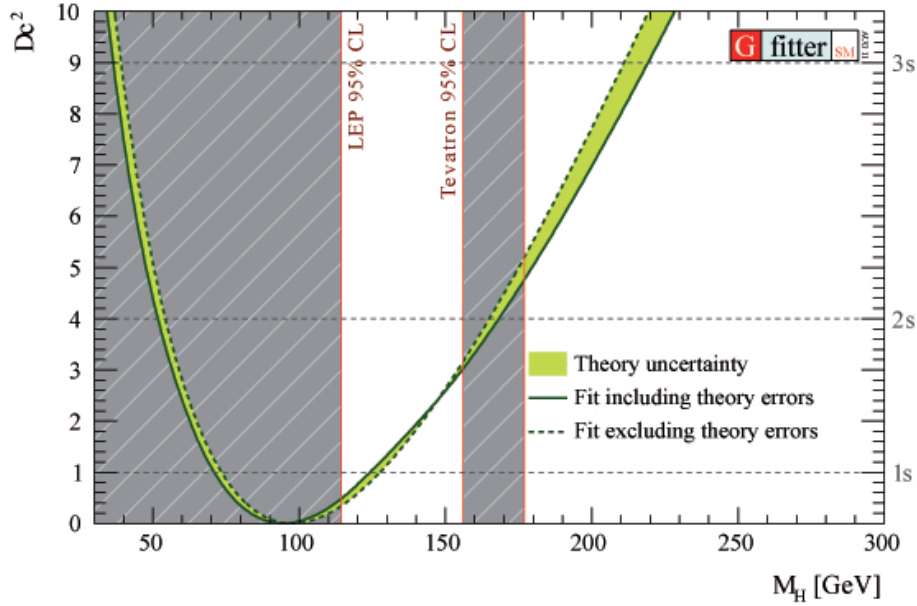
Figure 2.9: $\Delta\chi^2$ of the fit to electroweak observables as a function of M_H. The solid (dashed) line is obtained when including (ignoring) theoretical errors [27].

2.3 Decays of the Standard Model Higgs boson

For a given value of M_H, the decay widths of the SM Higgs boson are univocally determined. At first order, the hierarchy in the decay channels reflects the strength of the Higgs boson coupling to the decay particles, which is proportional to their mass, for fermions, or to their mass squared, for vector bosons.

The Higgs boson decay into a vector boson $V = W^{\pm}, Z$ is mediated at leading order by the S-wave coupling:

$$\mathcal{L}_{HVV} = (\sqrt{2}G_{\mu})^{1/2}M_V^2 HV_{\mu}V^{\mu} \tag{2.23}$$

Depending on M_H, the decay to vector bosons is a two, three or four body process.

For $M_H > 2M_V$, the Born width into a pair of on-shell vectors V is given

by

$$\Gamma_{Born}(H \to VV) = \frac{G_\mu M_H^3}{16\sqrt{2}\pi} \delta_V \sqrt{1 - 4\frac{M_V^2}{M_H^2}} \left(1 - 4\frac{M_V^2}{M_H^2} + 12\left(\frac{M_V^2}{M_H^2}\right)^2\right)$$

(2.24)

where $\delta_V = 2$ (1) for $V = W$ (Z) accounts for the (un)distinguishability of the final–state particles [10].

For $M_H \gg M_V$, the decay width grows like $\sim M_H^3$. In fact, in this limit the matrix element squared is dominated by longitudinally polarized final states and is therefore proportional to M_H^4, while the phase–space flux goes like $\sim M_H^{-1}$.

Because the Higgs boson is scalar, the differential decay width $d\Gamma/d\Omega$ is simply proportional to $\sin\theta$, with θ azimuthal angle of V with respect to a given axis in the Higgs rest frame.

The decay width into longitudinally polarized vectors dominates for $M_H \gg M_V$ as a consequence of the HVV coupling:

$$\epsilon_{1L\,\mu}\epsilon_{2L}^\mu \propto p_{1\,\mu}p_2^\mu \sim M_H^2/M_V^2.$$

At the threshold ($M_H = 2M_V$), the transverse and longitudinal polarization states are democratically populated: $\Gamma_L \approx 2\Gamma_T$.

For $M_H \lesssim 2M_V$, three and, to a lesser extent, four body decays, with at least one off–shell vector decaying to light fermions, are still sizeable when compared to a two–body $H \to f\bar{f}$ decay. This is a consequence of the HVV couplings being in general larger than the $Hf\bar{f}$ coupling. The $H \to VV^*$ decay prefers final-states where M_V^* is close to its kinematically allowed maximum and both V and V^* have small momentum in the H rest frame.

The Higgs boson decay to a fermion pair ($H \to f\bar{f}$) is mediated at tree–level by the coupling

$$\mathcal{L}_{Hf\bar{f}} = (\sqrt{2}G_\mu)^{1/2}m_f H\bar{f}f$$

(2.25)

The Born decay width is given by

$$\Gamma_{Born}(H \to f\bar{f}) = \frac{G_\mu N_C}{4\sqrt{2}\pi} M_H m_f^2 \left(1 - 4\frac{m_f^2}{M_H^2}\right)^{3/2}$$

(2.26)

where the m_f^2 factor comes from the coupling in Eq. (2.25), and

$$\beta^3 \equiv (1 - 4\frac{m_f^2}{M_H^2})^{3/2}$$

is the cube of the fermions velocity in the Higgs rest frame. As pointed out in Ref. [10], the β^3 factor, which induces a very sharp suppression near the kinematical threshold $M_H \approx 2m_f$, is a consequence of the CP–even nature of the $Hf\bar{f}$ coupling, whereas a pseudo–scalar coupling gives a milder suppression $\propto \beta$. The Born width of Eq. (2.26) is proportional to M_H in the limit $M_H \gg m_f$: the matrix element $|\bar{f}f|^2$ is proportional to M_H^2, while the phase–space flux goes like M_H^{-1}.

For decays into light quarks, QCD radiative corrections can be very important, especially for $M_H \gtrsim 100$ GeV, reducing the Born width by a factor 2 to 4. The dominant effect comes from the running of the quark mass m_f, which decreases at large energies. In particular, the c and b quarks mass at the M_H scale are a factor ~ 2 and ~ 1.5 smaller than the respective pole mass.

The SM Lagrangian does not contain tree–level couplings that can mediate the decay $H \to gg$, $H \to \gamma\gamma$ or $H \to Z\gamma$, where g (gluon) and γ (photon) are the standard notation for the quanta of the G_μ^a and A_μ fields, respectively. This happens because neither the gluon nor the photon are massive, therefore they do not couple directly to the Higgs field. Nevertheless, these couplings can be generated at the quantum level (Fig. 2.10).

Naively, the loop–induced decays should be less important than decays to fermions or gauge bosons (which happen already at tree–level), because they are suppressed by two extra powers of the coupling constants (α_s or α). The suppression is however mitigated by the large coupling of the Higgs boson to the virtual particles propagating into the loop. Ultimately, some of the loop–induced decays compete, at low M_H, with the tree–level decays.

Because of its very clean signature, the decay $H \to \gamma\gamma$ is of particular importance in the context of an experimental detection of the Higgs boson. It is a loop–induced process and the dominant contributions to it arise from W and top quarks propagating in the loop. The Born decay width is given by [10]

$$\Gamma_{Born}(H \to \gamma\gamma) = \frac{G_\mu \alpha^2 M_H^3}{128\sqrt{2}\pi^3} \left| \sum_f N_C Q_f^2 A_{1/2}^H(\tau_f) + A_1^H(\tau_W) \right|^2 \qquad (2.27)$$

where $\tau_i = M_H^2/4M_i^2$ and $A_{1/2}^H(\tau_f)$, $A_1^H(\tau_W)$ are form factors for the fermions and vectors, respectively. The fermion form factors in Eq. (2.27) are normalized such that $A_{1/2}(\tau_f) \to 4/3$ if $\tau_f \ll 1$, i.e. when M_H is far below the threshold for decay into a pair of real fermions f, whereas it vanishes in the opposite limit, i.e. when M_H is much larger than the fermion mass. In the latter case, the contribution to the decay width arising from light fermions is negligible. This is not the case for the vector form factor $A_1(\tau_W)$, which
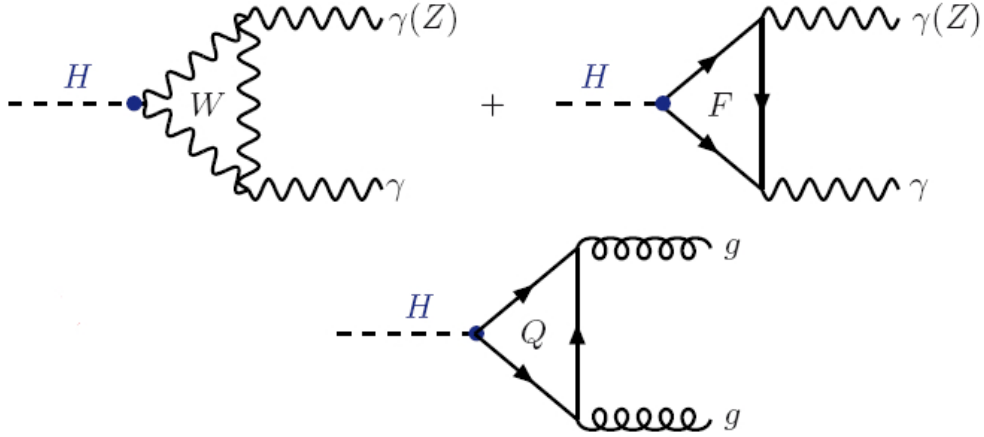
Figure 2.10: Leading order diagrams contributing to the loop–induced decays $H \to gg$ and $H \to \gamma\gamma(Z)$.

is finite in the $\tau_W \to \infty$ limit, implying that the partial width ultimately increases as M_H^3 for large M_H. The W and top contributions have opposite sign, and the Born width is dominated by the former for $M_H \lesssim 2M_W$ (Fig. 2.11).
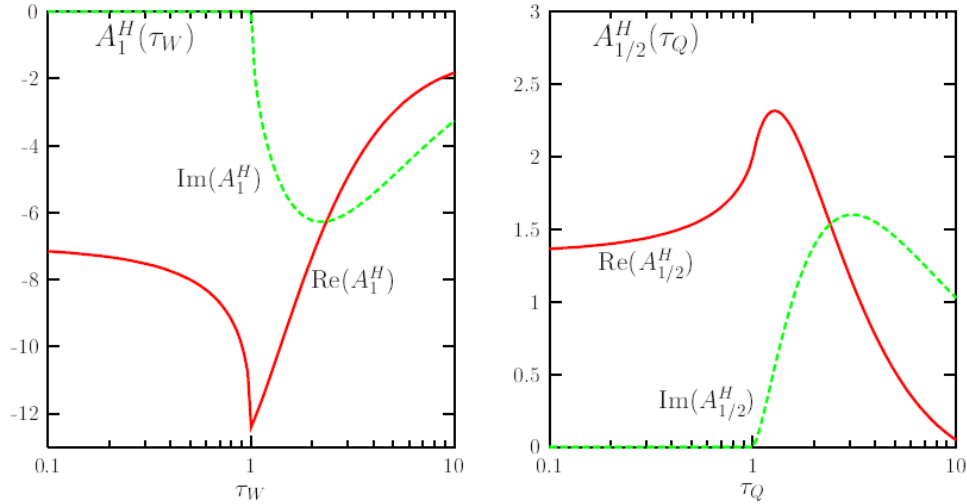
Figure 2.11: Real and Imaginary part of the form factors $A_{1/2}^H$ and A_1^H in the $H \to \gamma\gamma$ decay as a function of $\tau_i = M_H^2/4M_i^2$ [10].

The process $H \to Z\gamma$ is similar to the di–photon decay, but this time M_H needs to exceed M_Z. In the limit $M_H \gg M_Z$, the $H \to Z\gamma$ and $H \to \gamma\gamma$ decay widths are equivalent, modulo the different couplings of the Z boson to the W and top quark.

The Higgs boson decay into a pair of gluons is mediated by loops involving quarks. Again, the contribution arising from the top quark, and, to a lesser extent, the bottom quark, dominates in the loop because of the large y_t and y_b Yukawa couplings. The Born width is given by [10]:

$$\Gamma_{Born}(H \to gg) = \frac{G_\mu \alpha_S^2 M_H^3}{36\sqrt{2}\pi^3} \left| \frac{3}{4} \sum_Q A_{1/2}^H(\tau_Q) \right|^2 \tag{2.28}$$

where the quark form factor $A_{1/2}^H(\tau_Q)$ is again normalized such that it approaches $4/3$ (0) in the $\tau_Q \ll 1 \ (\gg 1)$ limit.

The total width of the SM Higgs boson as a function of M_H is shown in Fig. 2.12.
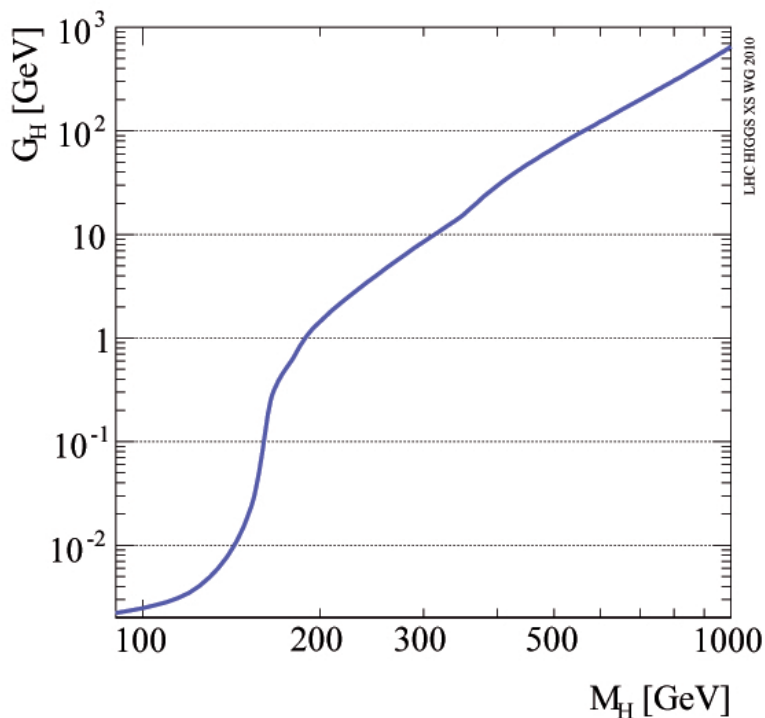
Figure 2.12: Total width Γ_H of the SM Higgs boson as a function of M_H [28].

This curve has been obtained with the following procedure: first, all decay

widths are computed by the HDECAY program [29] to the best theoretical accuracy achievable by present calculations, and the total width

$$\Gamma_H \equiv \Gamma(H \to \text{anything})$$

is defined by taking their linear sum. The decay widths $\Gamma(H \to ZZ)$ and $\Gamma(H \to WW)$ for all four–lepton final states are more accurately computed by the PROPHECY4F program [30]. Therefore, the HDECAY predictions for these decay channels are replaced with those from PROPHECY4F.

The total Higgs width is a few MeV large for $M_H \lesssim 130$ GeV, it steeply grows once the decay into on–shell vector bosons is open, and then continues to rise $\propto M_H^3$ as seen from Eq. (2.24). For $M_H \gtrsim 500$ GeV, the Higgs boson is quite broad, and it definitely fails to behave as a resonance at the TeV scale, where $\Gamma_H \approx M_H$. Given that the best measured mass resolution at hadron collider experiments will be limited by the detector energy resolution to about 1% (e.g. in the $H \to \gamma\gamma$ channel), a mass measurements will not be able to resolve the intrinsic width of the Higgs boson for a mass below about 220 GeV.

The branching ratio for the process $H \to X_i$ is defined as

$$\text{BR}(H \to X_i) = \frac{\Gamma(H \to X_i)}{\Gamma_H}$$

The branching ratios of the SM Higgs boson as a function of M_H are shown in Fig. 2.13. The phenomenology of the Higgs boson decay depends dramatically on M_H. Three scenarios can be identified:

- *low mass*: $110 \lesssim M_H \lesssim 130$ GeV
  The Higgs boson decays mostly to b quarks (BR $\approx 50\% - 75\%$) and τ leptons (BR $\approx 5\% - 7\%$). Decays to c quarks and gluons are also sizeable (BR $\approx 2\% - 3\%$ and $\approx 7\%$). The $\gamma\gamma$ and γZ decays are at the per mill level, but VV^* final states are already important: $H \to WW^*$ is at the 30% level for $M_H = 130$ GeV, while $H \to ZZ^*$ decays are produced with a percent probability.

- *intermediate mass*: $130 \lesssim M_H \lesssim 180$ GeV
  The Higgs boson decays mainly into $b\bar{b}$, WW^* and ZZ^*, with one of the off–shell vectors decaying into light fermions. The WW^* channel dominates over ZZ^* and it crosses–over with $H \to b\bar{b}$ around $M_H \approx 135$ GeV, after which the branching ratio to b quarks falls rapidly and reaches the percent level at $M_H \approx 180$ GeV.

- *high mass*: $M_H \gtrsim 180$ GeV
  The Higgs boson decays into two real vector bosons. The ratio between

the branching ratio of $H \to WW$ and $H \to ZZ$ is roughly $2 : 1$ because of the undistinguishability of the two Z bosons. The decay into a pair of top quarks is sizeable above the $t\bar{t}$ threshold, reaching BR $\approx 30\%$. This branching ratio eventually decreases as a function of M_H because the width $\Gamma(H \to t\bar{t})$ grows only like $\sim M_H$ (Eq. (2.25)), compared to $\sim M_H^3$ for the vector bosons (Eq. (2.24)).

The theoretical uncertainties affecting the main decay widths are summarized in Table 2.1 taken from Ref. [28]. They account the scale dependence and for missing orders in electroweak and QCD corrections.

Process	QCD	EW
$\Gamma(H \to bb/cc)$	0.1-0.2%	1-2% ($M_H < 135$ GeV)
$\Gamma(H \to \tau\tau)$	-	1-2% ($M_H < 135$ GeV)
$\Gamma(H \to tt)$	5%	2-5% ($M_H < 500$ GeV)
$\Gamma(H \to gg)$	10%	1%
$\Gamma(H \to \gamma\gamma)$	< 1%	< 1%
$\Gamma(H \to WW/ZZ)$	< 0.5%	0.5%

Table 2.1: Theory uncertainty affecting the decay widths of the SM Higgs boson [28].

2.4   Higgs boson production at the LHC

There are four main production mechanisms of the SM Higgs boson at the LHC pp collider: gluon–gluon fusion (GGF), vector–boson fusion (VBF), Higgsstrahlung, i.e. the production in association with a vector boson (VH, $V = W, Z$) and associated production with heavy quarks (ttH and bbH). Diffractive and higher–order Higgs production are not discussed here.

2.4.1   Gluon–gluon fusion

Although the Hgg coupling is loop–induced, the GGF mechanism has the largest cross–section at the LHC thanks to the sizeable y_t Yukawa coupling and the high gluon luminosity of the colliding protons.

At leading order (LO), the partonic cross-section is proportional to the Born width in Eq. (2.27), i.e. it is of $O(\alpha_s^2)$. The total cross–section falls steeply as a function of M_H: the probability of finding gluons A and B with a fraction x_A and x_B of the proton momentum such that $x_A x_B \sqrt{s} = M_H$, rapidly decreases as a consequence of the soft gluon parton distribution
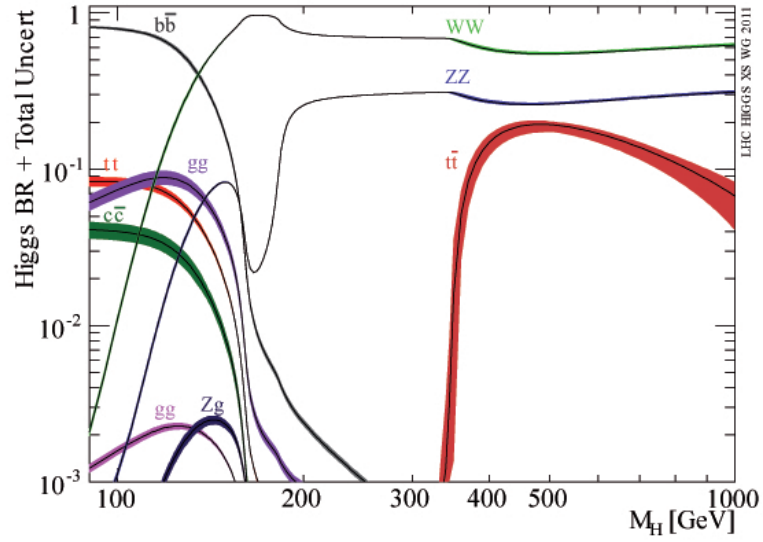
(a)
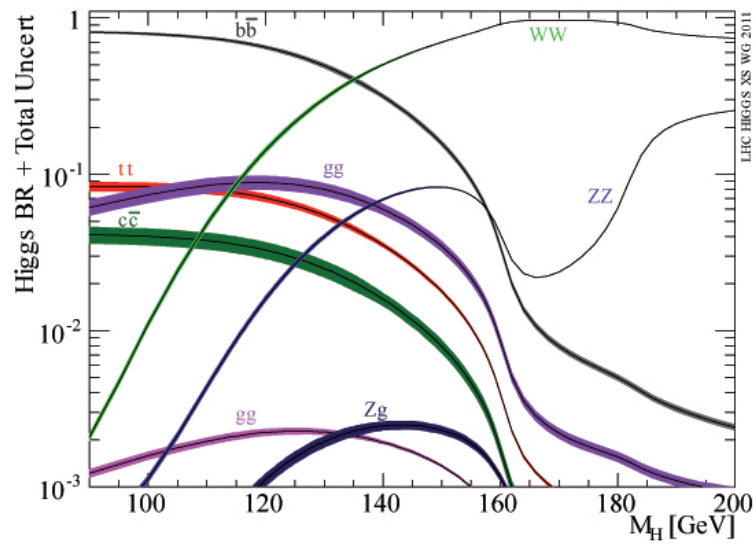
(b)

Figure 2.13: a) Branching ratios of the SM Higgs boson as a function of M_H; b) zoom showing in detail the reach phenomenology expected in the low to intermediate mass range (from Ref. [28]).

functions. At $M_H \approx 350$ GeV, the GGF cross–section has a kink because the amplitude $A_Q^H(\tau_Q)$ in Eq. (2.27) develops an imaginary part right above the $t\bar{t}$ threshold (Fig. 2.11).
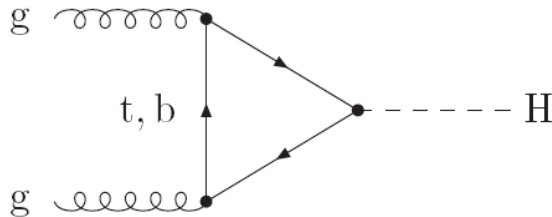
Figure 2.14: Leading order diagram contributing to the GGF mechanism.

I will refer to the CERN Yellow Report [28], and references therein, for a discussion on the theoretical uncertainties. The next–to–leading order (NLO) QCD corrections are known with their full m_t and m_b dependence. They increase the Born cross–section by about 80%-100%. The next–to–next–leading order corrections (NNLO) are instead known only in the $m_t \to \infty$ limit. They increase the cross-section by another 25%. The NNLO calculation has been improved by resuming the divergent soft–gluon logarithms up to next–to–next–leading-log (NNLL), bringing to a further increase in the cross–section (by $\lesssim 10\%$) as well as a reduced sensitivity to the choice of the factorization (μ_F) and renormalization scales (μ_R), i.e. the unphysical cut–offs introduced to match the matrix element computation to the parton distribution functions and to regularize the divergent higher orders of the perturbative series. The computation appears to be quite stable: the NNLO+NNLL prediction nicely overlaps with the error band for the NLO, where μ_F and μ_R are varied within $M_H/2 < \mu_F, \mu_R < 2M_H$. Two–loops electroweak corrections have been also computed, modifying the cross-section by a factor $[-2\%, 5\%]$ depending on M_H. The largest theoretical uncertainties arise from the residual scale dependence of the NNLO+NNLL calculation ($\approx 10\%$) and from the uncertainties on the parton density functions and α_s. The latter range between $3\% - 10\%$ depending on M_H and $\sqrt{s}$, since, for a given collider energy, the production of an heavy Higgs boson probes the large x fractions of the protons, which are less precisely measured.

2.4.2 Vector–boson fusion

In the VBF mechanism, the Higgs boson is produced from the fusion of two weak gauge bosons (W^+W^- or ZZ), radiated off the incoming quarks:

$$q(k_1)q'(k_2) \to q(k_3)q'(k_4)V^*(k_3-k_1)V^*(k_4-k_2) \to q(k_3)q'(k_4)H(k_3-k_1+k_4-k_2)$$

At leading order, there are three contributing diagrams with the vector bosons exchanged in the t, u and s channel (Fig. 2.15).
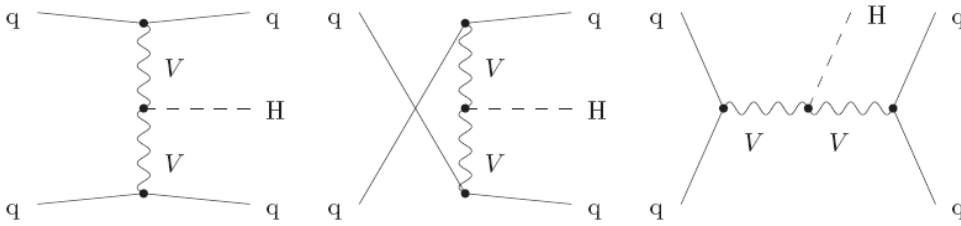
Figure 2.15: Leading order diagrams contributing to the VBF mechanism.

The interference between the t/u and s channel is significantly reduced in the particular region of phase–space where the two jets are forward–backward directed. Because this peculiar signature offers a handle to reduce other SM backgrounds, the VBF production mode is often considered after a set of cuts on the two outgoing (*tagging*) quarks, also known as VBF cuts. In the latter case, the contribution from the $s-$channel can be neglected.

Because of the lack of color exchange between the incoming quarks, there is an angular ordering on the initial and final–state parton radiation governed by the quarks scattering angle. By virtue of this, the QCD radiation comes out collimated around the direction of the outgoing quarks. This is another powerful handle that can be exploited to reduce the SM background.

The partonic cross–section for the leading order $qq' \to qq'H$ scattering can be easily computed in the limit where the transverse momentum of the scattered quarks is small compared to the center–of–mass energy $\hat{s}$. In this approximation [31]:

$$\hat{\sigma}_{Born}(\hat{s}) = \frac{1}{16M_W^2}\left(\frac{\alpha}{\sin^2\theta_W}\right)^3\left[\left(1+\frac{M_H^2}{\hat{s}}\right)\log\frac{\hat{s}}{M_H^2} - 2 + 2\frac{M_H^2}{\hat{s}}\right] \quad (2.29)$$

The partonic cross–section in Eq. (2.29) grows with energy because it is asymptotically sensitive to the fusion of longitudinally polarized vectors. For

this reason, this process is increasingly important for larger $\sqrt{s}$ (for example, it is important at the LHC and by far less at the TeVatron).

In proton–proton collision, the cross–section for W^+W^- fusion is larger than ZZ fusion by a factor ≈ 3 as a result of the larger couplings of the W boson to fermions.

The NLO QCD contributions to the cross–section consist of $Vf\bar{f}$ vertex corrections and real gluon emissions. They can be re–absorbed in large part as a redefinition of the parton distribution functions, changing the LO cross–section by $\approx 5-10\%$. Next–to–leading order electroweak corrections are also sizeable and comparable to those from NLO QCD. Next–to–next–to–leading order QCD corrections to the total cross-section are known only in the DIS approximation [32]. They reduce the scale dependence to less than 1-2%.

2.4.3   Associated production with W/Z bosons

The Higgsstrahlung production mechanism (VH), where the Higgs boson gets radiated off a virtual gauge boson, is a benchmark process for low M_H both at the TeVatron and LHC. These events can be triggered by one or two isolated and high–momentum charged leptons, and the Higgs boson can be searched for in all its decay modes. Because of the dominant branching ratio to b quarks, the process $pp \rightarrow V(\rightarrow \ell\ell')H(\rightarrow b\bar{b})$ has the largest sensitivity among the VH channels.

The Higgsstrahlung partonic cross–section is of $O(G_\mu^2)$ (Fig. 2.16).
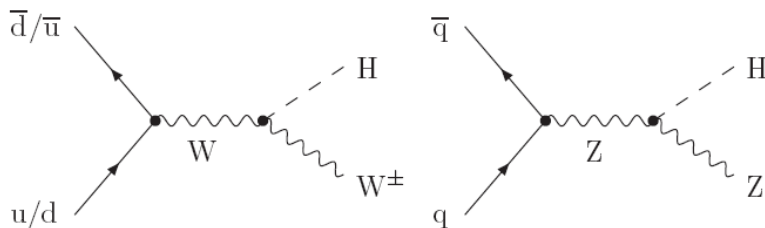
Figure 2.16: Leading order diagrams contributing to the Higgsstrahlung mechanism.

This process can be thought of as a two steps reaction: first, a pair of quarks undergo an s–channel Drell–Yan scattering into a gauge boson V^* with virtuality $\hat{s}$; then, V^* decays to an on-shell V and an Higgs boson H. The partonic cross–section $\hat{\sigma}$ can be then factorized as:

$$\hat{\sigma}(\hat{s}) = \sigma(V^*(\hat{s})) \cdot \frac{d\Gamma(V^*(\hat{s}) \rightarrow VH)}{d\hat{s}} \tag{2.30}$$

For $V = W$, this picture holds up to NNLO [28] and the QCD corrections reduce to the well-known QCD perturbative contributions to the Drell-Yan cross–section $\sigma(V^*(\hat{s}))$. This is not true for $V = Z$, because at $O(\alpha_s^2)$ the electrically neutral $Z + H$ final state can be produced in GGF via triangle and box loops.

The total cross–section for the process $pp \to VH$, $V = W, Z$ is known to NNLO accuracy in QCD and NLO in the electroweak expansion. At the LHC, the NLO corrections increase the LO cross–section by about 20%, while at NNLO the results change by less than 5%. The scale dependence is suppressed to less than 1% for $V = W$, and is slightly larger ($\lesssim 2\%$) for $V = Z$ because of the appearance of the process $gg \to ZH$ at $O(\alpha_s^2)$, which maintains a significant uncertainty due to the scale variation.

Because of the s–channel structure of Eq. (2.30), and since $\hat{s}^2 \geq M_V^2 + M_H^2$), the inclusive cross–section for $pp \to VH$ drops as a function of M_H faster than GGF or VBF, contributing to only $2 - 3\%$ of the production cross–section at 7 TeV already for $M_H = 200$ GeV.

2.4.4 Associated production with heavy-quarks

The production of an Higgs boson in association with a pair of heavy quarks $Q\bar{Q}$ ($Q = b, t$) has the fourth largest cross–section at the LHC.

At leading–order, this process originates from $q\bar{q}$ annihilation into a pair of top or bottom quarks, with the Higgs radiated off one of the final state quarks. At large center–of–mass energy, where the gluon luminosity becomes important, other diagrams initiated by gluon pairs are relevant. Examples of leading order Feynman diagrams are shown in Fig. 2.17. Interestingly, the
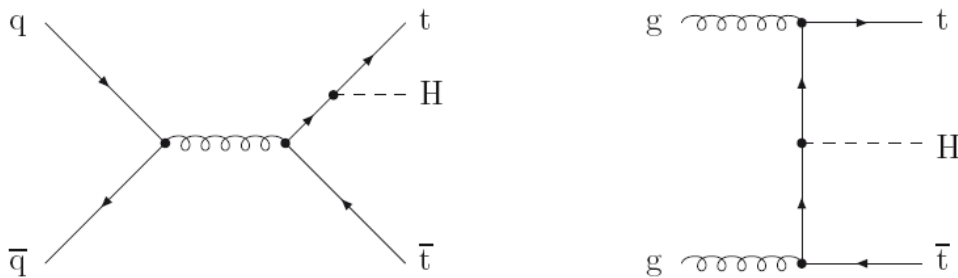

Figure 2.17: Leading order diagrams for the $t\bar{t}H$ mechanism

bbH cross–section can exceed that for $t\bar{t}H$ because the larger phase–space available for the production of b quarks compensates the smaller Yukawa

coupling. This is the case at the TeVatron and, to a lesser extent, at the LHC. The large combinatory and the complicated three heavy–particles phase–space formulas make the analytical computation of the partonic cross–section quite involved already at LO. At NLO, it becomes very challenging. The inclusive cross–section is known up to NLO in QCD, and it changes the LO prediction by at most 20%, reducing the scale dependence from $O(50\%)$ to $O(10\%)$.

2.4.5 Summary and experimental implications

The inclusive $pp \rightarrow H + X$ cross–section in proton–proton collisions at $\sqrt{s} = 7$ and 14 TeV is shown in Fig. 2.18 (top) as a function of M_H. The Higgs boson cross–section broken–up by production mechanism is shown in the bottom part of the same figure. The colored bands span the range of values covered by the theoretical uncertainties estimated by varying the factorization and renormalization scales, the input value of α_s and the parton distribution functions, according to the recipe explained in Ref. [28]. For reference, Table 2.2 reports the cross–sections, split by production mechanism, for five selected values of M_H. The cross–section times branching ratio for the five most sensitive decay channels at the LHC, namely $VH(\rightarrow b\bar{b})$, $H \rightarrow \tau_\ell \tau_h$, $H \rightarrow WW^{(*)} \rightarrow 2\ell\,2\nu$, $H \rightarrow ZZ^{(*)} \rightarrow 4\ell$ ($\ell = e, \mu$) and $H \rightarrow \gamma\gamma$, have been summarized in Table 2.3.

M_H (GeV)	cross–section (pb)				
	GGF	VBF	WH	ZH	ttH
120	16.6	1.27	0.656	0.360	0.0975
125	15.3	1.21	0.573	0.316	0.0863
130	14.1	1.15	0.501	0.278	0.0766
150	10.6	0.962	0.300	0.171	0.0487
200	5.38	0.637	0.103	0.0610	0.0185
400	2.05	0.162	-	-	-

Table 2.2: Cross–sections per production mechanism of the SM Higgs boson in pp collisions at $\sqrt{s} = 7$ TeV, for five selected values of M_H (from Ref. [28]).

The GGF mechanism is the dominant production mode for the SM Higgs boson at the LHC, accounting for the bulk of the cross–section up to very large mass ($M_H \sim 1$ TeV), where the VBF production eventually becomes strong and competes with GGF.

M_H (GeV)	cross–section × BR (fb) ($\ell = e, \mu$)				
	$H \to b\bar{b}$	$H \to \tau_\ell \tau_h$	$H \to 2\ell 2\nu$	$H \to 4\ell$	$H \to \gamma\gamma$
120	658	469	129	1.43	42.1
125	513	385	186	2.19	39.9
130	385	309	241	3.01	36.2
150	73.9	76.2	420	4.61	16.6
200	-	-	259	7.13	-
400	-	-	76.3	2.66	-

Table 2.3: Cross–sections times branching ratio for the five most sensitive channels of the SM Higgs boson at the LHC ($\sqrt{s} = 7$ TeV), for five selected values of M_H (from Ref. [28]). For the $H \to b\bar{b}$ channel, only the VH production mode has been considered.

At low mass ($M_H \lesssim 135$ GeV), VBF and VH have comparable cross–section, but the latter decreases more rapidly as a function of M_H. Higgs production in association with heavy quarks has only a modest cross–section of $O(100)$ fb.

The total cross–section is sizeable at the LHC, ranging between 10 and 30 pb for low to intermediate masses, meaning that with the instantaneous luminosity $\mathcal{L} = 10^{33}$ cm^{-2}s^{-1} typical of the late 2011 LHC operations, Higgs bosons are expected to be produced at a rate of $O(1)$/minute.

However, only a fraction of this rate is effectively accessible for searches. Indeed, at low mass the Higgs boson decays mostly to b quarks and gluons, and the overwhelming QCD multi–jet background makes it difficult to extract, and even trigger, such final states.

The decay into tau leptons has smaller branching ratio but potentially higher trigger efficiency, especially when one or both taus decay into lighter leptons (which however reduces the rate by an additional factor ~ 2). On the other hand, the cross–section times branching ratio for the irreducible background $Z/\gamma^* \to \tau\tau$ is orders of magnitude larger than $\sigma(H \to \tau\tau)$.

For the decay channels with a high–rate, it is often more convenient to sacrifice the bulk of the production, which is either trigger or systematics limited, and concentrate on exclusive production modes, which provide extra handles to suppress the background. Searches for $H \to b\bar{b}$ in association with a gauge boson decaying to leptons, or $H \to \tau\tau$ plus two VBF-like jets are well representative examples.

The situation is simpler for large M_H, where the decay to gauge bosons ($H \to VV$) is the only relevant channel, but then an extra reduction factor

for the branching ratio of $V \rightarrow$ leptons has to be paid to guarantee large purity.

2.5 A minimal extension of the Higgs sector

The Higgs sector of the SM contains the minimal amount of scalar degrees of freedom that can trigger the electroweak symmetry breaking (at least three would–be Goldstone bosons are needed to give mass to the Z and $W^{\pm}$), and at the same time fullfil the requirement $\rho = 1$ at tree-level (Eq. (2.18)).

The minimal extension of the scalar sector consists in adding one extra doublet of scalar fields, Φ_2, and rewriting the potential in terms of Φ_1 and Φ_2. Such an extension was first discussed in the context of the Minimal Supersymmetric Model (MSSM) [33]. Theories with two doublets of scalar fields belong to the class of models denoted as Two Higgs Doublets Models (2HDM) [34].

In the context of a 2HDM, the phenomenology of the scalar sector after symmetry breaking is richer than in the SM. Out of the eight scalar degrees of freedom, three are eaten by the W and Z bosons. The remaining five give rise to as many scalar particles: in absence of tree–level CP violation, two of them are CP–even and neutral (h and H, with $M_h < M_H$), one is a CP–odd and neutral (A) and two are charged (H^+ and its charge–conjugate H^-). The theory now contains four unknown masses (M_h, M_H, M_A, $M_{H^{\pm}}$) and two extra angles, α and β, that rotate the CP–odd/charged and the CP–even light/heavy gauge eigenstates into the A/H^+ and h/H mass eigenstates, respectively. The coupling of the neutral Higgs bosons to the quarks, leptons and gauge bosons will be in general modified with respect to the SM prediction by functions of α and β. In addition, new vertices appear (e.g. ZH^+H^-, ZAh, $W^{\pm}H^{\mp}h$,...).

There are four classes of 2HDM models (denoted as Type–I,II,III and IV) that guarantee no tree–level flavor changing neutral currents (FCNC) [35], in agreement with the experiment. They differ with respect to which doublet(s) give(s) mass to the up/down leptons and quarks. In Type–II models, one doublet acquires a vacuum expectation value v_u and gives mass to the up–type fermions ($\Phi_1 \equiv \Phi_u$) and the other gets a vacuum expectation value v_d, giving mass to the down–type fermions ($\Phi_1 \equiv \Phi_d$). The two vacuum expectation values are related to the electroweak vacuum by the identity relation $v^2 = v_u^2 + v_d^2$. This class of models is of particular interest because it is exactly what the MSSM model implements (see Ref. [36] for a concise review of Supersymmetry).
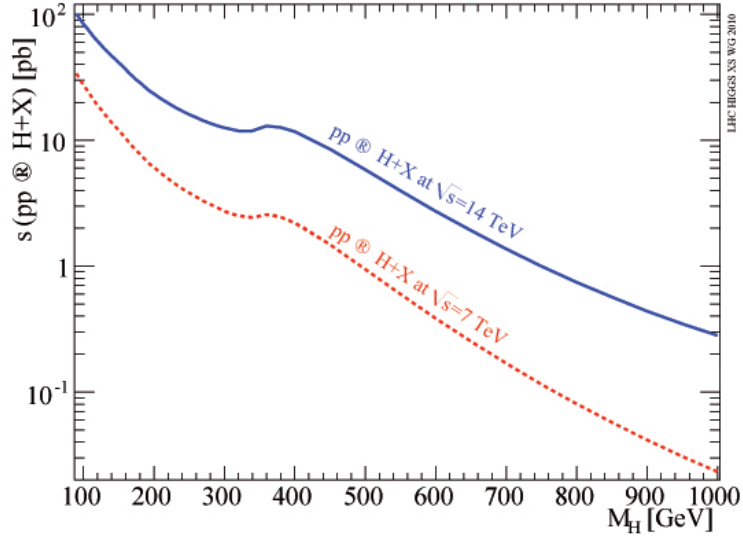
(a)
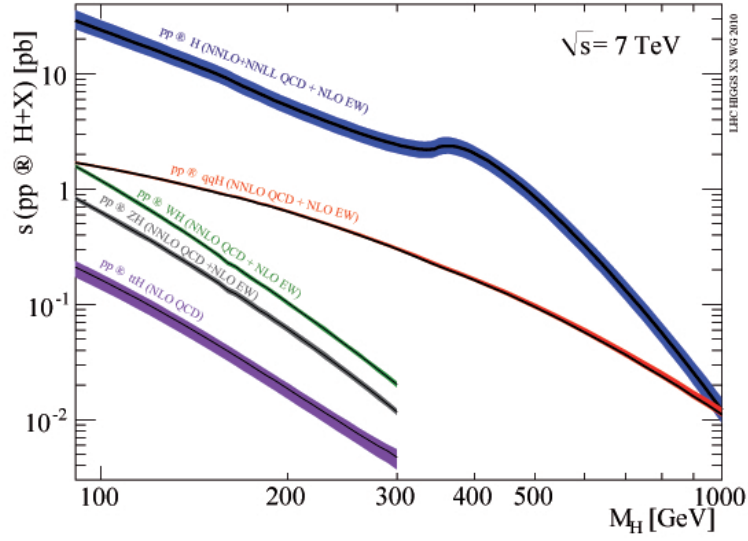
(b)

Figure 2.18: a) Inclusive $pp \rightarrow H + X$ cross–section at the LHC for $\sqrt{s} = 7$ and 14 TeV. b) Inclusive cross–section at the 7 TeV LHC split by production mechanism. The colored bands indicate the total theory uncertainty as discussed in the text (from Ref. [28]).

The invariance under superymmetry dictates the form of the potential $V(\Phi_u, \Phi_d)$, which in turn determines particular relations between the parameters. In the MSSM, the number of unknown parameters needed to describe at tree–level the Higgs sector reduces to two: it is a customary choice to use M_A and $\tan\beta \equiv v_u/v_d$ as the two independent parameters. The superpartners of the SM particles enter Higgs related observables only through radiative corrections. At tree–level, the masses of the CP–even and charged Higgs bosons are related to M_A and $\tan\beta$ via the relations

$$
M_{h,H}^2 = \frac{1}{2}(M_A^2 + M_Z^2 \mp \sqrt{(M_A^2 - M_Z^2)^2 + 4M_A^2 M_Z^2 \sin^2(2\beta)})
$$
$$
M_{H^\pm}^2 = M_A^2 + M_W^2,
$$
(2.31)

which have two important phenomenological implications: first, the lightest CP-even neutral boson is lighter than the Z boson: $M_h < M_Z|\cos(2\beta)|$; second, in the so–called *decoupling regime* $(M_A \gg M_Z)$, the heavy CP–even, the CP–odd and the charged boson are nearly degenerate in mass. While the latter result holds true in general, the former conclusion is invalidated by quantum correction: M_h receives large self–energy contributions by loops involving the top quark and stop squark. As a result, a much weaker upper bound

$$
M_h \lesssim 135 \text{ GeV}
$$

is obtained under the assumption of maximal stop mixing, and assuming that the mass of the heaviest supersymmetrical particle entering the radiative corrections to M_h is at most of $O(1)$ TeV.

In the MSSM, the Yukawa coupling of the fermions are modified with respect to the SM values:

$$
y_u \rightarrow \frac{y_u}{\sin\beta}, \quad y_d \rightarrow \frac{y_d}{\cos\beta}
$$
(2.32)

In the large $\tan\beta$ limit, $y_d/y_u \sim m_d/m_u \tan\beta \gg 1$: the coupling to bottom quarks or taus, for example, becomes more and more important as $\tan\beta$ increases. Something similar happens for the couplings of A to fermions, which are proportional to $(\tan\beta)^{\pm 1}$ for the $\mp\frac{1}{2}$ isospin components. In the decoupling regime, the couplings of the light CP–even Higgs (h) to fermions approach those of the SM: over a significant region of the MSSM parameter space, the search for the light h boson is equivalent to the search for the SM boson [37].

2.5.1 MSSM Higgs boson production at the LHC

There are two main production mechanisms for the three neutral MSSM Higgs bosons (collectively denoted by $\phi = h, H, A$) at the LHC: GGF and

associated production with b quarks. These processes are analogous to those described in the context of the SM, but the enhanced coupling to bottom quarks can substantially alter their rate. The relative strength between GGF and bbH depends on $\tan\beta$: for large $\tan\beta$ (typically $\tan\beta \gtrsim 30$), the process where ϕ is radiated off a b quark dominates over GGF, whereas the latter becomes competitive, and even larger, for $\tan\beta \lesssim 5$ (Fig. 2.19). Some of the most recent CMS public results on searches for the MSSM Higgs bosons decaying to tau leptons will be presented in the final chapter.
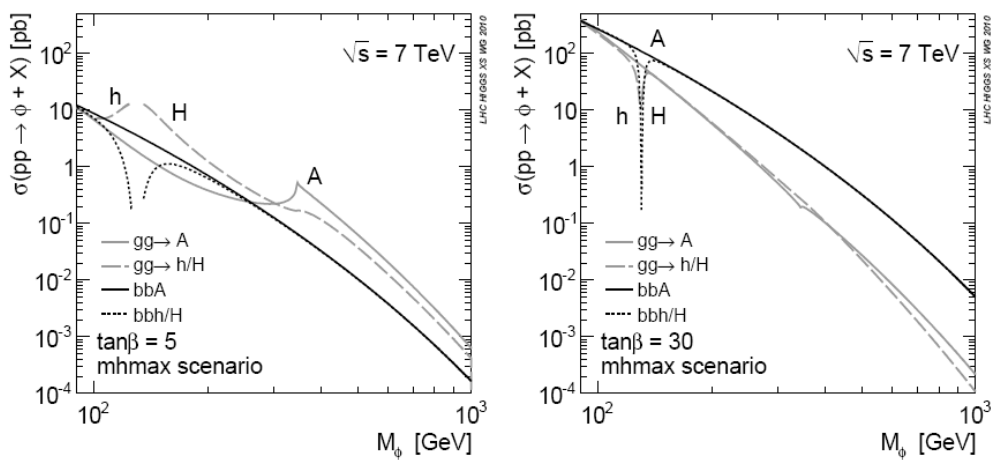

Figure 2.19: Central prediction for the total MSSM production cross–section at $\sqrt{s} = 7$ TeV as a function of M_ϕ for two values of $\tan\beta$ (from Ref. [28]).

Chapter 3

The CMS apparatus at the CERN LHC

The Compact Muon Solenoid (CMS) experiment [39] is a general purpose detector operating at the proton–proton (*pp*) LHC collider at CERN. In this chapter, I introduce the experimental apparatus. The main subdetectors used for particle identification and reconstruction are described. The performances of the detector has been extensively validated with collision data, confirming in general the design expectations.

3.1   The LHC

The Large Hadron Collider (LHC) is a hadron–hadron collider hosted inside the former LEP tunnel. The collider contains high frequency accelerating cavities, focusing quadrupole magnets, and superconducting dipole magnets for the bending of the protons (or heavy ions) in the plane of the 27 km long accelerator ring. Some 1232 superconducting dipole magnets are needed which operate at a field of 8.3 Tesla, and are maintained at a fixed temperature via superfluid Helium at 1.9 °K. Two separate beam pipes are incorporated for the proton beams to circulate in opposite directions

Four experiments are operating along the ring: two large and multipurpose experiments, ATLAS ("A Toroidal LHC ApparatuS") [38] and CMS ("Compact Muon Solenoid") [39], and two smaller and dedicated experiments, LHCb [40] for *b*–physics and the study of CP–violation and ALICE ("A Large Ion Collider Experiment") [41] for heavy ions and the study of the quark–gluon plasma.

The LHC beams are bunched: by design, two beams of 25 ns spaced bunches are circulated in opposite directions. Each bunch consists of $\approx 10^{11}$

protons and is characterized by a transverse emittance $\epsilon_n = 3.75 \ \mu$m at the high–luminosity crossing points situated at diametrically opposite points along the ring, where the ATLAS and CMS experiments are located. Magnetic optics in proximity of the intersection points focuses the beams to achieve a betatron function $\beta^* \approx 0.5 \ \mathrm{m}^{-1}$.

The instantaneous luminosity $\mathcal{L}$ at the collision points is given by [42]

$$\mathcal{L} = \frac{\gamma f k_B N_p^2}{4\pi\epsilon_n\beta^*} F \tag{3.1}$$

where $\gamma = E_{\mathrm{beam}}/m_p$, f is the bunch frequency, k_B is the number of bunches per beam, N_p is number of protons per bunch and F is a reduction factor due to a non-π intersecting angle. Using the design parameters, and assuming $E_{\mathrm{beam}} = 7$ TeV, an instantaneous luminosity $\mathcal{L} \approx 10^{34} \ \mathrm{cm}^{-2}\mathrm{s}^{-1}$ is obtained. By construction, the rate of events dN/dt (Hz) expected from a process with cross–section σ (cm^2) is given by

$$\frac{dN}{dt} = \mathcal{L} \cdot \sigma. \tag{3.2}$$

The LHC beams are formed inside the Proton Synchrotron (PS) with an initial energy of 26 GeV and with the correct bunch spacing; they are further accelerated to 450 GeV in the Super Proton Synchrotron (SPS) and finally injected into the LHC ring, where they are progressively accelerated with radio frequency to the final beam energy. The maximal beam energy of 7 TeV is limited by the largest magnetic field intensity sustainable by the present dipoles.

At the 2009 startup, beams with $E_{\mathrm{beam}} = 450$ GeV have been circulated in the LHC, thus providing first pp collisions at center–of–mass energy $\sqrt{s} = 2 \times E_{\mathrm{beam}} = 900$ GeV. Within weeks, collisions at a record center–of–mass energy of $\sqrt{s} = 2.36$ TeV were established and used for the commissioning of the detectors. The first major high energy physics run started in Spring 2010 at $\sqrt{s} = 7$ TeV, with instantaneous luminosities around $10^{29} \ \mathrm{cm}^{-2}\mathrm{s}^{-1}$ to begin with, and rising by steps to reach up to about $3 \times 10^{33} \ \mathrm{cm}^{-2}\mathrm{s}^{-1}$ by the end of the proton–proton running in October 2011. A total of about $5.7 \ \mathrm{fb}^{-1}$ of integrated luminosity was delivered to CMS by the LHC collider in 2011. About 86% of this is available for the physics analysis described in this thesis. The energy of the collisions was further increased to $\sqrt{s} = 8$ TeV for the 2012 runs, mainly to improve the sensitivity at the TeV scale for the searches beyond the SM, with an instantaneous luminosities reaching up to about $7 \times 10^{33} \ \mathrm{cm}^{-2}\mathrm{s}^{-1}$, allowing to double the available integrated luminosity by June 2012. Some of the latest results obtained using all of

the available 2011–2012 data will be mentioned for comparison in the final chapter of this thesis.

In dedicated time slots, heavy ions beams (Pb) with the record nucleon–nucleon c.o.m. energy $\sqrt{s_{nn}} = 2.76$ TeV are circulated inside the LHC. The Pb–Pb collisions are used to cover the Heavy–Ion LHC physics programme.

3.2 The Compact Muon Solenoid experiment

A full description of the CMS apparatus can be found in Ref. [39]. The design and the detector performances of CMS have been determined to meet the goals of the LHC physics programme [42].

3.2.1 The physics programme

Not surprisingly, the search for the Higgs boson plays a main role in the physics programme of CMS. As discussed in Chapter 2, the decay rates of the SM Higgs boson in the favored region $114 \lesssim M_H \lesssim 2M_Z$ can change very rapidly as a function of M_H. The experimental apparatus has been designed to achieve maximal flexibility in order to i) be sensitive to the largest range of M_H, ii) measure as many decay channels as possible to extract couplings and quantum numbers.

At low mass, the decay modes $H \to b\bar{b}$ and $H \to \tau\tau$ are predominant, requiring a performing tracker to reconstruct charged particles arising from the b quark and τ lepton decays; granular and high–resolution electromagnetic calorimeters are mandatory in order to detect the rare $H \to \gamma\gamma$ decays as a peak on top of an overwhelming continuous background. In the intermediate mass range, high efficiency in lepton reconstruction, identification and isolation are needed to detect the Higgs boson decaying to gauge bosons in the leptonic final states (e.g. $H \to ZZ^* \to 4l$, $H \to WW^* \to 2l\,2\nu$). If the Higgs boson is not found in direct searches, it will become important to study the WW scattering at large energy, a process that eventually violates unitarity in the SM without Higgs boson. To measure the forward jets typically produced in these events, the detector needs to have the largest possible acceptance, with a coverage extended as close as possible to the beam pipe.

The search for the Higgs boson does not conclude the LHC physics programme. Indeed, one of the main roles of the LHC is to shed light on the TeV scale, where new motivated physics may eventually, and spectacularly, show up. In many plausible scenarios, new invisible or weakly interacting particles are expected to be produced, resulting in a substantial amount of missing transverse momentum, $\vec{E}_T^{miss}$. A precise measurement of $\vec{E}_T^{miss}$ re-

quires an hermetic detector with good jet energy resolution to minimize the experimental noise.

Motivated extensions of the SM predict the existence of new heavy gauge bosons weakly coupled to the SM fermions (e.g. Z', W'). If the new resonances are accessible at the LHC energy, they can be first and cleanly detected via their decay to electrons and muons. This requires stringent conditions on the detector performances: linearity of the electromagnetic calorimeter up to an energy of $O(1)$ TeV, good muon momentum resolution and unambiguous charge determination up to $p_T^\mu \sim 1$ TeV.

The high instantaneous luminosity at which the LHC operates imposes demanding requirements on the detector performances for at least a twofold reason: first, the trigger system and the detector response and readout need to cope with the 40 MHz rate at which LHC collisions are delivered for a 25 ns spaced beam; second, the rate of inelastic proton–proton collisions occurring in the same bunch crossing will be as large as ≈ 30 for $\mathcal{L} = 10^{34}$ cm^{-2}s^{-1}: for every hard–scattering event, hundreds of softish hadrons and photons stemming from these extra interactions will pile–up on the detector, with obvious increase of occupancy and confusion, degradation of isolation, jet and missing energy resolution. The situation can be even worse if the time response of the detector is slower than the inter–bunch spacing, because the previous and subsequent bunch–crossings will also pile–up in the same event.

3.2.2 The CMS geometry

The CMS apparatus features a cylindrical symmetry around the beam axis (Fig. 3.1).

The global coordinate system adopted by CMS has the origin in the nominal interaction point. The x-axis points radially inward towards the center of the LHC and the z–axis runs tangent to the beam axis in the direction of the Jura mountains. This defines the direction of the y-axis to point vertically upward. The azimuthal angle $\phi \in [-\pi, \pi]$ is measured in the x–y plane (transverse plane) starting from the x-axis. The polar angle θ is measured with respect to the z-axis. The projection in the r–z plane, where $r = \sqrt{x^2 + y^2}$, defines a longitudinal plane. The pseudorapidity $\eta \in [-\infty, \infty]$ is defined as

$$\eta \equiv -\ln \tan\left(\frac{\theta}{2}\right), \qquad (3.3)$$

The pseudorapidity of a particle with four–momentum $p^\mu = (E, p_x, p_y, p_z)$
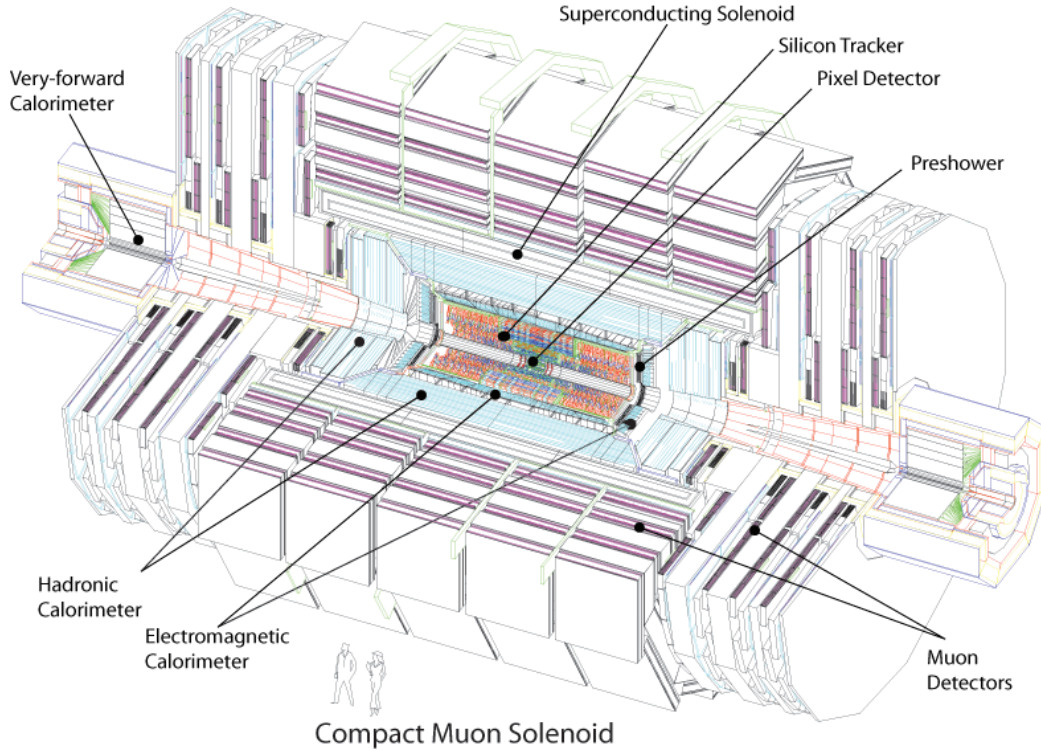
Figure 3.1: Cut–away perspective view of the CMS detector. The instrument occupies a volume of cylindrical shape of about 22 m in length and 15 m in diameter, and has a total weight of 14500 t.

converges to the rapidity [43]

$$h \equiv \frac{1}{2} \log \left(\frac{E + p_z}{E - p_z} \right) \tag{3.4}$$

in the limit $m^2 = E^2 - \vec{p}^2 \to 0$. The rapidity is linear under a longitudinal Lorentz boost. The transverse momentum p_T is defined as the magnitude of the projection of the three–momentum on the transverse plane:

$$p_T \equiv \sqrt{p_x^2 + p_y^2}. \tag{3.5}$$

The transverse energy is defined as $E_T = E \sin \theta$. The distance R between two particles with pseudorapidity $\eta_{1,2}$ and azimuthal angle $\phi_{1,2}$ is defined as

$$R \equiv \sqrt{(\eta_1 - \eta_2)^2 + (\phi_1 - \phi_2)^2}, \tag{3.6}$$

which is also invariant under longitudinal boosts.

One of the distinguishing features of CMS is the solenoidal magnetic field with a central intensity of 3.8 Tesla. The high field provides the bending power (Fig. 3.2) necessary to meet the goals of high momentum resolution required by the physics programme, even for a compact detector like CMS. The magnetic field in the central region has a direction parallel to the beams. The return field is guided by an external yoke, and is intense enough to saturate, to a value of about 2 T, the 1.5 m thick iron slabs.
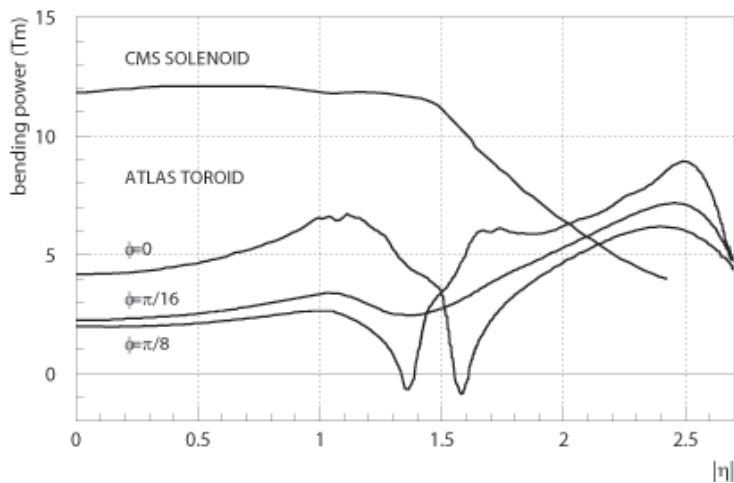

Figure 3.2: Bending power as a function of $|\eta|$ in CMS and ATLAS.

The CMS detector is longitudinally segmented into a central part (barrel), covering the range $|\eta| \lesssim 1.5$, and two lateral segments (endcaps), with $1.5 \lesssim |\eta| \lesssim 3.0$.

Both the barrel and the endcap are equipped with vertexing and tracking detectors, electromagnetic (ECAL) and hadronic (HCAL) calorimeters and muon detectors. For the latter, the detector type changes from barrel to endcap, while the other detectors adopt the same technology, with possibly different readout devices. The endcaps are subject to a higher flux of particles than in the barrel, thus requiring more radiation-hardness than for the former. A pre–shower (PS) sampling calorimeter is hosted in front of the ECAL endcap.

The tracking detectors and the calorimeters are hosted inside the superconducting coil. The muon detectors are integrated within the iron bars of the return yoke.

Additional coverage in the forward regions, $3.0 < |\eta| < 5.0$, is provided by two forward calorimeters (HF).

3.2.3   Pixel and strip tracker

The inner tracking system (Fig. 3.3) allows for the reconstruction of charged particle tracks, from which the primary and displaced vertices can be identified. The occupancy on a detector located at radial distance r from the interaction point decreases as r^{-2}: for a given sustainable occupancy, the spatial granularity needs to be larger at a closer distance. This has driven the choice of a finely grained pixel detector close to the interaction point, and silicon strips with variable pitch in the outer region.
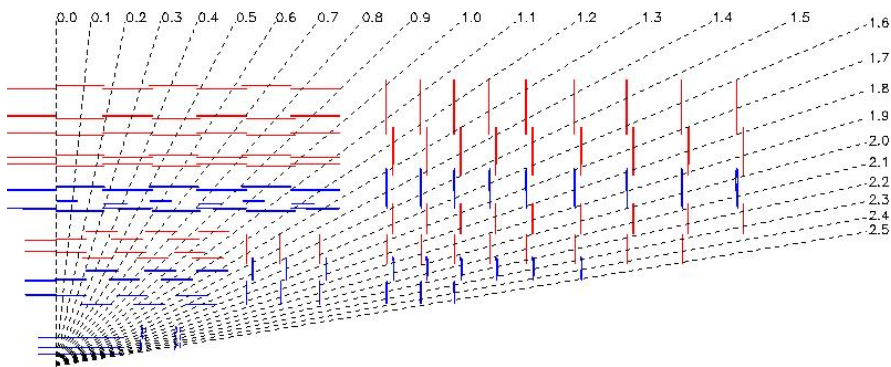

Figure 3.3: View of the CMS tracker silicon layers projected in the longitudinal (r–z) plane (from Ref. [42]).

The pixel detector consists of matrices of 100×150 μm silicon pixels arranged in three concentric barrel layers and four endcap disks, two per each extremity. The barrel layers are positioned at distance $r = 4.4$, 7.3 and 10.2 cm from the beam line, while the endcap disks extend from $r = 6$ to 15 cm, and are placed at $|z| = 34.5$ and 46.5 cm. The pixels provide a spatial resolution of about 10 (20) μm in x–y (z) view.

In the barrel, the silicon tracker consists of an inner section (TIB) of four layers with variable pitch (80–120 μm), covering the volume $|z| < 65$ cm, and an outer part (TOB) of six layers with larger pitch (120-180 μm), covering up to $|z| = 110$ cm. The strips are in general arranged parallel to the z-axis, thus providing maximal spatial resolution in the ϕ coordinate. The first two layers in both the TIB and TOB are realized with stereo modules, tilted one from the other by about 100 mrad, thus allowing for a more precise measurement of the z–coordinate. The single point ϕ–resolution in the TIB and TOB is in the range 23–34 and 35-52 μm, respectively. The resolution in the z–coordinate is typically a factor 10 larger.

In the endcap region up to $|\eta| < 2.4$, the strip tracker is arranged into six (three per side) disks (TID), hosted in the z–gap between the TIB and TOB

$(65 < |z| < 110)$, and eighteen (nine per side) outer disks (TEC), extending in the region $120 < |z| < 180$ cm. The strips are arranged perpendicular to the beam line and have a variable pitch between 100 and 180 μm. The first two TID and TEC layers have stereo modules glued together.

3.2.4 Muon system

The muon system consists of three different types of gaseous detectors. This choice has been driven by the very large surface to be covered. Specific solutions have been adopted to cope with different radiation environments (Fig. 3.4). In the barrel ($|\eta| < 1.2$), where the flux of particles is low and stray magnetic fields small, drift tube (DT) chambers are used. In the endcaps ($0.9 < |\eta| < 2.4$), the higher radiation environment requires the deployment of more robust detectors, like cathode strip chambers (CSC). In addition, a set of resistive plate chambers (RPC) is deployed both in the barrel and in the endcaps, providing fast response with good time resolution but coarser position resolution. The RPCs can unambiguously assign a muon to the correct bunch crossing.
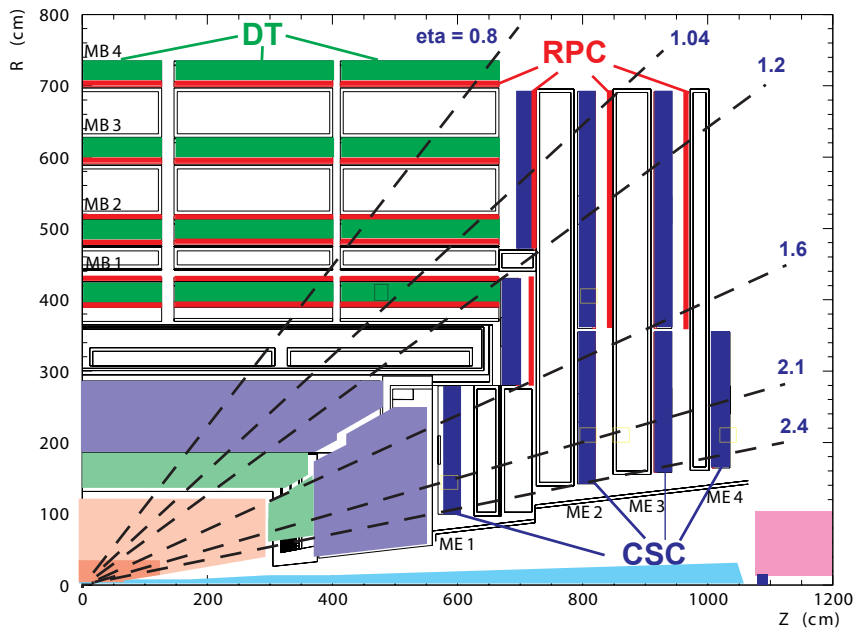

Figure 3.4: Longitudinal (r–z) view of the CMS muon system (from Ref. [42]).

The barrel region is longitudinally segmented into five 2.7 m long wheels. Each wheel has a dodecagonal shape resulting from twelve sectors with 30

degree opening angle. In each sector, four stations of DTs are interleaved with the three iron slabs of the return yokes. The first muon station is at a radial distance of about 4.5 m and the last is at about 7 m.

In each of the two endcaps, layers of CSC and RPC are arranged in four disks perpendicular to the beam axis, Each disk is in turn divided into two or more concentric rings. The first disk is situated at $|z| \approx 7$ m, the last is at about 10 m.

A DT station consists of three *superlayers* of four stacked layers of drift tube chambers: two superlayers have the wires stretched along the beam axis, in the third the wires are orthogonal. The four layers of DTs are staggered to solve left–right track ambiguities.

The track position in each DT is reconstructed by measuring the drift time of the avalanche electrons originating from the muon crossing. The hit point resolution inside a DT is about 150 μm. With the exception of the outermost station, which has no longitudinal view, DT stations can reconstruct 3D–segments by combining 2D–segments on the r–ϕ and r–z projections. The former have a smaller resolution than the latter because there are two ϕ–measuring superlayers (with a maximum of eight hits) against one θ–measuring superlayer (with a maximum of four hits): the azimuthal direction of the segment is measured with a resolution better than 1 mrad while the x–y (z) coordinate of the midpoint is measured with a precision better than 100 μm (150 μm).

In the endcaps, CSC detectors have been chosen because they can better tolerate the higher stray magnetic field and radiation doses. Each CSC consists of closely spaced anode wires stretched between two cathodes. The hit position is measured from the charge distribution induced by the avalanche on the cathode (coordinate orthogonal to the wire) and by the hit wire itself (longitudinal coordinate). Each station is composed by six layers of CSCs, with a point resolution of about 75-150 μm in the ϕ coordinate and 200 μm in the r coordinate.

3.2.5 Electromagnetic calorimeter

In addition to the intense solenoidal field and the silicon–based tracker, the other distinguishing feature of CMS is its fully active, scintillating, crystal-based electromagnetic calorimeter (ECAL).

The ECAL consists of about 75 thousands active cells made of a lead tungstate PbWO$_4$ (PbWO), packed together into a quasi–projective structure (Fig. 3.5).

Lead tungstate has been chosen because of its small radiation length ($X_0 = 0.89$ cm) and Molier radius ($R_M = 2.2$ cm), thus making it ideally

suited to be deployed for high granularity calorimeters inside the reduced volume of the coil. In addition, PbWO is particularly radiation–hard and the decay life of the scintillation light is short enough to ensure that 80% of the light yield is delivered before a new collision occurs.

Every crystal is machined to roughly the same trapezoidal shape, and covers a solid angle of about 0.0174×0.0174 units in (η, ϕ). The crystal height varies between 22 and 23 cm, corresponding to about 25 X_0.
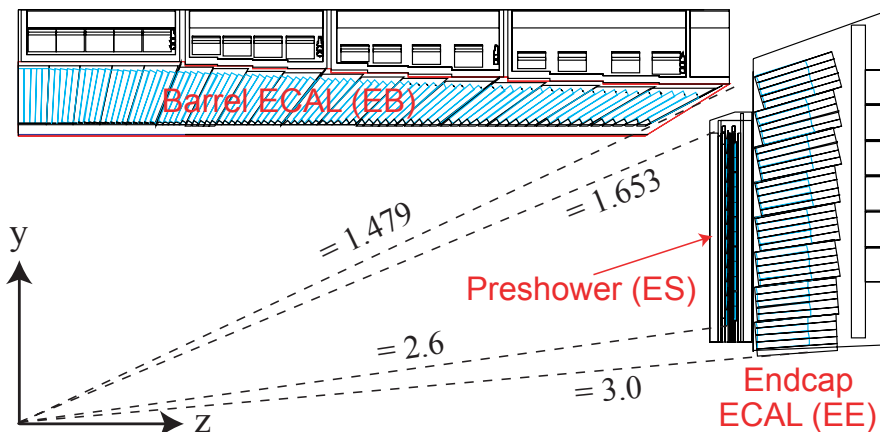

Figure 3.5: Longitudinal $(r$–$z)$ view of the CMS electromagnetic calorimeter (from Ref. [42]).

The blue–green scintillation light produced in the interaction with the electromagnetic shower is detected by the front–end photodetectors. In the ECAL barrel (EB), covering the range $|\eta| < 1.479$, silicon avalanche photodiodes (AVP) are used, while in the ECAL endcap (EE), covering $1.479 < |\eta| < 3.0$, vacuum phototriodes (VPT) are deployed. The light yield of PbWO is of about 30 γ/MeV, corresponding to ≈ 4.5 photoelectrons/MeV. The light yield is very sensitive to the lattice temperature, and has to be controlled with a precision of 0.1 degrees to attain the required energy resolution. An other challenge is posed by the necessity of a continuous monitoring of the crystal transparency, which decreases during the data–taking by effect of the nuclear interactions between the lattice and the crossing particles, resulting in local light traps with a finite life–time. The crystals transparency is monitored by lasers pulses asynchronous with the bunch crossing, which provide time–dependent calibration constants.

A preshower sampling calorimeter is located in front of the EE, covering $1.653 < |\eta| < 2.6$. It consists of two layers of lead radiators interleaved with active layers of silicon strips oriented along the x and y axes. The first (second) layer of lead is $\approx 2X_0$ ($\approx 1X_0$) thick: 95% of the incident photons

start showering before the second active layer, thus granting at least one high–resolution sampling of the shower.

3.2.6   Hadron calorimeter

The hadron calorimeter (HCAL) complements ECAL to form a full calorimetry system. The HCAL is located between ECAL and the coil of the solenoid. The intense magnetic field imposes the usage of non–ferromagnetic materials. Stainless steel and copper alloys (brass) have been chosen as constituent of the supporting structure and calorimetric absorbers. HCAL is a sampling calorimeter: absorbers plates are interleaved with tiles of plastic scintillators (active medium). The tiles are piled–up into quasi–projective towers. The scintillation light coming from each tile of one tower is channeled by optic fibers, added together, and finally translated into an analogical signal by hybrid photodiodes (HPD). The HCAL barrel (HB) covers $|\eta| < 1.4$, while the HCAL endcap (HE), spans the region $1.3 < |\eta| < 3.0$ (Fig. 3.6).

The HCAL readout towers are machined to variable size, ranging from a minimum of $\Delta\eta \times \Delta\phi = 0.087 \times 5$ deg in the barrel to a maximum of 0.302×20 deg in the endcap. An additional layer of absorbers and tiles, with independent readout, is located outside the solenoid, and extends the total depth of the calorimeter system to a minimum of $\approx 11\ \lambda_0$.
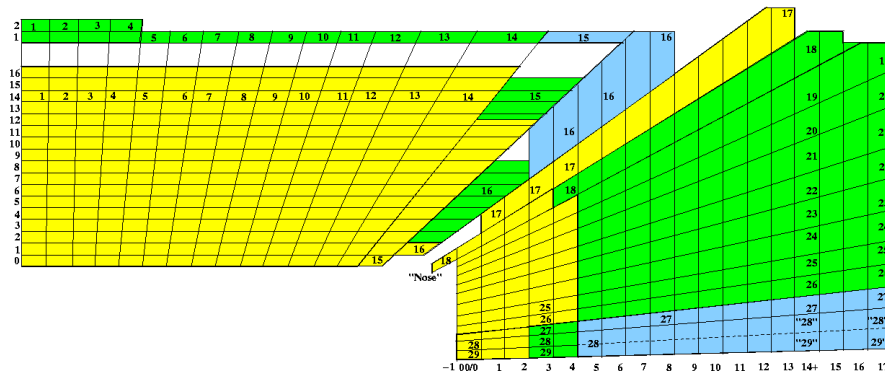
Figure 3.6: Longitudinal (r–z) view of the CMS hadronic calorimeter (from Ref. [42]).

The HCAL calorimeter is non–compensating: the relative response to the electromagnetic and hadronic fractions of the shower (e/π) induced by impinging hadrons is not unity.

The forward region ($3.0 \leq |\eta| \leq 5.0$) is instrumented with a separate hadronic calorimeter (HF) located 11 m away from the interaction point. The HF consists of steel absorbers with embedded quartz fibers that channel the

Cerenkov light emitted by the shower to photomultiplier tubes (PMT). Each HF detector is segmented into eighteen wedges of 24 towers each, covering a solid angle $\Delta\eta \times \Delta\phi = 0.171 \times 0.171$. The fibers are arranged into a grid with a half–centimeter step. A pseudo longitudinal sampling of the shower is provided by alternating long fibers, running across the whole depth of HF, with short fibers, that are deprived of the first ≈ 20 cm starting from the front surface. This solution allows for an effective separation between electromagnetic and hadronic particles: the former start showering earlier, delivering a signal in the long but not in the short fibers, while the latter give a similar response to both.

3.2.7 Trigger and data acquisition

The trigger and data acquisition (TriDAQ) system must provide the necessary rate reduction from the LHC bunch–crossing rate (40 MHz for 25 ns spaced beams) to an output rate of $O(100)$ Hz, suitable for mass storage of the full detector readout (≈ 1 Mb/event).

The rate reduction is achieved in two steps. A Level-1 (L1) on–line filter of collision events is realized by custom hardware processors housed in a room external to the experiment. It achieves a rate reduction factor of $O(10^3)$, for a maximum output rate of 100 kHz. The time needed for the Level–1 signals to travel back and forth from the subdetectors front–end to the L1 processors is a couple of microseconds. Technological constraints of the front–end pipelines (FIFOs) limit the maximum number of collisions that can be pipelined to 128. This leaves $\approx 1\mu$s of processing time to deliver the L1 accept.

The L1 decision is based on the reconstruction of *trigger primitives* above some suitable E_T threshold. A trigger primitive is a coarse–granularity and low–resolution estimation of the momentum of an energetic particle. The muon system and the calorimeters provide trigger primitives that are used to trigger on muons or energetic electromagnetic/hadronic energy deposits. Logical bits that encode the level of isolation of the trigger primitive can be used to discriminate prompt leptons, or photons, from jets. The high–resolution detector signals is digitalized and pipelined till receipt of the L1 decision. In case of a trigger, the full set of digits is buffered into random–access memories located at the subdetectors front-end. A system of switch transfer the data to the processors farm where the High-Level Trigger (HLT) software is run.

At the HLT level, more sophisticated algorithms, indeed close to the of-fline reconstruction, are run to reduce the rate by another factor of $O(10^3)$. The average timing necessary to fully process an event is a few tens of mi-

croseconds, but it can arrive at 1 second for some events. Track reconstruction can be performed and a better usage of the subdetectors information leads to a finer estimation of the energy, direction and isolation of the trigger primitives. Higher–level objects, like hadronically–decaying taus and b-tagged jets, can be searched for. Regional reconstruction around L1 seeds allows for a maximal exploitation of the subdetector granularity while keeping the timing low.
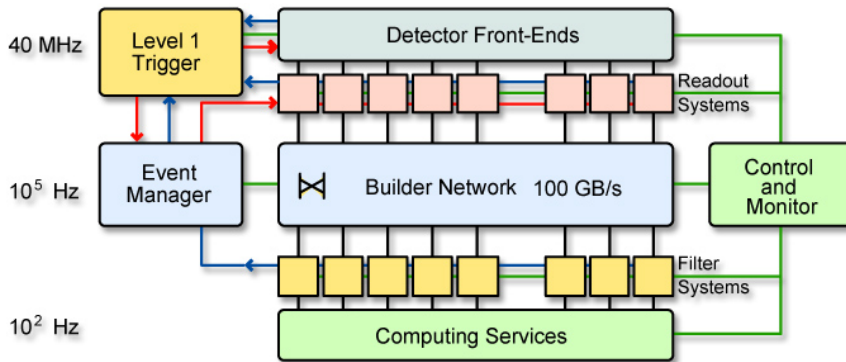

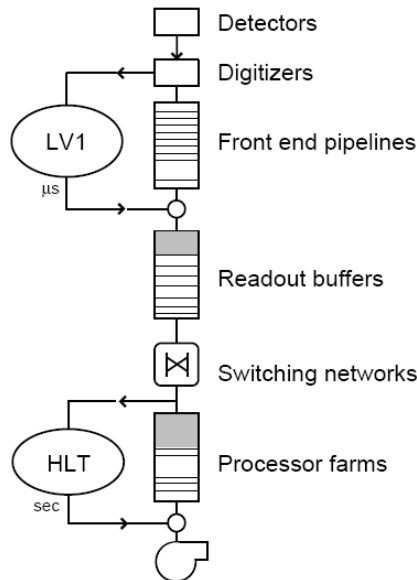Figure 3.7: Architecture of the CMS DAQ system (from Ref. [44]).

Figure 3.8: Data flow in the CMS TriDAQ system (from Ref. [44]).

Chapter 4

Particle–flow event reconstruction

In this chapter, I describe the particle–flow approach for the reconstruction of collision events in high–energy physics experiments.

Measuring the energy and direction of hadronic jets is a task traditionally assigned to calorimeters. In principle, the charged component of the jet could be measured with superior precision by tracking devices, leaving the detection of neutral particles to the calorimeters. However, the energy deposited by the charged and neutral particles eventually mixes in the calorimeter: the separation between the two becomes an involved procedure.

An appealing solution is provided by the particle–flow algorithm, i.e. a method which aims at reconstructing all stable particles in the event, making the best use of the different detectors to determine their type and energy.

After a brief historical excursus, I will describe the implementation of the particle–flow algorithm for the offline reconstruction of CMS events [46], showing the expected performances on the CMS simulation.

I will then present the results of the commissioning of the particle–flow algorithm with the first collisions, with some emphasis on the commissioning of the general algorithm [47] and the commissioning of the lepton reconstruction in the particle–flow [48], where I brought original contributions.

4.1   The particle–flow approach

In high–energy physics experiments, the energy and direction of the outcoming particles can be measured in two ways: using tracking detectors, which aim at reconstructing in the least invasive way the trajectory of electrically-charged particles, or using calorimeters, which detect the energy that inci-

dent particles release in their destructive interaction with the calorimetric medium.

Starting from the interaction point outwards, the traditional deployment of sub–detectors consists in i) micro–vertexing and tracking instrumentation, ii) electromagnetic calorimeter, iii) hadronic calorimeter, iv) muon detectors. Figure 4.1 illustrates a transverse section of the CMS apparatus (Section 3.2), chosen for the following discussion as a prototype for a 4π general–purpose detector.
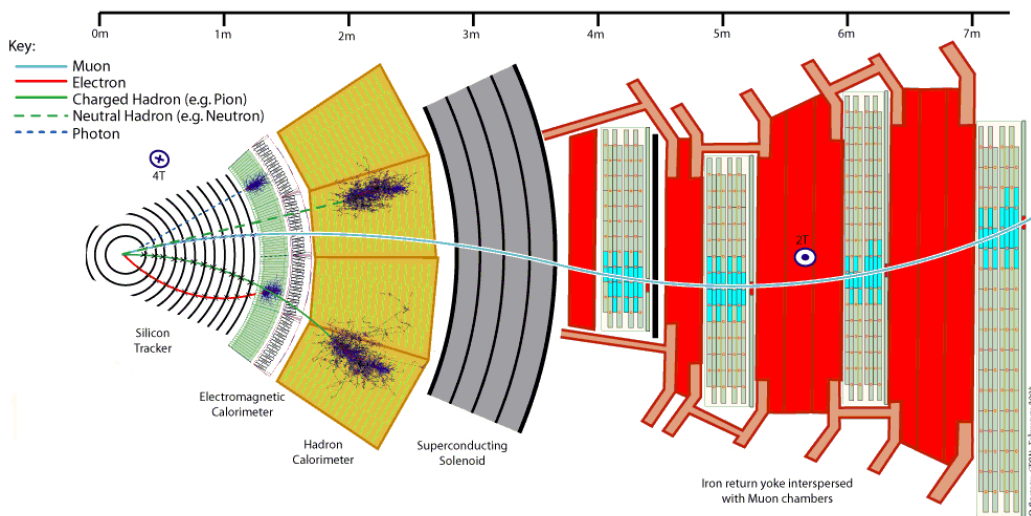

Figure 4.1: Illustration of the CMS detector response to different types of particles. A detector slice is shown in a plane transverse to the direction of the proton beams. The geometrical center of the CMS detector is situated in the circle on the left.

In order to maximize the performances for a fixed amount of integrated luminosity, an experiment ought to be instrumented in a way to provide as much as possible a comprehensive description of the final state, i.e. to detect the largest fraction of particles produced in the collision.

The visible particles that are stable over the typical detector length scale ($l \sim 1\,\mathrm{m}$) are electrons, muons, photons and hadrons (neutral or charged).

Electrons and Photons

Electrons and photons are absorbed by the electromagnetic calorimeter, resulting in localized deposits of energy. For electrons, the calorimetric measurement can be supplemented by the reconstruction of the impinging track.

The possibility of reconstructing a track is of particular importance for the sake of disentangling prompt electrons (directly produced in the hard interaction) from photons, converted or not, and also to improve the electron detection at low–energy. On the other hand, if the material budget of the tracking device is comparable with one radiation length [43], i.e. the length scale that governs radiative losses in matter, an important fraction of the electron energy is expected to be lost in the tracker volume in the form of bremsstrahlung radiation, with a consequent broadening of the electron signature and difficulties in reconstructing its track.

The relative energy resolution for an electron or photon with energy E (GeV) reconstructed by an electromagnetic calorimeter can be parametrized in the form [49]

$$\frac{\sigma(E)}{E} = \frac{a}{\sqrt{E}} \oplus \frac{b}{E} \oplus c \qquad (4.1)$$

where a (stochastic term) typically ranges between 0.5 and 5%, depending on the statistics of signal photons that arrive at the photodetectors. The b and c coefficients account for readout noise and detector inhomogeneity. For the CMS electromagnetic calorimeter, $a \approx 3\%$, $b \approx 120$ MeV and $c \approx 0.25\%$ [42], meaning that the energy of an electromagnetic particle with $E = 10$ (100) GeV is measured with a resolution of about 1.5% (0.5%).

Muons

Compared to electrons, the bremsstrahlung emission along the muon trajectory in matter is suppressed by a factor $(m_e/m_\mu)^2$. Since they are also blind to the nuclear force, most of the muons will traverse the whole detector before decaying via the charged weak interaction.

The measurement of the muon momentum relies on spectrometry. For a muon crossing an uniform magnetic field B (Tesla) in a spectrometer with lever arm L (m), the relative momentum resolution is given by:

$$\frac{\delta p}{p^2} = \frac{8\delta s}{0.3BL^2} \oplus \left(\frac{C}{0.3BL} \frac{1}{p} \right) \qquad (4.2)$$

where δs (m) is the error on the track sagitta [43], which depends on the number, inter–spacing and single–point resolution of the measurements, and C accounts for multiple scattering in the detector medium and is relevant at low momenta (in the CMS tracker, $C \lesssim 1\%$, while in the muon spectrometer $C \approx 15\%$). Typical values of $\delta p/p^2$ achievable by performing spectrometers is $\sim 10^{-4}$, meaning that the momentum of a 100 GeV muon is measured with a sub–percent uncertainty. This is for example the case in CMS [42].

Hadrons

Hadrons are produced either in the fragmentation of quarks and gluons from the hard–scattering event or in low–energy processes (minimum–bias, underlying event). In the first case, the outgoing hadrons come out in the form of a collimated jet, whose direction and energy keep memory of the original parton momentum. The energy of a jet is on average shared among charged, photons and neutral hadrons in the approximate proportion of 65:25:10.

Only a few type of hadrons can live enough to cross the tracking detectors all their way up to the calorimeters. The majority of stable hadrons is composed by charged pions $\pi^\pm$ ($c\tau \approx 8$ m), kaons $K^\pm$ ($c\tau \approx 3.7$ m) and K_L^0 ($c\tau \approx 15$ m), protons p, and neutrons n. Neutral pions decay almost immediately ($c\tau \approx 25$ nm) into a pair of photons.

There are also hadrons that live enough to leave the interaction point before decaying into lighter long–lived particles. Among these, there is a class of particles, denoted as V^0, that produce displaced vertices resolvable by typical tracking detectors (e.g. $K_S^0 \to \pi^+\pi^-$ and $\Lambda \to p\pi^-$).

Hadrons interact destructively with the calorimetric medium via the nuclear and electromagnetic force. For those particles that induce a shower inside the active medium, the initial momentum can be inferred from the total visible energy deposited by the shower. The energy resolution can be still parametrized in the form of Eq. (4.1), but this time the a coefficient is of $O(1)$. For example, in CMS the combined ECAL plus HCAL energy resolution for 100 GeV hadrons is about 10%, i.e. roughly $100\%/\sqrt{E}$. The performance of an hadron calorimeter depends to large extent on the relative response to electrons and pions, the so–called e/π factor [49].

Given the limited resolution of an hadron calorimeter, the energy of charged hadrons could be measured by the tracker with a much smaller uncertainty (see Eq. (4.2)) up to a few hundred GeV.

Another shortcoming of a pure calorimetric measurement comes from the fact that the charged particles, before arriving at the calorimeter surface, get deflected by the high magnetic field that is needed for e.g. muon spectrometry, resulting in a bias of the jet direction and a degradation of the angular resolution. A purely tracker–driven measurement is much less sensitive to the magnetic field.

Unfortunately, even if charged hadrons were measured using tracking devices, they will eventually release their energy in the calorimeter, thus mixing with the overlapping photons and neutral hadrons. The latter can be measured, with the worst resolution, by the hadron calorimeter only.

Neutrinos and other invisible particles

One is often interested in gathering evidence on particles that interact so weakly with the detector to be considered, to all effects, invisible. Such particles can be neutrinos or a new neutral, weakly–interacting, exotic particle (e.g. the lightest supersymmetric particles in R–parity conserving models). The azimuthal angle and transverse momentum of the invisible particles can be inferred from the total momentum imbalance in the transverse plane, the so–called *missing transverse energy*, or $\vec{E}_T^{miss}$. With the exception of muons, the calorimeters absorb the energy of all visible particles: the missing transverse energy can be obtained from the negative vectorial sum of all calorimetric deposits, corrected for the eventual presence of muons.

The biggest technological challenge in the event reconstruction comes from a precise measurement of the jet momentum, that will eventually reflect in a better $\vec{E}_T^{miss}$ resolution. Three possible ways to improve calorimetry towards a better measurement of jets can be followed.

An obvious way is clearly to act directly on the hardware, investing on the performances of the hadron calorimeter (for example, improving the intrinsic resolution by tuning $e/\pi \approx 1$).

Another approach consists in exploiting the granularity of the calorimeter to attempt a statistical separation between the hadronic and electromagnetic components of the shower, thus realizing a sort of offline compensation. The resulting *energy–flow* algorithm was first deployed by the H1 experiment at DESY [50], and was proved to significantly improve the jet energy resolution.

A third solution towards a performing calorimetry consists in resolving the jet into its individual constituents: charged particles, to be measured by the tracker, photons, to be measured by the electromagnetic calorimeter, and neutral hadrons, to be measured by the hadronic calorimeter. In this way, about 90% of the jet energy could be measured with the superior resolution of the tracker and electromagnetic calorimeter, while the hadronic calorimeter would be used only for the remaining 10%. An analytical approach to the ultimate goal of describing a jet, and in general the whole event, in terms of individually reconstructed particles, is called a *particle–flow* algorithm [45].

One of the first implementations of a particle–flow algorithm was attempted by the Aleph experiment at LEP [51]. In a nutshell, the Aleph algorithm consists in building *calorimeter objects* by connecting tracks reconstructed by the tracking system (vertex detector, drift chambers and TPC) to calorimetric towers reconstructed in the electromagnetic and hadron sections of the calorimeter. Muons, photons and electrons are identified us-

ing a redundancy of measurements, and their footprint is removed from the calorimeter object. Neutral hadrons are detected as an energy excess on top of the total momentum measured by the tracker. Thanks to this algorithm, the energy resolution for jets decreased from $1.2/\sqrt{E}$ of a calorimetric jet, to about $0.6/\sqrt{E}$, whereas a perfect separation of the individual components was expected to give $0.3/\sqrt{E}$ [51]. A weak point in the Aleph algorithm comes from the impossibility to separate the showers originating from nearby charged and neutral particles: the measurement of the neutral energy bears an extra uncertainty due to the unknown energy released by the overlapping charged particles, for which the tracker can only give the central value.

4.1.1 The particle–flow paradigm

In an ideal particle–flow algorithm, every particle inside a jet is correctly identified and its momentum is reconstructed using the best possible combination of subdetectors. By denoting as σ_{ch}, σ_γ and σ_{nh} the uncertainty characterizing the measurement of charged hadrons, photons and neutral hadrons, the total jet energy resolution is given by the weighted sum:

$$\sigma_{jet}^{PF-ideal} \approx 0.65\sigma_{ch} \oplus 0.25\sigma_\gamma \oplus 0.10\sigma_{nh}. \tag{4.3}$$

However, in real life the particle–flow algorithm has to deal with an imperfect detector, resulting in *loss* of particles, and *confusion*, i.e. wrong associations between subdetectors that results in a double counting of energy. Overall, these effects modify the right–hand side of Eq. (4.3) to a realistic form

$$\sigma_{jet}^{PF-realistic} = \sigma_{jet}^{PF-ideal} \oplus \sigma_{loss} \oplus \sigma_{confusion} \tag{4.4}$$

For a given detector, the performance of a particle–flow algorithm should be evaluated in terms of how close the limit (4.3) is approached (in some implementation of the particle–flow algorithm it was found that the contribution of the last two terms in the right–hand side of (4.4) is indeed dominant [52]).

Equation (4.4) can be turned around to indicate how a calorimeter should be designed for an optimal deployment of the particle–flow. The recipe suggested in Ref. [45] consists in

- an electromagnetic calorimeter with a large ratio between interaction (λ_I) and radiation length (X_0), in order to maximize the separation between photons and hadrons, and a transverse segmentation finer than the Molier radius R_M [49], as to increase the separation between photons and the other nearby particles. Optimizing the separation between

particles boils down to maximize the *separability* variable [52]

$$S_{\gamma\,h^{\pm}} = BL^2/(R_M \oplus \lambda_I \oplus D_P),$$

where L is the distance between the calorimeter surface and the interaction point, B is the magnetic field and D_P is the read–out pad size;

- an hadronic section dense, very granular in the transverse direction and with a longitudinal view, thus making it possible to separate the two components of the shower.

4.1.2   Summary

To summarize, a particle–flow algorithm is a reconstruction technique that is able to fully exploit the redundancy of the subdetectors towards an optimal determination of the type, energy and direction of all stable particles in the event. This requires a routine that solves the ambiguity that may arise when several particles accidentally overlap and have their signature merged in the detector. The output is a list of reconstructed particles, i.e a collection of four–vectors

$$\{p^\mu\},$$

that can be eventually delivered to high–level algorithms that reconstruct jets, hadronically–decaying taus, discriminate b-jets from light–quark jets, etc... Measuring the momentum of charged particles at the vertex automatically removes the direction bias typical of a calorimeter–based measurement. Besides, the tracker can still provide a measurement for those charged particles that are not energetic enough to reach the surface of the calorimeters (e.g. in CMS $p_T^{min} \approx 750$ MeV).

For an efficient particle–flow algorithm, two major conditions must be satisfied: the presence of a performing tracking system, able to cope with the busy environment typical of jets, and the presence of a calorimeter with a fine transverse granularity, to allow for an effective track–to–cluster association, and with enough energy resolution to detect neutral particles as local excesses over the momentum measured by the tracker.

If these conditions hold, one should expect the particle–flow reconstruction to outperform the calorimeter–based approach in terms of jet and $\vec{E}_T^{miss}$ measurement, and to adiabatically converge to the latter in the limit where the tracker becomes less performing than the calorimeters, e.g. for very hard jets.

4.2 Particle–flow with the CMS apparatus

The CMS method is ideally suited for a succesful deployment of the particle-flow [46]. The very performing tracking system (Section 3.2.3), immersed in the intense solenoidal field, can reconstruct, with large efficiency and negligible fake rate, tracks with $|\eta|$ up to 2.5 and transverse momentum as low as 150 MeV [53].

The tracker is surrounded by the electromagnetic calorimeter (Section 3.2.6), which features a uniform, finely–grained, transverse segmentation (0.0174×0.0174) all across its acceptance ($|\eta| < 3.0$). The granularity of ECAL is augmented by an order of magnitude in the endcaps by the presence of a pre-shower detector.

The ECAL is complemented by a hadronic calorimeter (Section 3.2.6), with a factor 25 coarser resolution, so that (5×5) ECAL cells map into one single HCAL cell.

Muons can be identified with very high efficiency and negligible fake rate by the muon system (Section 3.2.4). When crossing the calorimeters, muons lose part of their energy by ionization, depositing ≈ 3 (0.5) GeV in HCAL (ECAL).

4.2.1 Building bricks

Before being delivered to the particle–flow algorithm, the tracker, calorimeter and muon detector signals (*hits*) are processed into higher–level objects that are the true building bricks of the algorithm.

Tracker hits that are compatible with the same helix hypothesis are grouped together and give rise to tracks. A dedicated combinatorial track finding (CTF) algorithm [53] was developed for this purpose, allowing for very high efficiency and reduced fake rate. The algorithm consists in an iterative search for candidate tracks using the Kalman filter for the pattern recognition. At each iteration, the track selection conditions are progressively loosened and hits unambiguously associated to a track are ignored at later iterations, thus reducing the combinatorics and the fake rate. The last iteration has very relaxed track–to–vertex cuts, thus allowing for non prompt tracks to be efficiently reconstructed. Overall, the reconstruction efficiency is above 99.5% for isolated muons and above 90% for charged hadrons in jets.

The signature of particles impinging into the calorimeter, and inducing showers, extends over many cells. This requires an algorithm that groups together cells likely to originate from the same particle. The output of the clustering algorithm is a collection of *particle-flow clusters*. Each cluster is associated with one and only one particle. First, cells which have recorded a

local maximum of energy above a given threshold provide a seed for growing *topological* clusters, i.e. cluster of neighboring cells with energy above twice the standard deviation of electronic noise (e.g. > 80 MeV in ECAL barrel, > 300 MeV in HCAL). A topological cluster doesn't necessarily correspond to a single particle, whereas the number of seeds is interpreted as a counter of the individual particles, and hence of the total number of particle–flow clusters. For each topological cluster with more than one seed, a decision on how to share the energy of each cell among the different particle–flow clusters must be taken. This decision relies on the distance between the barycenter of the cluster and the cell, with an iterative determination of the former.

Figure 4.2 illustrates a simulated jet coming from a parton that hadronizes into four particles: π^+, π^-, π^0 and K_0^L. In this particular simulation, the two charged pions deposit energy in HCAL, but only the π^- leaves a detectable energy in ECAL. The K_0^L and the two photons (from the neutral pion decay) deposit all of their energy in ECAL. Overall, four topological clusters are identified, one in HCAL and three in ECAL. The one in HCAL has two seeds, corresponding to the charged pions, giving rise to a pair of particle-flow clusters. In ECAL, four particle–flow clusters are grown from three topological clusters: the two photons from the π^0 are so close that the respective cells are merged into the same topological cluster.

4.2.2 Linking algorithm

Tracks, clusters and muon tracks that are close together are linked into particle–flow *blocks*. Each pair of elements in the block is assigned a *link measure* to assess the level of mutual compatibility (for example a distance R or the χ^2 of a combined fit).

The linking algorithm proceeds as follows:

- a link between a charged particle track and a particle–flow cluster is defined by the distance R between the cluster position and the track extrapolated to the calorimeter at a depth where the shower is expected to occur (the shower maximum for ECAL, one interaction length for HCAL). The link is created only if the extrapolation lies within the boundaries of the cluster, possibly augmented to take into account multiple–scattering [43], track p_T resolution and dead channels;

- a link between an ECAL cluster and a track is created if the tangent to the track, extrapolated from any of the crossing with the tracker layers, points within the cluster boundaries;
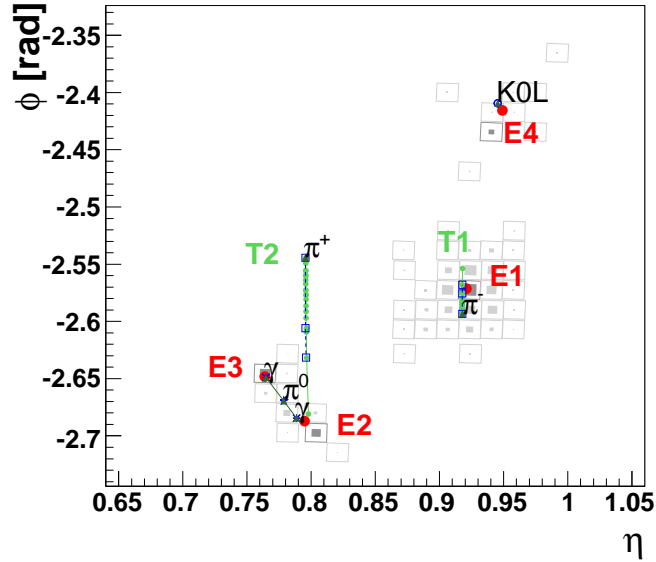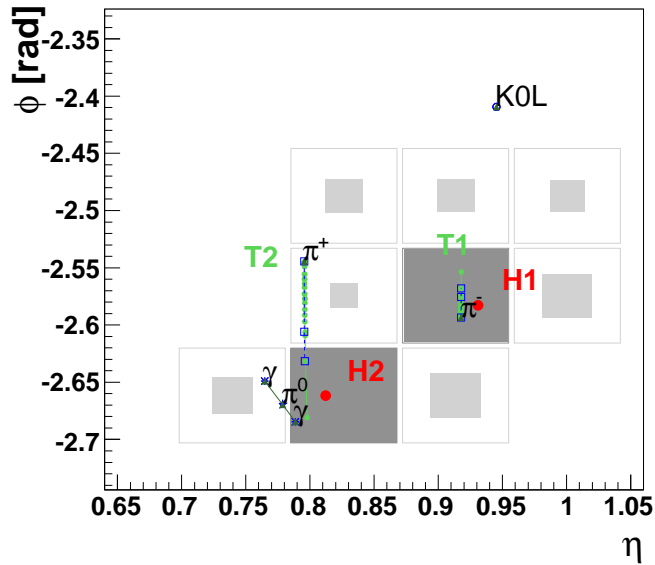
Figure 4.2: Illustration in the (η, ϕ) view of a simple hadronic jet as reconstructed by the (a) ECAL and (b) HCAL detectors. The labels E1–E4 (H1–H2) designate separate ECAL (HCAL) clusters. The labels T1–T2 indicate different topological clusters (from Ref. [46]).

- a link between two calorimeter clusters (ECAL–HCAL or ECAL–PS) is defined as the distance R between the cluster positions. The link is created only if the position of the cluster in the more finely grained detector lies within the boundaries of the coarser;

- a link between a track in the tracker and a track in the muon system is created if the combined fit returns a decent χ^2, which then becomes the link measure itself; in case more tracker tracks fit to the same muon track, only the one with the smallest χ^2 is retained.

The linking algorithm takes care of grouping the totality of the elements into the smallest possible number of unambiguously disconnected blocks. An element of the block may be linked to a multiplicity of other elements. The ambiguities are solved by the core of the particle–flow algorithm, which is the topic of the next section.

4.2.3 Particle reconstruction and identification

The particle–flow algorithm scans the content of one block at the time to definitely assign its elements to one and only one particle. Elements univocally assigned to a particle are progressively removed from the block to reduce the combinatorics. The algorithm is iteratively run until no more elements are left.

Muons

Muons can be identified with high purity. Consequently, the particle–flow algorithm starts by removing elements unambiguously associated to muons. The muon reconstruction is performed outside of the particle–flow algorithm [54], and using very loose quality criteria. The resulting collection of candidates is used as the main input for the identification of particle–flow muons. The algorithm first described in Ref. [46] has been revisited in Ref. [48] to optimize the identification of muons inside jets.

First, every *global* muon [54] with at least one valid hit in the muon system and for which the E_T sum of all neighboring tracks and calorimeter cells within a cone of radius $R = 0.3$ around the muon direction is less than 10% of the muon p_T, becomes automatically a particle–flow muon. The isolation cut already selects genuine muons with extremely high purity, so that no additional selection is needed. The identification of *tight* muons among the remaining candidates follows. This selection consists in the requirement for a minimum number of measurements of the muon track and for compatibility between the muon track and its linked cluster energy according to a

template derived from simulation. Tracks associated to the isolated or tight muons are removed from the block, and the expected HCAL deposit is taken into account for a later processing. After the particle–flow has run over the remaining elements, a relaxed search for muons allows for a few extra candidate to be found. The *loose* muon identification requires a minimum number of track measurements and valid matches between the track extrapolation and the muon chambers.

The importance of the muon identification prior to the processing of the block is well illustrated in Fig. 4.3: if a muon is not properly identified, it will be eventually treated as a charged hadron, with the consequence that any deposit from overlapping neutral hadron will be wrongly assigned to the HCAL cluster linked to the muon track, resulting in a degradation of the jet resolution and a bias to lower momentum.
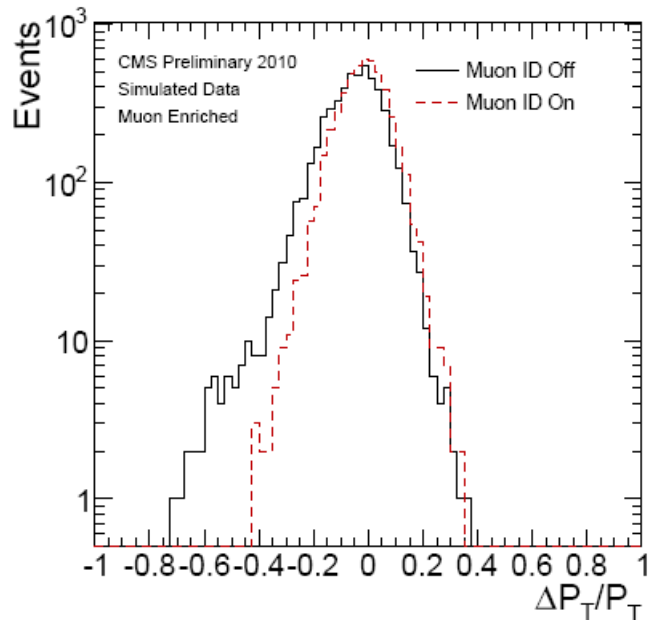
Figure 4.3: Relative p_T resolution for particle–flow jets with $100 < p_T < 150$ GeV in a simulated sample of μ–enriched QCD events. Figure published in Ref. [48].

Electrons

Electron reconstruction follows. It is crucial for the particle–flow to identify electrons with high efficiency: because electrons tend to shower in the tracker volume, their signature often extends over many subdetectors; if the various

elements are not properly linked together, part of the energy risks to be double–counted, with serious degradation of jet and $\vec{E}_T^{miss}$ resolution.

The standard CMS electron reconstruction algorithm [56] relies on the ECAL cluster to seed the electron track finding. By construction, this algorithm is more suited for isolated and high-p_T electrons than for electrons in jets. A large energy deposit in ECAL (*supercluster*) is constructed by grouping hot cells found inside a window that is centered around the cell with the maximal energy (seed) and extends over ± 0.3 radians in ϕ and by 0.09 units of η. From the supercluster barycenter, an helix is propagated back to the interaction point, modulo a charge ambiguity, using the supercluster energy as an estimator of the track momentum. If the extrapolation is compatible with a track seed, then a dedicated pattern recognition based on the Gaussian Sum Filter algorithm (GSF) [57] is pursued starting from that seed. Only superclusters which are backed up by an HCAL cluster with less that 15% of the total supercluster energy are used as seed.

This definition of supercluster results in a modest seeding efficiency for electrons in jets, which may exceed the 15% limit due to the hadronic component of the jet, and for low-p_T electrons, for which the supercluster is too small to accommodate all the bremsstrahlung photons.

To overcome these limitations and improve the reconstruction efficiency for low-p_T and non–isolated electrons, the particle–flow algorithm uses tracker–driven seeds as starting point to initiate the track reconstruction. Since the GSF filter is computing intensive, it can be run only for a fraction of the tracks. A loose track preselection, based on track–to–cluster matching and on the track quality, is used to reduce the number of track candidates. The resulting gain in seeding efficiency for electrons inside b-jets with $p_T > 2$ GeV is improved by a factor of two with respect to the ECAL–only seeding, while for isolated electrons the gain is between $15 - 50\%$ for $2 < p_T < 5$ GeV and reduces to $1 - 2\%$ for $p_T > 10$ GeV [58]. The tracker–driven and ECAL–driven seeds are merged into a combined collection of seeds, from which the GSF pattern recognition starts. Each GSF track gets linked to the particle–flow cluster that matches its extrapolation to the calorimeters.

A dedicated search for bremsstrahlung photons emitted by the electron in its way to the ECAL is performed starting from the track tangents at the intersection points with the tracker layers (Fig. 4.5). The energy containment for high–p_T and isolated electrons can be improved further by making use of the supercluster footprint. Converted bremsstrahlung photons are searched among the neighboring tracks by a dedicated algorithm. The electron energy response E^{reco}/E^{true} for electrons reconstructed by the particle–flow algorithm is compared in Fig. 4.4 to the response of the supercluster–based reconstruction, showing in general good agreement between the two algo-
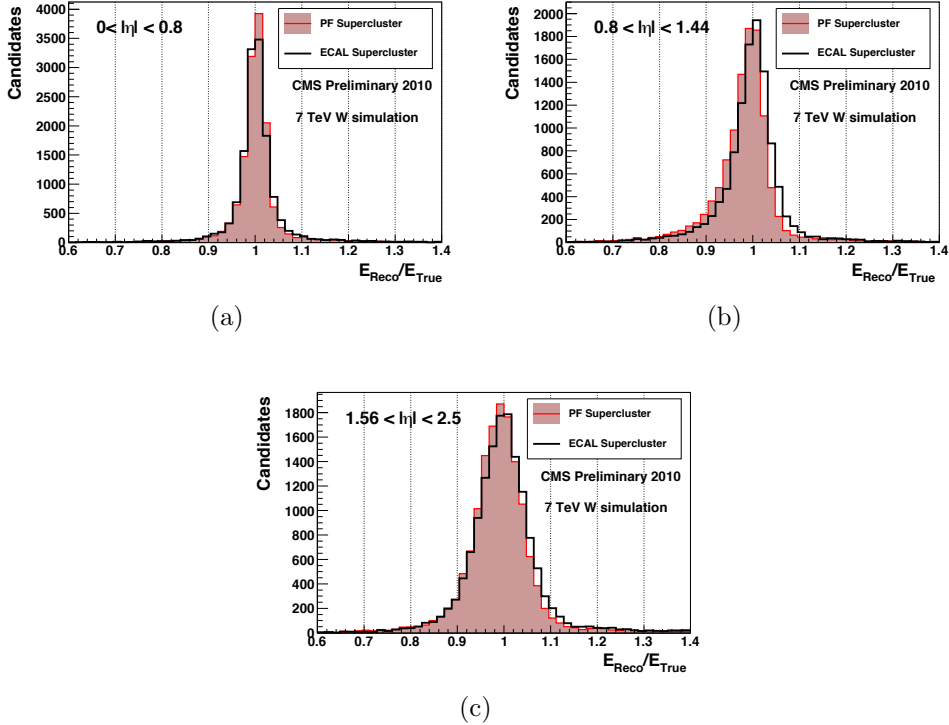
Figure 4.4: Comparison between the electron energy response (E_{reco}/E_{true}) in the particle–flow and in the supercluster algorithms obtained from a simulated sample $W \to e\nu$ for electrons with (a) $|\eta| < 0.8$, (b) $0.8 < |\eta| < 1.44$ and (c) $1.56 < |\eta| < 2.5$. Figures published in Ref. [48].

rithms.

The final electron identification is performed by a multivariate discriminator based on the output of a Boosted Decision Tree (BDT) [55], trained to optimally separate genuine electrons in jets from pions. The discriminator, denoted by ξ as in Ref. [48], peaks at a value of 1.0 for genuine electrons and at -1.0 for fakes (pions). It uses a set of fourteen variables [58]. Two of them are based on purely calorimetric information: the fraction of the total calorimetric energy measured by HCAL and the ECAL cluster dispersion along the eta direction. The remaining twelve variables mix calorimetric and tracking information to assess the compatibility of the energy deposit with the signature measured in the tracking system. These are: the total ECAL energy divided by the inner track momentum, the electron cluster energy divided by the outer momentum, the ratio between the energy loss by bremsstrahlung as measured by the tracker or by the calorimeter, a logical
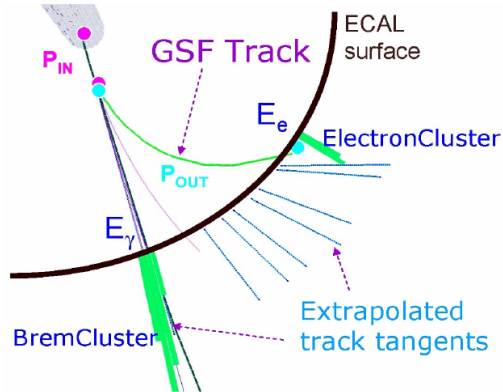
Figure 4.5: Cartoon showing an electron that loses energy by bremsstrahlung.

bit flagging tracks that are likely to have radiated photons in the early or late part of the tracker, the fraction of energy radiated by bremsstrahlung as measured by the tracker alone, the difference in pseudorapidity between the cluster position and the track position extrapolated to the calorimeter, the χ^2 of the fit to the tracker hits done with the KTF algorithm or with the GSF algorithm, the number of reconstructed hits in the tracker, the relative transverse momentum resolution of the GSF track fit, the logarithm of the GSF track transverse momentum and its pseudorapidity at the vertex. The particle–flow working point ($\xi > -0.1$) achieves an efficiency on real electrons inside b–jets of about 65% at the price of a 1% fake rate. If the electron identification is passed, all the elements linked to the GSF track are removed from the block. Otherwise, all the links between the track and the bremsstrahlung photons are released and the elements are returned to the particle–flow algorithm for further processing.

With this electron identification, the p_T resolution for b–jets with transverse momentum in excess of 20 GeV is improved by 10% compared to the case where no electron identification is attempted.

Charged hadrons, neutral hadrons and photons

Tracks for which the transverse momentum is measured with an error larger than the expected calorimeter resolution are removed from the block, thus retaining only a set of high quality tracks. A track can be linked to a number of ECAL and HCAL clusters. The separation of neutral hadrons and photons overlapping with the charged particles is achieved by comparing the total calibrated cluster energy with the momentum of the linked tracks. For the comparison to be reliable, the cluster energy needs to be calibrated. The

71

calibration corrects for the non–linear response of the calorimeters and for threshold effects [46].

If an HCAL cluster is linked to more than one track, its energy is compared to the sum of the momenta of all linked tracks; conversely, if a track is linked to more than one cluster, only the closest cluster is retained. The same happens for ECAL clusters, but this time the procedure is more involved and must be carefully thought: the presence of more ECAL clusters linked to the same track may be due to either a fluctuation of the shower, in which case the energy should be associated to the charged track and not double–counted, or to an overlapping photon, in which case the latter should be identified as an individual particle. To take the decision, the clusters are ordered by increasing distance to the track. The n-th cluster is considered as a shower fluctuation if the sum of the linked HCAL cluster (if any) and the first $n-1$ ECAL clusters is smaller than the total charged particle momentum. Otherwise, it gives rise to a particle–flow photon.

If the total calibrated cluster energy is smaller than the total charged particle momenta by more than three times the uncertainty associated to the cluster energy measurement, then a search for loose muons is performed. The remaining tracks are ordered by decreasing p_T–uncertainty (σ_{p_T}). Starting from the first in the list, tracks with $\sigma_{p_T} > 1$ GeV are progressively removed until either the total track momentum exceeds the cluster energy, or no more of such tracks are left. Each of the remaining tracks gives rise to a charged hadron, with momentum equal to the track momentum, if the calorimetric energy is not consistent within the uncertainty with the former, and by a fit to the track and cluster energy otherwise. Every charged particle is assigned the π^+ mass.

If the total calibrated cluster energy is larger than the total track momentum by more than one standard deviation of the cluster energy, then additional neutral particles are created. The algorithm gives priority to the identification of photons. This is supported by the observation that, in hadronic jets, the ratio between the energy carried by photons and neutral hadrons is about 2:1. If an ECAL cluster is linked to the track, and its energy is smaller than the total calorimetric excess, the the whole ECAL cluster energy is used to build a photon and the remaining part of the excess gives rise to neutral hadron; otherwise, the energy excess gives rise to a photon and the remaining ECAL energy is interpreted as an early shower of the charged hadron.

The remaining clusters not linked to a track give rise to neutral hadrons (which are assigned the mass of the K_L^0), or photons, depending on whether they are HCAL or ECAL clusters, respectively.

The forward part of the detector, $3.0 < |\eta| < 5.0$, is instrumented with the

forward calorimeter (Section 3.2.6). Depending on the energy measured in the long and short fibers, hadronic or electromagnetic particle–flow particles are created.

4.3   Expected performances

The response and resolution of particle–flow jets are compared in Figure 4.6 to those obtained from a pure calorimetric measurement. A calorimetric jet (*calo–jet*) is defined as a cluster of ECAL and HCAL cells arranged into projective towers. A tower consists of one HCAL cell and the corresponding 5×5 ECAL cells.

The response and resolution of the particle–flow (pf–$\vec{E}_T^{miss}$) and of the calorimetric (*calo*–$\vec{E}_T^{miss}$) missing transverse energy are compared in Fig. 4.7. The pf–$\vec{E}_T^{miss}$ is defined as the negative vectorial sum of all particles transverse momenta:

$$\text{pf–}\vec{E}_T^{miss} = (-\sum_i^N p_x^i, -\sum_i^N p_y^i), \qquad (4.5)$$

where $i = 1, ..., N$ runs over the N particles reconstructed by the particle–flow. The calo–$\vec{E}_T^{miss}$ is defined as

$$\text{calo–}\vec{E}_T^{miss} = (-\sum_j^M (E_T^j \cos\theta^j), -\sum_j^M (E_T^j \sin\theta^j)), \qquad (4.6)$$

where $j = 1, ..., M$ runs over the M calorimetric towers recorded in the event, with energy E_T^j and direction $(\cos\theta^j, \sin\theta^j)$. Equation (4.6) must be corrected for the presence of muons, if any.

The results shown in Fig. 4.6 and 4.7 have been obtained using a Monte Carlo simulated QCD sample. The superior performances expected from the particle–flow reconstruction are well illustrated by these plots. The use of the tracker to measure the charged component of the jet allows for a more precise measurement of the momentum and direction of hadronic jets. The energy response for uncalibrated particle–flow jets is already pretty close to unity ($\approx 95\%$), compared to a response of 40%–80% for uncalibrated calo–jets.

To test the robustness of the algorithm, several parameters have been varied in the Monte Carlo simulation of the detector within conservative confidence intervals [46]. This includes: *i*) a pessimistic increase in the electronic noise, which forces larger energy thresholds on the cells, *ii*) a poor modeling of detector response and resolution, which affects particle identification, *iii*) a reduction of tracking efficiency, which would increase the weight

of the calorimeter. These perturbations from the ideal detector description only affect at the percent level the expected performances of the particle–flow reconstruction in terms of jets and missing energy reconstruction.

Particle reconstruction around high energy leptons, which is relevant for the definition of a particle–flow based isolation, is studied in Fig. 4.8. The distributions of the distance R between a high–p_T prompt lepton (electron or muon), and the neighboring particles are shown for leptons in a simulated $W \to \ell\nu$ sample. For comparison, the R distribution between random directions tossed in the same events and the neighboring particles are also shown: discrepancies between the two distributions can be ascribed to either final state radiation, or to an imperfect treatment of the lepton footprint. The multiplicity of charged hadrons reconstructed around the electron direction rises linearly as a function of R (Fig. 4.8(a)), as expected from the uniform (η, ϕ) distribution typical of the underlying event. A high–rate of mis–identified electrons from conversions would manifest as a departure of the R distribution from a straight line. When looking specifically at particle–flow photons, three features are visible: $i)$ a depletion of photons in a cone of radius $R \sim 0.05$ around the electron, that is explained by the use of the 0.09×0.6 large supercluster to recover the electron footprint, $ii)$ an excess at $R \sim 0.1$, that is consistent with QED final–state photon radiation, and $iii)$ a second excess at $R \sim 0.3$ corresponding to bremsstrahlung photons that elude the supercluster recovery. As far as neutral hadrons are concerned, the small excess around $R \sim 0.05$ is due to a modest leakage of the electron shower into HCAL, which can potentially give rise to neutral hadrons.

For muons, the only relevant feature is the excess of QED final–state radiation photons consistent with the one observed for electrons.

4.4 Commissioning with first collision data

The particle–flow reconstruction has been commissioned using the first collision events delivered by the LHC at a center–of–mass energy $\sqrt{s} = 0.9$, 2.36 and 7 TeV. The work presented here has been documented in CMS papers [47, 48, 59].

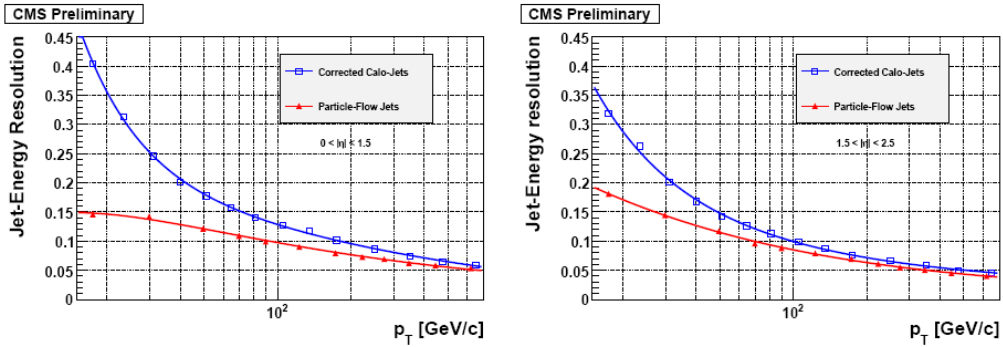### 4.4.1 Commissioning of the algorithm

The observed link measure R between the cluster position and the track extrapolation agrees well with the expectation, for both track–to–ECAL and track–to–HCAL matching (Fig. 4.9(a) and 4.9(b)). A sample of isolated tracks with p_T in excess of 1 GeV, and linked to a cluster, has been used
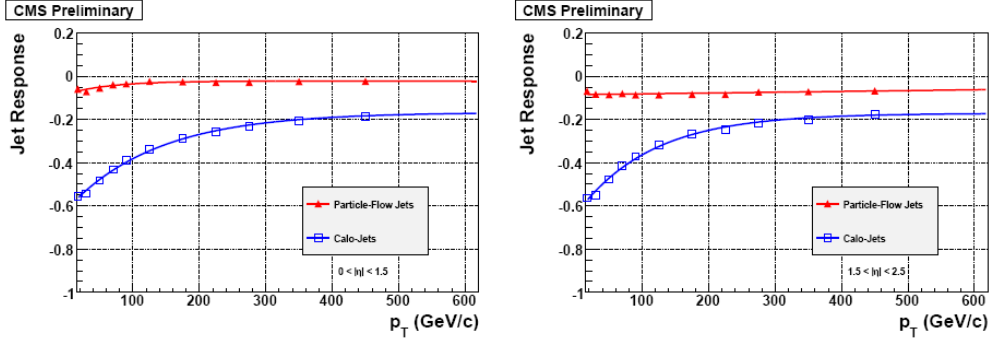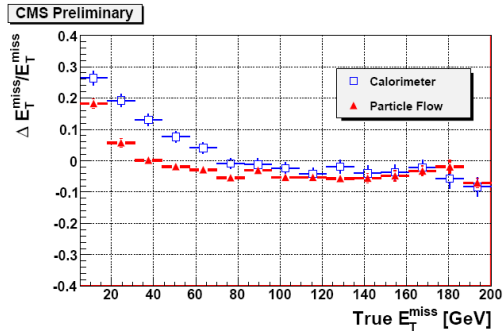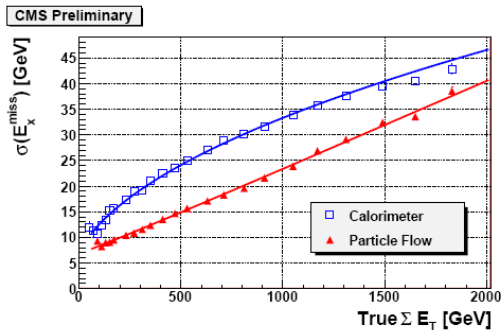
(a)
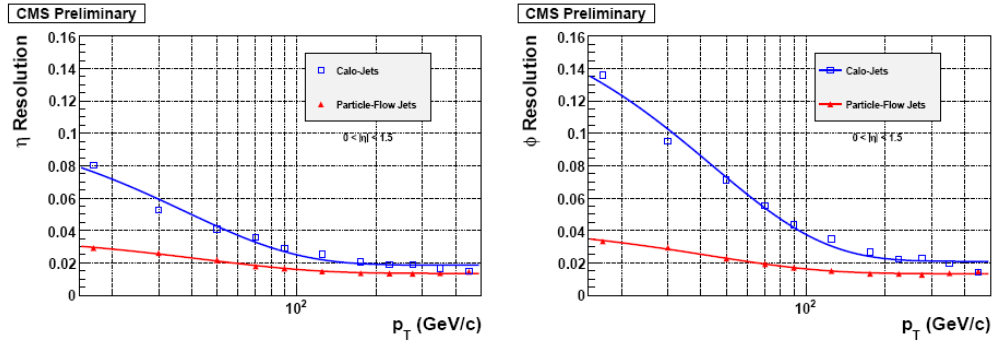
(b)

(c)

Figure 4.6: Performance of the particle–flow jets (red triangles) and calo–jets (blue squares) for (a) the mean relative response ($(p_T^{reco} - p_T^{gen})/p_T^{gen}$), (b) the direction, and (c) the momentum resolution. The performances here are obtained from QCD multi–jet events siumulated with flat $\hat{p}_T$ between 15 GeV and 1.5 TeV (from Ref. [46]).

75

Figure 4.7: The (a) response and (b) resolution for pf–$\vec{E}_T^{miss}$ (red triangles) and calo–$\vec{E}_T^{miss}$ (blue squares) from simulated QCD multi–jet events generated with flat $\hat{p}_T$ between 15 GeV and 1.5 TeV (from Ref. [46]).

for this study. The R distribution of the track–to–ECAL link constrains the systematic misalignment between the tracker and ECAL at the beginning of data–taking to be of order $\Delta R_{sys} \sim 0.001$, corresponding to a relative displacement of 1 mm. This comes with little or no harm for the link efficiency, considering that the cell size is about 0.02 (0.1) in ECAL (HCAL). This misalignment has been promptly accounted for.

Similar studies on the PS–to–ECAL links validate the geometrical simulation of these detectors [47].

The photon cluster calibrations have been validated using the π^0 standard candle [59]. The ECAL energy scale is already calibrated from test–beam data. However, the use of thresholds in the cluster algorithm requires a residual correction to be applied in order to recover unitary response for photons. The agreement between the π^0 mass peak found in data and in the GEANT–based simulation of the CMS detector [60] is within 1% (Fig. 4.10),
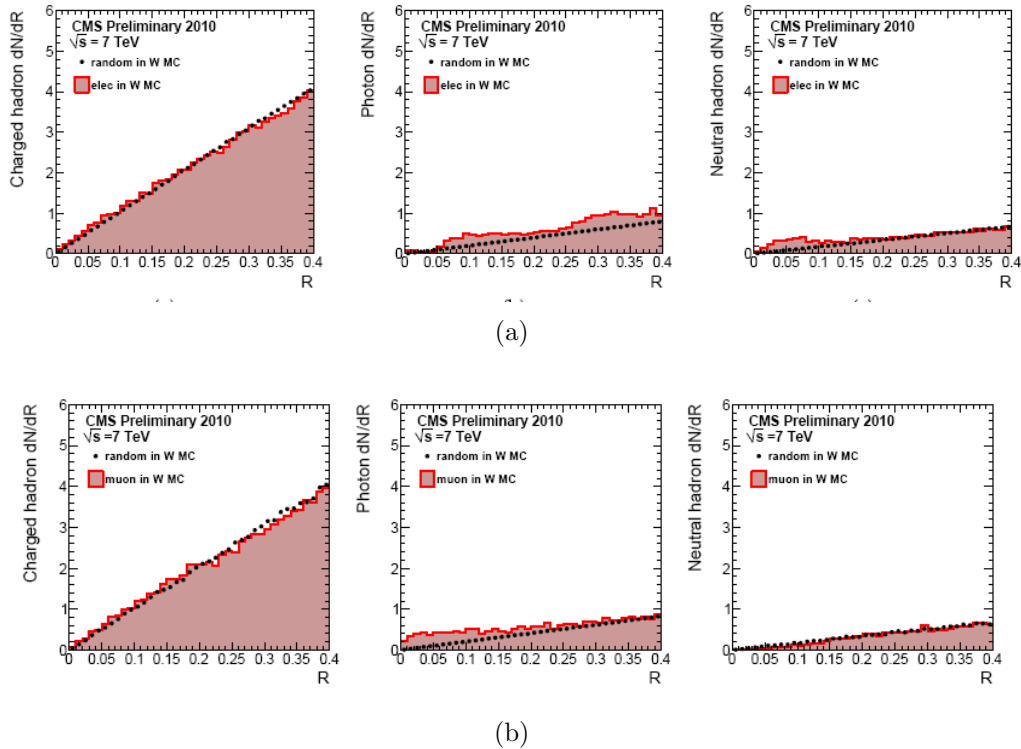
76

Figure 4.8: The distance R between (a) electrons or (b) muons and neighboring charged hadrons (left), photons (middle) and neutral hadrons (right), obtained from a simulated sample of $W \to \ell\nu$. A solid histogram showing the distance between random directions and neighboring particles is superimposed as a template for the unbiased particle density. Figures published in Ref. [48].

thus validating the particle–flow photon calibration.

The energy calibration for charged hadrons is validated using a sample of isolated, high–quality tracks pointing unambiguously to a calorimeter cluster. A comparison between the average cluster energy and the track momentum allows for a calibration of the calorimeter response (Fig. 4.11). Differences between data and simulation as large as 10% were observed as a consequence of an overcalibration of the HCAL response in data compared to the simulation. These discrepancies have been promptly corrected.

(a)   (b)
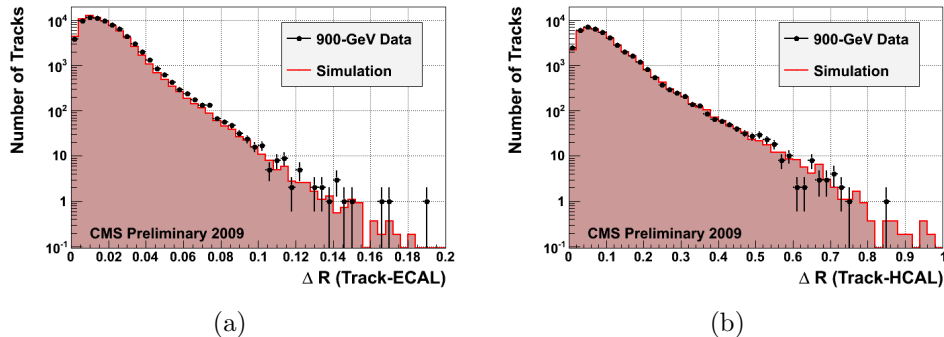
Figure 4.9: Track–to–cluster link distance R for (a) ECAL and (b) HCAL clusters, using tracks with p_T in excess of 1 GeV. Figures published in Ref. [47].

## 4.4.2 Commissioning of the objects

The early collision data revealed a number of non–simulated detector features that required a cleaning of the particle–flow elements prior to their processing by the particle–flow ([47, 59]).

Particle–flow jets and missing energy are extensively used in CMS analyses. They have been validated in different topologies and final states. References [47, 61, 62] collect the commissioning results at $\sqrt{s} = 900$ GeV and 7 TeV. A few key distributions are reported in Fig. 4.12, 4.13 and 4.14.

The fraction of the jet energy carried by the different type of particles is shown in Fig. 4.12 for jets recorded in minimum–bias events (left), compared to the Monte Carlo expectation (right). From bottom to top in the central region, the different colors correspond to: charged hadrons, photons, electrons and neutral hadrons; in the forward region, particle–flow particles are created from HF deposits and are categorized either as hadronic or as electromagnetic particles.

The transverse momentum resolution for central jets ($|\eta| < 0.5$) reconstructed in multi–jet events at $\sqrt{s} = 7$ TeV is shown in Fig. 4.13(a) (4.13(b)) for calo–jets (particle–flow jets). The resolution has been measured from data using the p_T–balance method documented in Ref. [61], and compared to the Monte Carlo expectation.

Finally, the E_T^{miss} resolution in multi–jet events as a function of the particle–flow $\sum E_T$, the scalar sum of all particles transverse momenta, is reported in Fig. 4.14 for three different algorithms [62]: calo–E_T^{miss}, after calibrating the response of the jets and of the unclustered calorimeter cells, tracker–E_T^{miss}, computed using only charged particles, and pf–E_T^{miss}.
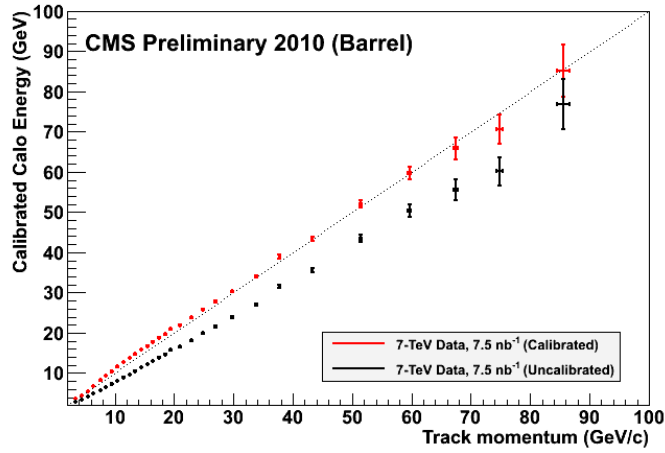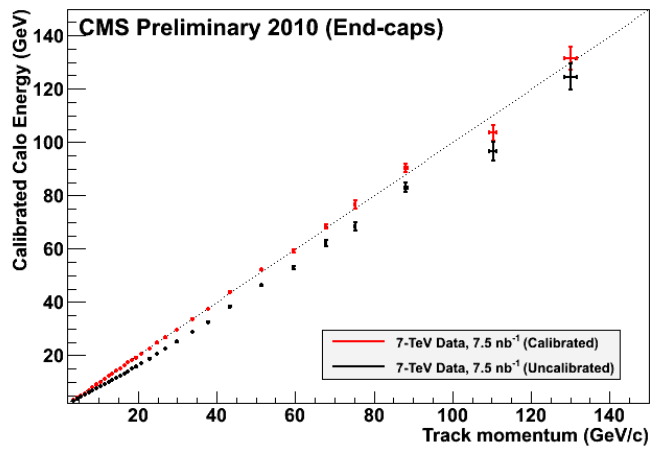
78
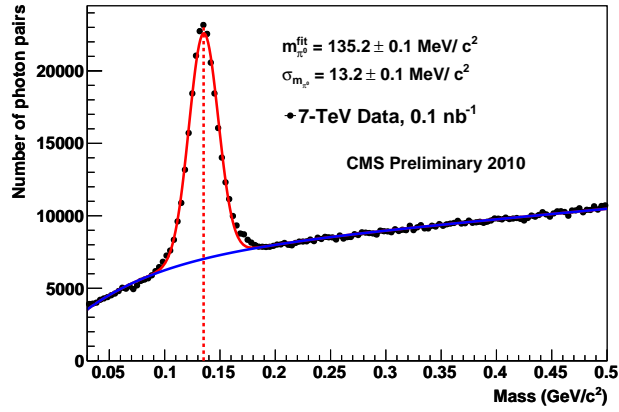
(a)
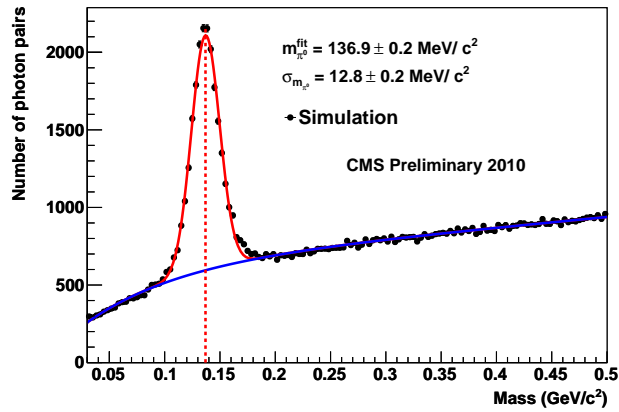
(b)

Figure 4.10: Di–photon invariant mass spectrum obtained by pairing all particle–flow photons with $E_T > 400$ MeV in the barrel. The distribution observed in (a) data is compared to the (b) Monte Carlo simulation. To reduce the combinatorics, only pairs with a total energy in excess of 1.5 GeV are considered. Figures published in Ref. [59].

(a)

(b)

Figure 4.11: Average raw (black) and calibrated (red) calorimeter response (a,b) of the calibrated calorimeter as a function of the track momentum for charged hadrons selected in the data, in (a) the barrel and (b) the endcaps. The diagonal dotted lines indicate the perfect calibration. Figures published in Ref. [59].

All distributions confirm the superior performances of the particle–flow reconstruction in terms of jets and missing energy reconstruction, when compared to a pure calorimeter–based approach.
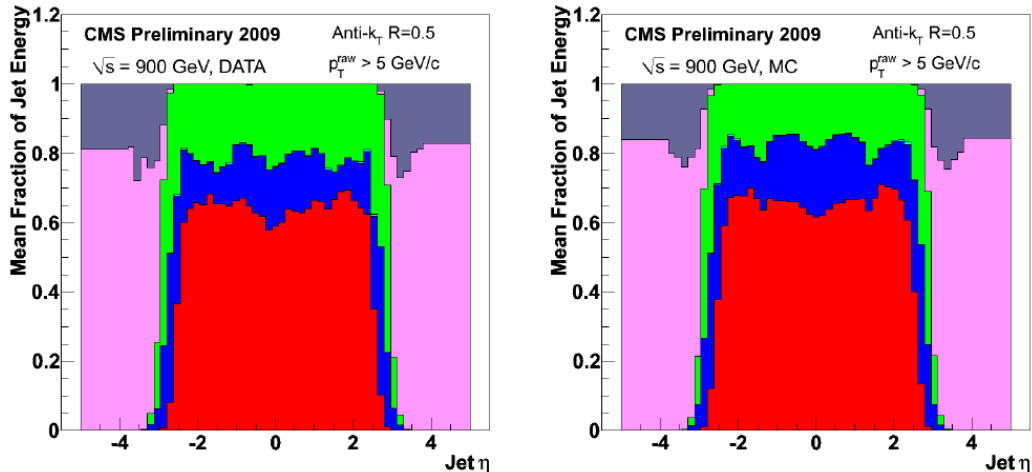
Figure 4.12: Fraction of the jet energy carried by the different constituents, for jets with $p_T > 5$ GeV in $\sqrt{s} = 900$ GeV minimum–bias events. The data distribution (left) is compared to the Monte Carlo expectation (right). From bottom to top in the central region, the different colors correspond to: charged hadrons, photons, electrons and neutral hadrons; in the forward region, particle–flow particles are created from HF deposits and are categorized either as hadronic or as electromagnetic (from Ref. [47]).

The identification and isolation efficiency for particle-flow electrons and muons have been validated in data using standard candles suitable for both low–p_T (J/Ψ, Υ) and high–p_T leptons (W, Z). The commissioning results are documented in Ref. [48].
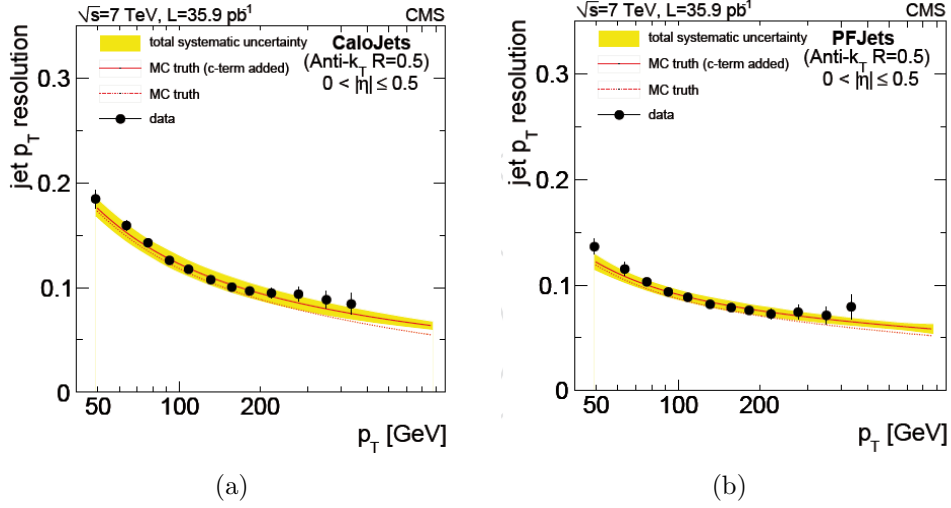
Figure 4.13: Transverse momentum resolution for central jets ($|\eta| < 0.5$) reconstructed in multi–jet events at $\sqrt{s} = 7$ TeV for (a) calo–jets and (b) particle–flow jets (from Ref. [61]).
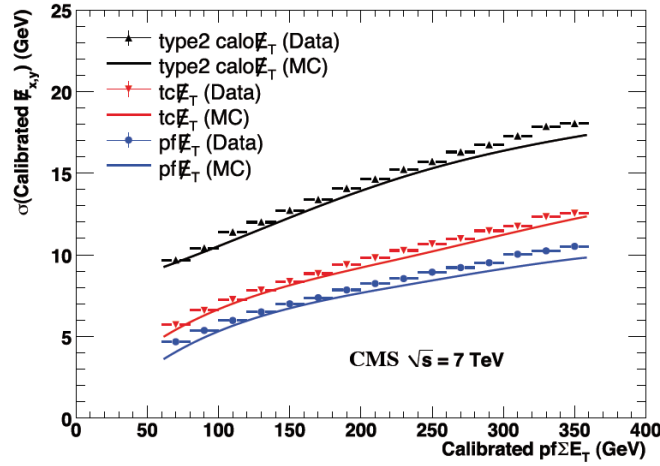

Figure 4.14: E_T^{miss} resolution in multi–jet events as a function of the particle–flow $\sum E_T$ (from Ref. [62])

Chapter 5

Tau reconstruction in CMS

This chapter first describes the reconstruction and identification of tau leptons decaying hadronically (τ_h) in CMS, and then reports on the commissioning with data.

First, I will make a concise summary of the tau lepton physics relevant for the following discussion. Then, I describe the strategy adopted in CMS for tau reconstruction. I will put emphasis on the two main tau identification algorithms, the so–called HPS and TaNC algorithms, and present commissioning results [63] using 7 TeV data, for which I brought original contributions. At last, I will discuss the discrimination between hadronically–decaying taus and lighter leptons (electrons and muons), with emphasis on my work concerning the misidentification of electrons [64].

5.1 Tau physics

The tau lepton is the heaviest among the three families of leptons [43]. Thanks to its large mass,

$$m_\tau = (1776.82 \pm 0.16) \text{ MeV},$$

i.e roughly seventeen times larger than the muon mass, the tau lepton can decay, via the weak interaction, into hadrons, a *uniqum* among leptons. Compared to e.g. the muon, the larger mass implies a shorter life–time by at least a factor of $(m_\mu/m_\tau)^5$. Taking into account even the large number of open decay channels, the tau life–time (times c) comes to be pretty short:

$$c\tau \approx 87 \ \mu\text{m}.$$

Therefore, τ leptons produced in collider experiments will typically decay in flight before interacting with any of the detectors.

The main decay channels of the tau lepton are listed in Table 5.1.

The purely leptonic decays account for $\approx 35\%$ of the total width; the rest is absorbed by semi–leptonic decays into one or three charged pions (prongs) plus additional neutral pions. The decay to kaons is Cabibbo–suppressed by an approximate factor $|V_{us}|^2/|V_{ud}|^2 \approx 5\%$, where V is the Cabibbo–Kobaiashi–Maskawa matrix introduced in Section 2.1.2.

The ratio R_τ between the tau decay width to hadrons and electrons can be decomposed as the sum of three terms [65]:

$$R_\tau \equiv \frac{\Gamma(\tau^- \to \text{hadrons } \nu_\tau)}{\Gamma(\tau^- \to e^- \bar{\nu}_e \nu_\tau)} = R_{\tau,V} + R_{\tau,A} + R_{\tau,S}$$

where V, A (S) indicate the vector and axial hadronic current acting between the vacuum and the u/d (s) hadronic final state. Neglecting the pion mass, the leading order prediction for the $V + A$ component is

$$R_{\tau,V+A} = N_C |V_{ud}|^2$$

with $N_C = 3$ number of colors, thus giving an approximate ratio of 2.8. At higher orders in perturbative theory, this ratio is increased by about 20%, mostly due to QCD perturbative corrections [65]. The resulting prediction is in agreement with the experimental results reported in Table 5.1.

Decay channel	BR (%))
$\tau^- \to \mu^- \bar{\nu}_\mu \nu_\tau$	17.36
$\tau^- \to e^- \bar{\nu}_e \nu_\tau$	17.85
$\tau^- \to h^- \nu_\tau$	11.6
$\tau^- \to h^- \pi^0 \nu_\tau$	26.0
$\tau^- \to h^- \pi^0 \pi^0 \nu_\tau$	9.5
$\tau^- \to h^- h^+ h^- \nu_\tau$	9.8
$\tau^- \to h^- h^+ h^- \pi^0 \nu_\tau$	4.8
others	3.1

Table 5.1: Main decay channels of the τ^- lepton. The symbol h^- denotes a charged meson. The decay to pions is dominant because final states with kaons (K^-) are Cabibbo–suppressed: $BR(\tau^- \to K^- \nu_\tau) \approx 0.063 \cdot BR(\tau^- \to \pi^- \nu_\tau)$. Decays to charmed mesons D^- are kinematically forbidden.

In about 53% of the cases, tau leptons decay to final state with more than one hadron. Since the taus relevant for hadron collision experiments are typically produced with an energy in the laboratory frame that vastly

exceeds m_τ, the decay hadrons are seen by the detector as a collimated bunch of particles, a signature that resembles a gluon/quark initiated jet.

The main handle to separate hadronic taus from QCD jets, which are produced with a cross–section that overwhelms tau production at hadron colliders, comes from the fact that the particle content inside a tau jet is limited to a handful of constituents, which can even feature Dalitz decays. The name of the game is therefore to resolve the individual tau decay products, i.e. to have a detector granular enough to spatially separate charged and neutral pions.

The decay kinematics of a spin-$\frac{1}{2}$ particle into a neutrino plus a spin-0 or 1 system bears information about the mother polarization that can be normally extracted in experiments, e.g. by analyzing the angles between the daughter hadrons and the tau lepton. This is also true for the leptonic decays, but the sensitivity to the tau lepton polarization is reduced as a consequence of the two final states neutrinos[1]. This *polarimeter* [66] property makes the tau lepton a privileged probe of new, and known, physics. For example, a resonance decaying to a pair of tau leptons introduces a spin correlation on the taus that is a fingerprint of its quantum numbers (J and CP).

An additional challenge in reconstructing tau leptons is posed by the presence of neutrino(s) in the final state, which escape undetected. The p_T spectrum of the visible particles from the tau decay is therefore softer than that of original tau lepton.

5.2 Tau reconstruction algorithms

As discussed in the Section 5.1, resolving the individual decay products inside an hadonically–decaying tau is of primary importance in order to discriminate genuine tau decays from gluon/quark initiated jets. CMS has adopted a particle–flow approach towards tau reconstruction [67]. Since the particle–flow algorithm is already implemented for the global offline reconstruction of CMS events (Section 4.2), the output of this algorithm can be used to seed the reconstruction of τ_h candidates.

First, all particle–flow particles are clustered into jets using the anti–k_T algorithm [68] with radius $R = 0.5$. For each jet, the particle content is scanned: π^0 candidates are built from the photons, if any, and finally

---

[1]For example, in the $\tau^- \to \pi^- \nu_\tau$ decay, the differential decay rate in the cosine of the angle θ between the pion and the tau polarization axis in the τ rest-frame is of the form $d\Gamma/d\cos\theta \propto 1 + P_\tau \cos\theta$, while for the $\tau^- \to l^- \bar{\nu}_l \nu_\tau$, the decay rate in the $\cos\theta$ of the lepton is $d\Gamma/d\cos\theta \propto 1 + \frac{1}{3}P_\tau \cos\theta$, so that the sensitivity to P_τ is suppressed by a factor of 0.33.

assembled with the charged hadrons to form an hypothesized decay mode, from which the τ_h four–momentum and the compatibility with a τ_h hypothesis can be measured. A cut–based (HPS) and a multivariate (TaNC) algorithm are currently used for this purpose [63].

5.2.1 The HPS algorithm

The Hadron Plus Strips (HPS) algorithm is designed to find the footprint of converted photons from π^0 decay by clustering electromagnetic objects, i.e. electrons and photons, into $\eta \times \phi$ *strips* (hence its name). The strips are broad in the azimuthal direction and thin along η in order to accommodate soft electrons from photon conversion that get deviated by the magnetic field before reaching the ECAL surface. The attention given to conversion is motivated by the large branching ratio of the tau lepton into final states with at least one π^0 (Table 5.1), times the probability that at least one of the photons converts while crossing the up to 1.5 X_0 of the tracker [39].

Strips are grown starting from the most energetic electromagnetic particle in the jet (pivot), by adding the most energetic particle found in a rectangular window (0.05×0.20) centered around the pivot. The four–momentum of the strip, computed by summing the two particles four–momenta, is then used as the new pivot. This procedure is repeated until no more particles are found. Only strips with a transverse momentum in excess of 1 GeV are considered further.

The ensemble of strips and charged particles (muons, electrons and charged hadrons not contained into strips) is used to build τ_h candidates in four different categories, or decay modes, depending on whether the ensemble contains:

1. one charged particle and no strips,

2. one charged particle and one strip,

3. one charged particle and two strips,

4. three charged particles.

These categories are designed to target the h^-, $h^-\pi^0$, and $h^-h^+h^-$ decay modes, thus accounting for about 75% of the tau width into hadrons. The decay $h^-\pi^0\pi^0$ and $h^-h^+h^-\pi^0$ are not explicitly searched for, but can still accidentally fall into one of the previous categories.

In each category, specific cuts are applied to the mass of the strip, to the pion–strip mass or to the three–pion mass, to enforce compatibility with the tau Dalitz decays.

86

In the first category, no cuts are applied, since the tau candidate consists of just one particle.

In the second, the strip mass is required to be in the range $[50, 200]$ MeV (i.e. compatible with the π^0 mass [43]), if the strip consists of more than one electromagnetic particle, otherwise the strip four–momentum is assigned the nominal π^0 mass; furthermore, the mass of the pion–strip pair is required to be in the range $[0.3, 1.3]$ GeV (i.e. compatible with the $\rho(770)$ resonance [43]).

The third category is similar to the second, with the additional request for the mass of the two strips to be compatible with the π^0 mass. Therefore, this class targets the $\pi^-\pi^0$ decay where the photons from the neutral pion are reconstructed as two separated ECAL clusters.

In the fourth category, the mass of the three charged pions is required to be in range $[0.8, 1.5]$ GeV (i.e. compatible with the $a_1(1260)$ resonance [43]).

For the second, third and fourth categories, the strip(s) and pion(s) momenta should be contained inside a shrinking cone with dynamical radius

$$R(p_T^{\tau_h}) = \min\left\{\max\left\{\frac{(2.8\ \text{GeV})}{p_T^{\tau_h}}, 0.05\right\}, 0.10\right\}, \qquad (5.1)$$

where $p_T^{\tau_h}$ is the transverse component of the vectorial sum of the strip and pion momenta. To ensure that no other hard structure arises inside the same particle–flow jet, tau candidates whose momentum is separated from the total jet momentum by a distance $R > 0.1$ are rejected (see Eq. (3.6) for the definition of R).

In case more than one reconstructed decay mode is found in the same jet, the one leading to the highest-p_T tau is chosen. Each tau candidate is assigned its own production vertex, defined as the primary vertex that is closest along the z axis to the backward extrapolation of the track linked to the leading (i.e. highest–p_T) charged particle of the seeding jet. The charged tau constituents are then required to be compatible with that vertex within $|d_z| < 0.2$ cm.

Any other electromagnetic or charged particle found within $R < 0.5$ from the τ_h direction is treated as an *isolation* particle. Isolation particles are used to discriminate hadronic taus from QCD jets: specific requirements on the multiplicity and/or energy of such particles select genuine taus with variable purity.

A *loose* (no photons with E_T in excess of 1.5 GeV, no charged hadrons with p_T in excess of 1.0 GeV), *medium* (no photons with E_T in excess of 0.8 GeV, no charged hadrons with p_T in excess of 0.8 GeV), and *tight* (no photons with E_T in excess of 0.5 GeV, no charged hadrons with p_T in excess

of 0.5 GeV) working points have been used in early physics analyses (see e.g. Ref. [70]). The expected efficiency for the three working points is shown in Fig. 5.1(a) as a function of the generated visible tau p_T.

In order to maintain the fake rate from QCD jets smaller than a percent or so, the p_T thresholds for isolation particles has to be lowered close to the mean value of the minimum–bias p_T spectrum. This implies a non negligible dependence of the isolation efficiency on the rate of pile–up interactions.

To reduce the sensitivity to pile–up, only those charged particles whose track is matched to the tau production vertex are considered as isolation particles. Because the pile–up photons cannot be unambiguously associated to a primary vertex, their contribution to the isolation deposit has to be estimated by other means. An event–by–event estimation of the pile–up photon energy ($\Delta\beta$) is obtained by a weighted p_T sum of all charged hadrons with p_T in excess of 0.5 GeV whose direction are closer than $R < 0.8$ from the tau direction and which are not matched to the τ_h production vertex (i.e. coming from pile–up vertices). The weight relates the charged pile–up deposit to the expected neutral pile–up contribution. Its value has been optimized using the Monte Carlo simulation. Finally, a continuous isolation value is defined by the p_T sum of all isolation particles, after subtracting $\Delta\beta$. Thresholds on the isolation value of 1.5, 0.8 and 0.5 GeV define the loose, medium, and tight $\Delta\beta$–corrected working point. The corresponding expected efficiencies are reported in Fig. 5.1(b) as a function of the generated visible tau p_T.

5.2.2 The TaNC algorithm

The Tau Neural Classifier (TaNC) algorithm reconstructs individual decay modes by combining charged particles and π^0 candidates. The latter are formed from combinatorial associations of photons. Each decay mode provides a list of discriminating variables that are fed as an input to an artificial Neural Network (NN) [71], trained to optimally separate genuine taus in a $Z \to \tau\tau$ Monte Carlo sample from jets in a QCD simulated sample.

First, the leading (highest–p_T) particle in the seeding jet is required to have p_T in excess of 5 GeV and to be closer than $R = 0.1$ from the jet direction. Then, all charged particles and photons with p_T above 0.5 GeV and within $R = 0.15$ of the leading particle are used to build the τ_h candidate.

The signal constituents (photons and charged particles) are required to be contained inside a shrinking cone with dynamical radius

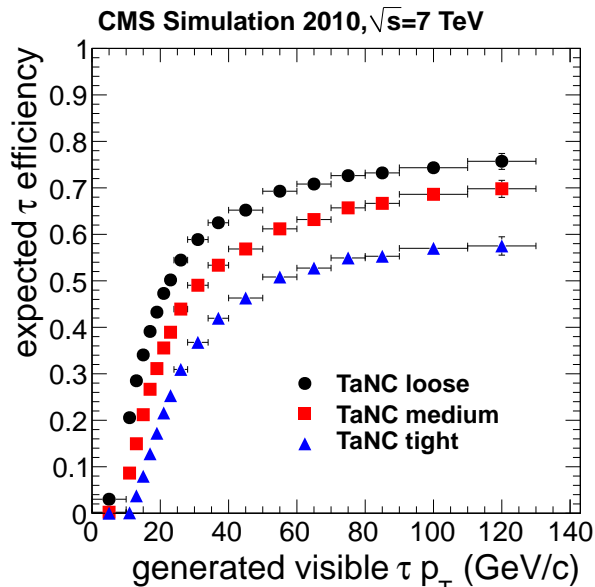$$R(p_T^{\tau_h}) = \min\left\{\max\left\{\frac{(5\text{ GeV})}{p_T^{\tau_h}}, 0.07\right\}, 0.15\right\}, \tag{5.2}$$
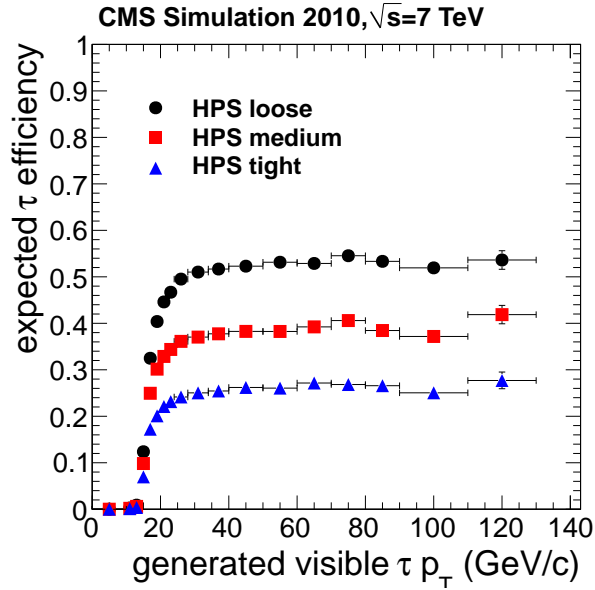
(a)
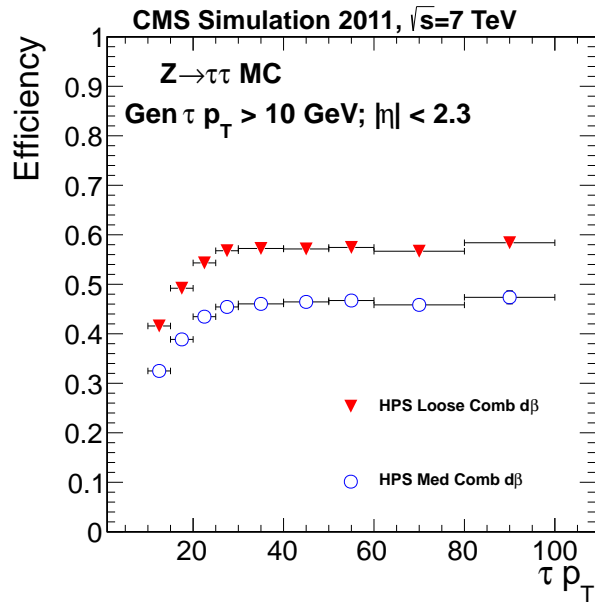
(b)

Figure 5.1: a) The expected efficiency of tau identification for the loose, medium, and tight working points of the HPS algorithm, without $\Delta\beta$ corrections (published in Ref. [63]); (b) the expected efficiency of tau identification for the loose and medium working points of the HPS algorithm, with $\Delta\beta$ corrections. The efficiency is shown as a function of the generated visible tau p_T [69].

where $p_T^{\tau_h}$ is defined as in Eq. (5.1). Neutral pion candidates are formed by grouping pairs of photons with mass below 200 MeV. The leftover photons are considered as additional pion candidates if their energy exceeds 10% of the τ_h energy. An isolation annulus extending from the signal cone up to a maximum of $R = 0.5$ is used to collect the isolation particles.

The multiplicity of particles found in the signal cone determines the reconstructed decay mode. Combinations other than h^-, $h^-\pi^0$, $h^-h^+h^-$, $h^-\pi^0\pi^0$, and $h^-h^+h^-\pi^0$ are discarded. Each decay mode maps to a specific NN, which uses the kinematics of the signal and isolation particles to discriminate genuine tau decays from jets. Lower cuts on the NN output define different working points. In analogy with the HPS algorithm, a *loose*, *medium*, and *tight* working point is defined (Fig. 5.2).

Figure 5.2: Expected efficiency of tau identification for the loose, medium, and tight working points of the TaNC algorithm as a function of the generated visible tau p_T. Figure published in Ref. [63].

The performances of the HPS and TaNC algorithms were found to be in the same ballpark. The turn–on effect clearly visible in Fig. 5.1 and 5.2 is induced by the p_T cut on the reconstructed τ_h, applied as a pre–selection. The HPS algorithm features a flat efficiency as a function of the generated tau momentum already for $p_T^{gen} > 30$ GeV; for the TaNC, the plateau is reached at around 100 GeV. By averaging over the p_T spectrum of τ_h reconstructed in the same $Z \to \tau\tau$ Monte Carlo sample, the total expected efficiency is

46% (54%), 34% (43%) and 23% (30%) for the HPS (TaNC) algorithms [63].

Being more simple and robust, the HPS was adopted for physics analyses, with the TaNC used for cross–checks. This motivates the larger weight given to the HPS algorithm in the following discussion.

5.2.3 Reconstruction and identification efficiency

The tau reconstruction and identification efficiency has been measured from data using a redundancy of techniques.

Tag–and–probe

A tag–and–probe like technique has been used to measure the identification efficiency of hadronically–decaying taus. An isolated, high–p_T, triggering muon defines the tag, while the probe is a particle–flow jet. A loose pre–selection on the probe, which biases it to be tau–like, helps in reducing the background. This selection can isolate a sizeable amount of $Z \to \tau\tau$ events, where one tau decays leptonically to a muon, and the other decays semi–leptonically into hadrons.

The tau efficiency is estimated by measuring the number of probes that pass or fail the tau identification and isolation criteria, using the Monte Carlo simulation to account for the pre–selection efficiency.

The number of passing and failing probes are extracted from a likelihood fit to the visible mass of the tag and probe pair (Fig. 5.3); the mass shapes for the signal and background are taken from the simulation.

With the 36 pb^{-1} collected in 2010 at $\sqrt{s} = 7$ TeV, the tau reconstruction and identification efficiency was measured to be compatible with the Monte Carlo expectation within an uncertainty in the range $25-30\%$ [63], depending on the algorithm and working point. The total uncertainty was statistically dominated. A similar measurement extended to the full data set collected in 2011 (≈ 5 fb^{-1}) found a data–to–simulation ratio consistent with unity within a 6%, systematically–dominated, uncertainty [76].

This method delivers a data-driven measurement of the tau efficiency that can be used in all physics analyses, provided that an eventual correlation with the passing probe sample is correctly accounted for. In particular, the result of the measurement does not depend on the tau provenance, as long as a resonance other than $Z \to \tau\tau$, if present, does not bias significantly the visible mass shape.
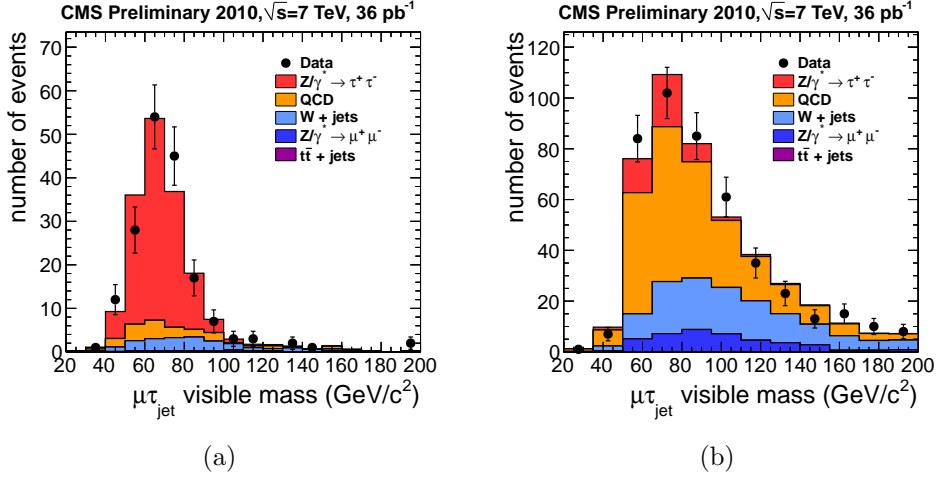
Figure 5.3: The visible invariant mass of the muon and jet system for preselected events which passed (a) and failed (b) the HPS loose tau identification requirements compared to predictions of the MC simulation. Figures published in Ref. [63].

Ratio $Z \to \tau\tau / Z \to ll$, $l = e, \mu$

This measurement is documented in Ref. [72]. It is based on the assumption of lepton family universality. The ratio between the number of $Z \to \tau\tau$ (recorded in the $\tau_\mu\tau_h$ and $\tau_e\tau_h$ channels) and $Z \to ll$ events measured in the same data set and properly corrected for acceptance and lepton reconstruction efficiency, provides a luminosity–independent measurement of the tau reconstruction and identification efficiency:

$$\epsilon_\tau = \frac{1}{\sigma_{Z \to \ell\ell}} \left(\frac{N_{l'h}}{\mathrm{BR}_{l'h} \cdot \mathcal{L} \cdot A_{l'h} \cdot \epsilon_{l'}} \right) \tag{5.3}$$

where $N_{l'h}$ ($l' = e, \mu$) is the observed number of $Z \to \tau\tau$ events in the $\tau_{l'}\tau_h$ channel, $A_{l'h}$ is the geometrical acceptance, $\epsilon_{l'}$ is the total lepton ℓ' reconstruction efficiency, $\sigma_{Z \to \ell\ell}$ is the $Z \to \ell\ell$ cross–section and $\mathcal{L}$ is the total integrated luminosity. If $\sigma_{Z \to \ell\ell}$ is measured in the same data set:

$$\sigma_{Z \to \ell\ell} = \frac{N_{\ell\ell}}{A_{\ell\ell} \cdot \epsilon_{\ell\ell} \cdot \mathcal{L}},$$

then the luminosity, and other systematics on the acceptance and lepton efficiency, cancel in the ratio.

Using the 36 pb^{-1} collected in 2010 at $\sqrt{s} = 7$ TeV, a data–to–simulation correction factor (0.96 ± 0.07) was determined for HPS loose taus [72].

In this method, the assumption is made that the number of $\tau_\mu\tau_h$ or $\tau_e\tau_h$ events, estimated from data after the background subtraction, originate exclusively from Z/γ^* production. Therefore, it is not suitable to be deployed in searches for resonances decaying to tau leptons that could mix with the Drell–Yan production. For example, a new resonance $\phi \to \tau\tau$ with $M_\phi \approx 90$ GeV and sizeable cross–section would artificially enhance the resulting tau efficiency.

Ratio $(\tau_l\tau_h)/(\tau_l\tau_l)$, $l = e, \mu$

Measuring the $Z \to \tau\tau$ yield in at least one semi–leptonic and one fully-leptonic channel allows to calibrate the tau efficiency on data independently from the origin of the measured taus, since the branching ratios do not depend on the tau production mechanism. This measurement is also luminosity–independent. Based on the 36 pb^{-1} collected in 2010 at $\sqrt{s} = 7$ TeV, a data–to–simulation correction factor (0.94 ± 0.09) was determined, for HPS loose taus, by a simultaneous fit of the $\tau_\mu\tau_h$, $\tau_e\tau_h$, $\tau_e\tau_\mu$ and $\tau_\mu\tau_\mu$ channels [72]. The larger uncertainty with respect to the $Z \to \tau\tau/Z \to ll$ method is due to the limited statistic of the fully leptonic channels.

This method cannot be used for the search of a resonance decaying to taus, because of the $\approx 100\%$ correlation with the data sample used to extract the measurement.

5.2.4 Tau energy scale and reconstruction modes

The HPS algorithm classifies hadronically–decaying taus into reconstructed decay modes that are designed to tag specific decay channels. The correlation between generated and reconstructed decay modes is represented in Fig. 5.4 in the form of a 3×3 matrix. Each entry (i, j) of the matrix represents the fraction of taus generated in the decay channel i,

$$i \in \{h^-,\ h^-\pi^0\text{s},\ h^-h^+h^-\},$$

that are reconstructed with decay mode j,

$$j \in \{\text{one–prong no strips, one–prong plus strip(s), three–prongs}\}.$$

The diagonal entries exceed 80%, showing that the algorithm reconstructs the correct decay mode for the bulk of the events.

Whenever one of the tau decay products is reconstructed by the particle–flow, but is not properly recognized by the HPS algorithm as a signal constituent, it will be most probably treated as an isolation particle. In this
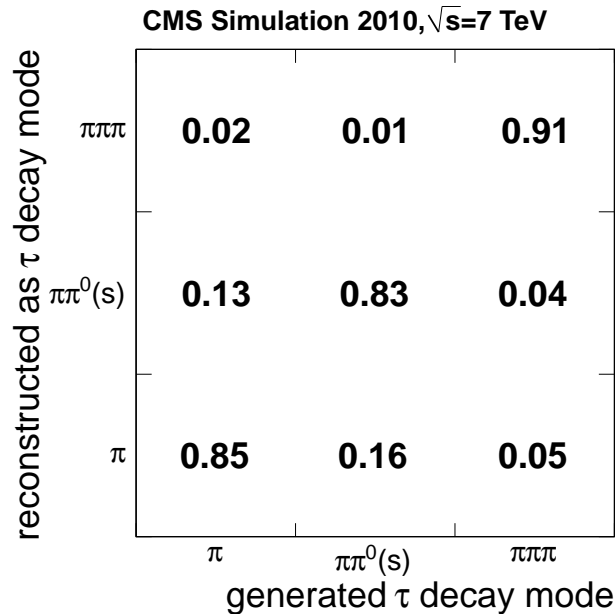
CMS Simulation 2010, $\sqrt{s}$=7 TeV

	π	$\pi\pi^0$(s)	$\pi\pi\pi$
$\pi\pi\pi$	0.02	0.01	0.91
$\pi\pi^0$(s)	0.13	0.83	0.04
π	0.85	0.16	0.05

reconstructed as τ decay mode (y-axis) / generated τ decay mode (x-axis)

Figure 5.4: The fraction of reconstructed and identified τ_h matched to the generated decay i, $i \in \{h^-,\ h^- \geq 1\pi^0,\ h^-h^+h^-\}$, that get classified with decay mode j, $j \in \{$one–prong no strips, one–prong plus strip(s), three–prongs$\}$, obtained from a $Z \rightarrow \tau\tau$ Monte Carlo sample. Figure published in Ref. [63].

case, the tau is likely to fail the isolation cut. If the isolation selection is still passed, the resulting tau candidate will be deprived of part of its original visible momentum. Conversely, if a spurious particle (e.g. from pile–up) is accidentally identified as a tau constituent, the tau candidate receives an extra momentum. These effects need to be well modeled by the simulation in order to have a precise knowledge of the tau energy scale (TauES). Mis–calibration of the tracker and ECAL energy response can also affect the TauES. The tau energy scale can be constrained from data using a variety of methods.

$\tau_\ell\tau_h$ mass shape

The visible mass of the muon and τ_h pair from $Z \rightarrow \tau\tau$ events ($\tau_\mu\tau_h$ channel) features a resonant structure, thus an enhanced sensitivity to the energy scale of both objects. The muon momentum scale is well measured from $Z \rightarrow \mu\mu$, and it can be assumed to be known with infinite precision. The $Z \rightarrow \tau\tau$ peak can be extracted from data with large purity (see e.g. Fig. 5.3 (a)). The

deviation of the TauES from the Monte Carlo expectation is measured by a maximum likelihood fit to the mass peak, where the likelihood is maximized with respect to TauES. Using 36 pb^{-1} of 7 TeV collision data, the tau energy scale is found to be consistent with the Monte Carlo expectation within error. A data–to–simulation ratio of (0.97 ± 0.03) has been measured [63].

This method could be however invalidated by the presence of a resonance $\phi \to \tau\tau$ with $M_\phi \sim M_Z$, which would potentially distort the observed mass shape and therefore bias the measurement.

Visible τ_h mass

The shape of the visible τ_h mass in a given decay mode is independent from the source of taus and is sensitive to the energy scale of the tau constituents, namely to the charged and photons energy scale for one charged plus strip(s), and to the charged energy scale for the three–prong decay mode. By comparing the τ_h visible mass spectrum observed in the $\tau_\mu\tau_h$ channel to templates obtained from simulation, where the energy scale of taus is systematically shifted up and down, the best fit value of the ratio between the observed and expected TauES was measured to be (0.97 ± 0.03) and (1.01 ± 0.02) [63], for the charged plus strip(s) and three–prong decay modes, respectively.
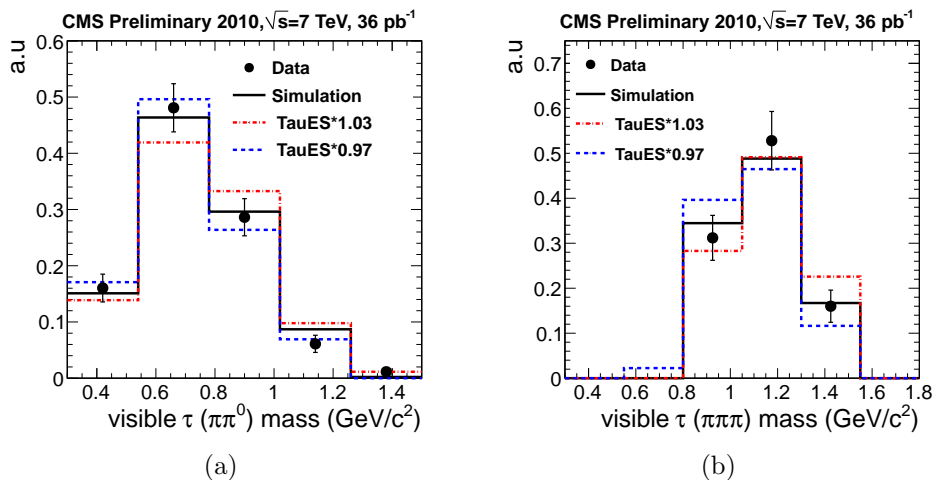
Figure 5.5: Observed and expected invariant mass of τ_h candidates selected in the $\tau_\mu\tau_h$ channel [63]. Taus are reconstructed either as single charged plus strip(s) (left) or three–prong (right) decay mode Figures published in Ref. [63].

However, this method is not sensitive to systematic migration from one reconstructed decay mode to another.

95

5.3   Fake rate from jets

As discussed in Section 5.1, the signature of hadronically–decaying taus resembles that of a quark/gluon initiated jets, an overwhelming background at hadron colliders. The isolation requirement is the main handle to reduce the contamination from QCD jets. Quarks and gluons typically fragment into a multiplicity of relatively soft hadrons. Fake taus reconstructed inside a jet are likely to be surrounded by a large number of hadrons that can potentially spoil the isolation. A tiny fraction of jets, which fragment into a few hard hadrons, will be however undistinguishable from hadronically–decaying taus.

Because the fragmentation functions depend on the initiating parton (light or heavy quark, gluon), the fake rate from jets is flavor–dependent. The fake rate from jets, measured as a function of the jet p_T, is compared to its Monte Carlo expectation in Fig. 5.6. The fake rate at a given jet p_T is defined as the fraction of jets with transverse momentum p_T that pass the tau identification criteria.

Different event selections bias the jet composition to be more quark or gluon–like. A di–jet triggered sample is expected to be enriched in gluon–initiated jets. A sample of events with an isolated, high–p_T muon (μ) and with large values of the transverse mass variable

$$M_T \equiv \sqrt{p_T^\mu E_T^{miss} - \vec{p}_T^\mu \cdot \vec{E}_T^{miss}}, \tag{5.4}$$

will mostly contain quark jets produced in association with a W boson. Finally, a sample of events with a muon, but low values of the transverse mass, will be enriched in b/c quarks.

Gluon–initiated jets feature the lowest fake rate. Indeed, jets arising from gluon fragmentation tend to be broader and to produce a larger multiplicity of particles, because of the larger color factor in the gluon splitting functions compared to quarks [73], and are therefore more likely to fail the isolation cuts.

As shown in Fig. 5.6, the observed fake rate agrees with the expectation within $\lesssim 20\%$.

5.4   Electron rejection

Genuine electrons, mis–identified as hadronically–decaying taus, represent an important, though reducible, source of background to many analyses with taus in the final state.

Isolated electrons with high transverse momentum, like those coming from the decay of the gauge bosons, are likely to pass the τ_h identification and isola-
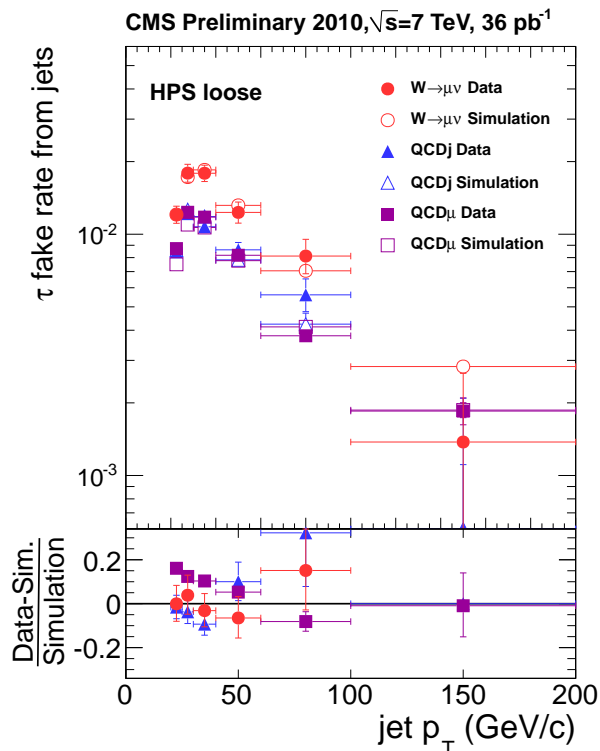
Figure 5.6: Expected and observed fake rate from jets as a function of the jet p_T, as measured in three data samples with different jet composition. Figure published in Ref. [63].

tion cuts. An anti–electron discriminator in addition to the tau identification selections is therefore necessary to prevent electrons from being identified as a τ_h.

The ability to separate electrons from pions in CMS is very good thanks to the combination of a finely grained electromagnetic calorimeter and a highly–performing silicon tracker which makes it possible to exploit, for discriminating purposes, tracking and ECAL–track matching variables in addition to the purely calorimetric ones.

A finite $e \to \tau_h$ fake rate, i.e. the probability that a real electron passes the anti–electron discriminator and identifies as a hadronically–decaying tau, is a price to pay to maintain also a high efficiency on hadronic taus.

In this section, I will discuss the existing anti–electron discriminators used in CMS physics analyses. At first, I will describe the discriminators used in early CMS analyses (see e.g. Ref. [70]), for which I measured the fake rate

from data. The studies presented here support the results published in the CMS tau commissioning paper [63].

As more data was collected, it became possible to tune and optimize the electron rejection and to measure the efficiency with more precision. In particular, the increase in instantaneous luminosity required actions to counteract the pile–up dependence featured by the early discriminators. A novel technique that I developed for the electron rejection is discussed in Section 5.4.8.

5.4.1 General considerations

The decay mode $Z \to \tau\tau \to \tau_e\tau_h$ provides the best example of a channel for which an efficient discrimination between τ_h and electrons is required: the decay $Z \to e^+e^-$ represents a background with five times larger branching ratio and with and higher acceptance.

In the approach followed here, discriminating between electrons and hadronic taus reduces to the problem of classifying the charged constituents of the tau candidate either as pions or as electrons.

Prompt electrons can give rise to fake taus with more than one signal particle. Indeed, before reaching the ECAL surface, electrons have to cross a large volume instrumented with the silicon tracker. The significant material budget of the tracker may induce photon emission by bremsstrahlung. In turn, these photons may convert into an electron/positron pair while crossing the tracker layers. The particle–flow algorithm deals with these cases by means of a dedicated bremsstrahlung–recovery algorithm (Section 4.2.3). From each tracker layer, straight line extrapolations, tangent to the track, are propagated towards the ECAL surface in the search for a brem photon; additional radiated photons can be recovered if they fall inside the supercluster footprint. Photon conversions are recovered by looking for tracks close to the GSF track of the prompt electron which exhibit a conversion–like topology.

However, if the electron identification fails, or if any of the photons (converted or not) slips through the bremsstrahlung–recovery algorithm, additional neutral or charged particles will be reconstructed around the original electron direction and subsequently merged into a single particle–flow jet. Particles from the underlying event or from pile–up, typically with a low-p_T, may be accidentally clustered in the jet.

The approach followed here is to apply the anti–electron discriminator to the leading (i.e highest–p_T) charged constituent of the reconstructed tau. As an alternative, the leading particle (charged or not) could be used. The two approaches are not equivalent, as it will be illustrated later–on. Two discriminators, a multivariate and a cut–based, have been studied.

98

Discriminator by ξ

The multivariate classifier ξ used for electron identification in the particle–flow algorithm (Section 4.2.3) provides a natural discriminator between electrons and pions. Since ξ is continuous variable, the cut value can be tuned to achieve the desired $e \to \tau_h$ fake rate.

Cut–based discriminator

In this approach, the cut–based discriminator documented in Ref. [74], usually employed to identify good electrons from jets, is instead used to veto electrons. Rectangular cuts on the value of four identification variables,

$$H/E, \ \sigma_{i\eta i\eta}, \ \Delta\phi_{in}, \ \Delta\eta_{in}, \tag{5.5}$$

have been optimized to optimally separate electrons in a $W \to e\nu_e$ simulated sample, from jets in Monte Carlo QCD events. The first and second variables measure the ratio between the energy recorded in HCAL and the total supercluster energy, and the supercluster dispersion along η, respectively. The other two variables measure the geometrical matching between the supercluster barycenter and the entrance position in ECAL of the track extrapolated outwards from its innermost measurement. By tuning the cut on each variable, working points WPϵ with efficiency $\epsilon\%$ on real electrons are defined [74].

5.4.2 Efficiency and fake rate

Two simulated $Z/\gamma^* \to \tau^+\tau^-$ and $Z/\gamma^* \to e^+e^-$ samples, generated with PYTHIA [75] and processed through the GEANT–based [60] simulation of the CMS detector, have been used to derive the efficiency vs. fake rate curve (ROC) for the two discriminators.

Taus reconstructed by the HPS algorithm are required to have a transverse momentum in excess of 15 GeV, to pass the tau identification and isolation (loose working point) and to be fully contained in the region instrumented by both the tracker and the calorimeters ($|\eta| < 2.3$).

For the estimation of the efficiency, reconstructed HPS tau in the $Z/\gamma^* \to \tau^+\tau^-$ sample are matched to a generated hadronic tau within $R < 0.15$. For the estimation of the fake rate, reconstructed HPS taus in the $Z/\gamma^* \to e^+e^-$ sample are matched to a generated electron within $R < 0.15$. This cut value has been found to have an efficiency $> 99\%$ for matching reconstructed τ_h with their respective generated tau.
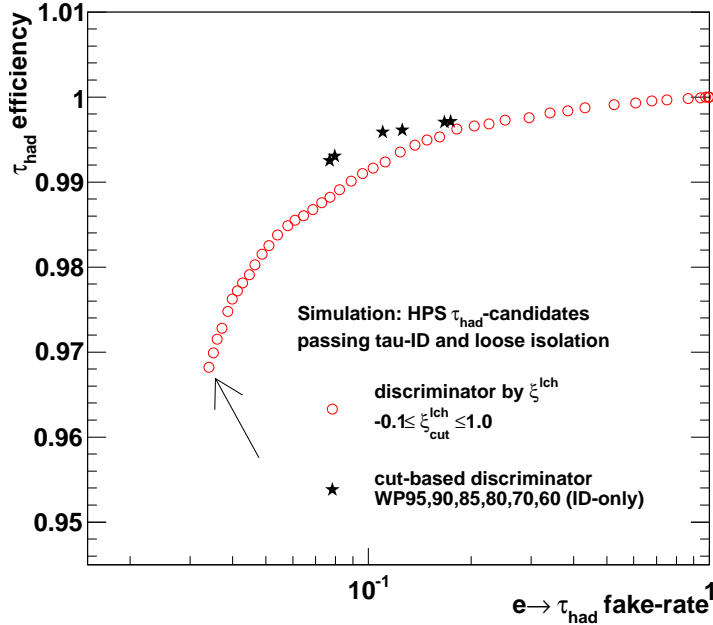
Figure 5.7: ROC curve for the ξ (empty circles) and the cut-based (full stars) discriminators. Tau candidates are required to have $p_T > 15$ GeV, to pass the tau identification and loose isolation, and to be inside the ECAL acceptance. Here, the anti–electron discriminator is applied to the leading charged tau constituent.

The ROC curves for the multivariate and cut–based discriminators are shown in Fig. 5.7. Each empty marker corresponds to a given cut on the output of the ξ discriminator of the leading charged hadron among the τ_h constituents (ξ_{cut}^{lch}). The particle–flow working point ($\xi_{cut}^{lch} > -0.1$) is indicated by an arrow. Solid stars are placed in correspondence of the efficiency and fake rate values expected from the different cut–based discriminators, with the leftmost marker referring to WP95. The ξ discriminator performs slightly worse than the cut–based. This is expected, since the particle–flow multivariate discriminator was optimized for low–p_T electrons in b−jets, while the electrons coming from the Z decay are typically isolated and produced with high–p_T.

Applying the ξ discriminator to the leading tau constituent, charged or neutral, brings a modest degradation of the efficiency. Indeed, in decays with at least one π^0 (e.g. $\tau \to a_1 \, \nu_\tau$, $\tau \to \rho \, \nu_\tau$), there is a finite probability that one of the photons from $\pi^0 \to \gamma\gamma$ converts into an e^+e^- pair; if the neutral

pion is particularly hard, the conversion electron may be clustered inside the tau signal constituents, becoming the highest–p_T candidate.

If at least one charged pion is reconstructed as well, the HPS algorithm can assign the electron to a strip, i.e. it properly identifies it as a conversion, and let the charged pion become the leading charged particle. However, this choice allows for a reduced fake rate. Indeed, if an accidental charged hadron from the underlying event, or even a conversion electron, is close in (η, ϕ) to the prompt, higher–p_T electron, than it is possible that it will be eventually clustered together with the latter. Then, the HPS algorithm reconstructs a candidate $\tau \to \rho(\to \pi\pi^0)\,\nu_\tau$, where the electron is eaten by one strip, and the spurious charged particle is promoted to the leading one.

In order to preserve the largest possible signal efficiency, the discrimination is applied to the leading charged hadron.

5.4.3   Fake rate measurement from data

The $e \to \tau_h$ fake rate was commissioned with 2010 data collected at $\sqrt{s} = 7$ TeV for three selected working points:

1. loose: $\xi < 0.6$,

2. medium–loose: failing WP95,

3. medium: $\xi < -0.1$,

listed in order of decreasing fake rate.

The first working point, which corresponds to a fake rate of $O(20\%)$, achieves an efficiency exceeding 99.5%. Therefore, it is indicated for channels where fake electrons represent a modest background.

The second working point preserves a relatively high efficiency, at the price of a modest fake rate of $O(5\%)$.

The third working point allows for a low fake rate of $O(3\%)$ at the price of about 4% loss in efficiency. Therefore, it is more suitable for analyses where the contamination from real electrons is important.

5.4.4   Event selection

Events are pre–selected by requiring at least one of the electron/photon HLT trigger to fire. A data set corresponding to a total integrated luminosity of 33 ± 3 pb^{-1} has been analyzed. The event selection starts with the requirement of at least one good reconstructed vertex. Events with a pathological tracking history are removed by requesting at least 25% of good tracks out of

at least ten reconstructed tracks. At least one electron and one particle–flow jet with opposite sign and with invariant mass between 40 and 120 GeV are required. The electron and the jet have to pass additional criteria which identify them as a valid tag and probe, respectively.

The tag must have a transverse momentum in excess of 25 GeV and pass a tight electron identification (WP70). The tag is further requested to point outside the crack region between the ECAL barrel and the ECAL endcap: $|\eta| < 1.44$ and $|\eta| > 1.56$. To avoid a trigger bias, the tag has to be matched within $\Delta R < 0.5$ to a trigger primitive passing the electron trigger path.

The probe is a reconstructed HPS tau with a transverse momentum in excess of 20 GeV, isolated (loose WP), and for which the entrance position of the leading charged particle track, extrapolated to the ECAL surface, is outside the crack regions between ECAL modules, namely

$$|\eta| \notin \{[0, 0.018], [0.423, 0.461], [0.770, 0.806], [1.127, 1.163], [1.460, 1.558]\}$$
(5.6)

This requirement is meant to reduce electron fakes that slip through the ECAL cracks and deposit a large amount of energy in HCAL, thus resembling ideal charged pions. This efficiency is factorized out from the measurement because it is a pure geometrical acceptance cut, that is supposed to be well modeled by the simulation.

For each tag and probe pair, the invariant mass m_{tp} is stored in a collection of mass points, $\{m_{tp}\}$. Each collection is split into two subsets depending on whether the probe passes, $\{m_{tp}\}_P$, or fails, $\{m_{tp}\}_F$, the anti–electron discriminator. If more than one probe is reconstructed for a given tag, a random selection among the candidates is performed.

Finally, the value of the transverse mass between the electron and the particle–flow missing transverse energy (Eq. 5.4) is required to be less than 50 GeV, as to reduce the contamination from W+jets.

5.4.5 Likelihood model

The $e \rightarrow \tau_h$ fake rate has been measured in two $|\eta|$ bins. The choice to split into barrel ($|\eta| < 1.44$) and endcap ($|\eta| > 1.56$) is motivated by the fact that the fake rate, as predicted by the simulation, is significantly different in these two regions of the detector.

The fake rate (ϵ_{fake}) for each of the working points listed in Section 5.4.1 is estimated by dividing the number of tag-probe pairs in the passing sample, N_P^{sgn}, by the total number of pairs $N^{sgn} = N_P^{sgn} + N_F^{sgn}$:

$$\epsilon_{fake} = \frac{N_P^{sgn}}{N_P^{sgn} + N_F^{sgn}}$$

Because of the presence of background (tags and/or probes that are not matched to a real electron from $Z/\gamma^* \rightarrow e^+e^-$), a background subtraction procedure is made necessary.

The background is most prominent in the passing sample. Here, it can be classified into a *reducible* and *irreducible* component. The reducible component comprises W+jets, QCD multi–jet, and γ+jet. The first and the last are unaffected by a tighter selection on the tag. The irreducible component is $Z \rightarrow \tau\tau \rightarrow \tau_e\tau_h$ where the electron identifies as the tag and the probe is a real hadronic tau, and $t\bar{t}$ in a similar final state.

In the failing sample, the background contribution is small. It is estimated to account for less than 0.5% of the total number of events.

The background subtraction exploits the difference in the mass shape for signal and background as a handle to disentangle between the two. A simultaneous extended maximum likelihood fit to the mass distributions of the passing and failing samples is performed. The *pdf* of the mass distribution in each sample is given by the superimposition of the signal and background *pdf*s. Two parameters correlate the likelihood of the passing and failing samples, which are chosen to be ϵ_{fake} and N^{sgn}, according to the following system of equations:

$$\begin{cases} F_P^{data}(m_{tp}) = N^{sgn} \cdot \epsilon_{fake} \cdot f_P^{sgn}(m_{tp}) + N_P^{bkg} f_P^{bkg}(m_{tp}) \\ F_F^{data}(m_{tp}) = N^{sgn} \cdot (1 - \epsilon_{fake}) \cdot f_F^{sgn}(m_{tp}) + N_F^{bkg} f_F^{bkg}(m_{tp}) \end{cases} \quad (5.7)$$

where f_I^J (F_I^J) denotes the (un)normalized *pdf* for the process J with status $I = P, F$ with respect to the anti–electron discriminator.

The signal *pdf*s, f_P^{sgn} and f_F^{sgn}, are obtained from the convolution of a Breit–Wigner,

$$b(m_{tp}; M_{Z^0}, \Gamma_{Z^0}),$$

with a Crystal–Ball function, which accounts for the Drell–Yan tale and for resolution effects:

$$f_P^{sgn}(m_{tp}) = \{b(M_{Z^0}, \Gamma_{Z^0}) * \rho(\mu_P, \sigma_P, \alpha_P, n_P)\}(m_{tp}) \quad (5.8)$$
$$f_F^{sgn}(m_{tp}) = \{b(M_{Z^0}, \Gamma_{Z^0}) * \rho(\mu_F, \sigma_F, \alpha_F, n_F)\}(m_{tp}) \quad (5.9)$$

The background *pdf* in the passing sample is modeled as a superimposition of the *pdf*s of the individual background components, defined as follows.

- $Z \rightarrow \tau\tau$
  A histogram of the mass distribution is obtained from a high–statistic $Z^0/\gamma^* \rightarrow \tau\tau$ Monte Carlo sample. The *pdf*, $f_P^{MC;Z\tau\tau}$, is given by a bin–by–bin interpolation of this histogram with a 4th power polynomial, in order to smooth out statistical fluctuations;

- QCD multijet

  The QCD mass template is taken from data. Events are required to pass the selections of Section 5.4.4 *but* for two cuts, namely the isolation of the tag and the opposite-sign requirement, which are reverted to obtain a QCD–enriched sample. The *pdf*, $f_P^{data;QCD}$, is determined by a fit to this mass distribution with a Landau function;

- $W \to e\nu_e+$ jets

  The *pdf*, $f_P^{MC;W}$, is obtained by fitting the Monte Carlo mass distribution with a Crystal–Ball function.

- $t\bar{t}$

  The mass distribution is assumed to be flat, resulting in a constant *pdf*, $f_P^{MC;t\bar{t}} \sim$ constant;

- $Z \to e^+e^- +$ jets, jet $\to \tau_h$

  The *pdf* $f_P^{MC;Zjet}$ is obtained by fitting the Monte Carlo mass distribution with a Crystal–Ball function.

Other SM processes, like $W \to \tau\nu$, di–bosons and single–top are here neglected. Their contribution is expected to be small. The contribution from γ+jet has been found to be negligible.

Examples of signal and background templates used in the fit are shown in Fig. 5.8.

The background *pdf* for the passing sample is then given by:

$$
\begin{aligned}
F_P^{bkg}(m_{tp}) = & \ n^{Z\tau\tau} f_P^{MC;Z\tau\tau}(m_{tp}) + n^{QCD} f_P^{data;QCD}(m_{tp}) + \\
& + n^W f_P^{MC;W}(m_{tp}) + n^{t\bar{t}} f_P^{MC;t\bar{t}}(m_{tp}) + \\
& + n^{Zjet} f_P^{MC;Zjet}(m_{tp})
\end{aligned}
\tag{5.10}
$$

The background *pdf* for the failing sample is obtained by histogramming the combined mass distribution for the backgrounds mix in the failing sample, as predicted by the simulation, leaving the overall normalization as a free parameter.

Sixteen parameters are left floating in the simultaneous fit:

$$
\begin{aligned}
& N^{sgn}, \epsilon_{fake}, N_F^{bkg}, \mu_P, \mu_F, \sigma_P, \sigma_F, \alpha_P, \alpha_F, \\
& n_P, n_F, n^{Z\tau\tau}, n^{QCD}, n^W, n^{t\bar{t}}, n^{Zjet}
\end{aligned}
\tag{5.11}
$$

Additional loose constraints on the Crystal–Ball tail parameters and on the background yields in the passing sample, modeled as Lognormal distributions, are added to the log–likelihood function to help the convergence.
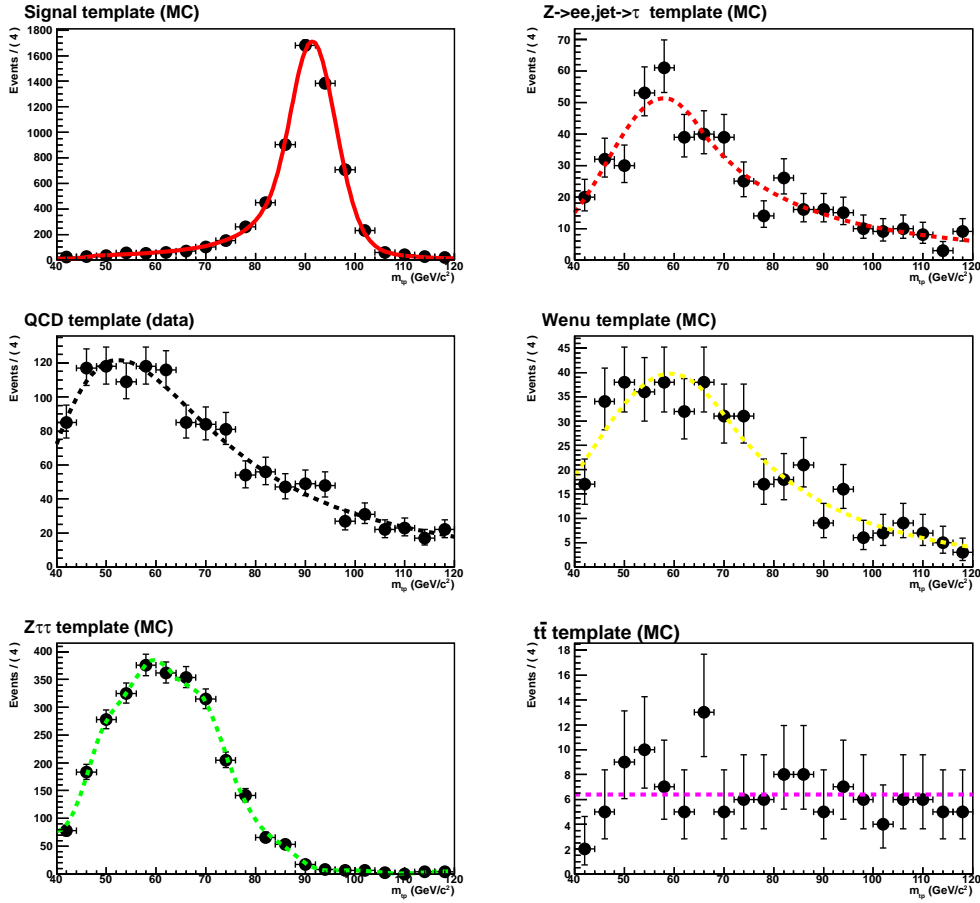
Figure 5.8: Some of the signal and background templates used in the likelihood fit.

5.4.6 Systematic errors

Uncertainties due to the background modeling are estimated by the maximal difference between the fake rates measured using the nominal templates or alternative templates obtained by varying the probe energy scale up and down by 3%, for backgrounds where the probe is expected to be a real τ_h, or 5%, in the background where the probe is a jet. This effect amounts to a relative uncertainty of about 8%,4% and 2% for the medium, medium–loose and loose working points, respectively.

The effect of a poor modeling of the non resonant Monte Carlo templates is further studied by repeating the fit without one of the template at the time. The exclusion of $f_P^{MC;t\bar{t}}$ leads to negligible effects, while a few percent

differences are found when $f_P^{MC;W}$, or $f_P^{MC;Zjet}$, is discarded. The reason for this is that all the non–resonant processes feature qualitatively the same mass spectrum with a broad maximum around 50–60 GeV, induced by the kinematic cuts on the tag and probe, and a long tail. Therefore, when one of the template is missing, the other components can float in order to account for it, thus making the model more robust.

Given the mild dependence of the fake rate on the p_T-threshold applied to the probe, the uncertainty on the electron energy scale is found to have a negligible impact even considering conservative scale uncertainty of 3%.

An additional systematic uncertainty due the limited Monte Carlo statistics (ranging from 0.5% to 2%) is attributed to the data–to–simulation ratios.

5.4.7 Results

The $e \to \tau_h$ fake rates measured in the two $|\eta|$ bins and for the three working points, are reported in Fig. 5.9, 5.10 and 5.11.

To validate the background subtraction procedure, the same simultaneous fit is run over a mix of Monte Carlo simulated samples corresponding to an equivalent integrated luminosity of 500 pb^{-1}. To avoid making a weighted fit, all Monte Carlo events are maintained with unitary weight. Since the available statistics for the QCD multi–jet samples is of the order of 30 pb^{-1}, a pseudo–simulated sample of QCD has been obtained by sampling the QCD template taken from data as many times as to achieve the target luminosity. The agreement within the statistical uncertainties between the tag–and–probe and the MC–truth efficiency predicted by the simulation validates the fit procedure. Figures 5.9 to 5.11 show the results of the measurement. Statistical errors on the data–to–simulation factors come from the MINOS error [77]. For the MC–truth, binomial errors are used. Systematic errors result from the sum in quadrature of all the uncertainties described in the previous section.

The numerical results are summarized in Table 5.2. The MC–truth expectation is also reported, together with the result of the Monte Carlo closure test.

Finally, the data–to–simulation ratios for the three working points are reported in Table 5.3.

5.4.8 Optimized electron rejection

The cut–based and multivariate discriminators of Section 5.4.3 are quite sensitive to pile–up. A significant increase in the fake rate was observed in the second part of the 2011 data taking, characterized by an average of ~ 10
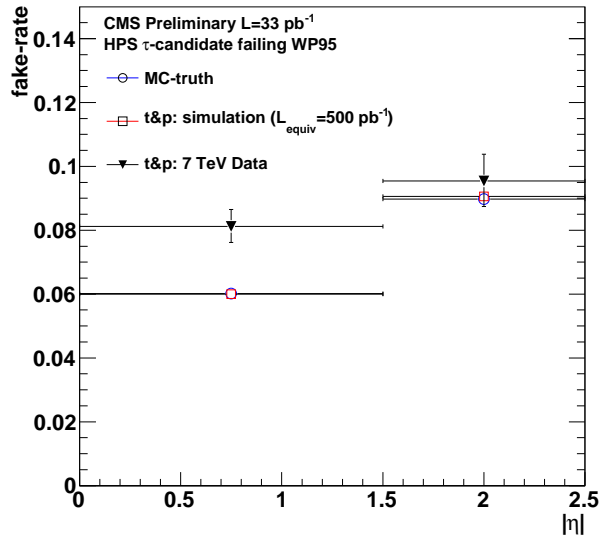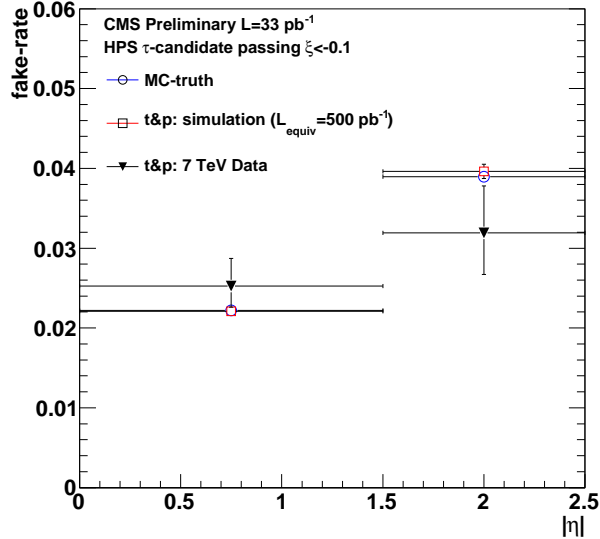
106
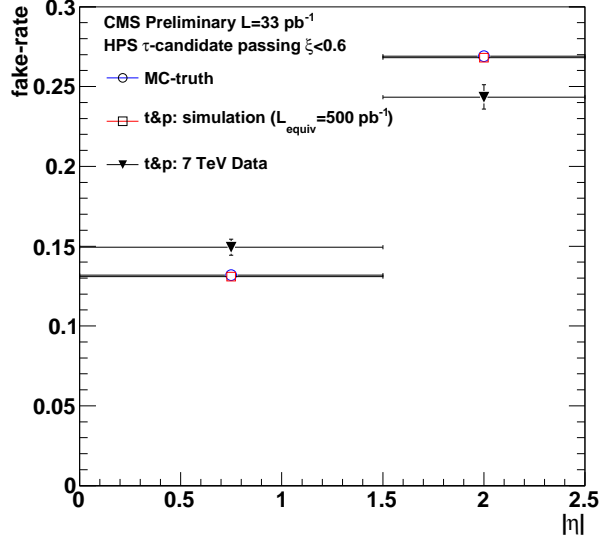
Figure 5.9: Fake rate in two $|\eta|$ bins for the loose working point of the anti–electron discriminator. Data measurements (triangles) are compared to the MC–truth expectation (circles) and to the Monte Carlo closure test (open circles).

Discr.	Bin	MC (exp.) (%)	MC (tnp) (%)	Data (%)
loose	$|\eta| < 1.5$	13.19 ± 0.06	13.10 ± 0.08	$14.93 \pm 0.49 \pm 0.18$
	$|\eta| > 1.5$	26.90 ± 0.13	26.80 ± 0.16	$24.33 \pm 0.75 \pm 0.56$
medium–loose	$|\eta| < 1.5$	6.01 ± 0.04	6.00 ± 0.07	$8.12 \pm 0.51 \pm 0.28$
	$|\eta| > 1.5$	8.97 ± 0.09	9.06 ± 0.12	$9.54 \pm 0.82 \pm 0.44$
tight	$|\eta| < 1.5$	2.22 ± 0.03	2.21 ± 0.05	$2.52 \pm 0.29 \pm 0.26$
	$|\eta| > 1.5$	3.90 ± 0.06	3.96 ± 0.09	$3.19 \pm 0.55 \pm 0.23$

Table 5.2: The expected and measured fake rates for the three working points of the anti–electron discriminator.

minimum bias interactions per event. In order to keep the fake rate from electrons at a reasonable level, more powerful discriminators were developed by combining topological information of the tau candidate into a cut based (tight) or multivariate analysis (MVA–tight).

Cut–based tight discriminator

A tighter discrimination is achieved by requiring that the tau candidate

- passes the medium working point,

107

Figure 5.10: Fake rate in two $|\eta|$ bins for the loose–medium working point of the anti–electron discriminator. Data measurements (triangles) are compared to the MC–truth expectation (circles) and to the Monte Carlo closure test (open circles).

Discriminator	Bin	Data/MC
loose	$|\eta| < 1.5$	1.13 ± 0.17
	$|\eta| > 1.5$	0.82 ± 0.18
medium–loose	$|\eta| < 1.5$	1.35 ± 0.10
	$|\eta| > 1.5$	1.06 ± 0.10
medium	$|\eta| < 1.5$	1.14 ± 0.04
	$|\eta| > 1.5$	0.90 ± 0.04

Table 5.3: Data–to–simulation ratio for the three working points of the anti–electron discriminator.

- satisfies Eq. (5.6),

- has a visible mass larger than 550 MeV, or a linked HCAL cluster energy of more than 10% of the track momentum, or less than 99% of the photon energy concentrated within less than 0.03 η units from the charged particle.

By using this working point, the fake rate from electrons is reduced by a factor of ≈ 2 with respect to the medium working point, at a price of a 10%

Figure 5.11: Fake rate in two $|\eta|$ bins for the medium working point of the anti–electron discriminator. Data measurements (triangles) are compared to the MC–truth expectation (circles) and to the Monte Carlo closure test (open circles).

loss in signal efficiency.

MVA–tight discriminator

Tau candidates that pass the medium working point of the anti–electron discriminator and which satisfy the condition in Eq. (5.6) are split into three mutually exclusive categories, depending on whether the τ_h consists of

1. one charged pion and no strips;

2. one charged pion plus strip(s), and the leading charged particle is linked to a GSF track;

3. one charged pion plus strip(s), and the leading charged particle is not linked to any GSF track.

Taus reconstructed in the three–prong decay mode automatically pass the MVA tight discriminator. Each category is further split into two $|\eta|$ bins, namely $|\eta| < 1.5$ and $|\eta| > 1.5$. Boosted Decision Trees (BDT) are then trained in each category to discriminate genuine taus (signal) from real electrons (background).
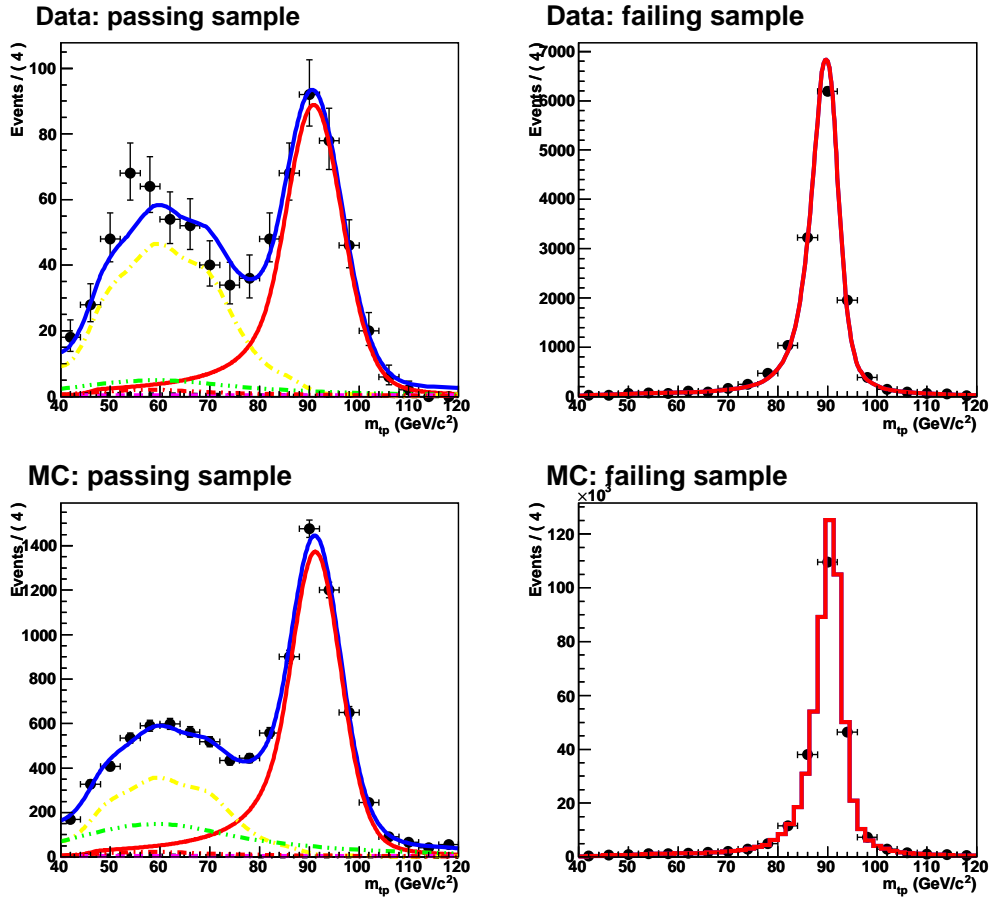
Figure 5.12: Tag–probe mass distributions for probes in the barrel passing (left) and failing (right) the medium working point of the anti–electron discriminator. The observed spectrum (top row) is compared to the Monte Carlo expectation (bottom row).
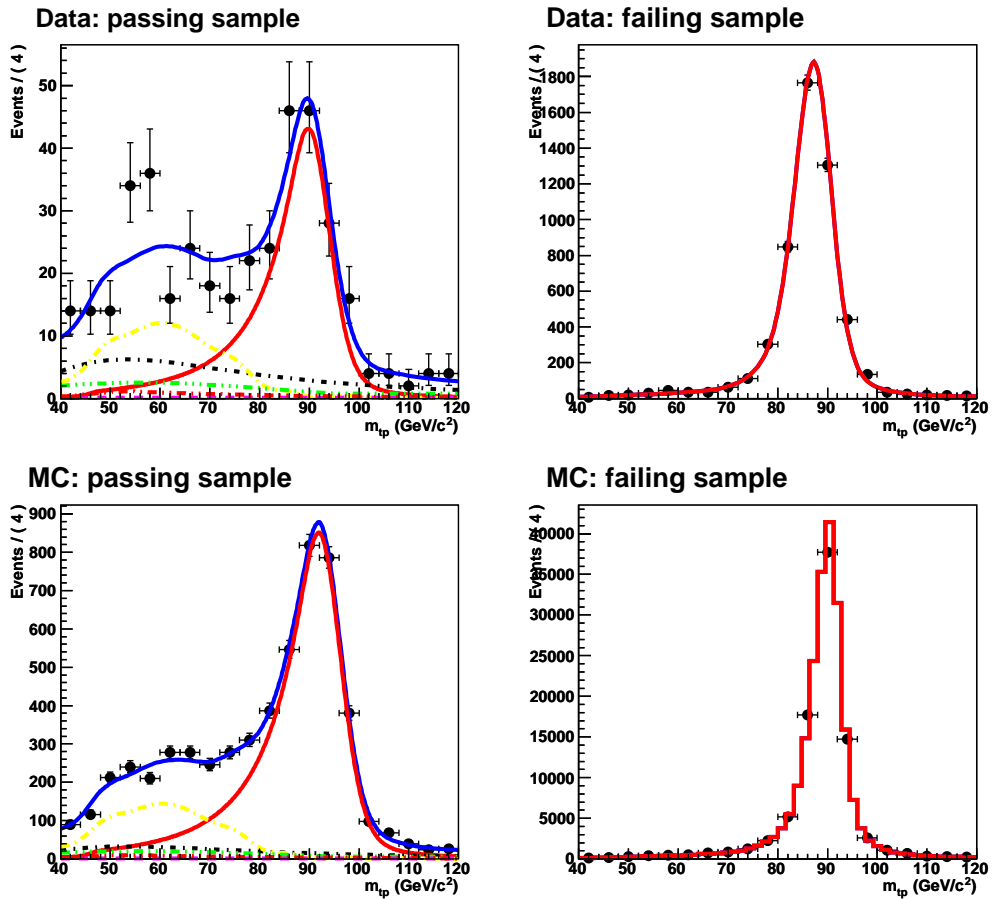
Figure 5.13: Tag–probe mass distributions for probes in the endcap passing (left) and failing (right) the medium working point of the anti–electron discriminator. The observed spectrum (top row) is compared to the Monte Carlo expectation (bottom row).
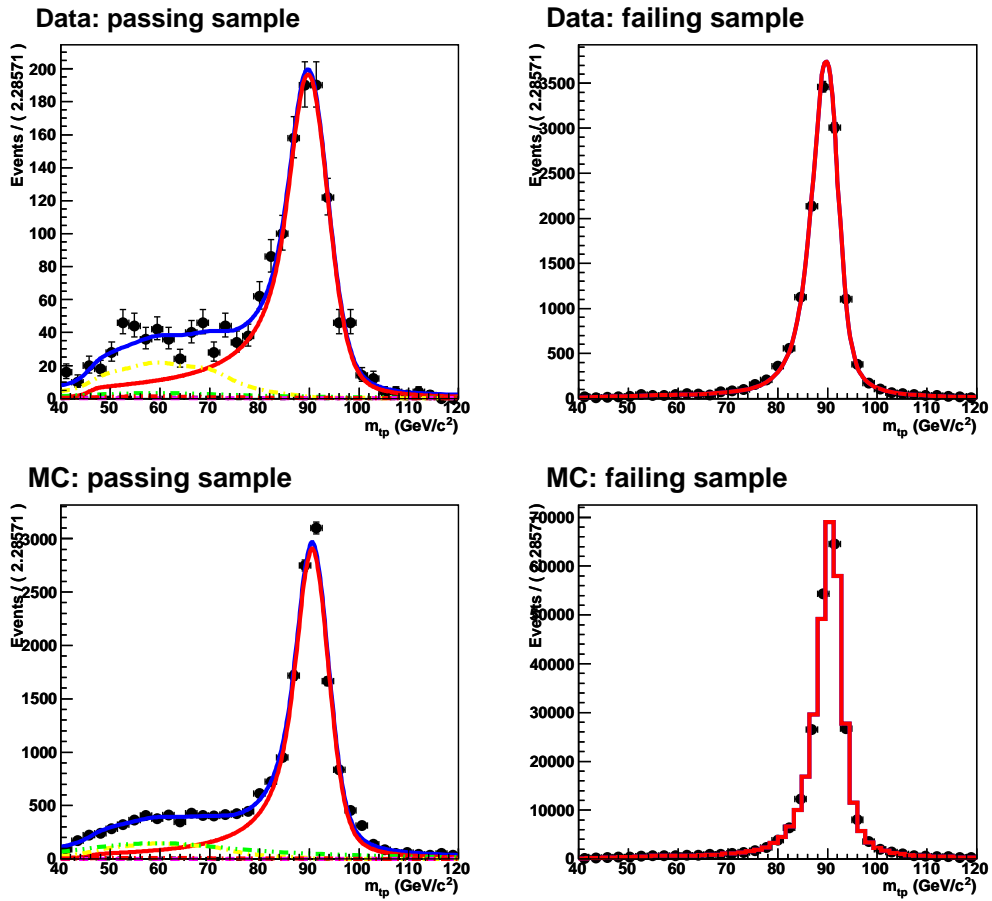
Figure 5.14: Tag–probe mass distributions for probes in the barrel passing (left) and failing (right) the medium–loose working point of the anti–electron discriminator. The observed spectrum (top row) is compared to the Monte Carlo expectation (bottom row).
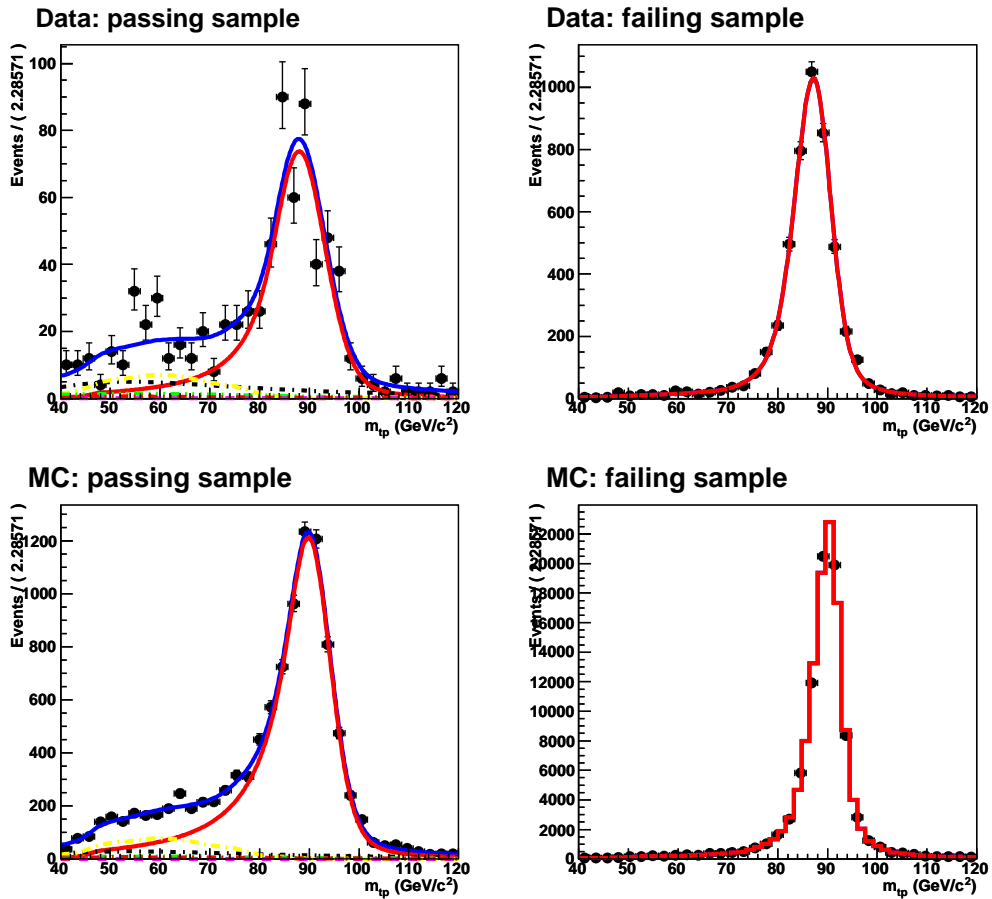
Figure 5.15: Tag–probe mass distributions for probes in the endcap passing (left) and failing (right) the medium–loose working point of the anti–electron discriminator. The observed spectrum (top row) is compared to the Monte Carlo expectation (bottom row).
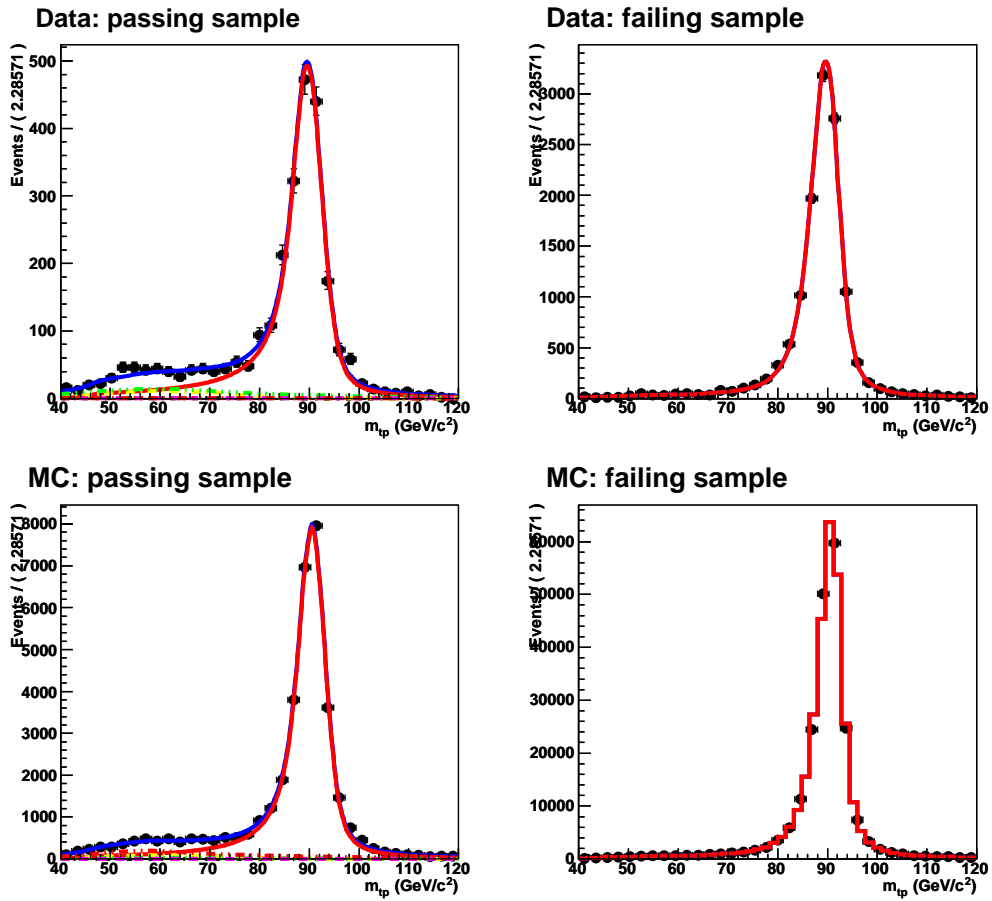
Figure 5.16: Tag–probe mass distributions for probes passing (left) and failing (right) the loose workin point of the anti–electron discriminator. The observed spectrum (top row) is compared to the Monte Carlo expectation (bottom row).
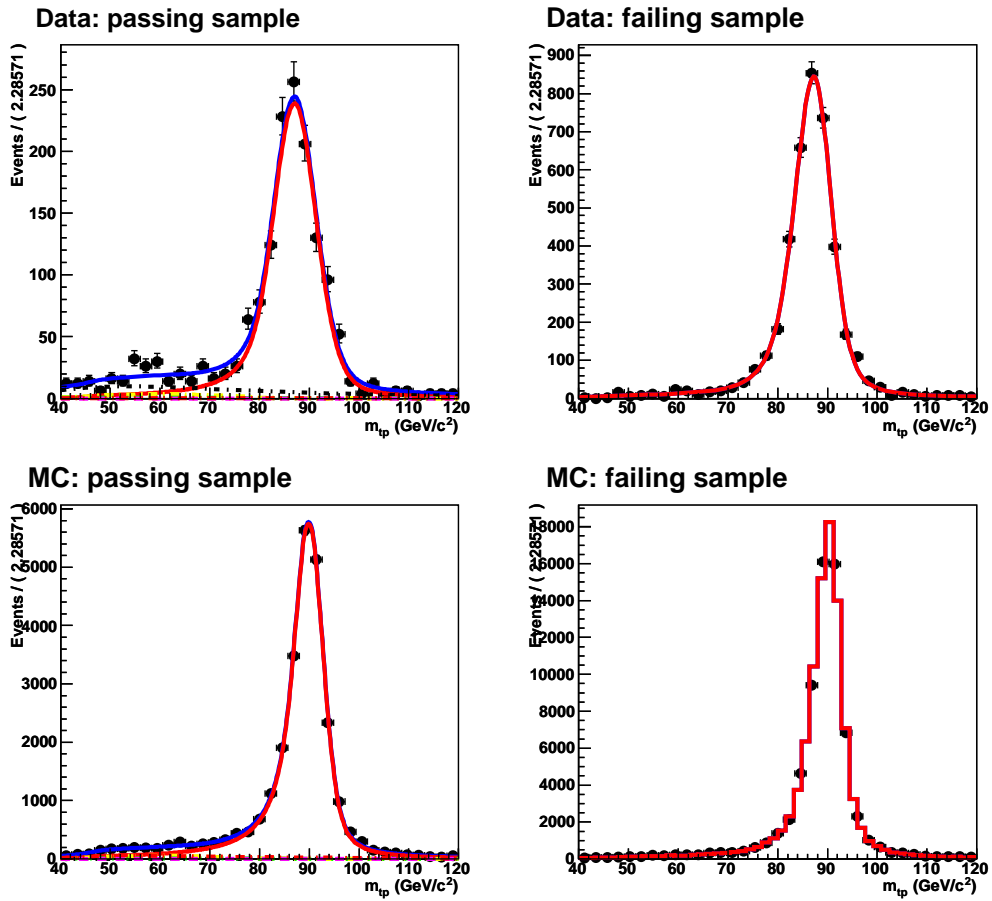
Figure 5.17: Tag–probe mass distributions for probes passing (left) and failing (right) the loose workin point of the anti–electron discriminator. The observed spectrum (top row) is compared to the Monte Carlo expectation (bottom row).

Each category uses an optimal set of discriminating variables, obtained from a super–set of variables by progressively eliminating those that did not improve much the separation. Input variables are either p_T independent, or are transformed to cancel, at first order, their dependence on the transverse momentum of the tau candidate. This is done to maintain the signal efficiency as much as possible independent from the τ_h kinematics.

In the first category, two variables are used: H/p and E/p, defined, respectively, as the ratio between the HCAL and ECAL cluster energy linked to the charged particle and the particle momentum.

The second category takes advantage of the geometrical pattern followed by photons around the charged particles: electrons feature a broad distribution of bremsstrahlung photons along the azimuthal direction, whereas photons inside real taus are more collimated. The second η and ϕ moments of the photons distribution are defined as:

$$\sigma_\eta \equiv \left[\frac{\sum_{i=1}^{N^\gamma} E_{T,i}(\eta_i - \eta_{ch})^2}{\sum_{i=1}^{N^\gamma} E_{T,i}} \right]^{\frac{1}{2}} \tag{5.12}$$

$$\sigma_\phi \equiv \left[\frac{\sum_{i=1}^{N^\gamma} E_{T,i}(\phi_i - \phi_{ch})^2}{\sum_{i=1}^{N^\gamma} E_{T,i}} \right]^{\frac{1}{2}} \tag{5.13}$$

To cancel the tau p_T dependence in Eq. (5.12) at first order, the moments are multiplied by an extra factor of

$$\left[\sum_{i=1}^{N^\gamma} E_{T,i} \cdot p_T^{\tau_h} \right]^{\frac{1}{2}}$$

The list of input variables for Category 2 is complemented by the fraction of the τ_h energy carried by the photons ($\sum_{i=1}^{N^\gamma} E_{T,i}/p_T^{\tau_h}$), the visible τ_h mass (M_{vis}), and the output of the ξ discriminator of the leading charged hadron (ξ^{lch}).

Category 3 is similar to Category 2, with the only difference that ξ^{lch} is not available due to the lack of a GSF track.

Distributions of the input variables in each category are shown in Fig. 5.18, 5.19 and 5.20.

The three categories of the MVA–tight anti–electron discriminator feature different purities. Upper cuts on the various BDT outputs were chosen on the basis of the expected purity and signal efficiency. The final working point was approximately optimized to achieve the same signal efficiency of the tight discriminator. The expected signal efficiency and fake rate are

116
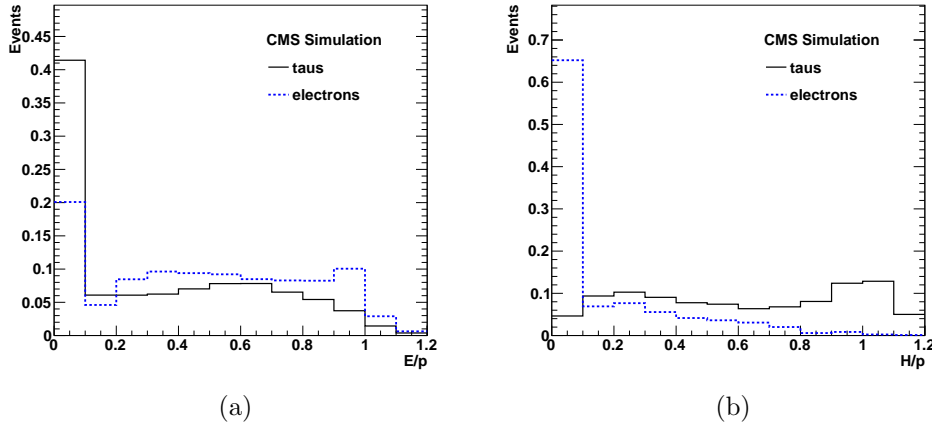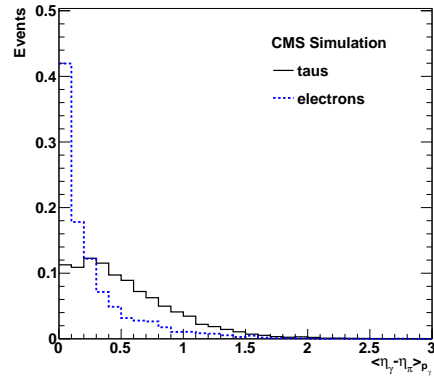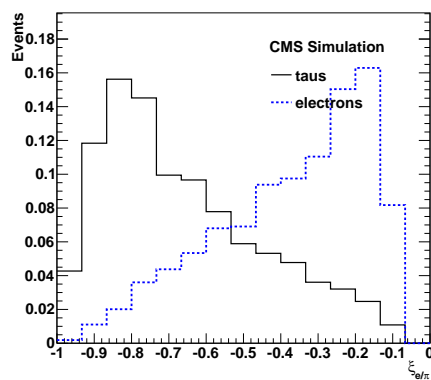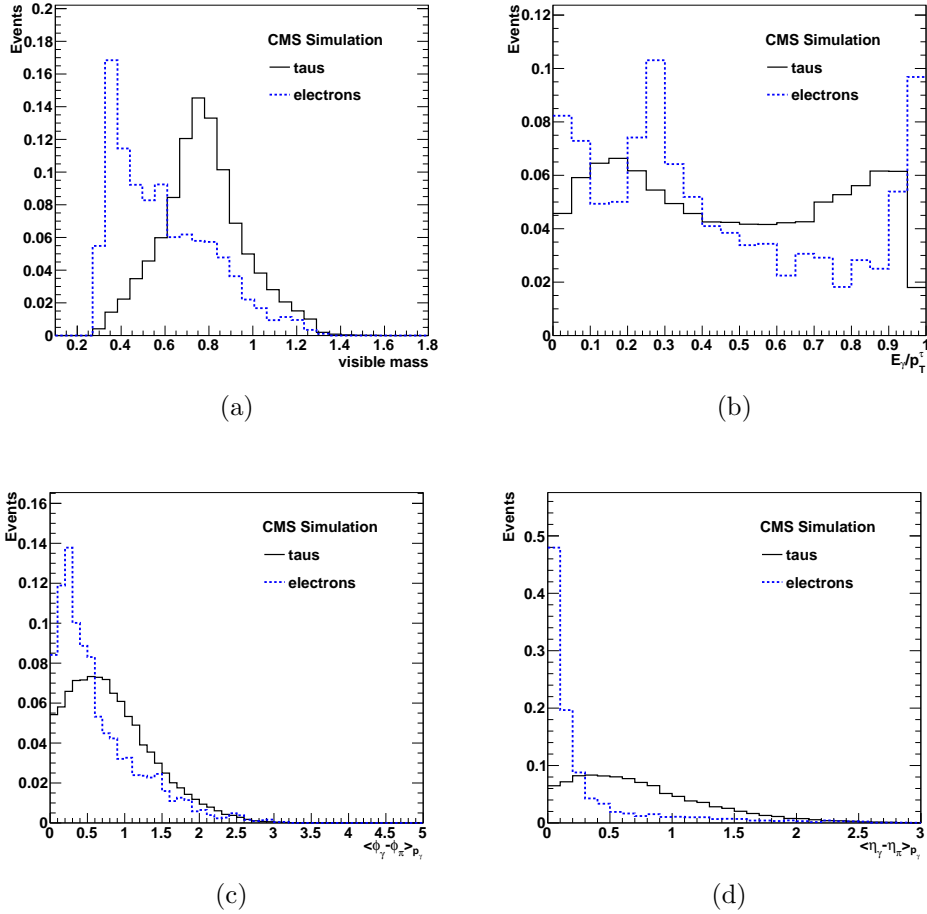
Figure 5.18: Signal and background distribution of the input variables chosen for the first category of the MVA–tight anti–electron discriminator.

shown in Fig. 5.21 as a function of the tau candidate p_T. A pile–up scenario characterized by ~ 6 minimum–bias interactions per bunch–crossing is assumed. The efficiency (fake rate) is measured relative to candidates passing the medium discriminator. Compared to the cut–based tight discriminator, the MVA tight anti–electron discriminator allows for about 50% reduction of the fake rate at the same signal efficiency. Given its superior performances, it has been adopted in the most recent CMS analyses (see e.g. Ref. [76]).

5.5 Muon rejection

Discriminating between muons and τ_h signatures is much easier than for electrons, because muons penetrate inside the outer part of the detector (muon system), while the tau decay products are stopped the calorimeters.

Detector inefficiencies or non–instrumented regions in the muon system, can cause the muon reconstruction to fail. In this case, the muon becomes a perfect one–prong tau candidate. Given the high detection efficiency provided by the CMS muon system, the fake rate from muons can be maintained at the per mill level with an efficiency on real taus exceeding 99%.

Three degrees of tightness in rejecting muons that fake hadronically–decaying taus are achieved by exploiting information from the muon system and by requiring compatibility with a minimum ionizing particle (MIP):

1. loose working point – no segments are matched to the extrapolation of the leading charged particle track to the muon chambers;

117
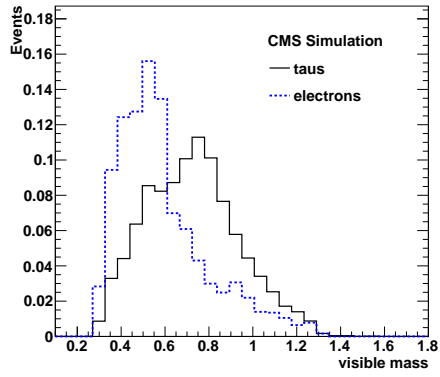
(a)
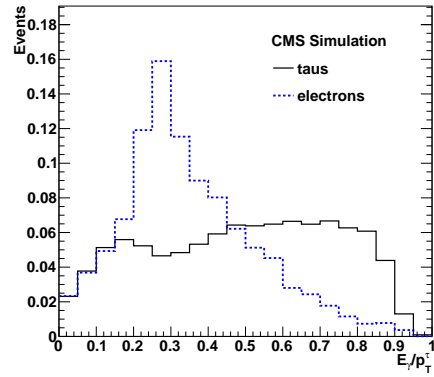
(b)
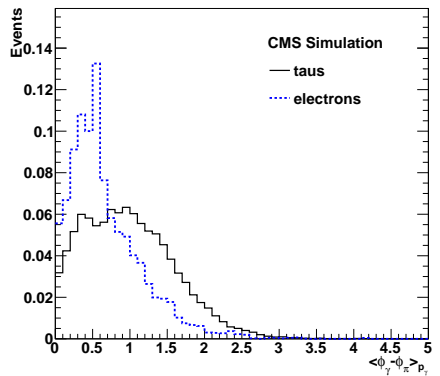
(c)

(d)

(e)

Figure 5.19: Signal and background distribution of the input variables chosen for the second category of the MVA–tight anti–electron discriminator.

(a)   (b)

(c)   (d)

Figure 5.20: Signal and background distribution of the input variables chosen for the third category of the MVA–tight anti–electron discriminator.

2. medium working point – no hits are matched to the extrapolation of the leading charged particle track to the muon chambers;

3. tight working point – no hits are matched to the extrapolation of the leading charged particle track to the muon chambers and the tau candidate, if reconstructed as one–prong, should not have a combined ECAL+HCAL energy smaller than 20% of the charged track momentum.
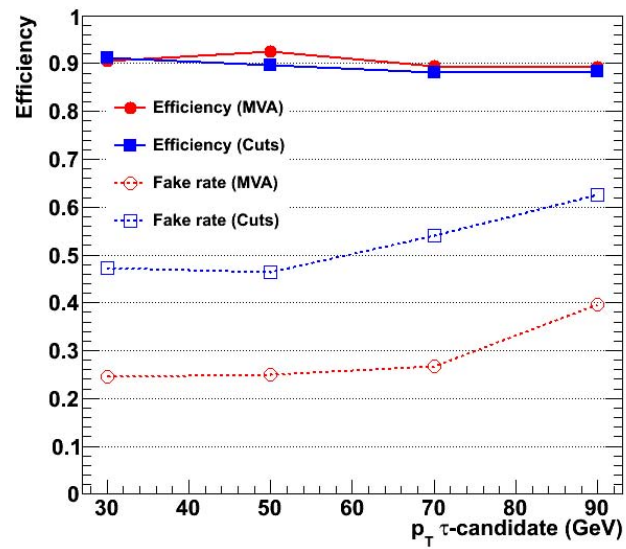
Figure 5.21: Efficiency and fake rate of the MVA–tight discriminator as a function of the tau candidate p_T. The efficiency of the tight discriminator are superimposed for comparison.

Chapter 6

Di–tau mass reconstruction

In this chapter, a study of existing and novel di–tau mass reconstruction techniques in hadron collider experiments is presented. A specific optimization for the CMS detector, which I contributed to develop, is described. The actual performance of this novel technique, used for the analysis presented in this thesis, will be discussed further in the next chapter.

6.1   General considerations

In searches for a narrow neutral resonance ϕ decaying to tau leptons, and with mass $M_\phi \gtrsim M_Z$, the di–tau mass offers the single most sensitive observable that can discriminate the signal ($\phi \to \tau\tau$), from its irreducible and most prominent background ($Z \to \tau\tau$). For example, let's specialize ϕ to be the SM Higgs boson with $M_H \lesssim 145$. The inclusive cross–section times branching ratio for this process is at least two orders of magnitude smaller than the Drell–Yan $Z/\gamma^* \to \tau\tau$ production. The sensitivity to a small excess over this overwhelming background relies on how efficiently the Z and H di–tau mass peaks can be separated.

Reconstructing the mass of a resonance from its decay to tau leptons poses a challenge at hadron colliders. Indeed, the presence of undetected neutrinos in the final state makes the kinematics of the di–tau system underconstrained. The di-tau mass estimators are essentially defined by their prescription on how to deal with the infinitely–many allowed solutions.

By measuring the four–momentum of the visible tau decay products (i.e. the electron or muon momentum in leptonic decays, the momentum and energy of the hadronic system for semi–leptonic decays), and the missing transverse energy in the event, $\vec{E}_T^{miss}$, the number of parameters that are

necessary to fully describe the di–tau system is given by

$$\# \text{ of parameters } = 3 \times [\# \text{ of } \tau_\ell] + 2 \times [\# \text{ of } \tau_h] - 2, \qquad (6.1)$$

i.e. two, three or four in the $\tau_h\tau_h$, $\tau_\ell\tau_h$ and $\tau_\ell\tau_\ell$ channels, respectively. The constraints that determine the counting rule in Eq. (6.1) can be applied either in the form of an analytical function of the measured observables, where the uncertainty on the measurement is neglected, or in the form of a likelihood function, which allows to account for detector mismeasurements.

To select one value for the parameters out of the infinitely–many allowed solutions, extra conditions on the parameter space must be applied. The different mass reconstruction techniques can be regrouped depending on the approach followed to reduce this ambiguity. Two main approaches can be identified.

1. In the first approach, experimental uncertainties on the measured observables are neglected. Constraints on the parameter space are applied in the form of equations on the observables and on the parameters. The manifold of solutions is then collapsed to a single point by imposing extra constraints. These can come from physically–inspired approximations of the tau decay kinematics (e.g. the collinear approximation), by projecting–out some of the unknowns at the price of sacrificing the physical constraints (e.g. by assuming that all neutrinos are emitted in the same direction and at $\eta = 0$, or that the energy of all neutrinos is exactly zero), or by requiring the *pdf* of the resulting mass estimator to feature some desirable property.

2. In the second approach, the physical structure of the manifold is maintained intact. Every point in this space is weighted by its *a priori* likelihood, which is evaluated either from Monte Carlo or from analytical parametrizations. Uncertainties on the measured observables can be naturally accommodated. Then, every event provides an *a posteriori* likelihood for the di–tau mass. The methods used in the second approach belong to the general class of Dynamical Likelihood Models estimators discussed in Refs. [85, 86].

A few example for each of the two groups of mass reconstruction techniques are described in more details in the following sections. A comparison between the performances of the different techniques is presented in the last section.

6.2 Collinear approximation

The collinear approximation has been one of the first di–tau mass reconstruction techniques advocated for $\phi \to \tau\tau$ searches at hadron colliders (see e.g. Ref. [78]). The di–tau kinematics is simplified by assuming that the momenta of all tau decay products are exactly collinear with the initial tau lepton momentum. This approximation is indeed good in the limit where the tau lepton energy in the laboratory frame ($E_\tau = \gamma m_\tau$) is much larger than the tau mass, because the 3D–angle between the visible decay products in the laboratory is shrunk by a factor of $1/\gamma \ll 1$.

Let's define

$$
\begin{aligned}
\vec{p}_{vis} &= (p_{vis},\, \theta_{vis},\, \phi_{vis}), \\
\vec{p'}_{vis} &= (p'_{vis},\, \theta'_{vis},\, \phi'_{vis}),
\end{aligned}
\tag{6.2}
$$

to be the measured visible tau momenta in polar coordinates. In the collinear approximation, the total momentum of the neutrinos emitted in the decay of the first (p_ν) and second (p'_ν) tau are obtained by solving a linear system of equations:

$$
\begin{pmatrix} E_x^{miss} \\ E_y^{miss} \end{pmatrix} = \mathbf{A}(\vec{p}_{vis}, \vec{p'}_{vis}) \begin{pmatrix} p_\nu \\ p'_\nu \end{pmatrix}
\tag{6.3}
$$

where the $\mathbf{A}$ matrix is given by

$$
\mathbf{A}(\vec{p}_{vis}, \vec{p'}_{vis}) = \begin{pmatrix} \sin\theta_{vis}\cos\phi_{vis} & \sin\theta'_{vis}\cos\phi'_{vis} \\ \sin\theta_{vis}\sin\phi_{vis} & \sin\theta'_{vis}\sin\phi'_{vis} \end{pmatrix}
\tag{6.4}
$$

If the square matrix in Eq. (6.4) can be inverted, the di–tau mass in the collinear approximation ($M_{\tau\tau}^{CA}$), is given by

$$
\begin{aligned}
M_{\tau\tau}^{CA} = [2m_\tau^2 + 2\frac{p_{vis}p'_{vis}}{xx'} \times \\
\times (1 - (\cos\theta_{vis}\cos\theta'_{vis} + \sin\theta_{vis}\cos\phi_{vis}\sin\theta'_{vis}\cos\phi'_{vis} + \\
+ \sin\theta_{vis}\sin\phi_{vis}\sin\theta'_{vis}\sin\phi'_{vis}))]^{\frac{1}{2}}
\end{aligned}
\tag{6.5}
$$

where $x = p_{vis}/(p_\nu + p_{vis})$ and $x' = p'_{vis}/(p'_\nu + p'_{vis})$ are the fraction of the tau energy in the laboratory frame carried away by the visible particles.

If the determinant of the $\mathbf{A}$ matrix in Eq. (6.4) vanishes, the system of equations (6.3) cannot be solved. The condition $|\det\mathbf{A}| = 0$ is equivalent to

$$
\tan\phi_{vis} = \tan\phi'_{vis} \Leftrightarrow (\phi_{vis} - \phi'_{vis}) = k\pi,\ k \in Z.
\tag{6.6}
$$

Equation (6.6) shows that the collinear approximation breaks down in case the resonance ϕ is produced with null transverse momentum, i.e. when the two tau leptons have opposite azimuthal direction. In real experiments, the condition expressed by Eq. (6.6) is never exactly satisfied, because either the detector resolution or the presence of extra radiation ($pp \to \phi + X$), always bring to $(\phi_{vis}^1 - \phi_{vis}^2) \neq 0$. However, when $(\phi_{vis} - \phi'_{vis}) \approx 0$ ($|\det A| \to 0$), the solutions $p_\nu^i \propto |\det A|^{-1}$ tend to be biased towards unphysical large values, implying large tails on the $M_{\tau\tau}^{CA}$ distribution (the tails appear only towards high value because $M_{\tau\tau}^{CA}$ is bounded from below by the visible mass).

Even outside the pathological region of Eq. (6.6), the collinear approximation brings to ill–defined solutions if at least one among p_ν and p'_ν from Eq. (6.3) comes out to be negative. This happens when the direction of $\vec{E}_T^{miss}$ lies outside the plane spanned by the transverse momenta of the visible particles.

The overall rate of physical solution for Eq. (6.3) is about $50\% - 60\%$ for $Z \to \tau\tau$, after typical kinematical cuts on the visible tau momenta and with a pile–up scenario similar to the one realized in the early 2011 LHC run [80].

The limitations inherent to the collinear approximation can be in part mitigated by taking physically–inspired arbitrations when an invalid solution is found. This drove me to define an improved collinear approximation [79], which will be discussed in the following subsection.

6.2.1 Improved collinear approximation

The angular correlation between the two taus and the reconstructed $\vec{E}_T^{miss}$ is shown in Fig. 6.2(a) for events in which the collinear approximation predicts negative neutrino energy (Eq. (6.3)). It is assumed here and henceforward that one taus decays fully–leptonically and the other semi–leptonically. The same technique can be extended to other decay channels in a straightforward manner.

In the bulk of the events, the two tau leptons have almost opposite azimuthal angle and the reconstructed $\vec{E}_T^{miss}$ is also close in ϕ to one of the taus. In the following, I describe a technique to recover a large fraction of these events. When both neutrino energy from Eq. (6.3) are predicted to be positive, the standard collinear approximation can be still used.

Let's define E_τ, E_ℓ and E_ν to be the energy of the tau lepton, of the visible decay particle and of the neutrinos for the leptonically–decaying tau, and E'_τ, E'_ℓ and E'_ν the same variables for the hadronically–decaying one. Let's also define $x = E_\ell/E_\tau$ and $x' = E'_\ell/E'_\tau$.

For unpolarized decays $\tau^- \to \ell^- \bar{\nu}_\ell \nu_\tau$, the probability for the lepton ℓ to take a fraction $x = E_\ell/E_\tau$ of the tau lepton energy in the laboratory frame

is given by [78]:

$$\frac{1}{\Gamma}\frac{d\Gamma}{dx} = \frac{1}{3}\left(1-x\right)\left(5+5x-4x^2\right) \tag{6.7}$$

From Eq. (6.7), the mean value of x can be derived in a straightforward way:

$$\langle x \rangle = \frac{1}{\Gamma}\int_0^1 x\frac{d\Gamma}{dx}dx = \frac{7}{20}.$$

Given a measured value of E_ℓ, an unbiased estimator of the neutrinos energy is therefore provided by $\frac{13}{7}E_\ell$, which shows that the presence of two final state neutrinos tends to make the charged lepton quite soft. This is not the case for the semi–leptonic decays, where the tau lepton momentum is democratically shared among the decay products. Now, if the visible decay products of the two tau leptons tend to have opposite direction and the direction of the reconstructed $\vec{E}_T^{miss}$ is close in ϕ to the leptonically (hadronically) decaying tau:

$$\max_i\{\cos(\phi_{\vec{E}_T^{miss}} - \phi_{vis}^i)\} > 0.94, \quad \cos(\phi_{vis} - \phi'_{vis}) < -0.90, \tag{6.8}$$

then the visible energy fractions x and x' are obtained from:

$$\begin{cases} E_\nu = \frac{13}{7}E_\ell \\ E'_\nu = (E_\nu \mp E_T^{miss})\Theta(E_\nu - E_T^{miss}) \end{cases} \Leftrightarrow \begin{cases} x = \frac{7}{20} \\ x' = \frac{E'_\ell}{(E_\nu \mp E_T^{miss})\Theta(E_\nu - E_T^{miss}) + E'_\ell} \end{cases} \tag{6.9}$$

The plus or minus applies to the two different cases, illustrated in Fig. 6.1 with labels "case 1" and "case 2", respectively.

The second category of ill–defined events consists of those cases where the tau momenta don't have opposite azimuthal direction, but at least one of the neutrino energy resulting from Eq. (6.3) is negative. This is illustrated in Fig. 6.1 as "case 3". It can be easily verified that this happens frequently when the fraction of energy carried away by the neutrinos is large for one tau and small for the other, driving the direction of $\vec{E}_T^{miss}$ close to either one or the other taus. Let's then consider events where

$$\max_i\{\cos(\phi_{\vec{E}_T^{miss}} - \phi_{vis}^i)\} > 0.94, \quad \cos(\phi_{vis} - \phi'_{vis}) > -0.90. \tag{6.10}$$

and for which the collinear approximations provides negative values of the neutrinos energy. Without loss of generality, let's assume that the missing transverse momentum is approximately aligned with the transverse momentum of the charged lepton arising from the leptonically–decaying tau $(\vec{p}_T^\ell)$. A good approximation is then to assume that the transverse momentum of the neutrinos emitted by the leptonically–decaying tau is approximately equal

125
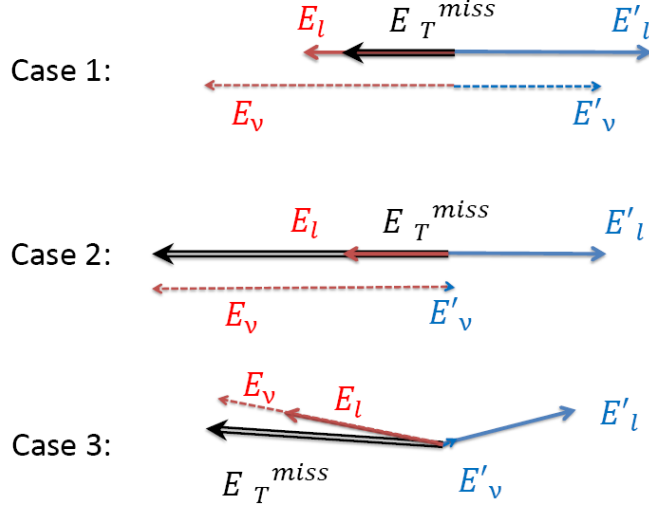
Figure 6.1: Cartoons illustrating the three arbitrations taken for events where the collinear approximation predicts negative neutrino energy.

to $\vec{E}_T^{miss}$, and the neutrinos emitted by the other tau are so soft that their energy can be neglected:

$$\begin{cases} x = \dfrac{1}{1 + \frac{\vec{E}_T^{miss}}{E_T^{miss}} \cdot \frac{\vec{p}_T^{\ell}}{p_T^{\ell}}} \\ x' = 1 \end{cases} \qquad (6.11)$$

About 25% more signal events, relative to the fraction of events for which the collinear approximation is valid, can be recovered without significant degradation of the mass resolution. As shown in Fig. 6.2(b), the di–tau mass for the $H \to \tau\tau$ recovered events peaks close to the true Higgs mass, even though the average mass scale is slightly lower than for events where the collinear approximation provides valid results.

6.3 Maximal lower–bound estimator

The di–tau mass reconstruction technique proposed in Ref. [81] consists in selecting, for every event, the kinematically–allowed solution for the neutrinos momenta that provides the smallest possible di–tau mass value compatible with the observed visible tau momenta and $\vec{E}_T^{miss}$. For a resonance $\phi \to \tau\tau$ with mass $M_\phi \gtrsim M_Z$, this estimator (denominated $M_{\tau\tau}^{bound}$, because by
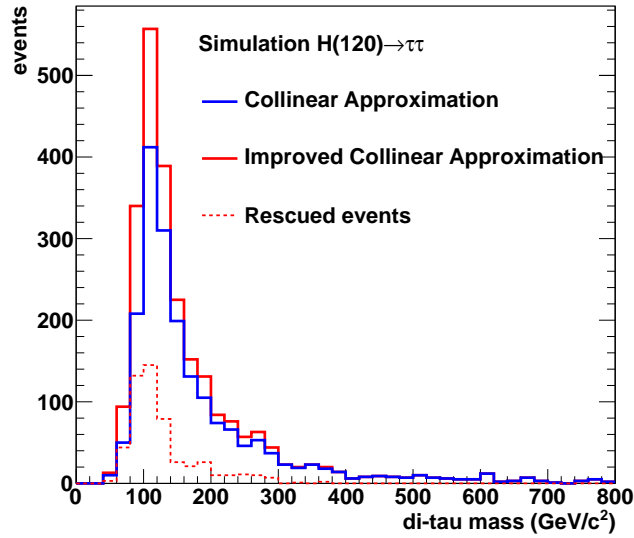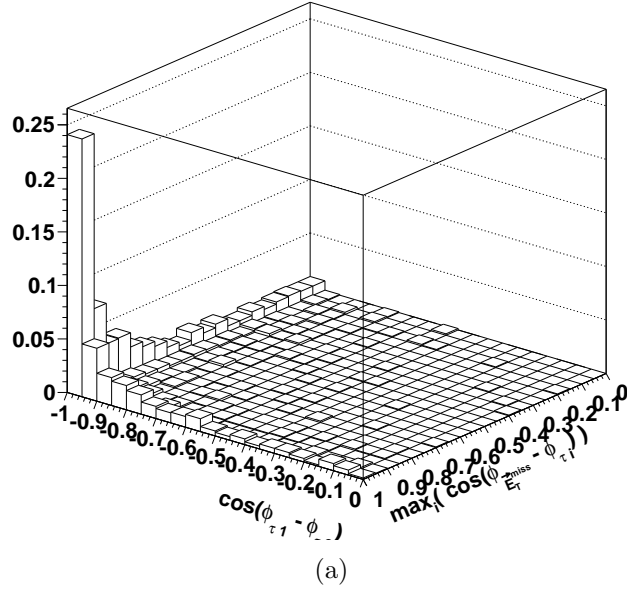
Figure 6.2: a) Azimuthal angle correlations between the missing transverse energy and the visible decay products in $H \rightarrow \tau\tau$ ($m_H = 120$ GeV) simulated events for which the collinear approximation predicts negative neutrino energy; b) di–tau mass reconstructed using the improved collinear approximation for a Monte Carlo simulated sample $H \rightarrow \tau\tau$ ($m_H = 120$ GeV), in the $\tau_\mu \tau_h$ channel.

construction provides the maximal lower–bound estimator of the true mass M_ϕ) satisfies the boundary condition

$$M_{\tau\tau}^{bound} \leq M_\phi,$$

at least in an ideal detector, i.e. when the visible particle momenta and $\vec{E}_T^{miss}$ can be reconstructed without errors (Fig. 6.3(a)). The idea behind this approach is that the major SM background to the signal $\phi \to \tau\tau$ is the irreducible $Z/\gamma^* \to \tau\tau$ production, characterized by a mass scale M_Z. A maximal lower–bound estimator would then leave the region $[M_Z, M_\phi]$ depleted from background events.

Given the reconstructed four–momenta of the visible tau decay products p_1^μ, p_2^μ, the maximal lower-bound $M_{\tau\tau}^{bound}$ is defined as

$$M_{\tau\tau}^{bound} = \min_{q_1^\mu, q_2^\mu \in \aleph} \sqrt{h^\mu h_\mu} \tag{6.12}$$

where $h^\mu = p_1^\mu + p_2^\mu + q_1^\mu + q_2^\mu$, and q_i^μ are the four momenta of the neutrino(s) associated to the i-th tau, satisfying the constraints

$$\begin{cases} q_1^\mu q_{1\,\mu} = 0 \\ q_2^\mu q_{2\,\mu} = 0 \\ (p_1 + q_1)^\mu (p_1 + q_1)_\mu = m_\tau^2 \\ (p_2 + q_2)^\mu (p_2 + q_2)_\mu = m_\tau^2 \\ \vec{q}_{1;T} + \vec{q}_{2;T} = \vec{E}_T^{miss} \end{cases} \tag{6.13}$$

The system in Eq. (6.13) identifies a manifold $\aleph$ of allowed solutions in the multi dimensional space where all possible values of q_i^μ, $i = 1, 2$, live. For illustration purposes, the case where both taus decay semi–letponically was considered. Because of the finite detector resolution, $\aleph$ may be empty. A solution to Eq. (6.13) exists if and only if the stranverse mass [82] satisfies the boundary condition

$$M_{T2}^2 \equiv \min_{\vec{q}_{1;T} + \vec{q}_{2;T} = \vec{E}_T^{miss}} [\max\{m_T^2(\vec{p}_{1;T}, \vec{q}_{1;T}), m_T^2(\vec{p}_{2;T}, \vec{q}_{2;T})\}] < m_\tau^2 \tag{6.14}$$

The performances of the estimator in Eq. (6.12) have been evaluated on $Z \to \tau\tau$ simulated events produced in pp collisions at $\sqrt{s} = 14$ TeV. All reconstructed jets with p_T in excess of 15 GeV, and all isolated stable particles with $|\eta| < 5$ and $p_T > 0.5$ GeV have been used to compute the missing transverse energy. For every generated jet, the energy E is smeared by a Gaussian probability density function

$$\sigma(E)/E = (0.6 \text{ GeV}^{1/2}/\sqrt{E}) \oplus 0.03$$

to simulate detector resolution effects. With this assumption, Eq. (6.14) is satisfied in about 70% of the events [81]. In the remaining 30%, the use of the *true mass*, defined in the next section, is advocated.
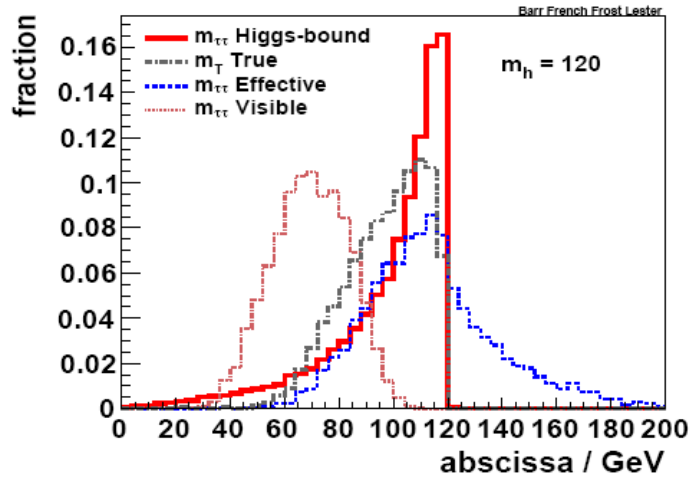
(a)
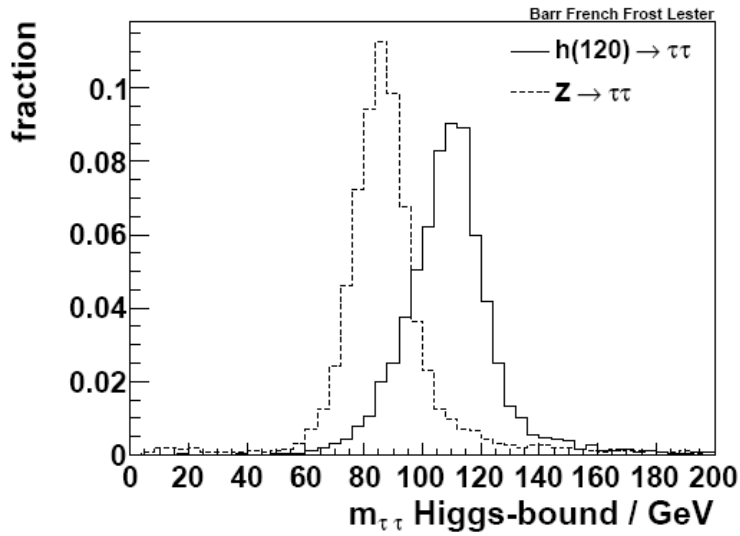
(b)

Figure 6.3: The normalized di–tau mass distributions reconstructed using the maximal lower–bound estimator at (a) generator–level event or (b) at reconstruction level. Only events for which Eq. (6.13) admits solutions are shown here (from Ref. [81]).

6.4 Visible, effective, and true mass

Given the visible tau four–momenta p_1^μ and p_2^μ, a simple mass estimator is provided by the *visible* mass, i.e.

$$M_{\tau\tau}^{vis} = \sqrt{(p_1 + p_2)^\mu (p_1 + p_2)_\mu}. \tag{6.15}$$

The visible mass has the advantage to be independent from the reconstructed missing energy. However, since the probability density functions for a tau lepton to decay into a bunch of visible particles with a fraction x of the tau lepton energy are quite broad, the visible mass suffers from a large random smearing.

An alternative to the visible mass is the so–called *effective*, or CDF–type [84] mass, defined by

$$M_{\tau\tau}^{eff} = \sqrt{(p_1 + p_2 + q)^\mu (p_1 + p_2 + q)_\mu}, \tag{6.16}$$

with $q^\mu = (E_T^{miss}, E_{Tx}^{miss}, E_{Ty}^{miss}, 0)$. Re–introducing the missing transverse energy into the game recovers to large extent the correct mass scale, though without a significant improvement of the mass resolution.

Finally, a yet different estimator of the di–tau mass is the so–called *true* mass [83], given by

$$M_{\tau\tau}^{true} = \sqrt{(p_1 + p_2)^2 + 2\left(\sqrt{((p_1 + p_2)^2 + (\vec{p}_1 + \vec{p}_2)^2)\vec{q}^2} - \vec{q} \cdot (\vec{p}_1 + \vec{p}_2)\right)}, \tag{6.17}$$

which was first proposed in the context of $H \to WW \to 2\ell 2\nu$ searches. The true mass estimator coincides with the invariant mass of a tau pair where the system of neutrinos from the tau decays has null mass (i.e. all neutrinos are emitted in the same direction), and the direction of the neutrino system has the same pseudorapidity of the visible decay products system.

Distributions of the visible, effective and true mass in $Z \to \tau\tau$ and $H \to \tau\tau$ simulated samples are shown in Fig. 6.4.

6.5 Missing mass calculator

The missing mass calculator (MMC) [87] is a recent likelihood–based mass reconstruction technique developed for di–tau searches at hadron colliders. Given the reconstructed missing transverse energy and the momentum of the visible tau decay products, the infinitely–many solutions for the neutrinos momenta are weighted by probability density functions obtained from

(a)

(b)

(c)
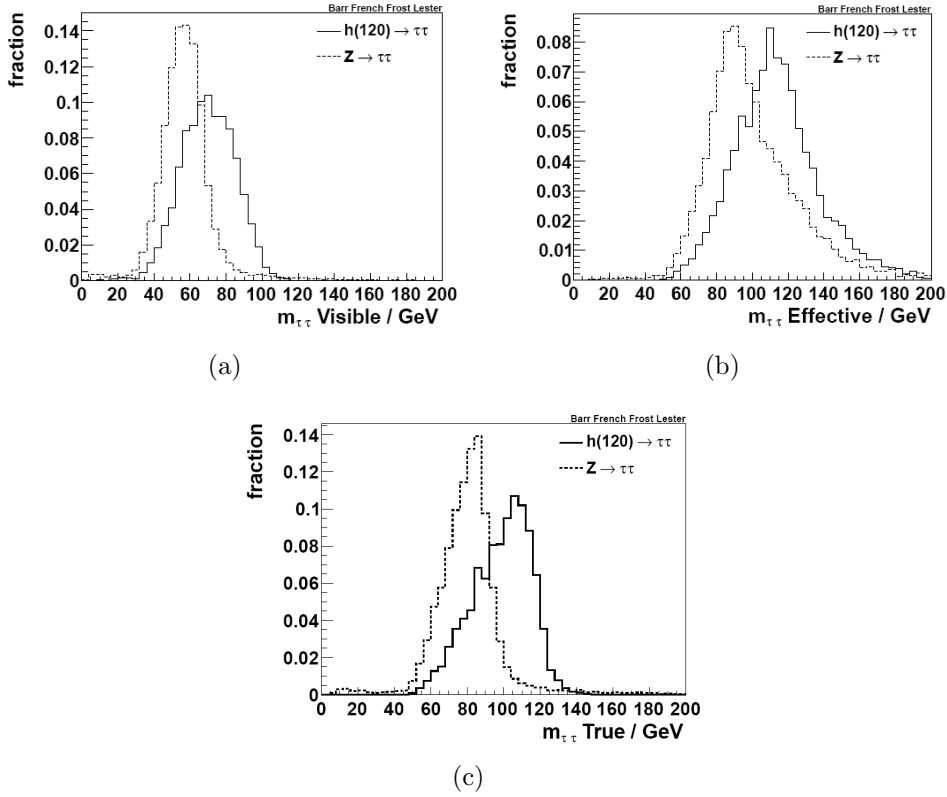
Figure 6.4: Distribution of the (a) visible, (b) effective, and (c) true di–tau mass in $Z \to \tau\tau$ and $H(120) \to \tau\tau$ simulated events (from Ref. [81])

a Monte Carlo parametrization. If the tau lepton polarization is neglected, these parametrizations do not depend on the tau origin, and can therefore be obtained from e.g. a simulated $Z \to \tau\tau$ sample.

For every decay mode, the probability density functions of the distance $\Delta R = \sqrt{(\phi_{vis} - \phi_\nu)^2 + (\eta_{vis} - \eta_\nu)^2}$ between the visible particles and the neutrino system produced in the tau decay, are obtained from Monte Carlo simulations in bins of the generated tau lepton momentum, resulting in a parametrical function:

$$P(\Delta R, p_\tau).$$

For events where both tau leptons undergo a semi–leptonic decay, a scan is performed over a grid in the (ϕ_ν^1, ϕ_ν^2) space. For a fully–leptonic decay, the dimensionality of the parameter space is augmented by the addition of the neutrino–pair mass $(m_{\nu\nu})$. The finite resolution of the reconstructed missing transverse energy is accounted for by increasing the dimensionality of the parameter space to include a random noise on the $\vec{E}_T^{miss}$ components,

namely ΔE_x^{miss} and ΔE_y^{miss}, defined such that the x (y) component of the neutrinos momentum is equal to $E_x^{miss} + \Delta E_x^{miss}$ $(E_x^{miss} + \Delta E_x^{miss})$. By constraining the invariant mass of the decay products to the tau lepton mass, and by requiring that the vectorial sum of the transverse neutrino momenta matches the reconstructed missing energy, modulo a noise term $\Delta E_{x,y}^{miss}$, every point in the grid maps univocally into a pair of neutrino four–momenta. The corresponding ΔR and p_τ values are readily determined and a total probability

$$\mathcal{P} = P(\Delta R^1, p_\tau^1) \times P(\Delta R^2, p_\tau^2) \times e^{-\frac{\Delta E_x^{miss}}{2\sigma_x^2}} \times e^{-\frac{\Delta E_y^{miss}}{2\sigma_y^2}} \qquad (6.18)$$

is assigned to this particular solution, where σ_x^2 and σ_y^2 are the variances which parametrize the detector missing energy resolution along the x and y direction. For every point in the parameter space, the di–tau mass $M_{\tau\tau}$ is computed and weighted by Eq. (6.18), resulting in a distribution $L^{MMC}(M_{\tau\tau})$. The mode of the distribution is used as an event–by–event estimator of the di–tau mass.

The failure rate for the algorithm to correctly solve the system of four equations during the grid scan and return a mass probability density is observed to be very low (below 3%) in events with realistic missing energy resolution. For a value $\sigma_{x,y} = 5$ GeV of the missing energy resolution, the expected MMC di–tau mass resolution is found to be about 14% in a Monte Carlo simulated sample of $H(115) \to \tau^-\tau^+$ ($\tau_h\tau_h$ channel). For a perfect detector, i.e. $\sigma_{x,y} = 0$, the mass resolution is found to be $\sim 8\%$ ($\sim 13\%$) in the $\tau_h\tau_h$ ($\tau_\ell\tau_\ell$) channel (Fig. 6.5).

6.6 The SVfit algorithm

The Secondary Vertex Fit algorithm [1] (SVfit) [88] adopts a strategy similar to the MMC technique, but with a purely analytical approach for the likelihood parametrization.

This proceeds as follows. Let's collectively denote the ensemble of experimentally measured observables (e.g. the momenta and mass of the visible decay products, the missing energy, etc...), as $\mathbf{x}_m$, and the collection of unknown dynamical parameters necessary to fully model the di–tau system as $\mathbf{x}_u$. Given a measured value of $\mathbf{x}_m$, the di–tau decay kinematic corresponding

---

[1]In the current implementation of the SVfit algorithm, the secondary decay vertices of the tau leptons (hence its name) are not used for the determination of the tau momenta, although the algorithm was originally designed with this functionality.
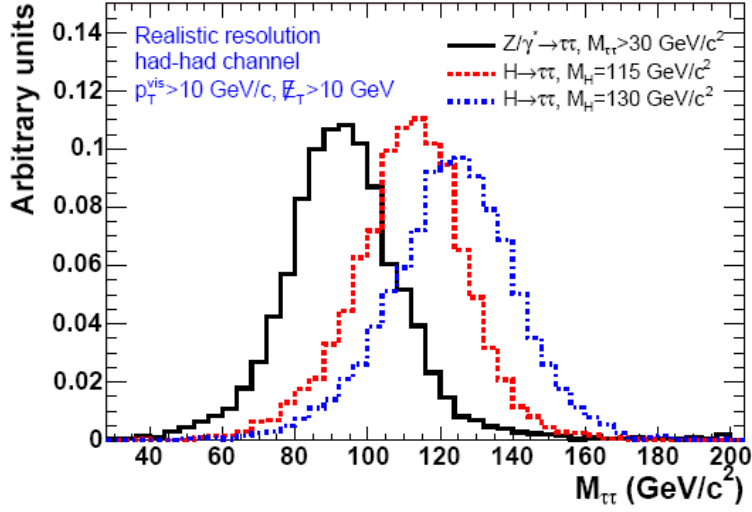
Figure 6.5: Expected di–tau mass distribution reconstructed by the MMC algorithm in the $\tau_h \tau_h$ channel for $Z \to \tau\tau$ and $H \to \tau\tau$ ($m_H = 115, 130$) Monte Carlo simulated events with missing energy resolution $\sigma_{x,y} = 5$ GeV (from Ref. [87]).

to the choice $\mathbf{x}_u$ is associated with an *a priori* probability density

$$\frac{df(\mathbf{x}_u|\mathbf{x}_m)}{d\mathbf{x}_u}.$$

The mass of the di–tau system is a well defined function of $\mathbf{x}_u$ and $\mathbf{x}_m$:

$$M_{\tau\tau} = M_{\tau\tau}(\mathbf{x}_u, \mathbf{x}_m). \tag{6.19}$$

The *a posteriori* probability density for $M_{\tau\tau}$ is then obtained by marginalizing the dynamical parameters:

$$\frac{dL(M_{\tau\tau})}{dM_{\tau\tau}} = \int_\Omega \frac{df(\mathbf{x}_u|\mathbf{x}_m)}{d\mathbf{x}_u} \delta(M_{\tau\tau} - M_{\tau\tau}(\mathbf{x}_u, \mathbf{x}_m)) d\mathbf{x}_u, \tag{6.20}$$

where Ω is a volume in the the $\mathbf{x}_u$ parameter space, subject to possible physical constraints.

The probability for the decay $\tau \to X$, in a phase–space element with volume dX, is proportional to

$$d\Gamma \sim |\mathcal{M}(\tau \to X)|^2 dX, \tag{6.21}$$

where $\mathcal{M}$ is the amplitude for that particular transition, which is known from theory. The decay width $1/\Gamma \, d\Gamma(\theta)/d\theta$, differential in another parameter θ,

133

can be readily obtained from Eq. (6.21) after inclusion of a Jacobian term $|dX/d\theta|$.

The following tau decay modes are considered in the SVfit algorithm:

- $\tau^- \to l^- \, \bar{\nu}_l \, \nu_\tau$, where $l = e, \mu$,

- $\tau^- \to \pi^- \, \nu_\tau$

- $\tau^- \to \pi^- \pi^0 \, \nu_\tau$, where the $\pi\pi$ system is mediated by the $\rho(770)$ resonance,

- $\tau^- \to \pi^- \pi^+ \pi^- \, \nu_\tau$ or $\pi^- \pi^0 \pi^0 \, \nu_\tau$, where the two final states originate from the decay chain $\tau \to a_1(1240) \, \nu_\tau \to \rho(\pi\pi) \, \pi \, \nu_\tau$.

The two helicity eigenstates of the tau lepton (L, R) have different decay widths. The invariance under CP implies equal amplitudes for τ_L^- and τ_R^+.

6.6.1 Tau decay parametrization

The Cartesian components of the neutrino momenta are re–expressed in terms of variables more directly connected to the tau decay kinematics. The following parametrization is adopted:

- $\tau_\ell \tau_\ell$:
  the fraction of the tau lepton energy in the laboratory frame taken by the decay leptons (x_ℓ, x_ℓ'), the mass of the two neutrino pairs $(m_{\nu\nu}, m_{\nu\nu}')$ and the azimuthal angle of the tau lepton momenta with respect to their visible decay products (ϕ_ℓ, ϕ_ℓ'). By convention, $\phi_l = 0$ corresponds to a direction in the plane spanned by the momentum of ℓ and the z–axis in the CMS reference frame:

$$\boldsymbol{x}_u = (x_\ell, m_{\nu\nu}, \phi_\ell, x_\ell', m_{\nu\nu}', \phi_\ell')$$

- $\tau_\ell \tau_h$:
  the fraction of the tau lepton energy in the laboratory frame taken by the visible decay particles (x_h, x_ℓ), the mass of the neutrino pair arising from the fully–leptonic decay $(m_{\nu\nu})$ and the azimuthal angle of the tau lepton momenta with respect to the direction of their visible decay products (ϕ_ℓ, ϕ_h):

$$\boldsymbol{x}_u = (x_\ell, m_{\nu\nu}, \phi_\ell, x_h, \phi_h)$$

- $\tau_h \tau_h$:

  the fraction of the tau lepton energy in the laboratory frame taken by the visible decay particles (x_h, x'_h) and the azimuthal angle of the tau lepton momenta with respect to the direction of their visible decay products (ϕ_h, ϕ'_h):

$$\boldsymbol{x}_u = (x_h, \phi_h, x'_h, \phi'_h)$$

When complemented with the measured momentum of the decay products and with the reconstructed $\vec{E}_T^{miss}$, these parameters fully describe the di–tau kinematics. The di–tau mass is then obtained as a function of these parameters and measurements. The formula can be derived in a straightforward manner but the expression is quite involved, and therefore it is omitted here. An algorithmic procedure to derive the di–tau mass from these parameters is described in Section 6.6.5.

6.6.2 Alternative parametrizations and physical constraints

An equally good choice of parameters is to replace the x fractions with $\cos\theta^*$, the cosine of the polar decay angle of the visible decay products $(\ell, \pi, \rho(\pi\pi)$ or $a_1(\pi\pi\pi))$ in the tau rest frame, with respect to the polarization axis of the tau, which for a state of definite helicity corresponds to the direction of flight in the laboratory frame. The relation between x and $\cos\theta^*$ can be obtained by solving for the visible energy E_{vis} in the laboratory frame, after a Lorentz boost $\gamma = E_\tau/m_\tau$ from the rest frame:

$$\cos\theta^* = \frac{E_{vis} - \gamma E_{vis}^*}{\gamma\beta p_{vis}^*} \tag{6.22}$$

where E_{vis}^* and p_{vis}^* are the energy and momentum of the visible particles in the tau rest frame and $\beta = \sqrt{1 - 1/\gamma^2}$. The energy and momentum in the rest frame are given by

$$E_{vis}^* = \frac{m_\tau^2 + m_{vis}^2 - m_{\nu\nu}^2}{2m_\tau} \tag{6.23}$$

$$p_{vis}^* = \frac{[(m_\tau^2 - (m_{\nu\nu} + m_{vis})^2)(m_\tau^2 - (m_{\nu\nu} - m_{vis})^2)]^{\frac{1}{2}}}{2m_\tau}, \tag{6.24}$$

with $m_{\nu\nu} = 0$ for a semi–leptonic decay (see e.g. [43]). Notice that $-1 \leq \cos\theta^* \leq 1$ implies the physical constraint on x: $m_{vis}^2/m_\tau^2 \leq x \leq 1$. In the collinear limit $\beta \to 1$, Eq. (6.22) simplifies to

$$\cos\theta^* = \frac{2x - 1 - m_{vis}^2/m_\tau^2}{1 - m_{vis}^2/m_\tau^2} \tag{6.25}$$

Equation (6.25) shows that, for a given value of the visible mass m_{vis}, the relation between x and $\cos\theta^*$ is linear.

For the fully–leptonic tau decay, an alternative parametrization consists in using the visible lepton energy in the tau rest frame (E_ℓ^*) and $\cos\theta^*$. Equations (6.22) and (6.23) can be used to derive the transformation from $(E_\ell^*, \cos\theta^*)$ to $(x_\ell, m_{\nu\nu})$:

$$\begin{cases} \cos\theta^* &= \dfrac{2x_\ell}{1 - \frac{m_{\nu\nu}^2}{m_\tau^2}} - 1 \\ E_\ell^* &= \dfrac{m_\tau}{2}\left(1 - \dfrac{m_{\nu\nu}^2}{m_\tau^2}\right) \end{cases} \tag{6.26}$$

The Jacobian matrix J for the transformation in Eq. (6.26) is

$$\begin{pmatrix} \frac{\partial\cos\theta^*}{\partial x_\ell} & \frac{\partial\cos\theta^*}{\partial m_{\nu\nu}} \\ \frac{\partial E_\ell^*}{\partial x_\ell} & \frac{\partial E_\ell^*}{\partial m_{\nu\nu}} \end{pmatrix} = \begin{pmatrix} \frac{2}{1 - \frac{m_{\nu\nu}^2}{m_\tau^2}} & \frac{4x_\ell m_{\nu\nu}}{(1 - \frac{m_{\nu\nu}^2}{m_\tau^2})^2 m_\tau^2} \\ 0 & -\frac{m_{\nu\nu}}{m_\tau^2} \end{pmatrix}, \tag{6.27}$$

with determinant

$$|J| = \frac{2m_{\nu\nu}}{m_\tau^2 - m_{\nu\nu}^2}.$$

In the approximation $m_\ell \sim 0$, the physical region for $(E_\ell^*, \cos\theta^*)$ is defined by $-1 \leq \cos\theta^* \leq 1$ and $0 \leq E_\ell^* \leq \frac{m_\tau}{2}$, which implies that $0 \leq x_\ell \leq 1$ and, for a fixed x_ℓ, $0 \leq m_{\nu\nu} \leq m_\tau\sqrt{1 - x_\ell}$.

6.6.3 Decay widths

In terms of the parameters described in Section 6.6.1, the probability density functions for the decay $\tau^- \to \ell^- \bar{\nu}_\ell \nu_\tau$, with a tau polarization $P_\tau = \pm 1$, is given by

$$\frac{d\Gamma}{dx_\ell dm_{\nu\nu}} \sim \frac{m_{\nu\nu}}{4m_\tau^2}[(m_\tau^2 + 2m_{\nu\nu}^2)(m_\tau^2 - m_{\nu\nu}^2) + P_\tau(m_\tau^2(2x_\ell - 1) + m_{\nu\nu}^2)(-m_\tau^2 + 2m_{\nu\nu}^2)], \tag{6.28}$$

which has been obtained from Ref. [66] using the transformation of Eq. (6.26). The distributions for the two polarization states are shown in Fig. 6.6 in the form of a density plot in the $(x_\ell, m_{\nu\nu})$ plane.

For the one prong decay $\tau^- \to \pi^- \nu_\tau$, with tau polarization $P_\tau = \pm 1$, the decay width differential in the pion x_h fraction is given by [66]

$$\frac{d\Gamma}{dx_h} = 1 + P_\tau(2x_h - 1) \tag{6.29}$$
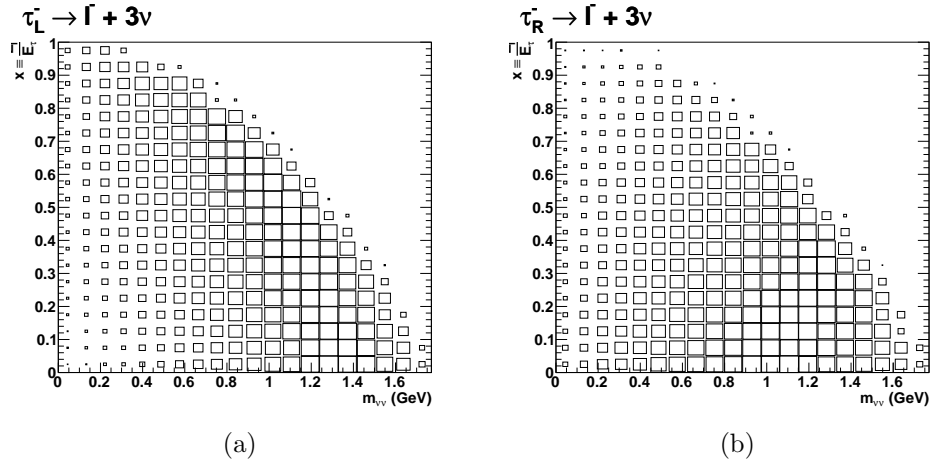
Figure 6.6: Probability density function of the visible energy fraction x_ℓ and neutrino–pair mass $m_{\nu\nu}$ in $\tau_P^- \to \ell^- 3\nu$ decays, with (a) $P = L$ and (b) $P = R$. Figure obtained from Eq. (6.28).

For the other hadronic decays, the formalism gets more involved due to the presence of spin one particles, for which, in addition, the finite decay width has to be taken into account [66]. By performing a numerical integration over the vector meson line shape parametrized as in Ref. [66], the distributions shown in Fig. 6.7 are obtained.

The decay widths are separately computed for longitudinally (L) or transversely polarized (T) vector mesons. The results are reported in Fig. 6.7 for the $\tau^- \to \rho^- \nu_\tau$ decay and in Fig. 6.8 for the $\tau^- \to a_1^- \nu_\tau$ decay.

As seen in the plots, there is a strong correlation between P_τ and $\langle x_h \rangle$, namely the transversely–polarized ρ^- or a_1^- inside the left–handed polarized tau decaying hadronically (τ_L^-) tends to be hard, and it prefers to share its laboratory energy uniformly among the daughter pions. Conversely, a right–handed polarized tau (τ_R^-) tends to decay into a hard longitudinally–polarized meson, for which the distinguishable pion (i.e. the pion with the same charge of the mother tau) is more likely to be soft, if the other pion(s) are hard, or the other way round. Therefore, if the tau polarization were known and if it were possibile to distinguish the single pions inside τ_h, the tau kinematics would be better constrained.

Even though P_τ is not measurable, the spin of the mother resonance imposes a selection rule on the polarization states of the two tau leptons, namely only RL or LR combinations are allowed for a spin–one resonance (e.g. the Z boson), only RR or LL are possible for a spin–0 (e.g. the Higgs boson).

137
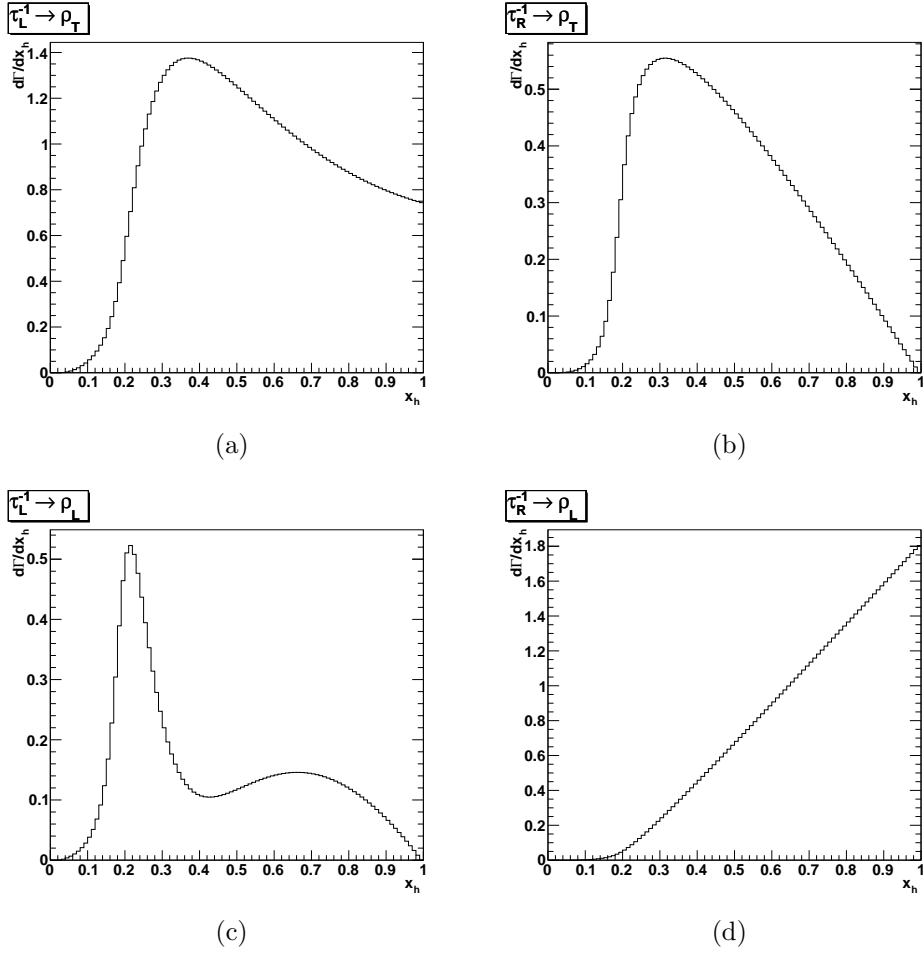
Figure 6.7: Probability density function for the decay $\tau_P^- \to \nu_\tau + \rho_\alpha$, with (a,c) $P = L$ or (b,d) R, and (a,b) $\alpha = T$ or (c,d) L. Figures obtained from a numerical integration of the analytical formulas in Ref. [66], performed with the ROOT [89] built–in integrator.
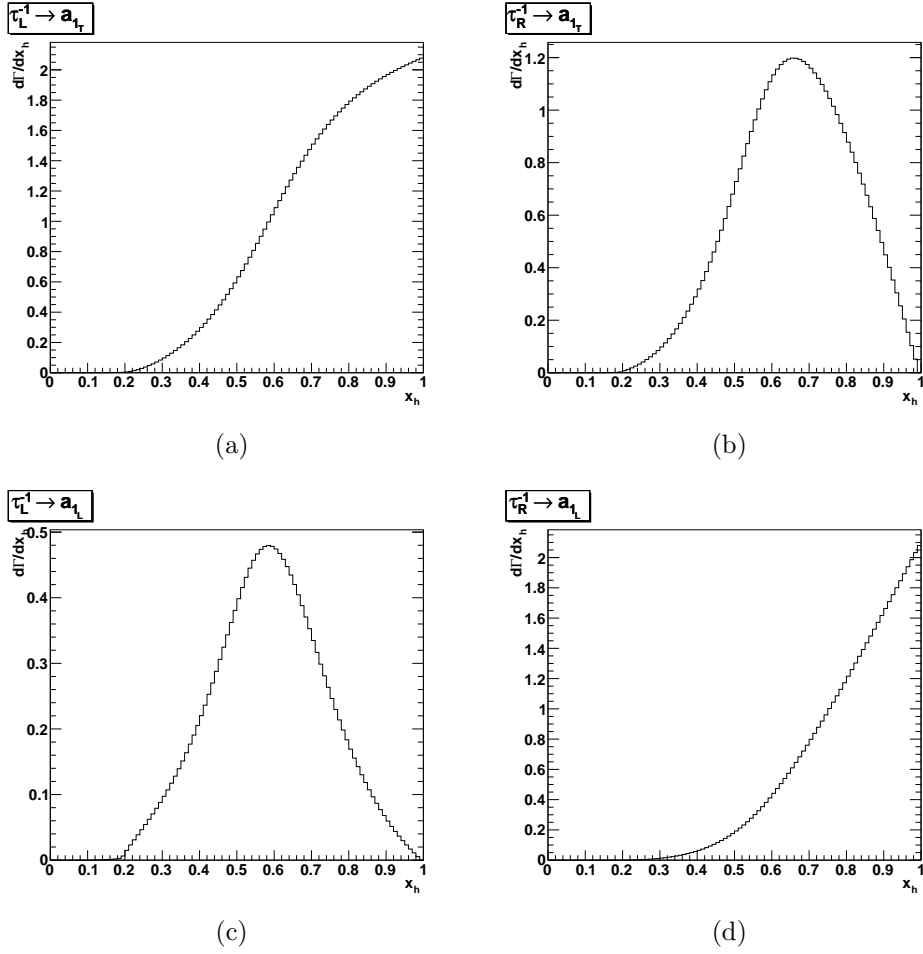
Figure 6.8: Probability density function for the decay $\tau_P^- \to \nu_\tau + a_{1\,\alpha}$, with (a,c) $P = L$ or (b,d) $P = R$, and (a,b) $\alpha = T$ or (c,d) $\alpha = L$. Figures obtained from a numerical integration of the analytical formulas in Ref. [66], performed with the ROOT [89] built–in integrator.

139

Let's assume that the individual pions can be resolved inside the hadronically–decaying tau, and let's define z to be the fraction of energy of the visible decay particles in the laboratory frame taken by the distinguishable pion: $z \equiv E_\pi / E_{vis}$. For the $\rho^- \to \pi^- \pi^0$ decay, the probability density function are given by [66]:

$$\begin{cases} \frac{d\Gamma(\rho_L^-)}{dz} & = 3(2z-1)^2 \\ \frac{d\Gamma(\rho_T^-)}{dz} & = 6z(1-z) \end{cases} \tag{6.30}$$

From Eq. (6.30), the *conditional* probability to observe x_h given z is

$$\frac{d\Gamma}{dx_h}(x_h|z) = \frac{\frac{d\Gamma_L}{dx_h}(x_h) \cdot \frac{d\Gamma(\rho_L^-)}{dz} + \frac{d\Gamma_T}{dx_h}(x_h) \cdot \frac{d\Gamma(\rho_T^-)}{dz}}{M_L \frac{d\Gamma(\rho_L^-)}{dz} + M_T \frac{d\Gamma(\rho_T^-)}{dz}} \tag{6.31}$$

where $M_\alpha = \int_0^1 \frac{d\Gamma_\alpha}{dx_h'}(x_h')dx_h'$.

A similar formula exists for the a_1^- decay. It is useful to distinguish the case where the three pions are individually resolved from the case that the undistinguishable pions cannot be resolved. In the former case, the ideal polarimeter to be used to condition the decay width is provided by the $\cos\psi$ variable introduced by Ref. [90]:

$$\cos\psi \equiv \frac{8m_\tau^2 \vec{p}_1 \cdot (\vec{p}_2 \times \vec{p}_3)/|\vec{p}_1 + \vec{p}_2 + \vec{p}_3|}{\sqrt{-\lambda(\lambda(m_\tau^2, m_{12}^2, m_\pi^2)\lambda(m_\tau^2, m_{13}^2, m_\pi^2)\lambda(m_\tau^2, m_{23}^2), m_\pi^2}} \tag{6.32}$$

with $\lambda(x,y,z) = x^2 + y^2 + z^2 - 2xy - 2yz - 2zx$. If the undistinguishable pions are not individually resolved, one needs to integrate them out. To do so, a numerical integration of Eq. (46) and (47) from Ref. [91] has been performed to obtain $d\Gamma(a_{1\,\alpha}^-)/dz$. The resulting distributions are reported in Fig. 6.9.

Using the numerical values of the histograms in Fig. 6.9, a conditional probability density $d\Gamma/dx_h$ for the a_1 decays, similar to Eq. (6.31), can be derived. The conditional probabilities for the ρ and a_1 decays are represented in Fig. 6.10 in the form of a density plot.

A simplified decay width for the semi–leptonic decays (phase–space), valid for unpolarized taus ($P_\tau = 0$), consists in assuming an uniform probability density:

$$\frac{d\Gamma}{dx_h} = \frac{1}{1 - \frac{m_{vis}^2}{m_\tau^2}}, \tag{6.33}$$

where m_{vis} is the measured visible τ_h mass. This simple formula already provides a good description of the hadronic decay widths. Figure 6.11 compares the visible energy fractions for hadronically–decaying taus in a $Z \to \tau\tau$
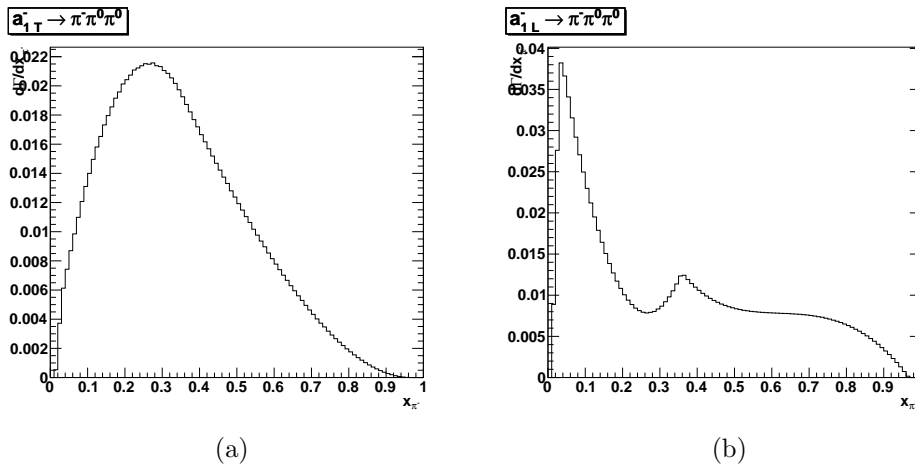
Figure 6.9: Probability density function of the distinguishable pion energy fraction in $a_{1\,\alpha} \to \pi^- \pi^0 \pi^0$ decay, with (a) $\alpha = T$ and (b) $\alpha = L$. Figures obtained from a numerical integration of the analytical formula in Ref. [91]. The unphysical kink in (b) is currently under investigation.

Monte Carlo sample, using Eq. (6.33) or from the full TAUOLA [92] simulation.

6.6.4 Missing transverse energy

For a given value of the dynamical parameters (Section 6.6.1), the four–momenta of the decay neutrinos are univocally determined:

$$p_\nu^\mu = p_\nu^\mu(\phi, x, m_{\nu\nu} | p^\mu), \tag{6.34}$$

once the four–momentum of the visible decay products ($p_\mu = (E, p_x, p_y, p_z)$) has been measured.

The $(\phi, x, m_{\nu\nu})$ parameters can be related to the tau lepton four–momentum in the laboratory frame ($E^\tau, p_x^\tau, p_y^\tau, p_z^\tau$) via the following transformations. First, the momenta p^* of the visible particles in the tau rest frame are obtained from the visible mass $m = (E^2 - p^2)^{1/2}$) and $m_{\nu\nu}$ using Eq. (6.23). The cosine of the decay angle θ^* between the direction of the visible particles and the tau momentum is obtained from x, p, p^* and m using Eq. (6.22). Given θ^*, p and p^*, the decay angle θ in the laboratory frame can be computed by taking advantage of the invariance of the momentum component orthogonal to the tau lepton direction of flight:

$$p^* \sin \theta^* = p \sin \theta.$$

141
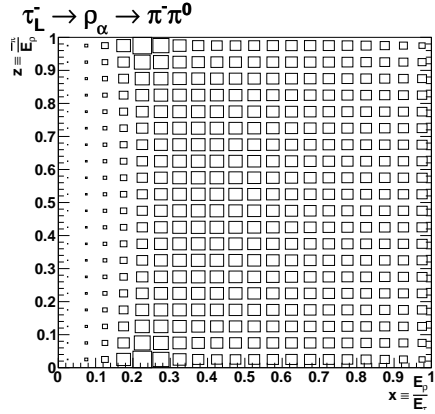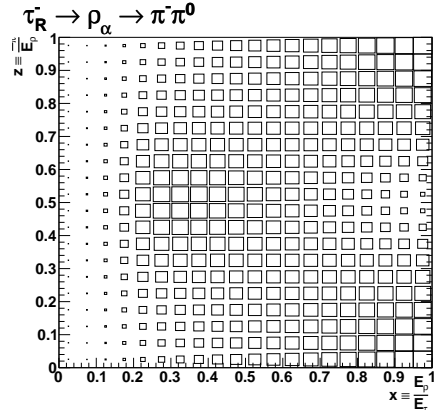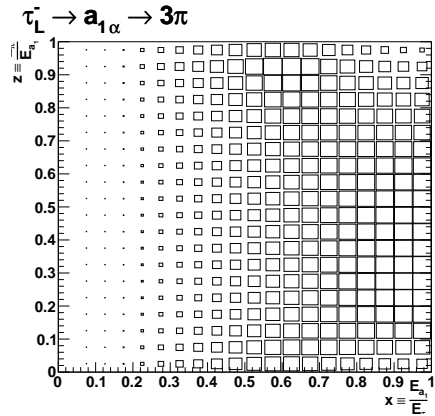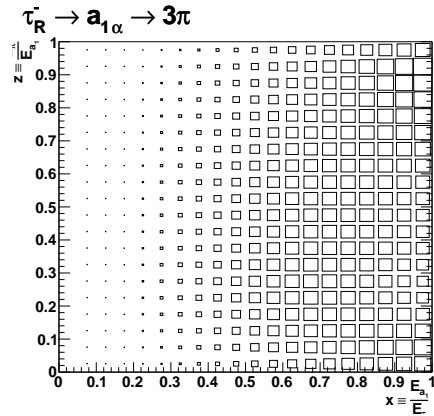
Figure 6.10: Conditional probability density functions of the visible energy fraction x_h in (a,b) $\tau_{L,R}^- \to \rho^-$ and (c,d) a_1^- decays for a fixed value of the the fraction of the ρ (a_1) energy taken by the distinguishable pion. Figures obtained from Eq. (6.31) and the numerical values taken from Fig. 6.9.
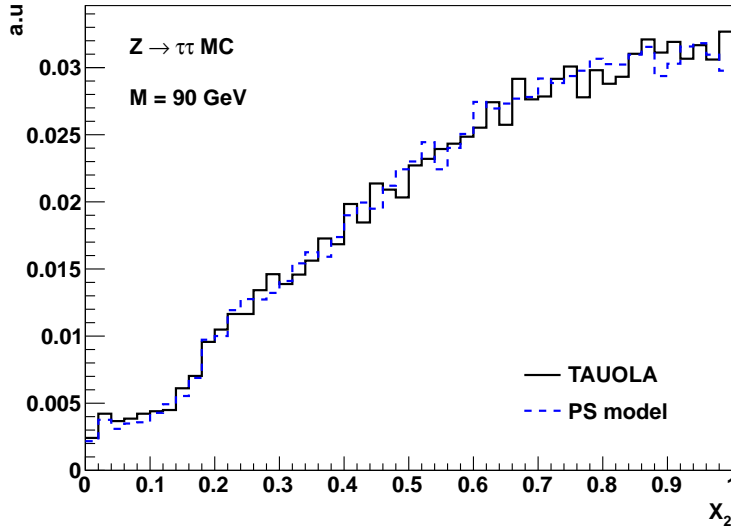
Figure 6.11: Comparison between the visible energy fractions x_h for hadronically–decaying taus in a $Z \to \tau\tau$ Monte Carlo sample, using Eq. (6.33) or from the full TAUOLA [92] simulation. Figure published in Ref. [93].

The polar coordinates of the tau lepton direction with respect to the visible particle are then given by $\mathbf{u} = (1, \cos^{-1}\theta, \phi)$.

To express $\mathbf{u}$ in the global Cartesian (x, y, z) reference frame with versors $(\mathbf{x}, \mathbf{y}, \mathbf{z})$, a rotation is needed. This is achieved by a rotation matrix with Euler angles (α, β, γ) satisfying

$$
\begin{cases}
\cos\alpha & = [(\vec{p}_T \times \mathbf{z}) \cdot \mathbf{x}]/p \\
\cos\beta & = p_z/p \\
\cos\gamma & = 1.
\end{cases}
\tag{6.35}
$$

The energy of the tau lepton is simply given by $E^\tau = E/x$.

If the neutrinos from the tau decay are the only source of invisible energy in the event, than the vectorial sum of their momenta is experimentally constrained by the missing transverse energy $\vec{E}_T^{miss}$. In realistic scenarios, detector resolution and fluctuations in the undetectable part of the event smear $\vec{E}_T^{miss}$ around the true value $\sum_i \vec{p}_T^{\nu\,i}$. The compatibility between the hypothesis $\sum_i \vec{p}_T^{\nu\,i}$ and an observed value of $\vec{E}_T^{miss}$ is quantified by the missing transverse energy likelihood $L(\vec{E}_T^{miss}| \sum_i \vec{p}_T^{\nu\,i})$.

The $\vec{E}_T^{miss}$ likelihood is obtained from the "particle–flow significance" al-

gorithm, documented in Ref. [62] and here summarized. Particles reconstructed by the particle–flow algorithm are grouped into exclusive collections of objects, depending on whether they are clustered inside jets, are isolated (e.g leptons), or unclustered. The transverse momentum $\vec{E}_T^i$ of the i–th object is measured with a covariance matrix

$$\mathbf{U}_i = \left(\begin{array}{cc} \sigma^2_{E_T\,i} & 0 \\ 0 & \sigma^2_{\phi\,i} \end{array} \right),$$

evaluated in the reference frame with axes parallel and perpendicular to $\vec{E}_T^i$. The U_{00} and U_{11} elements depend in general on the p_T and η of the object. After a rotation into the global (x, y, z) CMS reference frame, the covariance matrices are summed together:

$$\mathbf{V}_i = \sum_i R(\phi)^{-1} \mathbf{U}_i R(\phi).$$

In the gaussian approximation, the likelihood for observing $\vec{E}_T^{miss}$ given a true missing energy $\sum_i \vec{p}_T^{\nu\,i}$ is given by

$$L(\vec{E}_T^{miss} | \sum_i \vec{p}_T^{\nu\,i}) = \frac{1}{\sqrt{2\pi|\mathbf{V}|}} e^{\frac{1}{2}(\vec{E}_T^{miss} - \sum_i \vec{p}_T^{\nu\,i})^T \mathbf{V}^{-1}(\vec{E}_T^{miss} - \sum_i \vec{p}_T^{\nu\,i})} \qquad (6.36)$$

6.6.5 The SVfit likelihood

Let's denote by $\boldsymbol{x}_u = (\boldsymbol{x}_u^1, \boldsymbol{x}_u^2)$ the ensemble of dynamical parameters necessary to describe the decay of the first and second tau lepton (Section 6.6.1). The measurements from which the di–tau mass can be constrained consist of the four–momentum of the visible decay products (p_μ^1 and p_μ^2), the reconstructed missing transverse energy ($\vec{E}_T^{miss}$), and possibly the fraction of visible energy in the laboratory frame taken by the distinguishable pions (z_1 and z_2). Equation (6.20) then reads

$$L_{SVfit}(M_{\tau\tau} | p_\mu^1, p_\mu^2, z_1, z_2) \propto \sum_{\alpha=L,R} \sum_{\beta=L,R} \gamma_{\alpha\beta} \int_\Omega \frac{d\Gamma_1^\alpha(\boldsymbol{x}_u^1 | z_1)}{d\boldsymbol{x}_u^1} \frac{d\Gamma_2^\beta(\boldsymbol{x}_u^2 | z_2)}{\boldsymbol{x}_u^2}$$

$$\times \exp\left\{ \frac{1}{2} \left(\vec{E}_T^{miss} - \sum_i \vec{p}_T^{\nu\,i}(\boldsymbol{x}_u^i | p_\mu^i) \right)^T \mathbf{V}^{-1} \left(\vec{E}_T^{miss} - \sum_i \vec{p}_T^{\nu\,i}(\boldsymbol{x}_u^i | p_\mu^i) \right) \right\}$$

$$\times \delta(M_{\tau\tau} - M_{\tau\tau}(\boldsymbol{x}_u^1, \boldsymbol{x}_u^2 | p_\mu^1, p_\mu^2)) d\boldsymbol{x}_u^1 d\boldsymbol{x}_u^2$$
$$(6.37)$$

144

The integration volume Ω is subject to the physical constraints of Section 6.6.2. Uniform probability density functions for the ϕ angles has been assumed: $d\Gamma/d\phi = 1/2\pi$. The functions $d\Gamma/d\boldsymbol{x}_u$ are proportional to the decay widths in Eq. (6.28), (6.29) or (6.31). The sum runs over all possible combinations of tau polarizations, with the $\gamma_{\alpha\beta}$ matrix taking care of the correct combinatorics. In the SM,

$$\begin{cases} \gamma_{LL} = \gamma_{RR} = \frac{1}{2} \\ \gamma_{LR} = \gamma_{RL} = 0 \end{cases} \tag{6.38}$$

for the Higgs boson decaying to $\tau^-\tau^+$ and

$$\begin{cases} \gamma_{LL} = \gamma_{RR} = 0 \\ \gamma_{LR} = \frac{1}{2}(1 - \langle P_\tau \rangle) \\ \gamma_{RL} = \frac{1}{2}(1 + \langle P_\tau \rangle) \end{cases} \tag{6.39}$$

for the Z boson at the pole, where $\langle P_\tau \rangle = \frac{-2va}{a^2+v^2}$ and $v = 1/2 + 2\sin^2\theta_W$, $a = -1/2$ [43]. Numerically, $\gamma_{LR} \approx 0.576$ and $\gamma_{RL} \approx 0.424$, showing that a small polarization of the taus arises in the $Z \to \tau^-\tau^+$ decay as consequence of the chiral structure of the SM Lagrangian (Section 2.1.2).

The case $\gamma_{\alpha\beta} = 1/4 \ \forall \alpha, \beta$ corresponds to an uniform prior on the polarizations of the taus; it is equivalent to assume that the intial tau leptons are unpolarized ($P_\tau = 0$).

In real life, it is not possible to classify a priori one event as coming from the decay of the Z boson or from the decay of a resonance ϕ with different chiral coupling to tau leptons. One possibility is to re–interpret the γ matrix as a dynamical quantity that assumes the value predicted for the Z resonance (Eq. (6.39)) for $M_{\tau\tau} \approx M_Z$, and smoothly converges to Eq. (6.38) for higher mass. For example, assuming $\phi = H$, $M_H \gtrsim 110$ GeV, one could use:

$$\begin{aligned} \gamma(M_{\tau\tau}) = &\left[\Theta\left(M_Z - M_{\tau\tau}\right) + \frac{M_{\tau\tau} - (M_Z + \sigma_Z)}{\sigma_Z} \right] \gamma^Z + \\ &\left[\frac{M_{\tau\tau} - M_Z}{\sigma_Z} + \Theta\left(M_{\tau\tau} - (M_Z + \sigma_Z)\right) \right] \gamma^H, \end{aligned} \tag{6.40}$$

where σ_Z is the expected resolution of the $Z \to \tau\tau$ peak.

Finally, it should be noted that Eq. (6.37) assumes that every tau decay is reconstructed with 100% purity. For the leptonic decays (τ_e, τ_μ) this is a good assumption. For the semi–leptonic decays, the approximation is less precise, as seen from Fig. 5.4. To account for migrations of tau decays from one reconstructed decay mode to another, Eq. (6.37) should be modified

by averaging over the generated tau decay modes, with weights equal to the probability for a generated decay mode to be reconstructed in the observed decay mode (i.e. the entries of the matrix in Fig. 5.4).

The integration on the right–hand side of Eq. (6.37) is performed numerically using the VEGAS program [94]. For each event, the estimator of the tau lepton mass is chosen as the value that maximizes $L_{SVfit}(M_{\tau\tau})$. More specifically, L_{SVfit} is computed for a grid of 2.5 GeV spaced values of $M_{\tau\tau}$ in the range $[0, 100]$ GeV, followed by 2.5% spaced values up to 3 TeV. The computing time needed to perform the numerical integration for all points of the grid is about 1 sec. on a 2.27 GHz Intel® Xeon® L5520 processor. The L_{SVfit} values for the mass point giving the maximum likelihood, and for the point before and after, are fitted with a parabola. The mass value at which the parabola fit is at a maximum provides the final di–tau mass estimator, $M_{\tau\tau}^{SVfit}$.

Different combinations of the likelihood functions for the tau decay have been compared. The simple phase–space formula for the τ_h decay (Eq. (6.33)) already provides pretty good performances for all hadronic final states. Including the tau polarizations in the SVfit likelihood Eq. (6.37) brings only to a modest improvement. In light of the substantially longer computing time needed to process the four different polarizations hypothesis, it was preferred to choose Eq. (6.33), for the semi–leptonic tau decays, and Eq. (6.28) for the fully–leptonic. The expected performances of the SVfit algorithm, with this choice of the likelihood function, are compared in Fig. 6.12 for a simulated sample $Z \to \tau\tau$ and for three signal samples $H \to \tau\tau$ with $M_H = 120, 180, 250$ GeV ($\tau_\ell\tau_h$ channel). The missing energy simulated in these events has a RMS of about 10 GeV in the x and y direction. The resulting relative mass resolution is found to be $\approx 20\%$ for $M_H \lesssim 145$ GeV. For higher Higgs masses, the SVfit mass shape departs more and more from a gaussian. Interestingly, this peculiar triangular–like shape, with a mode close to the true mass and a long tail extending down to the lowest possible value $M_{\tau\tau}^{SVfit} \geq M_{\tau\tau}^{vis}$, resembles very closely the maximal lower–bound estimator discussed in Section 6.3.

6.7 Conclusions and comparison between different techniques

In terms of sensitivity to a narrow neutral resonance $\phi \to \tau\tau$ with mass M_ϕ close to the Z mass, the performance of a di–tau mass reconstruction technique is gauged on two properties, namely the expected separation power

146
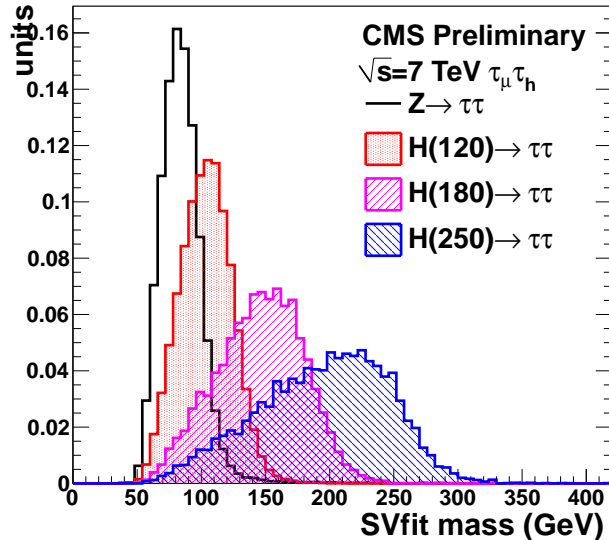
Figure 6.12: SVfit mass distributions in a sample of simulated $Z \to \tau\tau$ and $H \to \tau\tau$ in the $\tau_\mu\tau_h$ channel, obtained using the phase–space likelihood (Eq. (6.33)) for the τ_h decay and the matrix element likelihood for τ_μ (Eq. (6.28)). The missing transverse energy has a RMS of about 10 GeV.

between two nearby resonances, in light of discriminating the signal from its most prominent SM background $Z \to \tau\tau$, and on the rate of succesful reconstructions, i.e. the efficiency to yield a valid di–tau mass solution. These two properties have to be weighted against other desirable features: the robustness of the performance to changes in the detector or event conditions (e.g. pile–up, jet multiplicity, etc...), the average computing time needed to deliver a mass value, and the flexibility of the method.

The reconstruction techniques that follow the first of the approaches outlined in Section 6.1 give in general a modest mass resolution, either due to large non–gaussian tails (see e.g. the collinear approximation), or to the reduced amount of information that is injected into the mass estimator (see e.g. the visible and effective mass, where the missing energy is either not used at all, or not directly used to constrain the neutrino momenta sum). On the other hand, these thechniques are very fast to be executed, since the di–tau mass solution comes either from explicit functions of the observables (collinear approximation, visible, effective, and true mass) or from a numerical minimization (maximal lower–bound estimator). The visible and effective mass are fully efficient, whereas the rate of success of the collinear approximation and of the maximal lower–bound estimator is very sensitive

147

to detector resolution effects, with up to 30%–40% of signal events failing the reconstruction in typical detector resolution scenarios. The maximal lower–bound estimator is more well–behaved than the collinear approximation in terms of separation power: by definition, the reconstructed mass value is bounded from above by the true resonance mass, thus preserving the mass interval $[M_Z, M_\phi]$ from the tails of the $Z \to \tau\tau$ distribution; conversely, the collinear approximation brings to prominent tails towards high mass values.

The likelihood–based reconstruction techniques feature a good mass resolution ($\lesssim 20\%$) and a very high efficiency, with a failure rate at the percent level for the MMC [87], and at the permill level for SVfit [88]. The flexibility of the likelihood approach allows to account for the finite detector resolution at essentially no price of the reconstruction efficiency. On the other hand, these techniques are more CPU–intensive, with an average computing time of $O(1 \text{ s/event})$. The MMC algorithm relies on a Monte Carlo driven parametrization of the differential widths for the various tau decays. In the current implementation, the tau polarization cannot be accounted for. The purely analytical approach of SVfit overcomes the dependence on the Monte Carlo simulation, and is therefore more flexible to accommodate additional prior knowledge on the event.

Thanks to the performing separation power, the almost full reconstruction efficiency, and the built–in flexibility (all of this at a sustainable computing time), the SVfit algorithm has been finally adopted in all recent CMS di–tau analyses in the context of Higgs boson(s) searches.

Chapter 7

Search for the SM Higgs boson decaying to tau pairs

In this chapter, I present a search for the Standard Model Higgs boson decaying to tau leptons in pp collisions at $\sqrt{s} = 7$ TeV. The analysis is performed on the data set collected by the CMS experiment during 2011. The work presented here describes and supports results documented in Ref. [95], which finally entered, using also the 2012 data, the CMS Higgs combination paper [96].

7.1   Introduction

The search for the SM Higgs boson in the decay channel $H \to \tau\tau$ is expected to contribute in a significant manner to a discovery at the LHC, provided that the Higgs boson is indeed light, $M_H \lesssim 145$ GeV. Furthermore, this channel will directly probe the Higgs coupling to leptons, thus providing a fundamental test of the SM predictions.

Given the trigger bandwidth allocated for Higgs searches in the CMS experiment, the $H \to \tau\tau$ signature can be efficiently triggered regardless of the production mode, i.e. just requiring for a pair of tau candidates reconstructed online. This is not the case for e.g. $H \to b\bar{b}$, where an extra tag (lepton or E_T^{miss}) needs to be required at the trigger level to maintain a sustainable rate.

As discussed in Section 2.4, the process $pp \to H{+}X$ in the SM receives the largest contributions from gluon–gluon fusion (GGF), vector–boson fusion (VBF) and from the associated production with vector bosons (VH) or heavy quarks (ttH). The offline search can be optimized for a specific production mechanism by requiring extra tags in the event. The analysis described

in this chapter is specifically optimized for the GGF and VBF production modes. The production of the Higgs boson in association with a W, Z or a pair of heavy quarks, is considered as signal but not explicitly searched for.

A total integrated luminosity $\mathcal{L} = 4.93 \pm 0.11$ fb^{-1} of pp collision collected in 2011 at $\sqrt{s} = 7$ TeV has been analyzed. Events are searched where one tau decays semi–leptonically into a neutrino plus hadrons (τ_h) and the other decays leptonically into lighter leptons, electrons or muons, and two neutrinos (τ_ℓ).

7.2 Data and Monte Carlo simulation

7.2.1 Data

The data sample collected by CMS during the 2011 Run is split into two sets characterized by different beam configurations and, in particular, pile–up rate. The number of minimum–bias events recorded simultaneously with each hard scattering collision increased from an average of ~ 6 in the first period of the Run (A) to an average of ~ 10 in the second part (B). The total luminosity integrated during Run A (B) is of about 2.2 fb^{-1} (2.7 fb^{-1}). The first ≈ 47 pb^{-1} of Run A have been dropped from this analysis because of a problem in the trigger used for the online selection of signal events. The name and corresponding integrated luminosity of the data sets used for the search and for control studies are listed in Table 7.1.

Signal events are searched in the *TauPlusX* data sets, which contain events that fire at least one of the High Level Trigger (HLT) paths based on the online coincidence of a τ_h and an extra tag (electron, muon, tau, or E_T^{miss}).

Dedicated data sets containing single–lepton triggered events (*SingleMu* and *SingleElectron*) are used to measure the trigger and reconstruction efficiency of the analysis objects. Di–muon triggered events (*DoubleMu*) are used to model the $Z \to \tau\tau$ background after replacing the reconstructed muon with a Monte Carlo simulated tau lepton.

7.2.2 Simulation

Monte Carlo generators are used to simulate the signal and its SM backgrounds. Generated events are propagated through the full GEANT based simulation of the CMS apparatus [60], and reconstructed using the CMS event reconstruction software [39] (version 4.2).

The list of Monte Carlo simulated processes is reported in Table 7.3.

Data set name	Run–range	Luminosity (fb^{-1})
Search		
/TauPlusX/Run2011A*	163269-173692	2.22
/TauPlusX/Run2011B*	175860-180252	2.71
Control samples		
/SingleMu/Run2011*	163269-180252	4.93
/SingleElectron/Run2011*	163269-180252	4.93
/DoubleMu/Run2011*	163269-180252	4.93

Table 7.1: Data sets used in the analysis.

The GGF and VBF processes are generated by POWHEG [97] interfaced with PYTHIA [75] for the parton shower. The PYTHIA generator is used to simulate the production of the Higgs boson in association with a vector boson or a heavy–quark pair (VH and ttH). For each production mechanism, independent samples are generated for eight different values of M_H, ranging from 110 to 145 GeV every 5 GeV. The generated Higgs boson is then decayed into tau leptons, which are in turn decayed into stable particles by the TAUOLA program [92]. Each sample is normalized to the cross–section recommended by the LHC Higgs cross–section working group [28] and reported for reference in Table 7.2. In the GGF sample, the Higgs boson p_T distribution has been re–weighted according to the NNLO k–factors obtained with the FeHiPro program [98].

M_H (GeV)	BR	cross–section (pb)				
		GGF	VBF	WH	ZH	ttH
110	$8.02 \cdot 10^{-2}$	19.8	1.40	0.875	0.472	0.126
115	$7.65 \cdot 10^{-2}$	18.1	1.33	0.755	0.411	0.111
120	$7.10 \cdot 10^{-2}$	16.6	1.27	0.656	0.360	0.0975
125	$6.37 \cdot 10^{-2}$	15.3	1.21	0.573	0.316	0.0863
130	$5.48 \cdot 10^{-2}$	14.1	1.15	0.494	0.278	0.0766
135	$4.52 \cdot 10^{-2}$	13.1	1.10	0.439	0.245	0.0681
140	$3.54 \cdot 10^{-2}$	12.1	1.05	0.386	0.217	0.0607
145	$2.61 \cdot 10^{-2}$	11.3	1.00	0.341	0.193	0.0543

Table 7.2: Cross–sections and branching ratios of the SM Higgs boson at $\sqrt{s} = 7$ TeV [28].

The Drell–Yan $Z/\gamma^* \to \ell\ell$ ($m_{\ell\ell} > 50$ GeV) production is generated by MadGraph interfaced with PYTHIA, and is used to derive the acceptance times efficiency for backgrounds involving the production of a leptonically–

decaying Z boson. The inclusive normalization is instead obtained by counting di–muon events collected in the same run range used for the analysis, after correcting for data–to–simulation differences in the trigger and reconstruction efficiency.

The W+jets production is generated by MadGraph [99] interfaced with PYTHIA. The W+jets normalization in the signal region is derived from data sidebands. When two extra jets are required in the event, the statistics of the inclusive W+jets Monte Carlo sample is not sufficient and a high–statistics exclusive sample of W+3 jets is used instead. For the sake of comparing the data–driven yield with the Monte Carlo expectation, the NNLO cross–section obtained from the FEWZ [100] program is used.

Top–pair production plus jets are simulated by MadGaph interfaced with PYTHIA. As for W+jets, the top–pair normalization is derived from data, and compared to the NNLO theory prediction.

Inclusive di–boson production (WW,WZ, and ZZ) is simulated by PYTHIA and normalized to the CMS measured cross–section [101].

Pile–up interactions are simulated by superimposing minimum bias events, generated by PYTHIA, to the hard scattering event. The multiplicity of pile–up interactions in the simulation is sampled from a distribution that does not exactly reproduce the one observed in data (Fig. 7.1). To match the pile–up conditions in data, every Monte Carlo event simulated with N in–time pile–up interactions is assigned a weight equal to the ratio between the probability of observing N in data and in the simulation (pile–up reweighting).
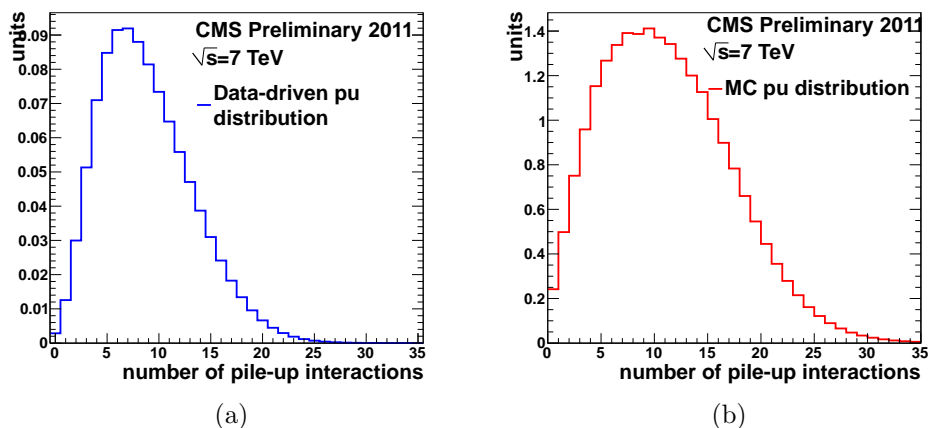
Figure 7.1: a) Pile–up distribution in data; b) pile–up distribution in the unweighted Monte Carlo simulation.

152

Process	Generator	cross–section	$\mathcal{L}$ equivalent fb^{-1}
Signal			
$gg \rightarrow H \rightarrow \tau\tau$	POWHEG	$1.59 - 0.29$ pb	> 100
$qq \rightarrow H \rightarrow \tau\tau$	POWHEG	$0.112 - 0.026$ pb	> 1000
$pp \rightarrow VH + t\bar{t}H, \; H \rightarrow \tau\tau$	PYTHIA	$0.118 - 0.015$ pb	> 1000
Background			
$Z/\gamma^* \rightarrow \ell\ell + \leq 4$ jets	MadGraph	3.048 nb	$\approx 4(10)$
$W \rightarrow \ell\nu + \leq 4$ jets	MadGraph	31.314 nb	$\approx 2(2.5)$
$W \rightarrow \ell\nu + 3$ jets	MadGraph	305 pb	$\approx 20(25)$
$t\bar{t}$	MadGraph	157.5 pb	$\approx 200(350)$
WZ→X	PYTHIA	18.2 pb	$\approx 200(100)$
ZZ→X	PYTHIA	5.9 pb	$\approx 550(500)$
WW→X	PYTHIA	43 pb	$\approx 9(40)$

Table 7.3: Monte Carlo samples used in the analysis. The cross–section and the equivalent integrated luminosity (before pile–up reweighting) are reported in the third and fourth column, respectively. The Monte Carlo luminosity available for the $\tau_h\tau_\mu$ ($\tau_h\tau_e$) channel depends on the total number of generated events as well as on the success rate of processed jobs.

7.3 Trigger

The online trigger menu has been evolving very rapidly to cope with the increase of instantaneous luminosity during the 2011 data–taking period.

The Level-1 (L1) trigger selection is based on a single lepton seed, electron (EG) or muon (Mu), with p_T and η thresholds evolving in time.

After a L1 accept, the High Level Trigger (HLT) algorithm is run to reconstruct an HLT object around the L1 seeding lepton. The resulting trigger object is characterized by a finer estimation of the momentum, isolation, and identification variables. A regional particle-flow algorithm is run around jets above a given threshold to reconstruct τ_h candidates at the HLT level. The coincidence of a lepton and tau trigger objects spatially separated and satisfying specific quality and kinematical cuts is the condition for the HLT filter to select the event.

The L1 and HLT specifics of the triggers used to record the data events in the $\tau_e\tau_h$ and $\tau_\mu\tau_h$ channel are reported in Table 7.4.

The trigger algorithms emulated in the Monte Carlo simulation differ from those run online. A data–to–simulation correction factor is applied to the simulation to reproduce the turn–on curves measured in data.

The turn–on curves for the ℓ and τ_h part of the cross–triggers of Table 7.4 have been measured with tag–and–probe as a function of the e, μ, and

L1	HLT	Run–range	Luminosity
$\tau_e\tau_h$ channel			
L1_SingleEG12	IsoEle15_LooseIsoTau15	163269-163869	0.18 fb^{-1}
L1_SingleEG12	IsoEle15_LooseIsoTau20	165088-167913	0.97 fb^{-1}
L1_SingleEG12	IsoEle15_TightIsoTau20	170249-173198	0.82 fb^{-1}
L1_SingleEG12	IsoEle18_MediumIsoTau15	173236-178380	2.0 fb^{-1}
L1_SingleEG18	IsoEle20_MediumIsoTau15	178420-179889	0.74 fb^{-1}
L1_SingleEG20	IsoEle20_MediumIsoTau15	179959-180252	0.02 fb^{-1}
$\tau_\mu\tau_h$ channel			
L1_SingleMu10	IsoMu12_LooseIsoTau10	163269-163869	0.18 fb^{-1}
L1_SingleMu10	IsoMu15_LooseIsoTau15	165088-173692	1.8 fb^{-1}
L1_SingleMu14*	IsoMu15_LooseIsoTau20	175860-180252	2.8 fb^{-1}

Table 7.4: Trigger paths used in the analysis.

τ_h transverse momentum. The results are reported in Fig. 7.2, 7.3, 7.4, and 7.5. For this purpose, single–lepton triggered events have been used, where the tag is required to pass stringent quality criteria, while the probe is a reconstructed electron, muon, or tau passing the full selection criteria applied in the analysis.

For each trigger path and η bin, the turn–on curve has been parametrized with a physically–inspired analytical form (the cumulative distribution function of a Crystal Ball) and fitted to data. The curve corresponding to the average trigger efficiency over the full data set is then obtained by averaging the fitted functions in a weighted sum, where the weights are proportional to the fraction of data events collected by each particular trigger (Fig. 7.6).

7.4 Object reconstruction

The reconstruction and identification of the objects employed in the analysis are described in the following. The optimization of the working points is driven by the achievement of the best figure of merit, which is chosen to be the expected 95% CL exclusion limit on the production cross–section of a SM–like Higgs boson with $M_H \approx 120$ GeV.

7.4.1 Primary vertex

Primary vertices are reconstructed using the Deterministic Annealing (DA) [103] algorithm. Only those vertices that pass a set of quality requirements are
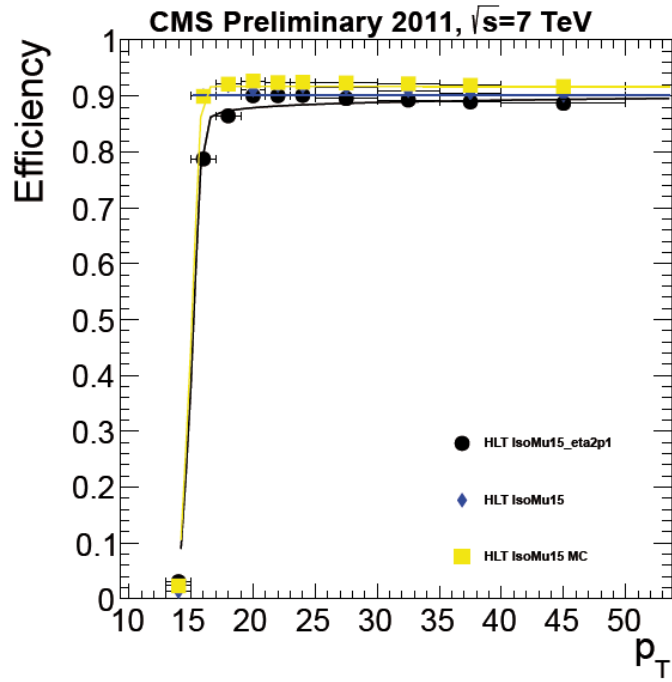
(a)
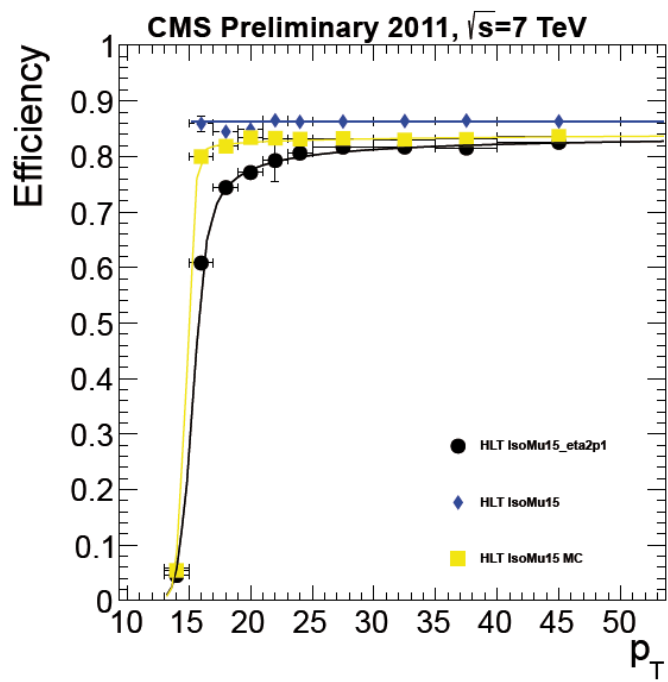
(b)

Figure 7.2: Trigger turn–on curves for the muon part of the cross triggers in the (a) barrel and (b) endcap, as a function of the muon p_T (Figures published in Ref. [102]).
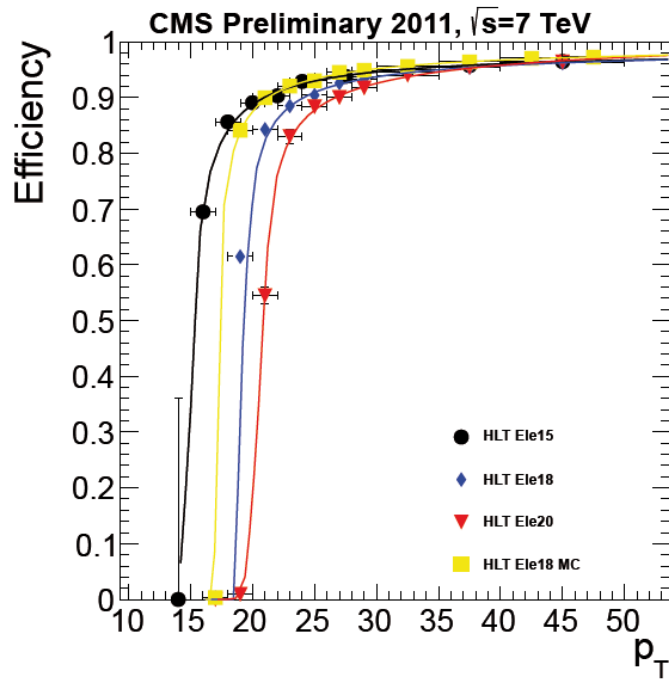
(a)
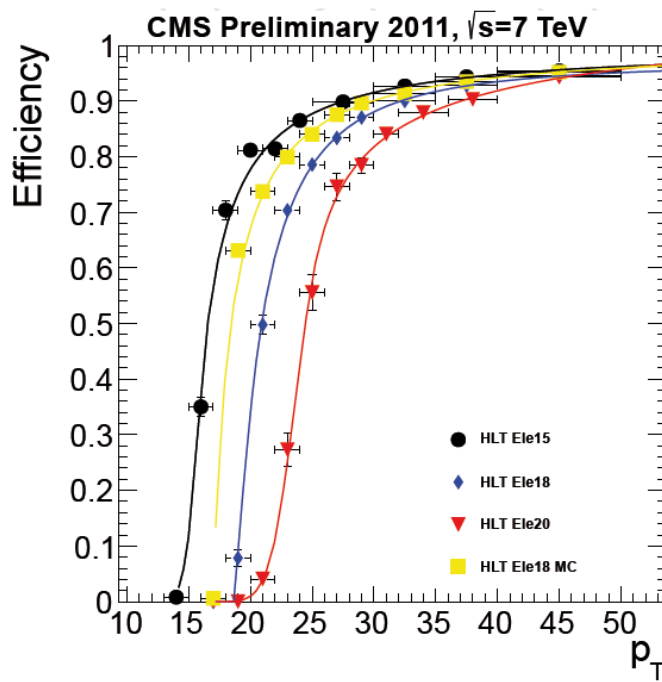
(b)

Figure 7.3: Trigger turn–on curves for the electron part of the cross trigger in the (a) barrel and (b) endcap, as a function of the electron p_T (Figures published in Ref. [102]).
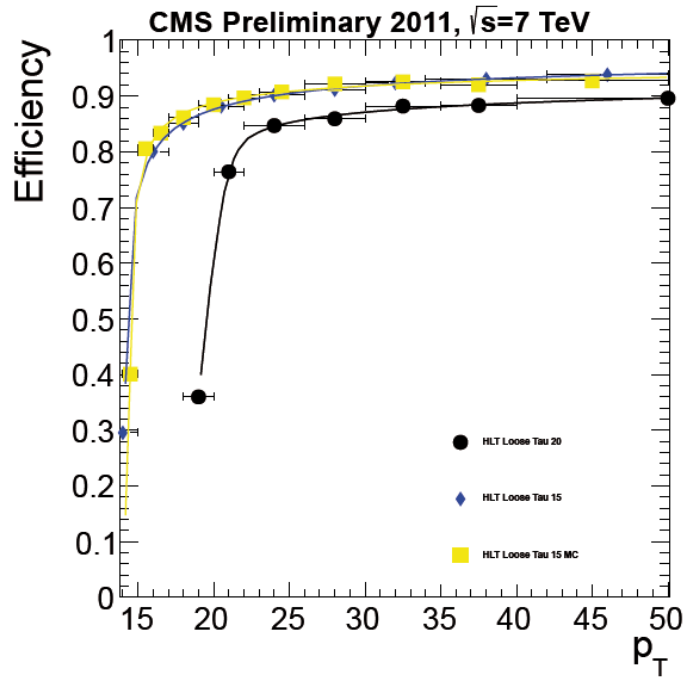
(a)
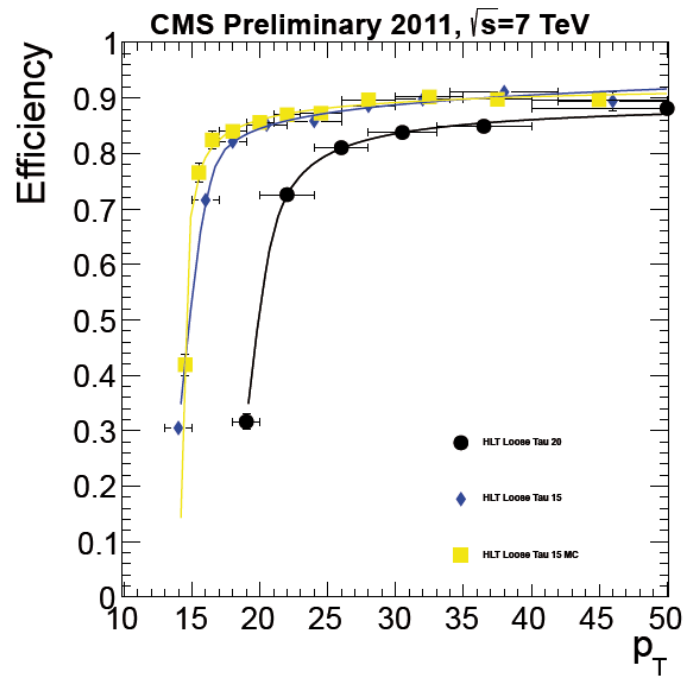
(b)

Figure 7.4: Trigger turn–on curves for the τ_h part of the cross trigger in the (a) barrel and (b) endcap, as a function of the τ_h transverse momentum (Figures published in Ref. [102]).
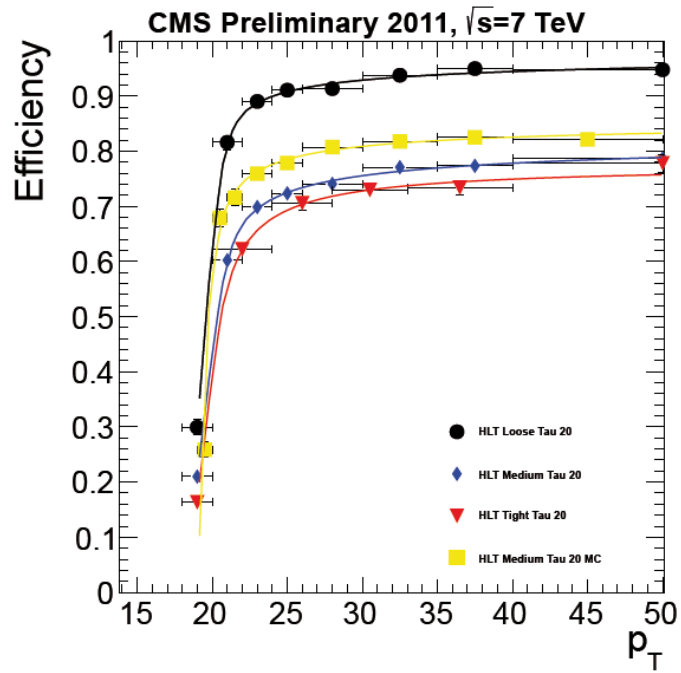
(a)
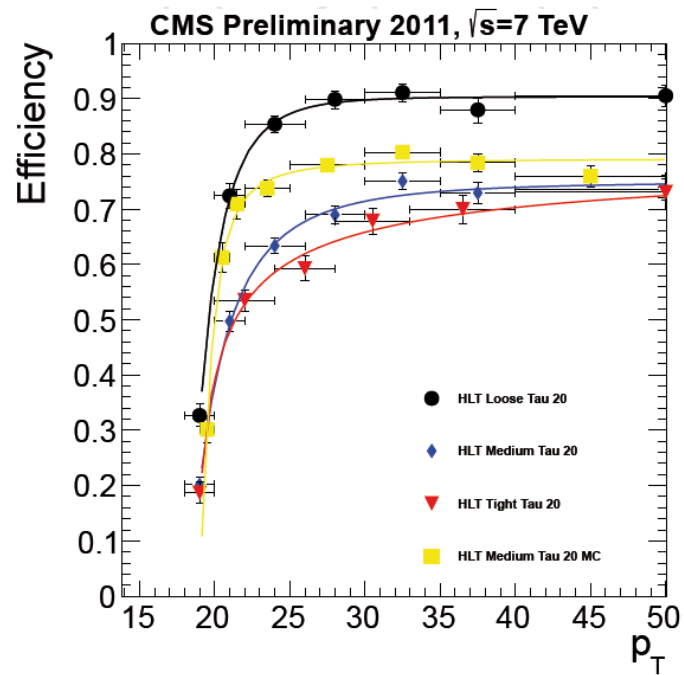
(b)

Figure 7.5:   Trigger turn–on curves for the τ_h part of the cross trigger in the (a) barrel and (b) endcap, as a function of the τ_h transverse momentum (Figures published in Ref. [102]).
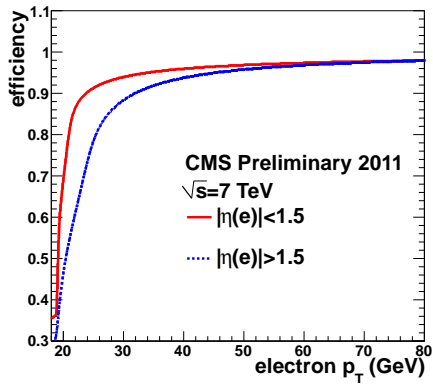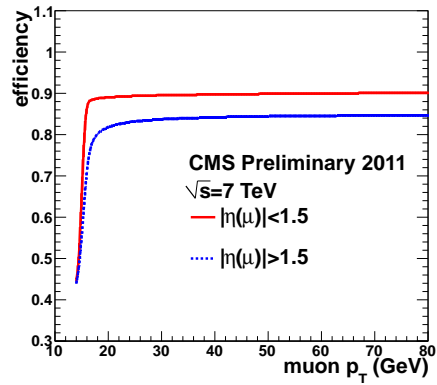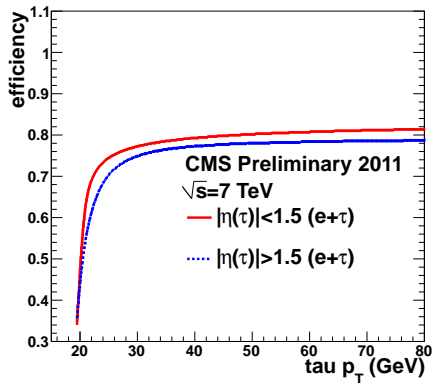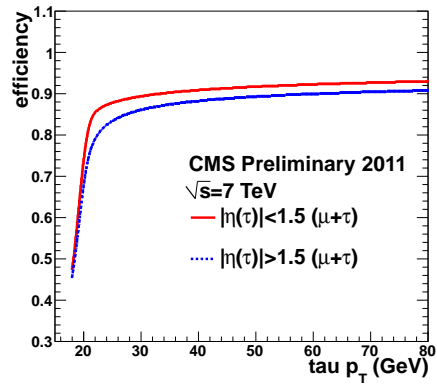
Figure 7.6: Trigger turn–on curves for the (a) electron, (b) muon, and (c,d) tau part of the $\tau_e\tau_h$ and $\tau_\mu\tau_h$ cross–triggers, averaged over the full data set (from Table 7.4).

considered further: a vertex should be identified from a fit with at least 4 degrees of freedom, and the distance between its position from the beamspot should be smaller than 24 cm in z and 2 cm in the transverse coordinate r. From the set of vertices passing this selection, the one with the highest $\sum p_T^2$, the sum of the squares of the transverse momenta of tracks associated to that vertex, is chosen as the production vertex of the signal event.

7.4.2   Muons

The reconstruction of muons is described in Ref. [54]. Two sets of quality criteria, a *loose* and a *tight*, identify genuine muons with increasing purity. The variables used for the identification and the corresponding cut values are detailed in Table 7.5.

The *tight* identification is used to select muon candidates arising from the leptonic decay of the tau lepton. Tight muons are required to be identified by the particle–flow algorithm as described in Section 4.2. Muons reconstructed only in the muon system detector (the so–called *standalone* muons) are rejected because they are typically measured with a poor momentum resolution. The identification efficiency for genuine muons at this stage is extremely high. However, the muon trigger conditions are typically more selective. Additional offline cuts, tighter than the trigger selection, are further imposed (Table 7.5).

The compatibility of the muon candidate with the primary vertex is ensured by requiring that the distance in z between the primary vertex and the point of closest approach of the muon inner track is less than 2 mm. A similar condition is applied to the r coordinate. In reason of the better resolution of the transverse distance, the upper threshold is however tightened to 0.45 mm.

Tight muons are required to have transverse momentum in excess of 17 GeV, the lowest threshold for which the trigger has been fully efficient over the whole data set. The geometrical acceptance is restricted to $|\eta| < 2.1$ to ensure the maximal trigger efficiency.

Muon candidates passing the *loose* identification are selected for the purpose of vetoing $Z \to \mu\mu$ background events, and their identification is kept as loose as possible to maintain the highest rejection power. Loose muons are required to be reconstructed as *global* muons, to have p_T in excess of 15 GeV, $|\eta| < 2.4$, and to be compatible with originating from the primary vertex (in the sense explained above).

Prompt muons are separated from muons originating from heavy quark decays and from hadronic punch–through by means of the isolation variable

I^{PF}, defined as:

$$I^{PF} = \sum \{p_T^{charged}(d_z < 2 \text{ mm})\} + \max \left(\sum \{p_T^{h^0} + p_T^{\gamma}\} - \Delta\beta, 0 \right). \quad (7.1)$$

The sum in Eq. 7.1 is computed over particle–flow particles whose directions are separated from the muon momentum by less than $R = 0.4$ (see Eq. (3.6) for the definition of R), and which pass the following quality criteria:

- charged hadrons, electrons, and muons should be matched to the event vertex within $d_z < 2$ mm and their direction should lie outside of a "veto" cone of radius 10^{-4} around the muon direction;

- neutral hadrons should have $p_T > 0.5$ GeV and point outside of a veto cone of size 0.01 around the muon direction;

- photons should have $p_T > 0.5$ GeV and point outside of a veto cone of size 0.01 around the muon direction.

The exact values of the thresholds and veto size has been optimized to minimize the contribution of the muon footprint to the isolation variable.

In order to make the muon isolation efficiency as much as possible independent from the rate of pile–up interactions, an event–dependent compensation term ($\Delta\beta$) is used to account for the pile–up contribution in the isolation cone, in analogy with what described in Section 5.2.1. The $\Delta\beta$ term is proportional to the p_T sum of charged particles within a maximal distance $R = 0.4$ from the muon direction, associated to a vertex *other* than the primary vertex and passing the same selection criteria as required for the neutral hadrons:

$$\Delta\beta = \alpha \cdot \sum \{p_T^{charged}(d_z > 2 \text{ mm})\}. \quad (7.2)$$

The constant α is set to 0.5, i.e. roughly equal to the ratio between the amount of neutral to charged hadrons stemming from minimum–bias interactions (see e.g. Fig. 4.12). In this way, the $\Delta\beta$ term does relate, on an event–by–event basis, the energy deposit measured from charged pile–up particles (e.g. $\pi^{\pm}$, $K^{\pm}$) to the expected flow of energy arising from neutral pile–up particles (e.g. π^0, K_L^0). For tight (loose) muons, the isolation variable I^{PF} should be less than 10% (30%) of the muon transverse momentum. The efficiency of the isolation cut as a function of the number of reconstructed primary vertices is shown in Fig. 7.7. To highlite the contribution of the $\Delta\beta$ correction, the isolation efficiency for an alternative isolation variable, where the α constant in Eq. 7.2 is set to zero, is shown in the same figure.
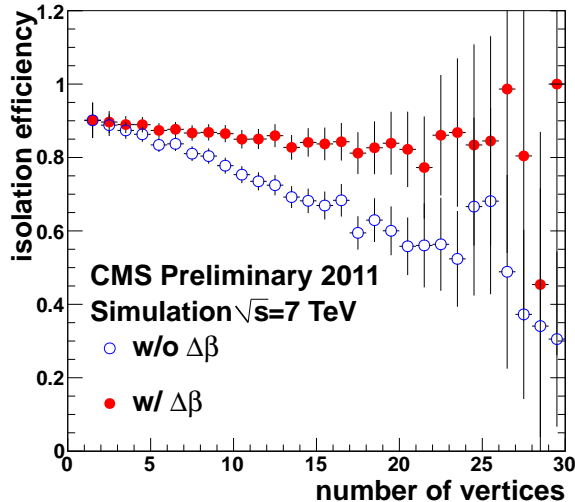
Figure 7.7: Efficiency for muons in a simulated $Z \to \tau\tau$ sample to pass the *tight* isolation cut, computed with (solid markers) or without (empty markers) the $\Delta\beta$ correction, as function of the number of reconstructed primary vertices.

The identification and isolation efficiency for tight–muons has been measured from data using tag–and–probe with $Z \to \mu\mu$ events. A set of p_T and η dependent correction factors to the simulation is derived and used to rescale the Monte Carlo simulation (Table 7.6).

7.4.3 Electrons

The offline reconstruction of electrons in CMS is thoroughly described in Ref. [56], and it has already been summarized in Section 4.2.3.

Electron candidates should be reconstructed both as GSF tracks in the silicon tracker and as energy deposit in ECAL (superclusters). Quality cuts on the GSF track and on the supercluster, as well as on their mutual compatibility, are applied to discriminate genuine electrons from jets. Two sets of identification criteria, a *loose* and a *tight*, select electrons with increasingly higher purity. The complete list of such requirements is summarized in Table 7.7.

The *tight* electron identification starts with a set of rectangular cuts on four discriminating variables: the supercluster dispersion along η ($\sigma_{i\eta i\eta}$), the η and ϕ distance between the supercluster barycenter and the extrapolation of the GSF track from the vertex ($|\Delta\eta_{in}|$ and $|\Delta\phi_{in}|$), and the ratio between

Variable	*Loose*	*Tight*
Algorithm	*global*	*PF–muon & global*
Strip hits	-	≥ 6
Pixel hits	-	≥ 1
Muon chambers with segments	-	≥ 2
Global fit	-	$\chi^2_{dof} < 10$
Hits in muon system	-	≥ 1
Transverse impact parameter	$|d_{xy}| < 0.045$ cm	$|d_{xy}| < 0.045$ cm
Longitudinal impact parameter	$|d_z| < 0.2$ cm	$|d_z| < 0.2$ cm
Transverse momentum	> 15 GeV/c	> 17 GeV/c
Geometrical acceptance	$|\eta| < 2.4$	$|\eta| < 2.1$
I^{PF}	$< 0.30 \cdot p_T^\mu$	$< 0.10 \cdot p_T^\mu$

Table 7.5: Muon identification criteria.

p_T bin (GeV)	Barrel	Endcap
	Identification	
$17 \leq p_T \leq 20$	0.997 ± 0.002	0.986 ± 0.004
$20 < p_T \leq 30$	0.995 ± 0.001	0.986 ± 0.001
$30 < p_T$	1.030 ± 0.002	0.990 ± 0.001
	Isolation	
$17 \leq p_T \leq 20$	0.930 ± 0.008	0.929 ± 0.013
$20 < p_T \leq 30$	0.977 ± 0.002	0.984 ± 0.004
$30 < p_T$	1.010 ± 0.001	0.997 ± 0.001

Table 7.6: Data–to–simulation correction factor for the tight muon identification and isolation efficiency. Errors quoted in the table are statistical only.

the energy measured in HCAL and in ECAL (H/E). The cut values on these variables are meant to reproduce the online selection applied by the HLT filter.

A tighter identification is achieved using a Boosted Decision Tree (BDT). The BDT makes use of up to eighteen discriminating variables and is separately trained for three complementary $|\eta|$ regions. The working point of

163

the BDT is optimized in the context of the $\tau_e \tau_h$ analysis. The cut values for electrons with $|\eta| < 0.8$, $0.8 < |\eta| < 1.479$, and $|\eta| > 1.479$ and reported in Table 7.7.

The tight electron selection is complemented by a conversion rejection cut, which requires i) a low probability for the electron track and any nearby track to originate from a same displaced vertex, ii) no missing hits in any of the pixel or tracker modules crossed by the electron track.

As for muons, the impact parameter of the electron GSF track is required to be compatible with the primary vertex. Finally, tight electrons with a transverse momentum in excess of 20 GeV and pseudorapidity in the range $[-2.1, 2.1]$ are selected. Even though the electron trigger and reconstruction extends up to $|\eta| < 2.4$, the reduced η acceptance still provides better performances. This is because most of the fake electrons originate from mis–identified jets in the endcap region.

A *loose* electron selection is defined for the sake of identifying, and rejecting, $Z \rightarrow ee$ events. In addition to the rectangular cuts on $\sigma_{i\eta i\eta}$, $|\Delta \eta_{in}|$, $|\Delta \phi_{in}|$, and H/E, loose electrons are required to pass the conversion rejection and to be compatible with the primary vertex. The p_T and $|\eta|$ thresholds are relaxed to 15 GeV and 2.4, respectively.

Variable	*Loose* EB (EE)	*Tight* EB (EE)
Cluster shape σ_{inin}	< 0.01 (0.03)	< 0.01 (0.03)
$|\Delta\eta|$	< 0.007 (0.01)	< 0.007 (0.01)
$|\Delta\phi|$	< 0.8 (0.7)	< 0.8 (0.7)
H/E	< 0.15 (−)	< 0.15 (−)
BDT cut	−	$> 0.925, 0.975$ (0.985)
missing tracker hits	< 1	< 1
secondary vertex probability	$< 10^{-6}$	$< 10^{-6}$
Transverse impact parameter	$|d_{xy}| < 0.045$ cm	$|d_{xy}| < 0.045$ cm
Longitudinal impact parameter	$|d_z| < 0.2$ cm	$|d_z| < 0.2$ cm
Transverse momentum	> 15 GeV/c	> 20 GeV/c
Geometrical acceptance	$|\eta| < 2.4$	$|\eta| < 2.1$
I^{PF}	$< 0.30 \cdot p_T^e$	$< 0.10 \cdot p_T^e$

Table 7.7: Electron identification criteria

The electron isolation is computed in the same way as for muons (Eq. 7.1), except for the choice of veto cones, which has been re–optimized for a better

removal of the electron footprint. Particles contributing to the I^{PF} variable are required to pass the following selection criteria:

- charged hadrons, electrons, and muons should be matched to the event vertex within $d_z < 2$ mm, and their direction should lie outside of a "veto" cone of radius 0.01 (0.015) around the electron momentum, if the electron is within the barrel (endcap) acceptance;

- no selection is applied to neutral hadrons;

- photons are required to be outside a veto cone of radius 0.08 around the electron direction.

The identification and isolation efficiency for tight electrons has been measured on data using tag-and-probe with $Z \to ee$ events. A data–to–simulation correction factor is derived in several p_T and $|\eta|$ bins, and used to rescale the Monte Carlo simulation (Table 7.8).

p_T bin (GeV)	Barrel	Endcap
	Identification	
$20 \leq p_T \leq 30$	0.955 ± 0.002	0.938 ± 0.007
$30 < p_T$	1.044 ± 0.001	0.977 ± 0.001
	Isolation	
$20 \leq p_T \leq 30$	0.980 ± 0.003	0.967 ± 0.006
$30 < p_T$	0.984 ± 0.001	0.989 ± 0.001

Table 7.8: Data–to–simulation correction factors for the tight electron identification and isolation efficiency.

7.4.4 Taus

Hadronic taus are reconstructed by the HPS algorithm, extensively described in Section 5.2. A set of discriminators is applied to the reconstructed τ_h candidates in order to separate genuine tau decays from quark/gluon initiated jets and from electrons or muons.

The cut–based isolation discriminators described in Section 5.2 have been here replaced by a more performing multivariate classifier, developed in the context of the $H \to \tau\tau$ analysis and first documented in Ref. [95]. The discrimination is based on the output of a Boosted Decision Tree based on

the multiplicity and p_T sum of particles within solid rings around the tau candidate. The BDT efficiency as a function of the tau lepton p_T is shown in Fig. 7.8 for genuine tau decays in a Monte Carlo $Z \to \tau\tau$ sample. The BDT discriminator is seen to achieve a larger signal efficiency (by about 10%) than the $\Delta\beta$ discriminator (Section 5.2.1), for the same fake rate.
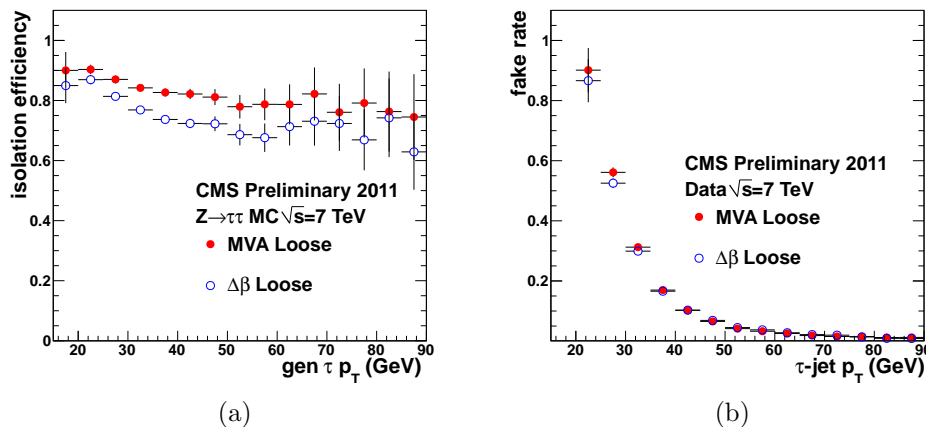
Figure 7.8: a) Isolation efficiency of the MVA and $\Delta\beta$ discriminator for hadronically–decaying taus in a Monte Carlo $Z \to \tau\tau$ sample as a function of the tau lepton p_T; b) fake rate of the MVA and $\Delta\beta$ discriminator as a function of the seeding jet p_T for jet fake taus reconstructed in a QCD enriched data sample.

The working point for the anti–electron and anti–muon discriminators (Section 5.4) differ between the $\tau_e\tau_h$ and $\tau_\mu\tau_h$ channels, depending on whether the dominant background contributions arises from $Z \to ee$ ($\tau_e\tau_h$ channel) or from $Z \to \mu\mu$ ($\tau_\mu\tau_h$ channel).

The full set of kinematic selections and identification cuts for the hadronic taus used in the $\tau_e\tau_h$ and $\tau_\mu\tau_h$ channels are reported in Table 7.9.

7.4.5 Jets

Jets are reconstructed by the anti–k_T algorithm [68] with distance parameter $R = 0.5$, using as input the list of particles reconstructed by the particle–flow algorithm (Section 4.3).

By definition, the raw jet momentum is equal to the sum of the momenta of all particles in the jet. A calibration of the raw momentum is performed as a function of the raw jet kinematic to match, on average, the initiating parton momentum. Three levels of corrections are sequentially applied to the raw

Variable	Channel	
	$\tau_e\tau_h$	$\tau_\mu\tau_h$
Identification	decay mode rec.	decay mode rec.
Isolation	loose	loose
anti–e discriminator	MVA–tight	loose
anti–μ discriminator	loose	tight
Longitudinal impact parameter	$|d_z| < 0.2$ cm	$|d_{xy}| < 0.2$ cm
p_T	> 20 GeV	> 20 GeV
$|\eta|$	< 2.1	< 2.1

Table 7.9: Tau identification criteria. The various discriminators are documented in Section 5.2

jet momentum to account for spurious particle contamination and to correct for the response, non–linearity, and inhomogeneity of the calorimeters [62].

The contribution to the jet momentum stemming from pile–up interactions and from hadrons produced in the underlying–event is estimated using the FastJet technique [104]. First, the transverse energy density (ρ) of the extra hadronic activity is determined by the median energy density obtained from all particle–flow jets reconstructed in the event with p_T in excess of 5 GeV. An amount equal to ρ times the jet area [105] is then subtracted from the jet transverse momentum.

A set of quality cuts based on the particle content of the jet is applied in order to separate real jets from detector noise (Table 7.10).

Variable	Cut value	
	$|\eta| < 2.4$	$|\eta| > 2.4$
no. of constituents	> 1	> 1
neutral hadron energy fraction	< 0.99	< 0.99
gamma energy fraction	< 0.99	< 0.99
no. of charged constituents	> 0	–
charged energy fraction	> 0.0	–
electron energy fraction	< 0.99	–

Table 7.10: Jet quality cuts used to discriminate real jets from detector noise.

In events with a large number of pile–up interactions, fake jets may arise from the accidental clustering of many neighboring particles, or from the superimposition of soft jets from different production vertices. In order to separate prompt jets from pile–up jets, a multivariate discriminator based on the output of a BDT is applied. The BDT exploits a variety of input

variables including track–related information (for jets within the tracker acceptance) and shower–shape variables. A loose working point of the pile–up jet discriminator is chosen. The corresponding efficiency has been measured in data as a function using a tag–and–probe technique on $Z \to \mu\mu$+jets events, where the tag is the hadronic recoil to the di–muon system and the probe is the recoiling jet (Fig. 7.9). The data–to–simulation correction factors are well compatible with unity everywhere except in the forward region, where they depart from one by up to 10%. Instead of applying a jet–by–jet correction, a systematic uncertainty based on this study is assigned to Monte Carlo event yields in categories defined by jet counting.

Jets passing the quality and pile–up cuts are required to have a corrected transverse momentum in excess of 30 GeV, $|\eta| < 5.0$, and to be separated from the identified electron/muon and τ_h candidates by $R > 0.3$.

Jets originating from the fragmentation of b/c quark are separated from light–quark or gluon initiated jets by dedicated tagging algorithms [107]. For jets within the geometric acceptance of the silicon detectors, the medium (M) working point of the *combined secondary vertex* (CSV) discriminator is used. The efficiency of this working point is shown in Fig. 7.11 as a function of the jet p_T. All jets passing the CSVM discriminator and with p_T in excess of 20 GeV are tagged as b–jets.

7.4.6   Missing transverse energy

The missing transverse energy ($\vec{E}_T^{miss}$) is defined as the negative transverse momentum sum of all particles reconstructed by the particle–flow algorithm (Eq. (4.5)).

Because of an imperfect modeling of the detector response and of the hadronic activity (e.g. pile–up), the distribution of the missing energy defined in Eq. (4.5) is not expected to be well reproduced by the simulation.

An event–by–event correction of Eq. (4.5) in simulated events is derived from a control sample of $Z \to \mu\mu$ events recorded in the same data period. First, the hadronic recoil $\vec{u}$ is defined as the sum of the momenta of all visible particles recoiling against the di–muon system:

$$\{\vec{p_T}^{\mu\,1} + \vec{p_T}^{\mu\,2}\} + \vec{u} + \vec{E}_T^{miss} = 0 \tag{7.3}$$

The recoil $\vec{u}$ is then projected onto the direction parallel and perpendicular to the transverse direction of the di–muon system ($\hat{p}_T^Z$):

$$\begin{cases} u_{\parallel} = \vec{u} \cdot \hat{p}_T^Z \\ u_{\perp} = |\vec{u} - u_{\parallel}\hat{p}_T^Z| \end{cases} \tag{7.4}$$
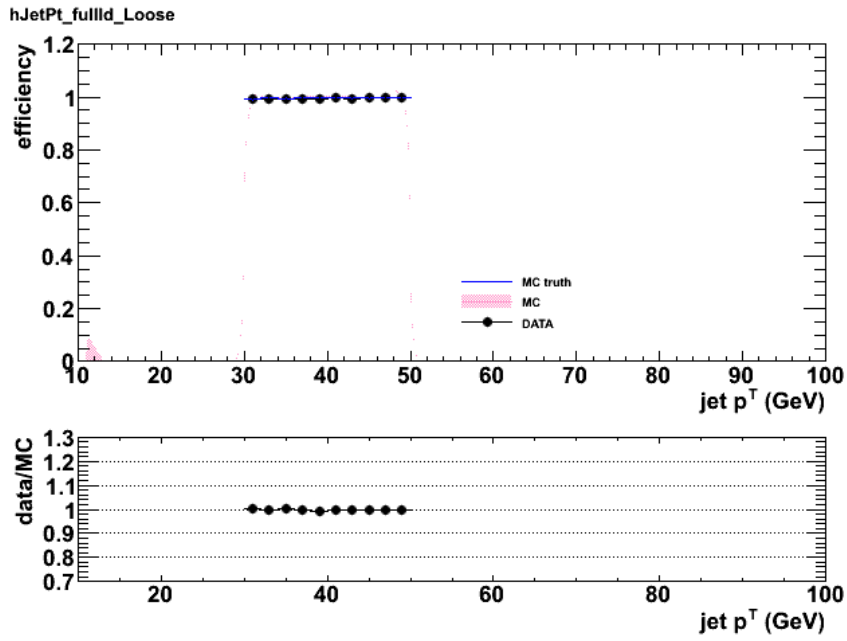
(a)
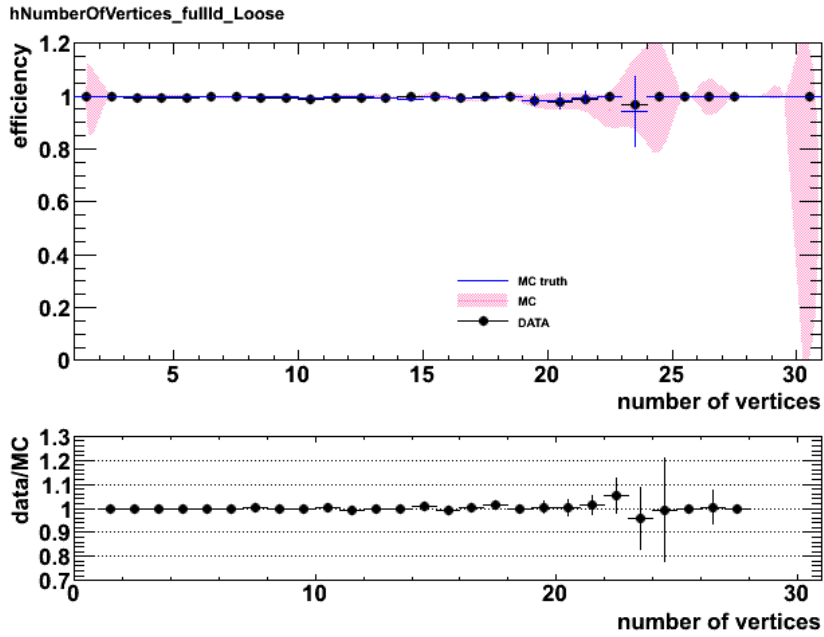
(b)

Figure 7.9: Efficiency of the loose pile–up jet-ID working point for jets with $30 < p_T < 50$ GeV within the tracker acceptance. The efficiency is shown as a function of the (a) jet p_T and (b) the number of primary vertices (from Ref. [106]).
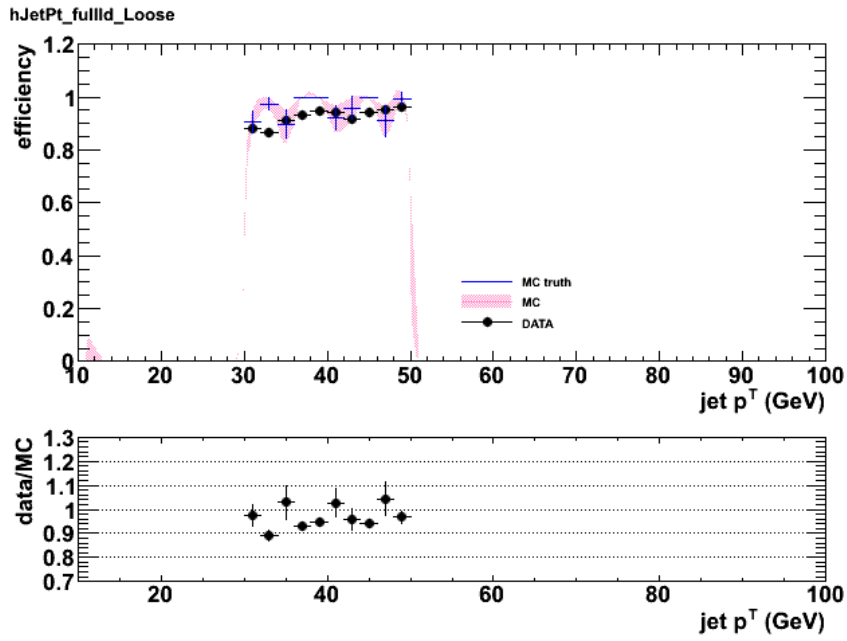
(a)
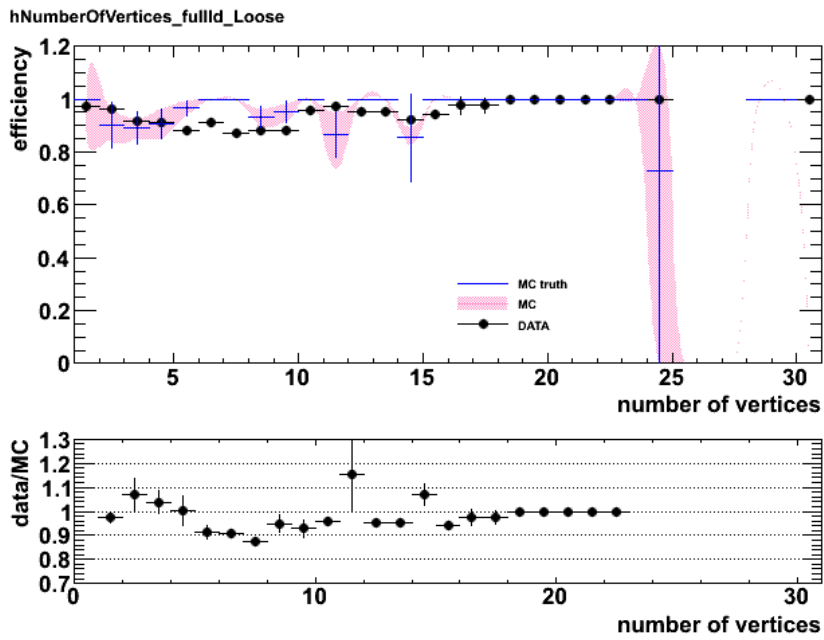
(b)

Figure 7.10: Efficiency of the loose pile–up jet-ID working point for jets with $30 < p_T < 50$ GeV within the HF acceptance. The efficiency is shown as a function of the (a) jet p_T and (b) the number of primary vertices (from Ref. [106]).
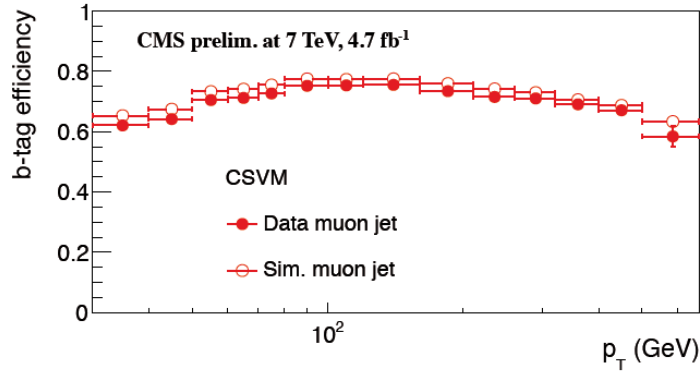
Figure 7.11: Efficiency of the CSVM working point used for b–tagging (from Ref. [109]).

The response and resolution of $u_\parallel$ and $u_\perp$ is parametrized, in data and in $Z \to \mu\mu$ Monte Carlo, as a function of the di–muon p_T and in bins of jet multiplicity (Fig. 7.12).
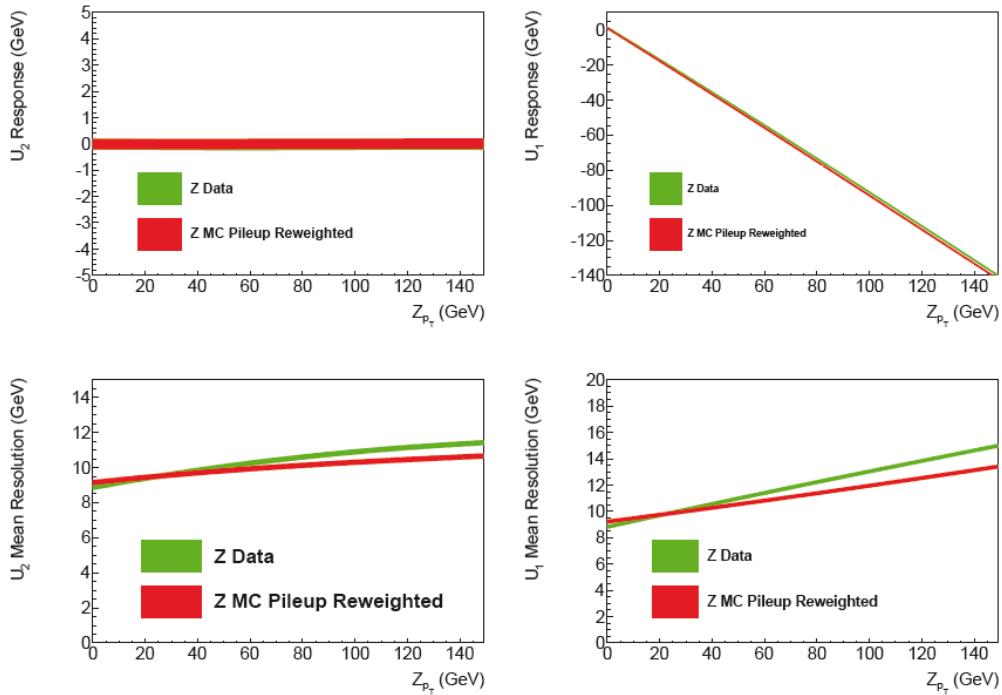
Figure 7.12: Fits to the $u_\parallel$ and $u_\perp$ response and resolution for an inclusive $Z \to \mu\mu$ sample. Figures published in Ref. [102].

A parametric data–to–simulation correction is derived and used to rescale the response and smear the resolution of the recoil in simulated events:

$$\vec{u} \rightarrow \vec{u}_{corr} \tag{7.5}$$

A recoil–corrected missing energy ($\vec{E}_{T\ corr}^{miss}$) is then obtained by inverting Eq. 7.3:

$$\vec{E}_{T\ corr}^{miss} = -\{\vec{p_T}^{\mu\,1} + \vec{p_T}^{\mu\,2}\} - \vec{u}_{corr} \tag{7.6}$$

This procedure can be applied in a straightforward way to all Drell–Yan and $H \rightarrow \tau\tau$ Monte Carlo samples, where the visible momenta of the leptons are not considered as part of the recoil, and the $\vec{\xi}$ direction is provided by the transverse momentum of the generated Z or H. For $W \rightarrow \ell\nu$, the same procedure is applied, and only the reconstructed momentum of the visible lepton ℓ is subtracted from the recoil (Fig. 7.13). No corrections are applied to the $t\bar{t}$ or di–boson samples.

7.4.7 Di–tau mass

The di–tau mass is reconstructed by the SVfit algorithm (Section 6.6). In the SVfit likelihood function Eq. (6.37), unpolarized tau decays are assumed. The decay widths for τ_ℓ and τ_h are parametrized as in Eq. (6.28) and (6.33), respectively. The mean and RMS of the SVfit mass distribution in simulated $Z \rightarrow \tau\tau$ and $H \rightarrow \tau\tau$ samples are reported in Fig. 7.14(a) ($\tau_\mu\tau_h$ channel). The SVfit mass distribution for $Z \rightarrow \tau\tau$ and for $H(125) \rightarrow \tau\tau$ events are compared in Fig. 7.14(b).
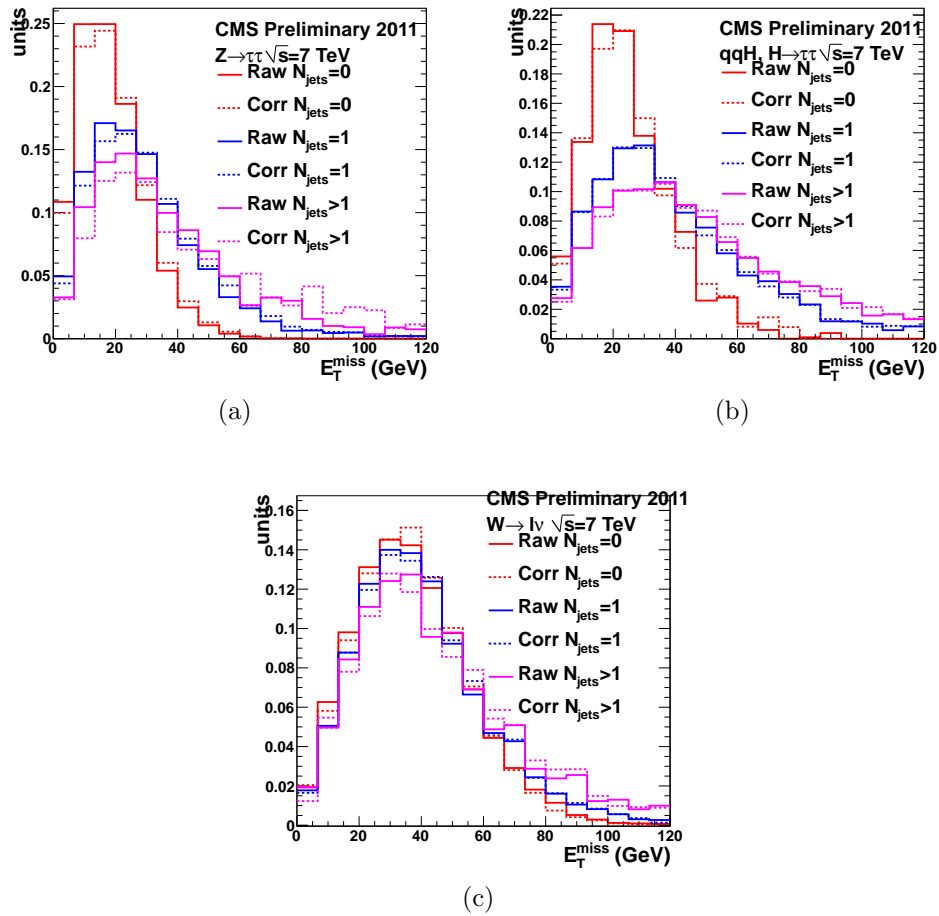
Figure 7.13: Comparison between the missing transverse energy in (a) $Z \to \tau\tau$, (b) VBF $H \to \tau\tau$, and (c) $W \to \ell\nu$ before (solid line) and after (dashed line) recoil corrections applied. The distributions are shown in three inclusive bins of jet multiplicity: $N^{\mathrm{jet}} = 0$, $N^{\mathrm{jet}} = 1$, and $N^{\mathrm{jet}} \geq 2$

(a)	(b)
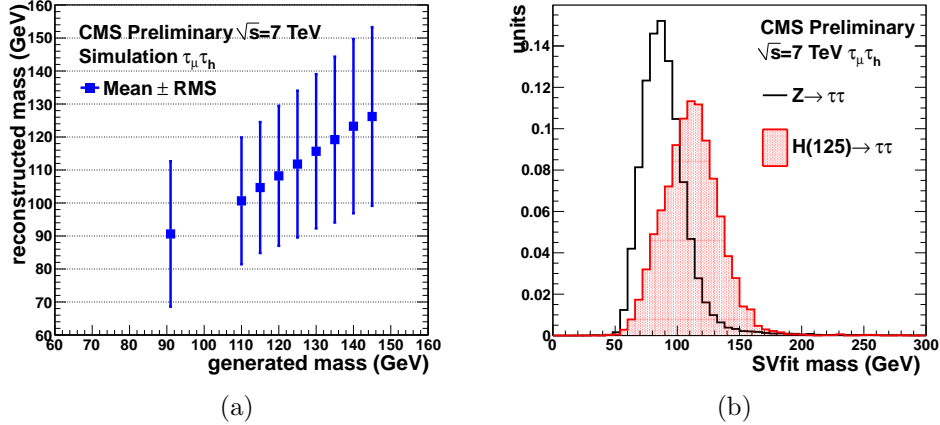
Figure 7.14: a) Mean and RMS of the SVfit mass distribution as a function of the generated di–tau mass; b) comparsion between the SVfit mass templates for $Z \to \tau\tau$ and $H \to \tau\tau$ ($M_H = 125$ GeV).

7.5 Event selection

An inclusive di–tau selection collects signal candidates independently of anything else present in the event. The request for a pair of leptonically (τ_ℓ, $\ell = e, \mu$) and semi–leptonically decaying taus (τ_h), passing the tight quality criteria described in Section 7.4, is complemented by topological and event–wise cuts that are specifically devised to suppress the reducible backgrounds.

7.5.1 $\tau_\mu \tau_h$ channel

Signal events in the $\tau_\mu \tau_h$ channel are selected by requiring the following criteria:

- the event must fire one of the $\tau_\mu \tau_h$ cross–trigger paths listed in Table 7.4;

- at least one primary vertex passing the quality cuts illustrated in Section 7.4.1;

- at least one tight muon (τ_μ) as defined in Section 7.4.2, matched within $R < 0.3$ to a trigger object passing the last muon–specific filter in the HLT path;

- at least one hadronic tau (τ_h) as defined in Section 7.4.4, matched within $R < 0.3$ to a trigger object passing the last tau–specific filter in the HLT path;

- of all the $\tau_\mu \tau_h$ pairs satisfying the above selections, the one with the highest scalar sum of muon and tau p_T is chosen as the signal candidate;

- the τ_μ and τ_h must have opposite charge;

- the transverse mass $M_T^{\mu\nu}$ of the τ_μ plus missing transverse energy in the event, defined below, is required to satisfy $M_T^{\mu\nu} < 40$ GeV. For simulated events, the recoil–corrected missing energy is used;

- no additional loose muons should be found in the event.

7.5.2 $\tau_e \tau_h$ channel

Signal events in the $\tau_e \tau_h$ channel are selected by requiring the following criteria:

- the event must fire one of the $\tau_e \tau_h$ cross–trigger paths listed in Table 7.4;

- at least one primary vertex passing the quality cuts illustrated in Section 7.4.1;

- at least one tight electron (τ_e) as defined in Section 7.4.3, matched within $R < 0.3$ to a trigger object passing the last electron–specific filter in the HLT path;

- at least one hadronic tau (τ_h) as defined in Section 7.4.4, matched within $R < 0.3$ to a trigger object passing the last tau–specific filter in the HLT path;

- of all the $\tau_e \tau_h$ pairs satisfying the above selections, the one with the highest scalar sum of muon and tau p_T is chosen as the signal candidate;

- the τ_e and τ_h must have opposite charge;

- the transverse mass $M_T^{e\nu}$ of the electron plus missing transverse energy in the event, defined below, is required to satisfy $M_T^{e\nu} < 40$ GeV. For simulated events, the recoil–corrected missing energy is used;

- no additional loose electrons should be found in the event.

The transverse mass is defined for the final state with a muon ($\ell = \mu$) or and electron ($\ell = e$) as

$$M_T^{\ell\nu} = \sqrt{\left(p_T^\ell + E_T^{miss}\right)^2 - \left(\left(p_x^\ell + E_x^{miss}\right)^2 + \left(p_y^\ell + E_y^{miss}\right)^2\right)}, \qquad (7.7)$$

7.6 Event categorization

Events passing the inclusive selection criteria described in Section 7.5.1 and 7.5.2 are further classified into mutually exclusive categories. Three driving principles have inspired the definition of the categories:

1. exploit handles that distinguish, on a statistical basis, the signal from the background (e.g. jet kinematics);

2. tune the kinematic cuts on the objects to maximize the signal–to–background ratio (e.g. p_T or E_T^{miss} thresholds);

3. separate events with high and poor di–tau mass resolution (e.g. by asking for a boost of the di–tau system).

The best expected exclusion limit on the SM Higgs boson cross–section has been used to optimize the exact category definition.

A total of six categories are used to classify the events. Five of them are used for the statistical interpretation of the results. One category is specifically designed for a resonance decaying to taus and produced in association with b–quarks. Since the SM does not predict high rate for such a process, this category is dropped from the final SM interpretation. The remaining five categories are optimized for the two main production mechanisms of the SM Higgs boson: GGF and VBF.

The higher rate of gluon radiation expected from the gluon–gluon fusion mechanism as compared to Z production is exploited by separating events with and without jets.

One category enhances the VBF production mode by tagging final states with a pair of jets in a kinematic configuration that is typical of the VBF reaction (Section 2.4). To better exploit the full event information, a multivariate approach is used to select VBF–like events [95]. A Boosted Decision Tree is trained to separate $H \to \tau\tau$ events produced via VBF (signal) from $Z \to \tau\tau$+jets (background). The MadGraph Drell–Yan sample does not contain the electroweak Z production diagrams, which behaves pretty much like the signal, and is therefore used to model the kinematics of the reducible QCD Drell–Yan production. Before training the BDT, signal and background events are pre–selected by requiring the presence of two jets with p_T in excess of 30 GeV (*tagging jets*) and no additional jet in between (*central jet veto*, or CJV).

The BDT is trained on the following eight discriminating variables.

- M_{jj}: the invariant mass of the two tagging jets;

- $\Delta\eta_{jj}$: the pseudorapidity separation between the two tagging jets, without sign;

- $\Delta\phi_{jj}$: the azimuthal separation between the two tagging jets, normalized between 0 and π;

- p_T^H: the magnitude of the vector obtained by summing the di–tau visible momentum and $\vec{E}_T^{miss}$;

- p_T^{jj}: the magnitude of the di–jet momentum;

- $\Delta\phi_{Hjj}$: the azimuthal separation between the di–jet momentum and the vector obtained by summing the di–tau visible momentum and $\vec{E}_T^{miss}$, normalized between 0 and π;

- $p_T^{\tau\tau}$: the magnitude of the di–tau visible momentum;

- $\Delta\eta_{min}$: the pseudorapidity separation between the di–tau visible momentum and the jet that is closest in η, without sign.

The signal and background distributions for the input variable are shown in Fig. 7.15. A working point corresponding to a lower cut on the BDT output at 0.50 is chosen to identify VBF–like topologies. It achieves a signal efficiency of about 53% with a 3.5% fake rate, as shown by a red marker in Fig. 7.17. For comparison, the signal and background efficiency for the cut–based working point documented in Ref. [76] is shown by a blue marker.

The event categories used in the analysis are defined as follows.

- **VBF**
  Events containing at least two jets with $p_T > 30$ GeV and $|\eta| < 5.0$, and for which the output of the VBF MVA is greater than 0.50. If a third jet with $p_T > 30$ GeV is found within the two tagging jets, the event is vetoed (CJV).

- **Boosted**
  Events containing at least one jet with $p_T > 30$ GeV and $|\eta| < 5.0$, and no b–tagged jet with p_T in excess of 20 GeV. Events in the *Boosted* category are required to fail the conditions to enter the *VBF* one. This category is further split into two complementary bins of the τ_h transverse momentum ($p_T^{\tau_h}$):

$$\text{Boosted } \downarrow: \ 20 \leq p_T^{\tau_h} \leq 40 \text{ GeV} \quad \text{Boosted } \uparrow: \ p_T^{\tau_h} > 40 \text{ GeV}$$
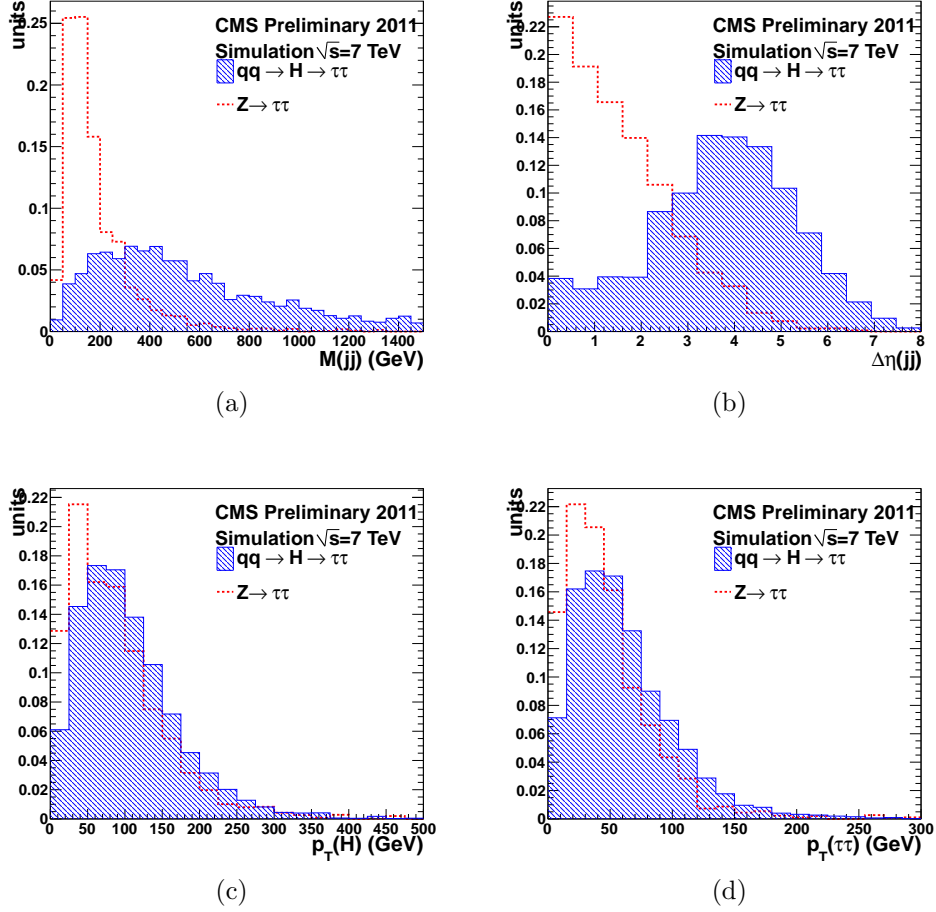
Figure 7.15: Distribution of the input variables of the VBF BDT, for signal (filled histogram) and background (hollow histogram).

In the $\tau_e \tau_h$ channel, an additional lower cut on the missing transverse enery is applied:

$$E_T^{miss} > 30 \text{ GeV}.$$

This cut helps reducing all backgrounds with instrumental missing energy ($Z \to ee$, QCD), at the price of sacrificing a large fraction of the signal ($\approx 80\%$). The exact cut value has been optimized to provide the best exclusion limits, resulting in a substantial improvement of the performances.

- b-**tag**
  Events containing at most one jet with $p_T > 30$ GeV and $|\eta| < 5.0$, at least one b–tagged jet with p_T in excess of 20 GeV and not in the *VBF*.
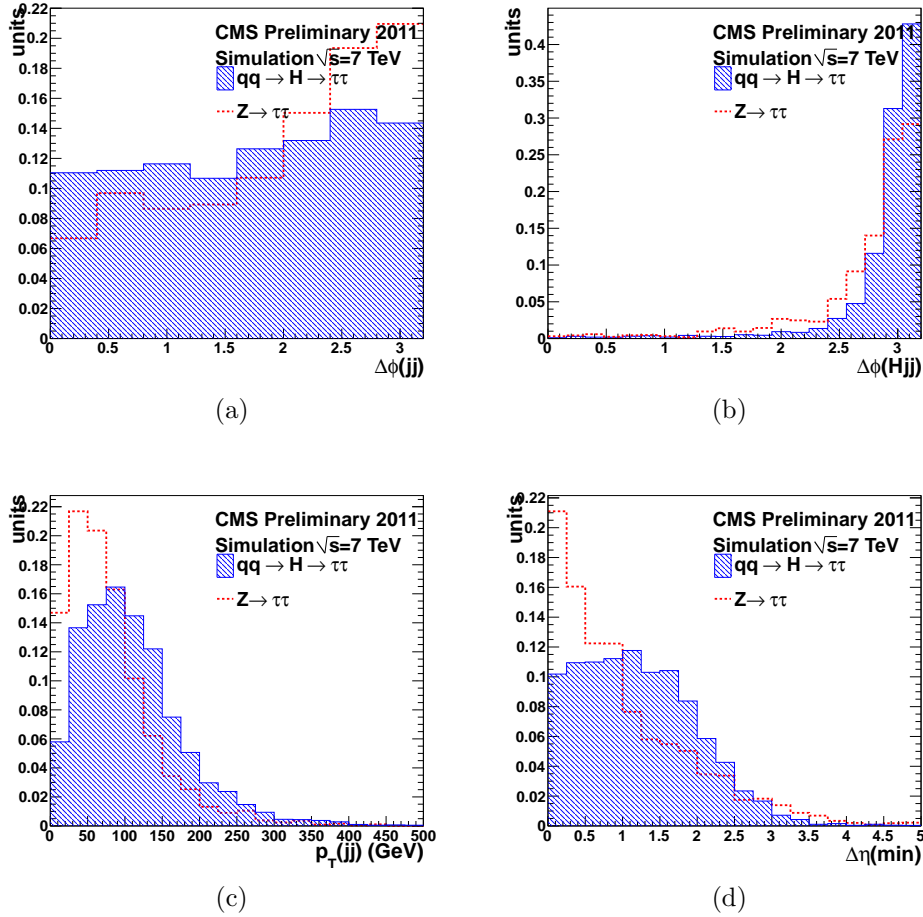
Figure 7.16: Distribution of the input variables of the VBF BDT, for signal (filled histogram) and background (hollow histogram).

- **0−*jet***

  Events that don't make it neither in the *VBF*, nor in the *Boosted*, nor in the *b-tag* category. This category is further split into a low and high $p_T^{\tau_h}$ bin, and complemented by the $E_T^{miss} > 30$ GeV cut for the $\tau_e\tau_h$ channel.
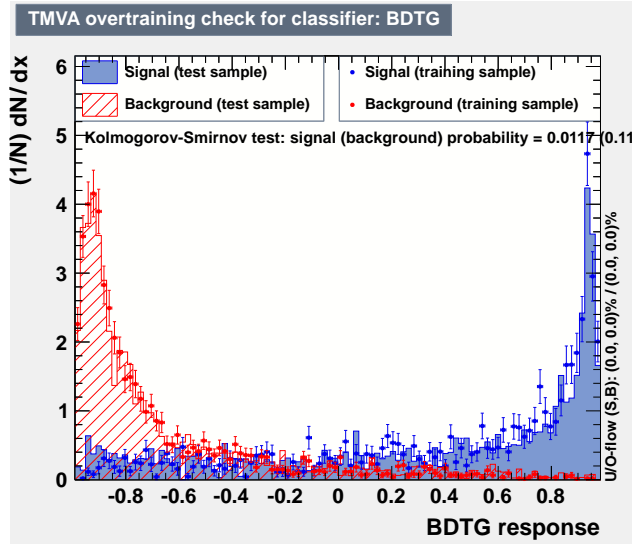
(a)
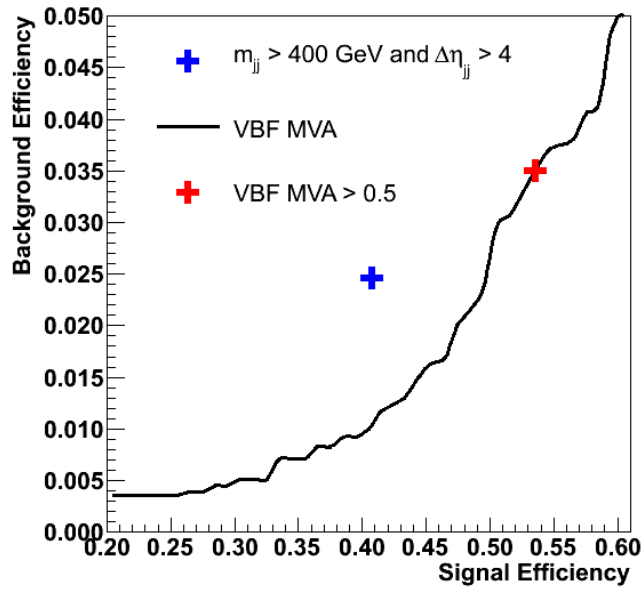
(b)

Figure 7.17: a) The output of the BDT used for the *VBF* classification of background (red) and signal (blue); b) the ROC curve for the same BDT. Figures published in Ref. [95].

7.7 Background evaluation

7.7.1 $Z/\gamma^* \to \tau\tau$

The efficiency and acceptance for $Z/\gamma^* \to \tau\tau$, after the inclusive selection, is derived from the Monte Carlo simulated Drell–Yan sample, after applying the complete set of data–to–simulation corrections (pile–up, trigger, identification, and isolation efficiency scale factors). The sample is then normalized to the number of di–muon events counted in the same data period. A scale factor of 0.94 ± 0.03 is observed by comparing the measured number of di–muon events with the Monte Carlo prediction normalized to the theory cross–section and luminosity.

The contribution of the $Z/\gamma^* \to \tau\tau$ background into each analysis category is estimated by multiplying the inclusive yield by the efficiency to pass the category selections. The corresponding "extrapolation factors" are measured on a sample of di–muon events, where the muons are replaced with generated taus (*embedded sample*): the muon footprint is removed from the event and a tau lepton with the same momentum as for the replaced muon is generated and decayed in flight. To remove systematic biases, the embedded samples need to be corrected as follows.

- **Generation**
  In order to maximize the statistical power of the samples, the visible decay products of the generated tau leptons are required to have transverse momenta close to the kinematical threshold used in the analysis. This is achieved by keeping decaying the simulated tau leptons until a decay with visible momentum above the threshold is obtained. Since the probability to pass the thresholds depends on the original muon momentum, the kinematic of the resulting $Z \to \tau\tau$ sample is distorted. To remove the bias, every event is reweighted by its probability to pass the preselection p_T cut.

- **Trigger**
  The $\tau_\ell \tau_h$ trigger used for the online selection of signal events modulates the p_T and η spectra of the τ_ℓ and τ_h from $Z \to \tau\tau$ production in a significant manner. The events that pass the embedding workflow are selected by di–muon triggers. To emulate the analysis trigger, the turn–on curves of Fig. 7.6 are applied as an event weight.

- **Muon efficiency**
  The efficiency for muons in data to be reconstructed and identified must be unfolded to remove detector biases in the kinematic of the simulated taus.

The extrapolation factors, obtained after applying all the corrections described above, are reported in Table 7.11. For the 0–jet and $Boosted$ category, the efficiency in each $p_T^{\tau_h}$ bin is computed with respect to the inclusive yield in that bin, thus factorizing out the effect of the $p_T^{\tau_h}$ cut.

Category	$\tau_e \tau_h$ Channel	$\tau_\mu \tau_h$ Channel
0–$jet \downarrow$	$(8.04 \pm 0.15) \cdot 10^{-2}$ (1.09)	$(8.48 \pm 0.01) \cdot 10^{-1}$ (1.00)
0–$jet \uparrow$	$(1.62 \pm 0.04) \cdot 10^{-1}$ (1.09)	$(6.90 \pm 0.03) \cdot 10^{-1}$ (1.01)
$Boosted \downarrow$	$(6.38 \pm 0.13) \cdot 10^{-2}$ (0.93)	$(1.40 \pm 0.01) \cdot 10^{-1}$ (0.98)
$Boosted \uparrow$	$(1.25 \pm 0.04) \cdot 10^{-1}$ (0.96)	$(2.89 \pm 0.03) \cdot 10^{-1}$ (0.96)
VBF	$(2.2 \pm 0.2) \cdot 10^{-3}$ (0.99)	$(1.6 \pm 0.1) \cdot 10^{-3}$ (1.07)

Table 7.11: Extrapolation factors from the inclusive to the analysis categories, as measured in the embedded samples. For comparison, the ratios between the extrapolation factor measured in the embedded sample and in the MadGraph Monte Carlo simulation are shown in parentheses.

Mass templates for the $Z \to \tau\tau$ background are finally obtained from the embedded samples.

7.7.2 $Z/\gamma^* \to \ell\ell$, $\ell = e, \mu$

The normalization of the $Z/\gamma^* \to \ell\ell$, $\ell = e, \mu$ background, where the hadronically–decaying tau is faked either by a lepton or by a jet, is obtained from the Monte Carlo simulation. The uncertainty on the $\ell \to \tau_h$ and jet $\to \tau_h$ fake rate, measured in independent control samples, is assigned as a systematic error.

The embedded–to–MadGraph scale factors (Table 7.11), which correct for jet mismodeling in the simulation, are used to correct the event yields in each category.

In the VBF category, the available Monte Carlo statistics is too small to get a smooth mass template and precise prediction of the normalization. For this specific category, the extrapolation factor is measured using events with reverted second–lepton veto and a relaxed cut on the discriminator against leptons. It has been checked on the simulation that this sideband provides unbiased estimation of the efficiency for $Z/\gamma^* \to \ell\ell$ events passing the full signal selection to fall into categories of jet multiplicity up to $N_{jets} \geq 2$. These factors are also significantly different from those measured using the embedded samples, since the request for a $\tau_\ell \tau_h$ pair above p_T thresholds introduces a significant bias in the jet content.

7.7.3 Di–boson

The di–boson background is small and is directly taken from Monte Carlo normalized to the cross–section measured by CMS [101].

7.7.4 W+jets and $t\bar{t}$

The W+jets production, where the W decays to either an electron/muon or to a leptonically–decaying tau, and one of the jets fakes the hadronic tau, represents, for every category, a major background. In addition to the tau isolation, the main handle to reduce its contribution comes from the $M_T^{\ell\nu}$ cut, which is $\approx 20\%$ efficient for W+jets events passing all other selections, compared to a $\approx 85\%$ efficiency for $H \to \tau\tau$. The W+jets yield depends on the jet $\to \tau_h$ fake rate, which is not expected to be well modeled by the simulation. Indeed, correction factors to the fake rate expected from simulation as large as 20% have been measured from dedicated studies in sidebands. The normalization of this background is therefore derived from data.

For each category, control regions dominated by W + jets (W–sideband) are selected by requiring $M_T^{\ell\nu} > 70$ GeV. Specifically to the *VBF* category, the requirement $M_T^{\ell\nu} < 120$ GeV is also applied to reduce the non–W contamination in the high $M_T^{\ell\nu}$ tails. This selection can effectively isolate sidebands that are 80%–90% pure, depending on the category. The second largest component of the sidebands is $t\bar{t}$, where at least one of the W from the top quark decay goes into electron/muon, thus giving rise to large transverse mass. Since the reconstructed τ_h in $t\bar{t}$ events comes more often from a mis–identified jet than from a genuine tau (the fraction of real taus is estimated from Monte Carlo to be about 40%), the $t\bar{t}$ yield in the sidebands is calibrated from control regions enriched in real $t\bar{t}$ events. These control region ($t\bar{t}$–sideband) are obtained by requiring a number of b–tagged jets in addition to the $M_T^{\ell\nu} > 70$ GeV cut. At least two b–tagged jets are required in the 0–jet and *Boosted* category. In the *VBF* category, the selection is relaxed to one to increase the statistics. These sidebands are more than 95% pure in $t\bar{t}$, the remaining backgrounds being estimated from Monte Carlo. The simulation is then used to extrapolate the event yield measured in the $t\bar{t}$–sideband into the W–sideband. A systematic uncertainty is assigned based on the limited statistics of the sideband and from the data–to–simulation difference on the b–tag efficiency [108], which is fully taken as a systematic. The $t\bar{t}$–sideband are also used to derive data–to–simulation scale factors that are applied to the $t\bar{t}$ yield in the signal region.

Minor contribution to the W–sideband come from Drell–Yan to $\ell\ell$, where

one lepton is lost and gives rise to a substantial E_T^{miss}, and di–boson production. They are estimated from Monte Carlo.

Multi–jet events have typically small E_T^{miss} and their contribution to the sidebands, estimated using the fake rate method described later–on, is found to be small.

The MadGraph Monte Carlo sample, corrected for all data–to–simulation discrepancies, is used to derive the extrapolation factors from the high–$M_T^{\ell\nu}$ sideband to the signal region:

$$r_W = \frac{P\{M_T^{\ell\nu} > 70\}}{P\{M_T^{\ell\nu} < 40\}} \tag{7.8}$$

In the *VBF* category, the available Monte Carlo statistics is too poor to extract a precise estimation of r_W. An exclusive $W+3$ jets sample is used instead. It has been verified that the r_W factor predicted by the exclusive and by the inclusive W sample agree within errors in a control category where two jets, without VBF cuts, are required.

The mass templates for $W+$jets and $t\bar{t}$ is obtained from simulation. To check the goodness of the modeling, the observed di–tau mass distribution in the W and $t\bar{t}$ sidebands is compared to the Monte Carlo templates (Appendix B). The agreement is in general good. Two alternative templates, obtained by vertically morphing the nominal shape corresponding to an energy scale variation on the fake tau by 3%, are compared.

In the 0–*jet* and *Boosted* category of the $\tau_e\tau_h$ channel, the W shape is obtained from Monte Carlo events with relaxed tau isolation (output of the tau isolation BDT larger than 0.0). Relaxing the tau isolation enhances the Monte Carlo statistics by a factor ~ 3. The template is compatible, within statistical errors, to the one obtained with full tau isolation.

In the *VBF* category, the mass template is obtained from the $W+3$ jets sample after relaxing the tau isolation and the VBF selection (output of the VBF BDT greater than -0.30). It was checked that the templates do not change significantly as a result of the looser cut. In Fig. 7.18(a), the template obtained from two–jets events passing the loose or full tau isolation cut are compared. In Fig. 7.18(b), the mass templates obtained from events with loose tau isolation passing the relaxed or full VBF cuts are shown.
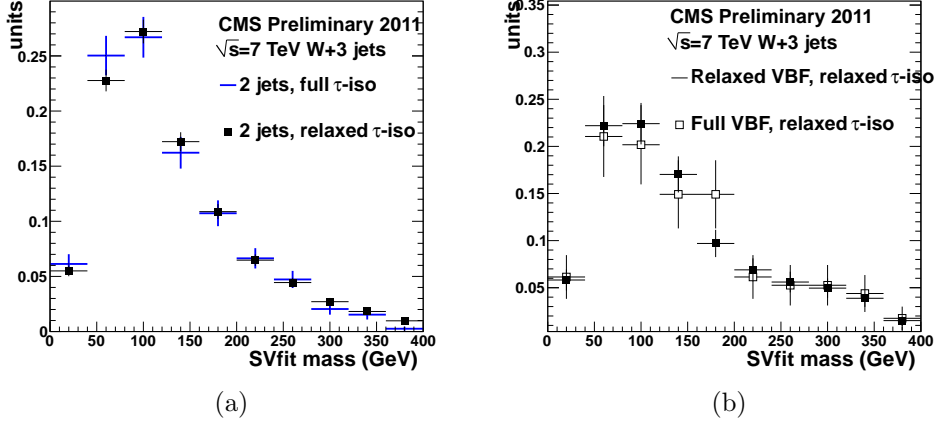
Figure 7.18: a) Comparison between the Monte Carlo W+jets template obtained from two–jets events passing the loose or full tau isolation; b) comparison between the W+jets mass template obtained from events with loose tau isolation passing the relaxed or full VBF cuts are shown.

7.7.5 Multi–jets (QCD)

The contamination from QCD multi–jet events, where the τ_ℓ is coming either from a heavy–flavor decay or from a mis–identified jet, while the τ_h originates from a jet, is entirely estimated from data.

For each category, events with same–sign $\tau_\ell\tau_h$ pairs are selected (QCD–sideband). This sample is expected to be 60%–80% pure in QCD. The rest comes from W+jets, with small contamination from $t\bar{t}$, di–boson and Drell-Yan. The W+jets ($t\bar{t}$) in the QCD–sideband undergoes the same calibration procedure performed for the W ($t\bar{t}$) evaluation in the signal region (Section 7.7.4), which passes through the definition of same–sign W ($t\bar{t}$) enriched sidebands, while the other backgrounds are estimated from Monte Carlo.

Monte Carlo driven mass templates for the non–QCD backgrounds in the QCD–sideband are normalized to the background prediction and subtracted from the observed mass distribution, thus providing a template for the same–sign multi–jet events. Studies based on the simulation and on data–driven control regions confirm that the mass distribution for same–sign and opposite–sign events are compatible [76]. However, the production cross–section is found to be asymmetric between the two, possibly due to charge asymmetric reactions (e.g. heavy flavor pair–production). The ratio between opposite–sign and same–sign events ($r_{OS/SS}$) is measured to be (1.11 ± 0.02) and (1.07 ± 0.02) for the $\tau_\mu\tau_h$ and $\tau_e\tau_h$ channel. The measurement is per-

	0–jet ↓	0–jet ↑	Boosted ↓	Boosted ↑	VBF
	opposite–sign W–sideband				
Observed	12763	2159	4357	1162	81
Di–Boson	152 ± 45	71 ± 21	104 ± 31	43 ± 13	1.5 ± 1.5
Drell–Yan	328 ± 98	66 ± 20	127 ± 38	53 ± 17	3.1 ± 0.9
SF($t\bar{t}$)	1.14 ± 0.11	1.15 ± 0.11	1.14 ± 0.11	1.14 ± 0.11	2.0 ± 0.6
$t\bar{t}$	887 ± 79	515 ± 51	223 ± 20	125 ± 13	19 ± 6
r_W	2.50 ± 0.15	2.51 ± 0.25	2.5 ± 0.2	2.0 ± 0.4	1.8 ± 0.2
W+jets	4554 ± 300	609 ± 61	1548 ± 155	470 ± 100	33 ± 7
Expected	5227 ± 100	963 ± 50	1512 ± 55	573 ± 35	23 ± 7
	same–sign W–sideband				
Observed	4111	480	2113	392	23
Di–Boson	23 ± 6	7 ± 2	33 ± 10	11 ± 3	0.5 ± 0.5
Drell–Yan	173 ± 52	38 ± 11	72 ± 22	26 ± 7	0.0 ± 1.0
SF($t\bar{t}$)	1.6 ± 0.2	1.1 ± 0.12	1.7 ± 0.2	1.1 ± 0.2	2.0 ± 2.0
$t\bar{t}$	272 ± 27	60 ± 12	99 ± 10	125 ± 13	1.7 ± 1.0
r_W	2.3 ± 0.2	1.9 ± 0.4	2.0 ± 0.2	1.9 ± 0.4	1.8 ± 0.2
W+jets	1563 ± 150	195 ± 40	928 ± 93	174 ± 34	11 ± 3
Expected	1580 ± 55	262 ± 23	800 ± 40	200 ± 20	2 ± 4
	same–sign QCD–sideband				
Observed	8383	652	2257	487	29
W+jets	1563 ± 150	195 ± 40	928 ± 93	174 ± 34	11 ± 3
$t\bar{t}$+di–boson	96 ± 10	34 ± 6	35 ± 5	11 ± 2	2.1 ± 1.2
Drell–Yan	316 ± 100	53 ± 15	167 ± 50	32 ± 10	5.9 ± 1.8
QCD	7103 ± 700	384 ± 46	1560 ± 170	264 ± 32	10 ± 5

Table 7.12: Background estimation in the W and QCD sidebands for the $\tau_\mu \tau_h$ channel. The ↓ (↑) symbol indicates the low (high) τ_h transverse momentum bin.

formed in an inclusive sample of events with anti–isolated leptons and the simulation is then used to extrapolate the ratio to isolated muons ($r_{OS/SS}$ is indeed predicted to be flat vs I^{PF}). To account for an unknown dependency of $r_{OS/SS}$ on the jet kinematics, a systematic uncertainty of 10% is assigned to the $r_{OS/SS}$ factors in each category which covers the difference between the inclusive measurement and the naive expectation $r_{OS/SS} = 1$. An additional uncertainty on the QCD yield comes from the statistical precision of the same–sign sideband and on the uncertainties on the yield of each subtracted background.

For some categories, the QCD template is enhanced by loosening the τ_ℓ isolation to $I^{PF}/p_T^\ell < 0.30$ (0–jet↑ and Boosted ↑ category of the $\tau_\mu \tau_h$ chan-

	0–jet ↓	0–jet ↑	Boosted ↓	Boosted ↑	VBF
	opposite–sign W–sideband				
Observed	6807	1105	2308	646	41
Di–Boson	75 ± 22	27 ± 8	44 ± 13	18 ± 5	0.21 ± 0.21
Drell–Yan	192 ± 56	51 ± 15	88 ± 27	44 ± 13	6.4 ± 1.9
SF($t\bar{t}$)	0.97 ± 0.11	0.94 ± 0.11	1.02 ± 0.11	0.99 ± 0.10	2.5 ± 0.9
$t\bar{t}$	352 ± 35	170 ± 18	92 ± 10	46 ± 5	10 ± 4
r_W	33 ± 3	7.8 ± 0.8	6.6 ± 1.3	5.3 ± 1.6	2.1 ± 0.2
W+jets	187 ± 19	109 ± 11	313 ± 62	102 ± 20	12 ± 5
Expected	188 ± 16	143 ± 12	278 ± 21	110 ± 12	6 ± 6
	same–sign W–sideband				
Observed	2068	264	1056	253	27
Di–Boson	9 ± 3	3 ± 1	15 ± 5	4.0 ± 1.2	0.3 ± 0.3
Drell–Yan	21 ± 7	10 ± 3	23 ± 7	6 ± 2	0.5 ± 0.2
SF($t\bar{t}$)	1.6 ± 0.3	0.9 ± 0.4	1.6 ± 0.2	0.9 ± 0.3	2.0 ± 2.0
$t\bar{t}$	121 ± 23	22 ± 10	41 ± 5	8 ± 3	7 ± 3
r_W	22 ± 3	6.5 ± 1.2	6.3 ± 1.2	4.7 ± 0.9	2.3 ± 0.2
W+jets	87 ± 16	35 ± 7	155 ± 31	50 ± 10	8 ± 3
Expected	73 ± 10	40 ± 7	110 ± 9	40 ± 7	8 ± 4
	same–sign QCD–sideband				
Observed	401	104	274	92	26
W+jets	87 ± 16	35 ± 7	155 ± 31	50 ± 10	8 ± 3
$t\bar{t}$+di–boson	26 ± 5	10 ± 4	10 ± 1	3.9 ± 1.2	5 ± 2
Drell–Yan	7 ± 2	6 ± 2	11 ± 3	6 ± 2	3 ± 1
QCD	299 ± 36	56 ± 11	80 ± 19	22 ± 7	9 ± 6

Table 7.13: Background estimation in the W and QCD sidebands for the $\tau_e\tau_h$ channel. The ↓ (↑) symbol indicates the low (high) τ_h transverse momentum bin.

nel), or the tau isolation (0–jet and Boosted category of the $\tau_e\tau_h$ channel), or both (VBF category), whatever gives the largest statistics and provides a shape that is still compatible, within errors, with the nominal templates.

An alternative method based on the fake rate of electrons/muons in jets to pass the isolation cut is used as a cross–check and to derive the expected QCD contribution in regions where the nominal method does not apply (e.g. the W–sideband). First, an inclusive sample of events with same–sign and anti–isolated $\tau_\ell\tau_h$ pairs ($0.2 \leq I^{PF}/p_T^\ell \leq 0.50$) are counted in bins of the lepton p_T. The number of QCD events in the same p_T bin, but with an isolated lepton, is estimated with the same technique used for the inclusive same–sign measurement. The ratio r_{iso} of events with anti–isolated to isolated leptons

is measured in bins of the lepton p_T. The p_T^ℓ–dependence is parametrized with an *ad hoc* function

$$r_{iso}(p_T^\ell) = c_0 e^{-c_1 p_T^\ell} + c_2, \tag{7.9}$$

and applied as a weight to same–sign events with anti–isolated leptons. The corresponding fits are reported in Fig. 7.19.
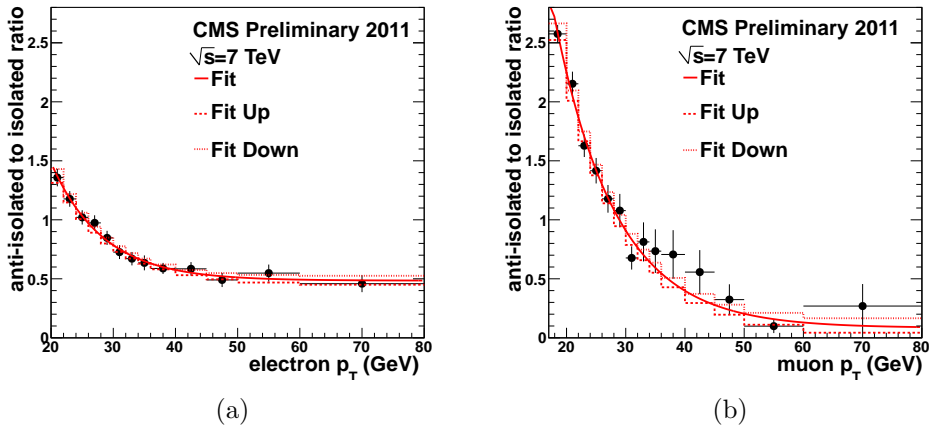
Figure 7.19: Ratio between the number of same–sign events with anti–isolated and isolated (a) electrons and (b) muons as a function of p_T^ℓ. Data points are fitted with an exponential function.

7.8 Systematic uncertainties

The signal and background yields are affected by a number of systematic uncertainties. The dominant sources are listed below.

- **Luminosity**
  The uncertainty on the CMS integrated luminosity is 2.2%. It affects the signal yield alone, since all the backgrounds are either estimated from data or normalized to the CMS measured cross–sections.

- **Muon/electron efficiency**
  The muon and electron trigger, reconstruction, identification, and isolation efficiency are measured from data with tag–and–probe (Section 7.4). Given the large di–lepton sample available for the tag–and–probe, the precison of the measurement is eventually limited by systematics

in the method (e.g. fit models for background subtraction). An uncertainty of 1% and 2% is assigned to the combined muon and electron efficiency, respectively. This uncertainty affects the yield of the signal and of all backgrounds except QCD and W+jets. It is fully correlated among the various channels.

- **Tau trigger and identification efficiency**
  The tau identification efficiency has been measured from data using a tag–and–probe technique (Section 5.2.3). The uncertainty of this measurements is 6% and comes from both statistical and systematic sources. The tau trigger efficiency is measured on single–muon triggered events. Due to the large backgrounds, the extraction of the trigger efficiency is systematically dominated. An extra 3.5% is added in quadrature to the tau–ID uncertainty, so that a total of 7% is assigned as a normalization uncertainty to the signal and $Z \to \tau\tau$.

- **Tau energy scale**
  An uncertainty on the τ_h energy scale of 3% is estimated from template fits to the visible τ_h mass (Section 5.2.4). The 3% value is an upper limit that covers the data–to–simulation differences measured for all decay modes and pseudorapidities. A variation of the τ_h energy scale affects both the normalization (due to the $p_T^{\tau_h}$ cut) and the shape of the mass template. For each process involving genuine hadronic taus, two alternative mass templates are obtained by i) rescaling the τ_h momentum up or down by 3%, ii) recomputing the $\vec{E}_T^{miss}$ using the shifted tau momentum, iii) feeding the new τ_h and $\vec{E}_T^{miss}$ momenta to the SVfit algorithm. It is correlated among all categories and channels.

- **Jet energy scale**
  An uncertainty on the jet energy scale propagates into a normalization uncertainty in each category. The full analysis chain is re–run by systematically shifting the momenta of all reconstructed jets up and down by their p_T–η dependent scale uncertainty [62]. This results in a reshuffling of events among the categories. Correlation are properly taken into account.

- E_T^{miss} **scale**
  As a consequence of the cut on the transverse mass, an uncertainty on the E_T^{miss} modeling propagates into a systematic uncertainty on the signal yield. By varying the recoil corrections within their errors, a 5% uncertainty on the signal yield has been assigned, fully correlated among all categories.

- $Z \to \tau\tau$ **normalization**
  The inclusive $Z \to \tau\tau$ normalization is calibrated from a di–muon control sample. An uncertainty of 3% is assigned to the resulting scale–factor. This inclusive measurement is extrapolated to the various categories using the embedded samples. The extrapolation factors have a statistical error that is directly propagated as a systematic uncertainty on the yields.

- $Z \to \ell\ell$, $\ell = \mu, e$
  The uncertainty on the Drell–Yan background with fake taus comes from the limited knowledge of the jet $\to \tau_h$ (20%), $\mu \to \tau_h$ (30%) and $e \to \tau_h$ (20%) fake rate.

- **Top and di-boson normalization**
  For each category, an uncertainty on the $t\bar{t}$ normalization is assigned due the limited statistics of the $t\bar{t}$–sidebands. An additional uncertainty of 8%, fully correlated among channels and categories, is assigned to cover the data–to–simulation difference in the efficiency of the double b–tagging selection used to define the sideband, which is not explicitly corrected but rather assigned as a conservative uncertainty. The di–boson background is small and can be safely estimated from simulation. Its normalization is assigned a 30% relative error, that covers both the cross–section and the jet $\to \tau_h$ fake rate uncertainty. In the *VBF* category, the uncertainty is raised to 100%.

- W **normalization**
  The normalization of the W+jets background in each category is derived from sidebands. The uncertainty on the W yield comes from the limited statistics of the sideband and from the systematic error on the extrapolation factors r_W. Studies based on an inclusive W+jets sample show that the combined effect of theory (PDF) and experimental uncertainties (E_T^{miss}, jet, lepton and tau energy scale) on the r_W factors is of the order of 6% [115]. An additional uncertainty comes from the limited Monte Carlo statistics of W+jets available to extract the r_W factors. The latter ultimately dominates for the low statistics categories and can be as large as 20%. In the *VBF* category, the high statistics W+3 jets sample allows for a rather precise evaluation of r_W, and the final normalization uncertainty is driven by the limited statistics of the W–sideband.

- **QCD normalization**
  The uncertainty on the QCD normalization gets contribution from the

opposite–sign to same–sign ratio (10%), and from the error on the QCD yield in the same–sign sideband (5%–50%) which stems from both the statistics of the sideband and from the systematic uncertainty on the non–QCD backgrounds that need to be subtracted.

- **Theory uncertainty**
  Theory uncertainties affecting the signal production rate and its acceptance are taken as fully correlated among all search analyses performed by CMS [110]. Varying the PDF sets as recommended in Ref. [28] gives a 3% normalization uncertainty on the three production modes. The effect of varying α_s and $\mu_{R/F}$ changes the rate and acceptance of each production mode for the various categories. The uncertainty for GGF production in the 0–*jet*, *Boosted*, and *VBF* is estimated to be 12%, 12% and 30%, respectively. The uncertainty for VBF production in the 0–*jet*, *Boosted*, and *VBF* is estimated to be 3.5%, 3.5% and 10%, respectively [95]. Variations of the parton shower and underlying event modeling can induce migrations of events from one jet category to another. This gives an additional 4% uncertainy on the signal yield, fully anti–correlated among the 0–*jet* and *Boosted* category.

7.9 Summary of background yields

The background yields in the various categories are reported in Table 7.14 and 7.15, together with the observed number of events and the expected signal yields for a SM Higgs boson with $M_H = 125$ GeV. A di–tau mass window ($0 \leq M_{\tau\tau} \leq 350$ GeV), consistent with that used for the final statistical interpretation, has been applied. The uncertainties on the yields are systematic only (Section 7.8).

	0–jet ↓	0–jet ↑	Boosted ↓	Boosted ↑	VBF
$Z \to \tau\tau$	24642 ± 1800	3766 ± 290	4075 ± 310	1571 ± 120	56 ± 5
Z+fakes	514 ± 150	169 ± 55	184 ± 55	59 ± 18	0.6 ± 0.2
W+jets	4554 ± 300	609 ± 61	1550 ± 155	470 ± 100	33 ± 7
QCD	7103 ± 700	385 ± 46	1560 ± 170	264 ± 32	11 ± 5
$t\bar{t}$	457 ± 40	288 ± 30	111 ± 11	74 ± 7	13 ± 4
Di–boson	77 ± 25	56 ± 16	72 ± 22	37 ± 12	1.1 ± 1.1
GGF	40	31	18	14.9	0.79
VBF	0.52	0.42	3.0	2.9	3.1
$VH + t\bar{t}H$	0.61	0.74	1.2	1.4	0.01
$\sum$ SM	37347 ± 2000	5270 ± 300	7550 ± 400	2477 ± 160	114 ± 11
Observed	37407	5237	8195	2453	110

Table 7.14: Expected and observed event yields in the $\tau_\mu \tau_h$ channel. The ↓ (↑) symbol indicates the low (high) τ_h transverse momentum bin.

	0–jet ↓	0–jet ↑	Boosted ↓	Boosted ↑	VBF
$Z \to \tau\tau$	936 ± 71	376 ± 27	743 ± 56	288 ± 22	31 ± 4
Z+fakes	64 ± 19	113 ± 33	25 ± 7	33 ± 10	4 ± 1
W+jets	187 ± 19	109 ± 11	313 ± 62	102 ± 20	12 ± 5
QCD	299 ± 36	56 ± 11	80 ± 19	22 ± 7	10 ± 6
$t\bar{t}$	103 ± 13	50 ± 7	27 ± 4	14 ± 2	7 ± 2
Di–boson	3.8 ± 1.1	6 ± 2	14 ± 4	8 ± 2	0.3 ± 0.3
GGF	2.0	4.2	5.6	3.4	0.36
VBF	0.09	0.09	1.0	0.89	1.6
$VH + t\bar{t}H$	0.15	0.27	0.62	0.60	0.01
$\sum$ SM	1590 ± 83	711 ± 46	1203 ± 86	467 ± 32	64 ± 9
Observed	1544	732	1158	492	62

Table 7.15: Expected and observed event yields in the $\tau_e \tau_h$ channel. The ↓ (↑) symbol indicates the low (high) τ_h transverse momentum bin.

7.10 Statistical interpretation

The binned di–tau mass distributions observed in the 5×2 categories are used for the statistical interpretation of the results. The input histograms have a 20 GeV binning (i.e. roughly the mass resolution for a ≈ 120 GeV Higgs boson, Fig. 7.14(a)) up to $M_{\tau\tau} \leq 200$ GeV, followed by three 50 GeV wide bins. The last three bins are populated mostly by W+jets and $t\bar{t}$, thus providing an *in situ* calibration sideband for these backgrounds.

An eventual $H \rightarrow \tau\tau$ signal is expected to distort the mass spectra from their background–only expectation in a coherent way among all categories. To assess how compatible the observed mass distributions are with either the *null* hypothesis (background–only) or with the *alternative* hypothesis (signal+background), a *test statistic* is defined. The choice of the test statistic and of the treatment of the nuisance parameters follows the recommendations of the LHC Higgs Combination group [110]. For the sake of defining confidence intervals on the signal strength, the modified frequentist approach (CL_s) is adopted [111].

The result of the actual observation is an array of $13 \times 5 \times 2$ measured data yields n_i, where $i = 1, ..., 130$ runs over the bins of all mass histograms. The expected event yield ν_i in bin i is parametrized as

$$\nu_i = \mu s_i(\vec{\theta}) + b_i(\vec{\theta}) \tag{7.10}$$

where s_i (b_i) is the expected amount of signal (background) in that bin, and is assumed to depend on some nuisance parameters $\vec{\theta}$. For a given value of M_H, the signal yield s_i is fixed to its SM prediction. A *signal strength modifier* parameter μ modifies, by the same scale, the signal rate from all production modes.

In the statistical model that describes the observation, every source of systematic uncertainty (e.g. signal and background normalizations, shape uncertainties,...) is associated with a nuisance parameter. The nuisance parameters $\vec{\theta}$ are constrained by auxiliary measurements that restrict their values within confidence intervals. Event counting in sidebands which constrain the background rates in the signal region is an example of an auxiliary measurement. Similarly, tag–and–probe measurements of efficiencies that affect the signal normalization (e.g. trigger, muon isolation,...) provide *a priori* knowledge on the related nuisance parameters.

For the class of nuisance parameters of the first example (counting), the prior *pdf* $\rho(\theta_j|\hat{\theta}_j)$ for the unknown event yield θ_j, given the observation $\hat{\theta}_j$ in

a sideband, is modeled with a *Gamma* distribution:

$$\rho(\theta_j|\hat{\theta}_j) = \frac{1}{\alpha}\frac{(\theta_j/\alpha)^{\hat{\theta}_j}}{\hat{\theta}_j!}\exp(-(\theta_j/\alpha)), \qquad (7.11)$$

where $\langle\theta_j\rangle = \alpha\langle\hat{\theta}_j\rangle$. For the second class of nuisance parameters (normalization), a *Log–normal* distribution with parameter $\kappa = 1+\epsilon$ (ϵ = relative scale of the uncertainty) is chosen:

$$\rho(\theta_j|\hat{\theta}_j) = \frac{1}{\sqrt{2\pi}\ln\kappa}\exp(-\frac{(\ln(\theta/\hat{\theta}))^2}{2(\ln\kappa)^2})\frac{1}{\theta} \qquad (7.12)$$

The same nuisance parameter θ_j can affect the signal or background yields in more than one bin, possibly with different scales. Errors in different bins but originating from the same nuisance parameter are taken as either fully correlated or fully anti–correlated: two observables A and B with 100% correlated errors coming from the same nuisance parameter θ_j are parametrized as $A = \tilde{A}\kappa_A^{\theta_j}$ and $B = \tilde{B}\kappa_B^{\theta_j}$, with $\kappa_A, \kappa_B > 1$ and θ_j distributed according to the normal distribution. The 100% anti–correlation is realized by taking e.g. $\kappa_A < 1$ and $\kappa_B > 1$.

The third class of nuisance parameters considered in this analysis have the property of changing the scale of a kinematical variable correlated with the di–tau mass, thus altering the shape of the templates. A shape uncertainty is modeled by defining a one–parameter family of alternative templates governed by a nuisance parameter λ. By construction, the template associated with $|\lambda| = 1$ corresponds to the one obtained by scaling down ($\lambda = -1$) or up ($\lambda = +1$) the unknown energy scale by ± 1 standard deviation characterizing the uncertainty on the energy scale. The nominal template is recovered by setting $\lambda = 0$. The family of templates is defined by a quadratic interpolation between the up and down template for $|\lambda| < 1$, and linear beyond. The *pdf* constraining the λ parameter is taken to be the normal distribution with mean 0 and $\sigma = 1$.

The systematic uncertainties *pdf*s $\rho(\vec{\theta}|\hat{\vec{\theta}})$ are incorporated into the likelihood model by re–interpreting them as posteriors $p(\hat{\vec{\theta}}|\vec{\theta})$ (Bayes theorem), assuming flat priors on $\vec{\theta}$.

The likelihood $\mathcal{L}$ of the model is then written as:

$$\mathcal{L}(\text{data}|\mu,\vec{\theta}) = \text{Poisson}\{\text{data}|\mu s(\vec{\theta}) + b(\vec{\theta})\} \cdot p(\hat{\vec{\theta}}|\vec{\theta})$$

$$= \prod_{i=1}^{130}\frac{[\mu s_i(\vec{\theta}) + b_i(\vec{\theta})]^{n_i}}{n_i!}e^{-[\mu s_i(\vec{\theta})+b_i(\vec{\theta})]} \cdot p(\hat{\vec{\theta}}|\vec{\theta}) \qquad (7.13)$$

Given $\mathcal{L}$, the test statistic q_μ is constructed from the profile likelihood ratio $\lambda(\mu)$, defined as

$$\lambda(\mu) = \frac{\mathcal{L}(\mu, \hat{\hat{\vec{\theta}}}_\mu)}{\mathcal{L}(\hat{\mu}, \hat{\vec{\theta}})}, \tag{7.14}$$

where $\hat{\hat{\vec{\theta}}}_\mu$ is the conditional maximum likelihood estimator of $\vec{\theta}$, i.e. the value of $\vec{\theta}$ that maximizes $\mathcal{L}$ for a fixed value of μ, while $\hat{\mu}$ and $\hat{\vec{\theta}}$ are the usual maximum likelihood estimators. Equation (7.14) is complemented by the condition

$$0 \leq \hat{\mu} \leq \mu$$

that ensures the signal rate to be positive ($\hat{\mu} > 0$) and that one–sided confidence intervals are obtained ($\hat{\mu} \leq \mu$) when setting limits on μ. The condition is implemented by forcing $\hat{\mu} = 0$, if a negative best fit value where found, and by collapsing q_μ at zero for $\hat{\mu} > \mu$:

$$q_\mu = \begin{cases} -2 \log \frac{\mathcal{L}(\mu, \hat{\hat{\vec{\theta}}}_\mu)}{\mathcal{L}(0, \hat{\hat{\vec{\theta}}}(0))} & \hat{\mu} < 0 \\ -2 \log \frac{\mathcal{L}(\mu, \hat{\hat{\vec{\theta}}}_\mu)}{\mathcal{L}(\hat{\mu}, \hat{\vec{\theta}})} & 0 \leq \hat{\mu} \leq \mu \\ 0 & \mu < \hat{\mu} \end{cases} \tag{7.15}$$

By construction, q_μ is non–negative. It takes small values if the observation is consistent with the $(\mu s + b)$ hypothesis, and large otherwise.

To establish an arbitrary confidence levels on μ, the sampling distribution of q_μ,

$$f(q_\mu | \mu' s + b),$$

is needed as a function of μ'. The construction of the sampling distributions can be realized by generating pseudo–data with Monte Carlo techniques. An alternative approach is based on asymptotic formulae for q_μ [112] that are strictly valid in the large sample limit. In this approximation,

$$-2 \log \lambda(\mu) \approx \frac{(\mu - \hat{\mu})^2}{\sigma^2} \tag{7.16}$$

where σ^2 is the variance of the $\hat{\mu}$ estimator. The latter can be estimated from the Asimov dataset [112], i.e that particular pseudo–experiment where the maximum likelihood esimators of all parameters coincide with their expectation values. Since $\hat{\mu}$ can be thought as normally–distributed, the asymptotic relation 7.16 allows for an analytical determination of $f(q_\mu | \mu' s + b)$.

Given an observed value of the test statistic q_μ^{obs}, the p–values in the $(\mu s + b)$ hypothesis (p_μ) and in the b only hypotesis (p_0), are defined as

$$p_\mu = \int_{q_\mu^{obs}}^{\infty} f(q_\mu | \mu s + b) dq_\mu, \quad p_0 = \int_{q_\mu^{obs}}^{\infty} f(q_\mu | b) dq_\mu, \qquad (7.17)$$

The signal strength modifier μ is then said to be excluded at a confidence level (CL) $1 - \alpha$, if the ratio

$$CL_s(\mu) = p_\mu / p_0$$

is equal to α. The observed 95% CL exclusion limit on μ (μ_{obs}^{95}) is then obtained by varying μ until $\alpha = 0.05$. It is useful to quantify the sensitivity of an experiment by reporting the median expected exclusion limit on μ in the background only hypothesis, μ_{exp}^{95}, together with the intervals where μ_{obs}^{95} is expected to lie in the 68% (1σ) and 95% (2σ) of the cases, always in the null hypothesis.

In case a relevant departure of the observation from the null hypothesis is found, the significance of the observed excess is quantified in terms of the p–value for the observation of q_0^{obs} in the null hypothesis:

$$p_0 = \int_{q_0^{obs}}^{\infty} f(q_0 | b) dq_0,$$

The significance of p_0 is often reported in the form of a gaussian probability $Z = \Phi^{-1}(1 - p_0)$, where Φ is the inverse cumulative function of the normal distribution.

7.11 Results

The di–tau mass distributions in the five categories of the $\tau_e\tau_h$ and $\tau_\mu\tau_h$ channels are shown in Fig. 7.20 and 7.21, respectively. The background normalizations are rescaled to their best–fit value from a maximum–likelihood simultaneous fit to the 5×2 categories in the background–only hypothesis.

No significant excess over the SM backgrounds is observed, therefore exclusion limits on the production cross–section of a SM–like Higgs boson are set.

The observed upper limits at 95% CL on the signal strength modifier, μ_{95}^{obs}, are reported in Table 7.16 for eight hypothesized values of M_H. The expected exclusion limit μ_{95}^{exp} in the absence of a signal (background–only hypothesis) is also reported together with its 1 and 2 σ confidence interval boundaries. The results have been summarized in Fig. 7.22(a).

The observed exclusion limits are compatible with the background–only hypothesis for all values of M_H. An Higgs boson with $M_H = 125$ GeV, produced at a rate 1.90 times larger than the SM prediction, is ruled out at 95% CL, while 1.98 times the SM is expected to be excluded in the absence of a signal.

The maximum likelihood fitted value of μ is shown in Fig. 7.22(b) as a function of M_H, together with its 1σ error band. For an Higgs boson with $M_H = 125$ GeV, the observation is better described by a negative value of μ as a result of a slight deficit of data. The best fit value is -0.16 ± 0.99, which is consistent with 0, but even compatible with unity within $\approx 1.2\sigma$

M_H (GeV)	-2σ	-1σ	expected	$+1\sigma$	$+2\sigma$	Observed
110	1.09	1.45	2.01	2.79	3.71	2.50
115	1.08	1.44	1.99	2.77	3.68	2.29
120	1.04	1.38	1.91	2.66	3.53	2.10
125	1.07	1.43	1.98	2.75	3.65	1.90
130	1.11	1.48	2.05	2.85	3.79	1.79
135	1.26	1.67	2.32	3.22	4.28	2.00
140	1.49	1.98	2.75	3.82	5.08	2.29
145	2.00	2.66	3.69	5.12	6.81	2.93

Table 7.16: Expected and observed 95% CL exclusion limit on the SM signal strength modifier
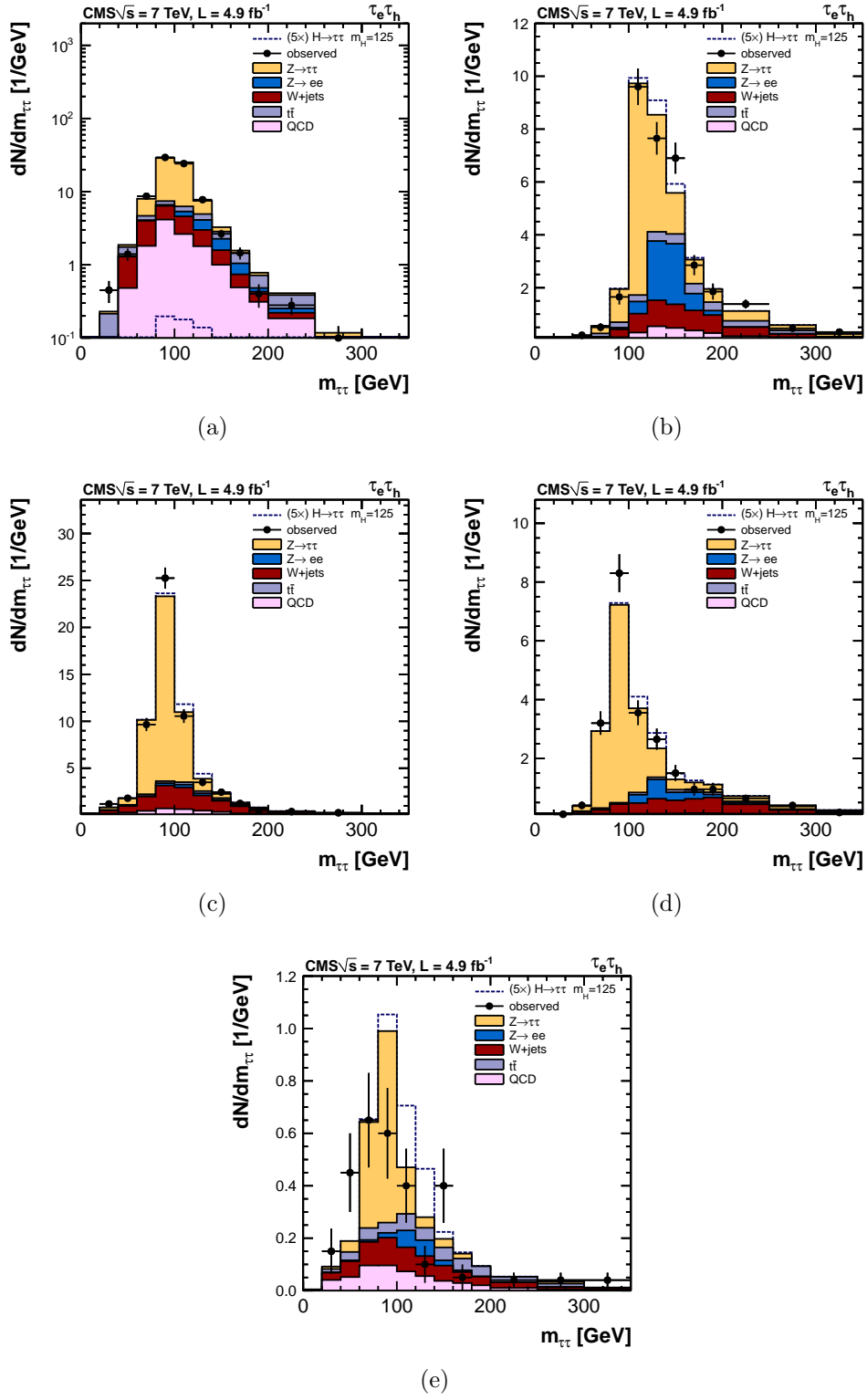
Figure 7.20: Di–tau mass distribution for the five analysis categories of the $\tau_e\tau_h$ channel.
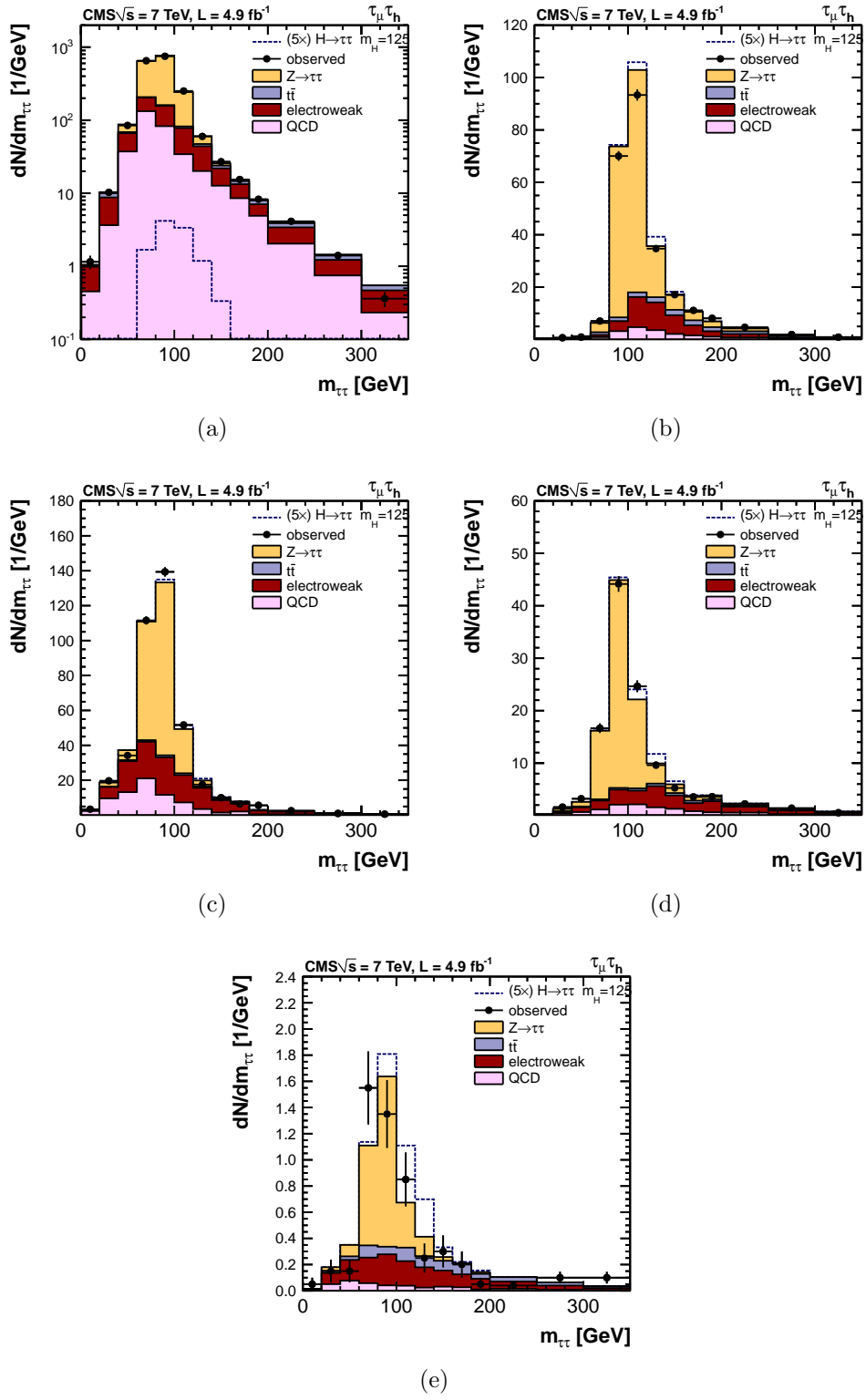
Figure 7.21: Di–tau mass distribution for the five analysis categories of the $\tau_\mu\tau_h$ channel.

199
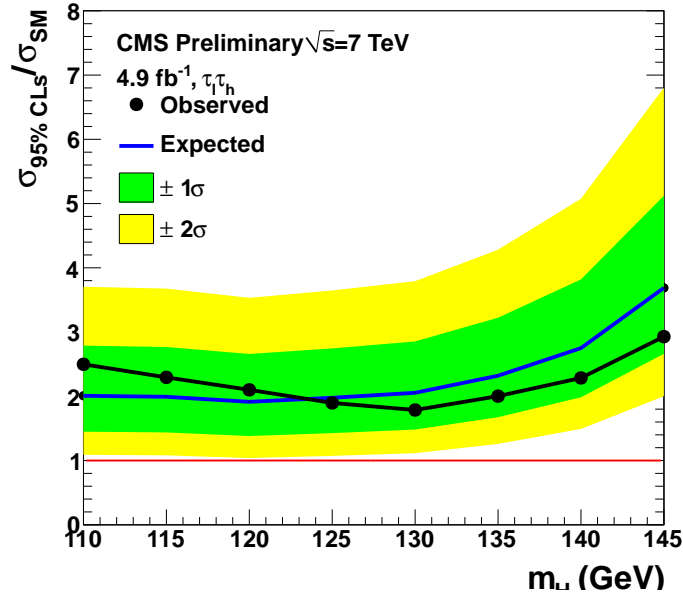
(a)
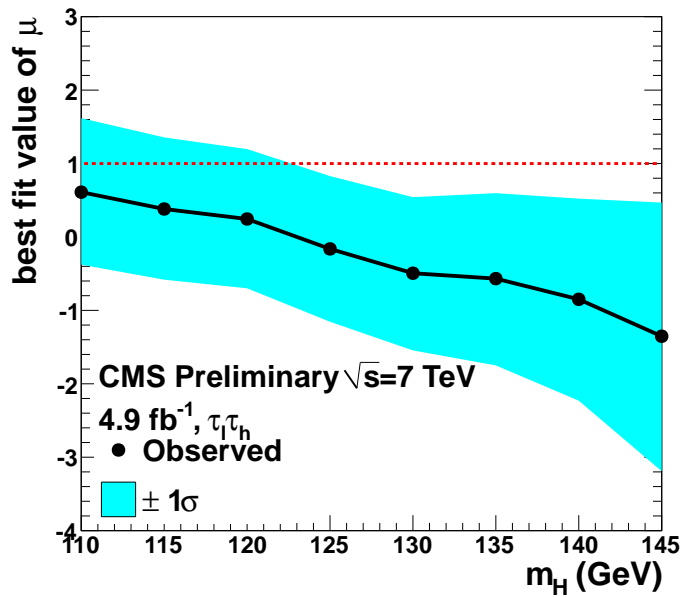
(b)

Figure 7.22: a) Expected and observed 95% CL exclusion limits on the SM
signal strength modifier; b) best fit value of the signal strength modifier
μ with its 1σ error band obtained from a maximum likelihood fit to all
categories and channels together.

7.12 Combinations with 2012 results and the discovery

7.12.1 The combined 2011–2012 results

The analysis presented for the $H \to \tau\tau$ channel in this thesis made use of the data collected by CMS at $\sqrt{s} = 7$ TeV during the 2011 Run. I had previously contributed to an early analysis of the 2011 data which was published in Ref. [76], following the Moriond 2012 international conference. I presented here the analysis performed up to June 2012, thus including the latest updates and improvements. The new analysis of the 7 TeV data described in this thesis was combined with a similar analysis extended to the 8 TeV data collected until June 2012[1]. The work is documented in Ref. [95]. The results, complemented by other di–tau channels also documented in Ref. [95], namely the purely leptonic $\tau_\mu\tau_e$ and $\tau_\mu\tau_\mu$ channels, are included in the CMS discovery paper [96], which become available in July 2012 following the public announcement at CERN and at the ICHEP 2012 international conference on the 4th of July. A new particle, a boson, has been observed in the context of the SM Higgs boson search, with a mass of about 125 GeV. In the following, I first describe the results obtained with the combination of the 2011 and 2012 data for the $H \to \tau\tau$ channel, and then discuss the results in the context of the recent discovery.

The main changes for the ICHEP analysis [95] compared to the Moriond analysis [76] are i) the usage of more performing reconstruction and identification algorithms for the offline objects (e.g. tau isolation, electron identification), ii) the definition of a VBF–like category based on a multivariate technique compared to a simple cut–based approach, giving up to 20% stronger expected limit for the *VBF* category, iii) a better resolution of the di–tau mass (by at least 30%), due to an improved description of the SVfit likelihood [93] (consistent with that described in Section 6.6), iv) an optimization of the analysis categories, in particular the introduction of two separate bins of the τ_h transverse momentum and the optimization of the jet p_T threshold in the *Boosted* category (lowered from 150 GeV to 30 GeV, which allowed to reduce significantly the theory uncertainty).

The Moriond analysis, which was later on complemented with a search for Higgs boson(s) decaying to tau leptons in the $\tau_\mu\tau_\mu$ channel [113], provides an additional interpretation of the results in the context of the MSSM (Section

---

[1]A few minor changes have been brought in addition to the work presented in this thesis, and which bring small differences on the background estimations; the main results remain however consistent.

2.5). A simultaneous search for the three neutral Higgs bosons (h, H, and A) is performed. In the absence of a signal, exclusion limits on the $\tan\beta$–M_A plane have been set. Conservative limits are obtained by assuming the so–called $m_h^{\max}$ scenario [114]: for a given value of the common SUSY–breaking sfermion masses (M_{SUSY}), and for a maximal value of $M_A = 1$ TeV, the other SUSY parameters are tuned to maximize M_h as a function of $\tan\beta$. The upper exclusion limit on $\tan\beta$, obtained from the combination of the $\tau_\mu\tau_h$, $\tau_e\tau_h$, and $\tau_e\tau_\mu$ channels [76], is measured to be 10.9, 7.8, and 35.4 for $M_A = 100$, 200, and 400 GeV, respectively. For all values of M_A in the range $[90, 500]$ GeV, the exclusion limits on $\tan\beta$ are consistent with the background–only median expected within a maximal excursion of 2σ.

Figure 7.23(a) compares the expected 95% CL limit on μ for the 7 TeV and for the 8 TeV analysis (all four channels combined). Figure 7.23(b) illustrates the evolution on the expected exclusion limits for the three CMS public analyses [115, 76, 95] based on 1.6, 4.9 and 10 fb^{-1}, respectively. This plot shows that the sensitivity in the $H \to \tau\tau$ channel has increased much faster than $\sim \mathcal{L}^{\frac{1}{2}}$, as a result of a continuous optimization of the analysis.

The expected limit for the combination of the 7 TeV and 8 TeV data, broken–up by decay channels and category, are shown in Fig. 7.23(c) and 7.23(d), respectively.

Finally, the combined 7 TeV and 8 TeV observed limit is shown in Fig. 7.24. The expected exclusion limit in the presence of a SM Higgs boson with $M_H = 125$ GeV has been superimposed for comparison.

7.12.2 Comparison with other $H \to \tau\tau$ searches at hadron colliders

The most recent public results on $H \to \tau\tau$ searches at the TeVatron collider are documented in Ref. [116] for the D0 experiment, and Ref. [117] for the CDF experiment. At present, the most stringent ATLAS public results on SM $H \to \tau\tau$ searches are based on 4.7 fb^{-1} of $\sqrt{s} = 7$ TeV data, and have been documented in Ref. [118].

The D0 analysis combines the results from three independent analyses of the following final states: $i)$ one muon, one semi–leptonic tau decay, and at most one jet ($\mu\tau0$), $ii)$ one muon, one semi–leptonic tau decay, and at least two jets ($\mu\tau2$), and $iii)$ one electron, one semi–leptonic tau decay, and at least two jets ($e\tau2$). These analyses are based on a total of 7.3, 6.2, and 4.3 fb^{-1} of $p\bar{p}$ data, respectively. A search range $105 < M_H < 200$ GeV is considered: the sensitivity at large mass is enhanced by explicitely searching
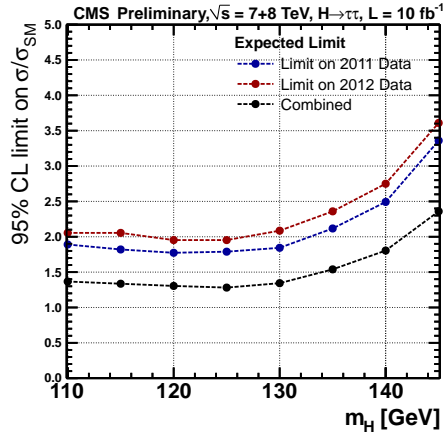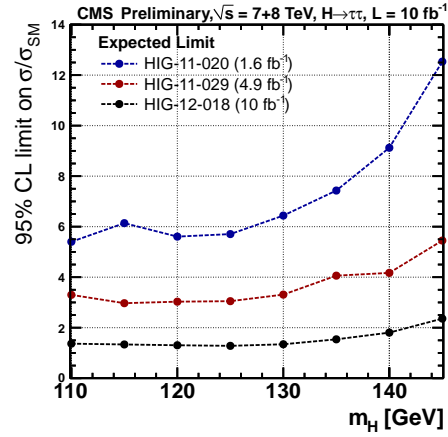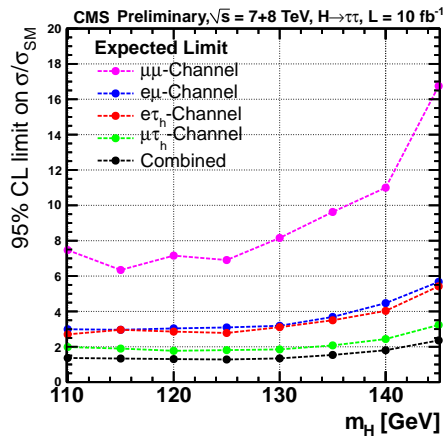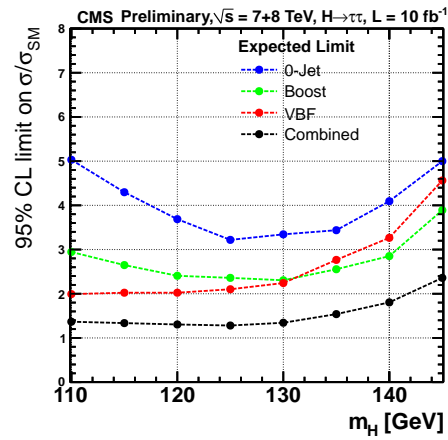
Figure 7.23: Expected 95% CL exclusion limits on the SM signal strength modifier per (a) data period, (b) evolving in time, (c) per decay channel and (d) per category. Plots from the CMS public results page [95].
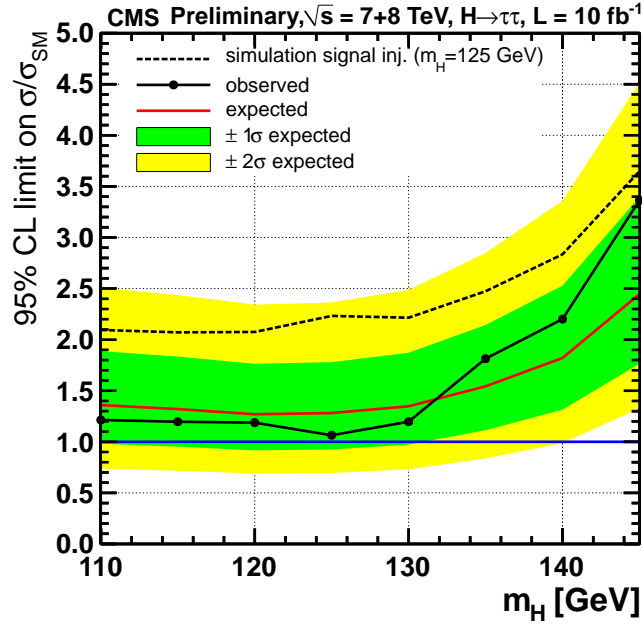
Figure 7.24: Expected and observed 95% CL exclusion limits on the SM signal strength modifier as a function of M_H. The expected exclusion limit in the presence of a SM Higgs boson with $M_H = 125$ GeV is shown superimposed. Figure published in Ref. [95].

for the decays $H \to WW^{(*)}$ and $H \to ZZ^{(*)}$ in one of the final states i)–iii). The analysis is also sensitive to ZH production, where the Higgs boson decays to b–quarks and the Z to τ–leptons. The statistical interpretation of the results is based on a binned fit to the output of a multivariate analysis (a Neural Network for the $\mu\tau0$ channel, Boosted Decision Trees for the other two). In the absence of a signal, exlusion limits on a common signal strength modifier have been set. A signal with a cross–section between a factor of 7 and 30 larger than in the SM is ruled out at 95% CL over the whole search range. Figure 7.25 shows the observed and expected exclusion limit from the combined analysis as a function of M_H.

The CDF analysis considers two final states ($\tau_\ell\tau_h$, $\ell = e, \mu$), which are further split in two categories each, depending on the presence of exactly one or at least two jets. The search makes use of up to 6.0 fb^{-1} of integrated luminosity. It is sensitive to GGF, VBF, and associated VH production, followed by the decay $H \to \tau\tau$. The final event selection relies on a set of BDTs trained to discriminate $H \to \tau\tau$ events from SM backgrounds with fake taus. A second set of BDTs classifies events as being more $H \to \tau\tau$
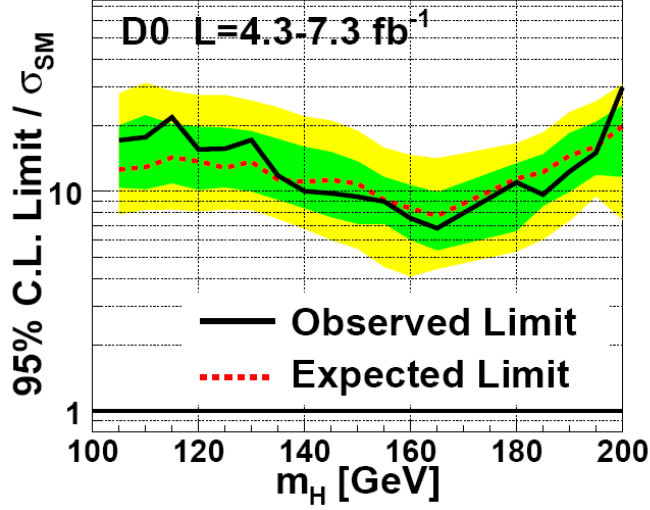
Figure 7.25: Expected and observed 95% CL exclusion limits on the SM signal strength modifier as a function of M_H, from the combined $H \rightarrow \tau\tau$ searches with the D0 experiment (from Ref. [116]).

or $Z \rightarrow \tau\tau$ like. A binned fit to the output of the second type of BDT is then used to set limits. The observed exclusion limits are consistent with the expectation from the background–only hypothesis (Fig. 7.26). The value of the expected (observed) limit for a Higgs boson mass of 120 GeV is 15.3 (14.6) times the SM expectation.

The ATLAS experiment has searched for $H \rightarrow \tau\tau$ decays in a data set corresponding to an integrated luminosity $\mathcal{L} = 4.7$ fb^{-1}. A total of three channels are separately analyzed: $\tau_{lep}\tau_{lep}$, where both taus decay leptonically in final states with a di–electron, a di–muon, or an electron–muon pair, $\tau_{had}\tau_{lep}$, where one tau decays leptonically into an electron or muon and the other decays semi–leptonically, and $\tau_{had}\tau_{had}$, where both taus decay semi–leptonically. No significant excess over the expected SM background is observed in the Higgs boson mass range of $[100, 150]$ GeV. The observed (expected) upper limits, at 95% CL, on the cross–section times the branching ratio for $H \rightarrow \tau^+\tau^-$ are found to be between 2.9 (3.4) and 11.7 (8.2) times the SM prediction for this mass range. Figure 7.27 shows the observed and expected limits on the signal strength modifier as a function of the Higgs boson mass.

Compared to other existing searches at hadron colliders, the CMS analysis [95] provides at present the world's most stringent $H \rightarrow \tau\tau$ result.
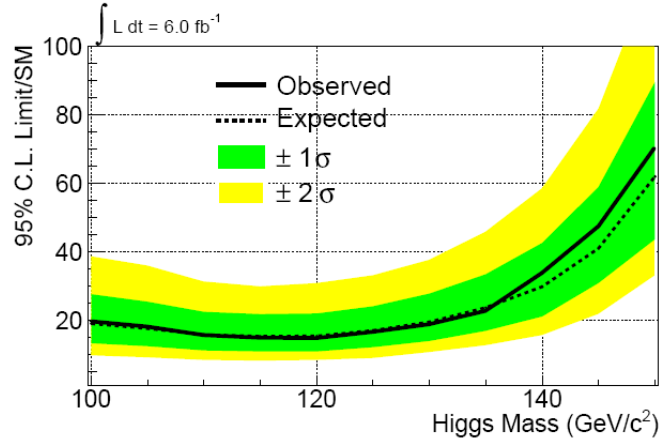
Figure 7.26: Expected and observed 95% CL exclusion limits on the SM signal strength modifier as a function of M_H, from the combined $H \to \tau\tau$ searches with the CDF experiment (from Ref. [117]).
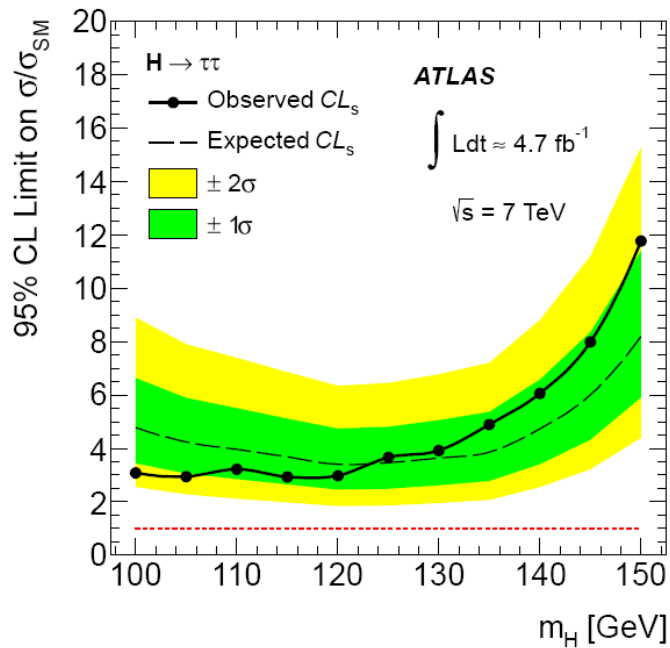
Figure 7.27: Expected and observed 95% CL exclusion limits on the SM signal strength modifier as a function of M_H, from the combined $H \to \tau\tau$ searches with the ATLAS experiment (from Ref. [118]).

7.12.3 The latest exclusion limits and the discovery

The CMS discovery paper [96] incorporates the results from the SM Higgs boson search in the various decays to gauge bosons ($\gamma\gamma$, ZZ^*, WW^*), as well as decays to fermions (b–quarks and τ–leptons). A main emphasis is put on the most sensitive and high mass resolution channels, i.e. $H \to \gamma\gamma$ and $H \to ZZ^* \to 4\ell$ ($\ell = e, \mu$). The decays in these channels imply that the boson is neutral. The decay into a pair of photons disfavors the $J = 1$ assignement, in agreement with Yang's theorem [119]. The combination of all channels shows that the SM Higgs boson is ruled out at 95% CL in the range $[110, 121.5]$ and $[128, 600]$ GeV. In the intermediate interval, a broad excess of events is observed, consistent with the expectation from a SM Higgs boson with a mass around 125 GeV. The high–resolution channels ($\gamma\gamma$ and 4ℓ) provide a rather precise mass measurement. The observed (expected) local significance for an hypothesized Higgs boson with $M_H = 125.5$ GeV is found to be 5.0σ (5.8σ). When accounting for the "look elsewhere effect" (LEE) in the search window 110–145 GeV, a global significance of 4.6σ is measured. The excess is essentially driven by the high–resolution channels: $\gamma\gamma$ (4.1σ observed, compared to a signal+background expectation of 2.8σ) and the four–leptons (3.1σ observed, compared to a signal+background expectation of 3.6σ). The WW^*, $\tau\tau$ and bb channels show less compatibility with the signal+background hypothesis than expected in the presence of the SM Higgs boson with $M_H = 125$ GeV. The decay channels into fermions don't show any significant departure from the background–only hypothesis at this stage. This is clearly illustrated by Fig. 7.28, which reports the best–fit values of μ in each decay channel: all the decay channels into gauge boson feature a consistent compatibility with a SM–like signal with mass around 125 GeV, whereas the decay channels into b–quarks and τ leptons, though less sensitive, don't show any significant departure.

When combining all channels together, the local significance of the excess becomes 5.0σ, compared to an expectation of 5.8σ. When performing a combined maximum–likelihood fit to all channels, with M_H and μ floating in the fit, the model–dependent best–fit value for the mass of the newly discovered resonance is measured to be 125.3 ± 0.4(stat.) ± 0.5(syst.), assuming the corresponding Higgs boson branching ratios. At a value of $M_H = 125.5$ GeV, the best–fit value of the signal strength modifier is measured to be $\mu^{fit} = 0.87 \pm 0.23$, i.e. consistent within 1σ with the SM Higgs boson expectation.

The ATLAS Collaboration has reported a consistent observation of a new particle with mass around 125 GeV [120]. The results are based on a sample corresponding to integrated luminosities of up to 4.8 fb^{-1}, at 7
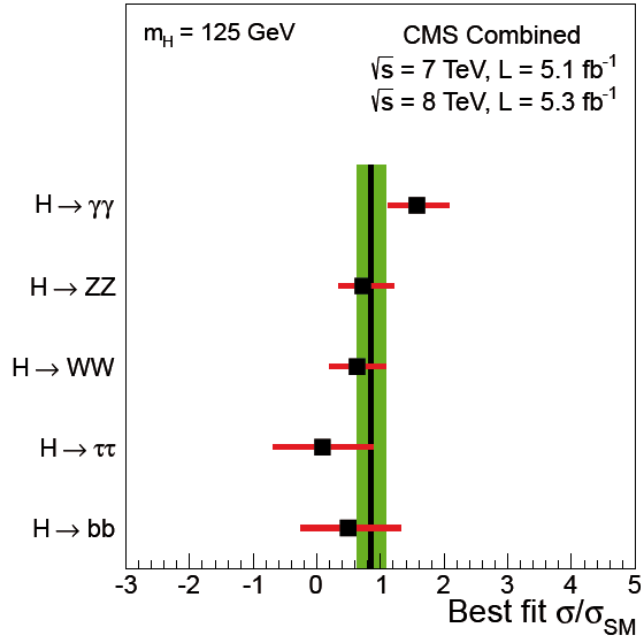
Figure 7.28: Best–fit value of the signal strength modifier μ for $M_H = 125$ GeV, broken–up by decay channel (from Ref. [96]).

TeV, and 5.8 fb^{-1}, at 8 TeV. The SM Higgs boson is searched in the same final states illustrated above. The SM Higgs boson is excluded at 95% CL in the range $[111, 122]$ and $[131, 559]$ GeV, compared to an expectation of $[110, 600]$ GeV. The region $[122, 131]$ cannot be excluded because of a broad excess of events, consistently observed in the three most sensitive channels ($\gamma\gamma$, ZZ^*, WW^*). The observed (expected) local significance of the excess for $M_H = 126.5$ GeV is 5.9σ (4.9σ), which is estimated to decrease to 5.1σ once the LEE effect in the entire search range is accounted for. The best–fit value of the newly discovered resonance mass is $126.0 \pm 0.4(\text{stat.}) \pm 0.4(\text{syst.})$, from model–independent fits to the $\gamma\gamma$ and four–leptons channels. The signal strength modifier for this value of mass is $\mu^{fit} = 1.4 \pm 0.3$, about one standard deviation from the SM expectation.

The CDF and D0 Collaborations at the Fermilab TeVatron $p\bar{p}$ collider have recently made public their latest combined results on the search for the SM Higgs boson based on up to 10 fb^{-1} of collision data [121]. In the absence of a signal, the two experiments together expect to exclude at 95% CL a SM Higgs boson with mass in the range $[100, 120]$ and $[139, 184]$ GeV. A broad excess in the region $[120, 135]$ makes the exclusion limit weaker than expected: the 95% CL exclusion intervals on M_H are measured to be $[100, 103]$ and

[147, 180] GeV. The excess is mostly concentrated in the $b\bar{b}$ channel ($V + b\bar{b}$, $V = W, Z$), where a local (global) significance of 3.3σ (3.1σ) is measured [122]. Assuming that the excess arises from a SM–like Higgs boson with $M_H = 125$ GeV, the best–fit value for the cross–section times branching ratio is somehow larger, though statistically compatible, with the theoretical expectation: $0.23^{+0.09}_{-0.08}$ pb, compared to an expected value of 0.12 ± 0.01 pb.

More data will be necessary to unravel the nature of the newly discovered particle. In particular, a measurement of its quantum numbers (J^{CP}) and couplings to the SM particles will be a first important step to understand if this is indeed the Higgs boson predicted by the Standard Model. In this respect, measuring the decay rate into taus will provide a unique chance to probe the coupling of this new boson to leptons.

Appendix A

Control plots

In this Appendix, control plots for the identification and kinematical variables of objects used in the analysis are presented. Plots refering to the $\tau_e \tau_h$ ($\tau_\mu \tau_h$) channel are reported on the top (bottom).
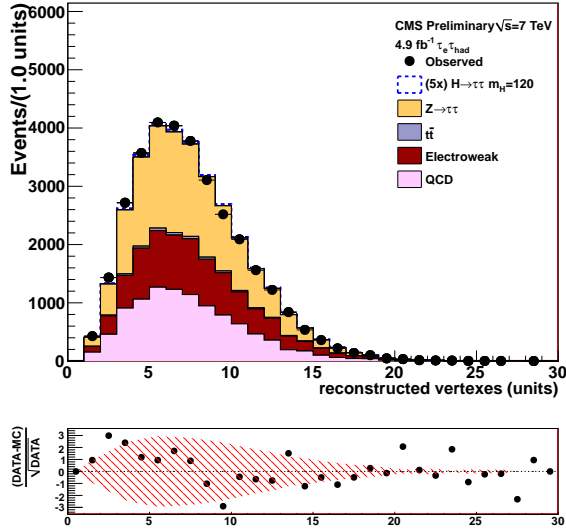
(a)
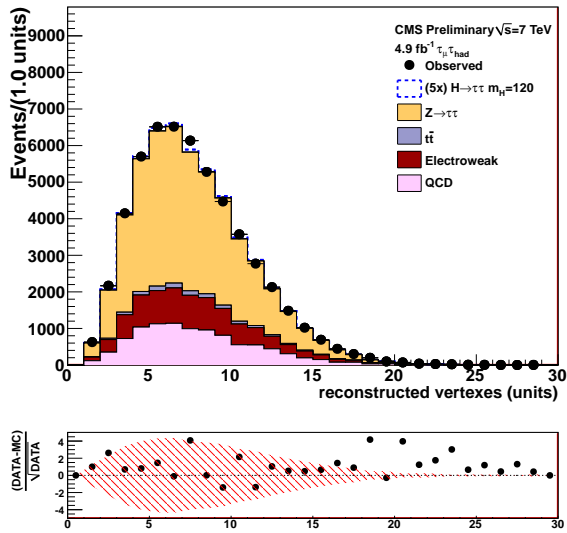
(b)

Figure A.1: Multiplicity of primary vertices.
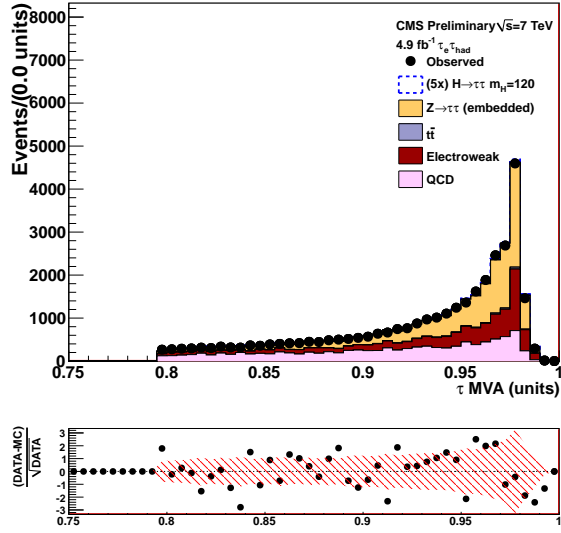
(a)
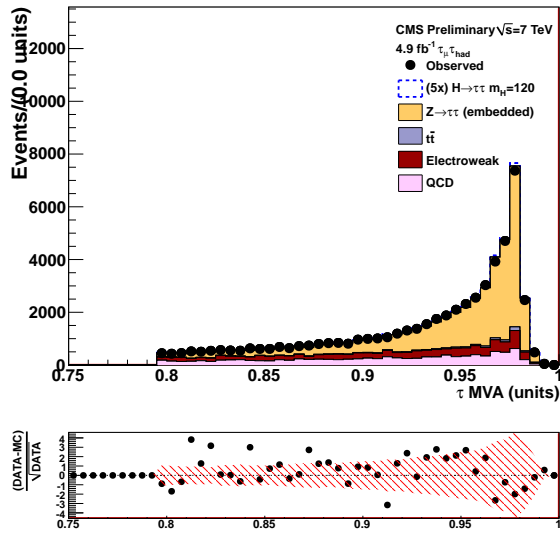
(b)

Figure A.2: Output of the BDT used for τ_h isolation

212
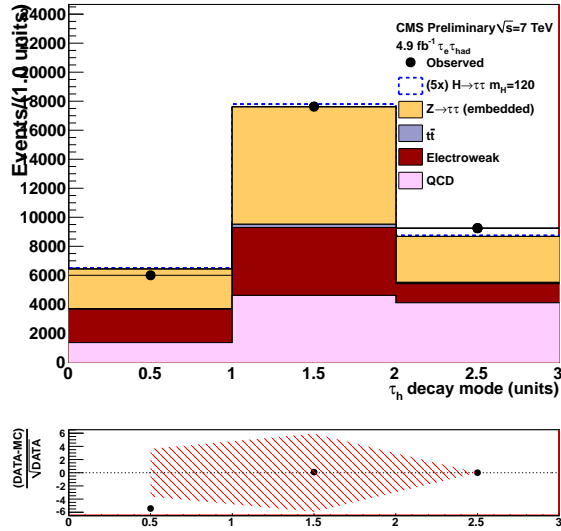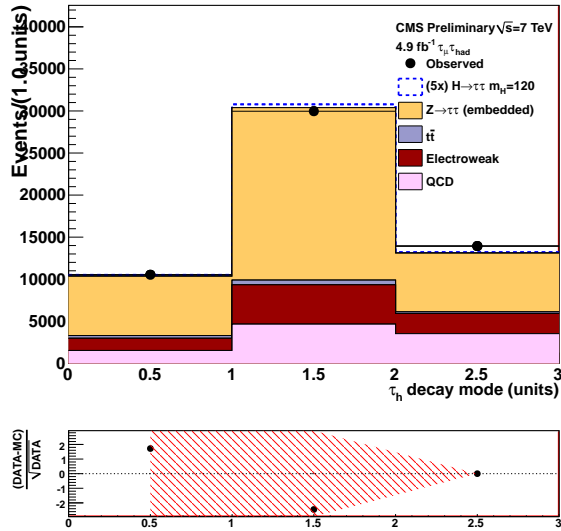
Figure A.3: Decay modes of the τ_h (0 = one prong without π^0, 1 = one prong with π^0, 2 = three prong).

213
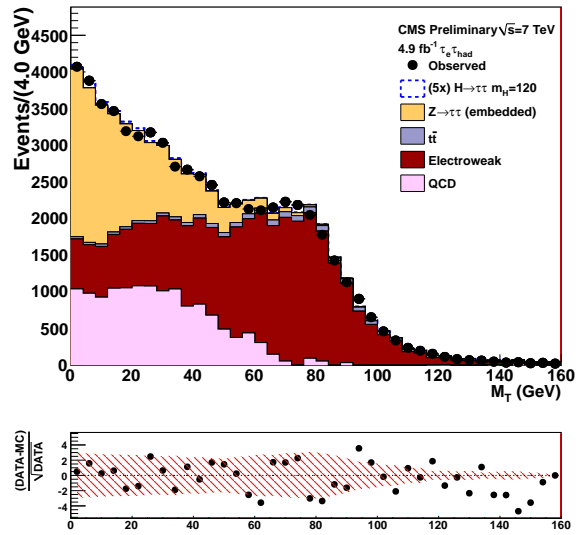
(a)
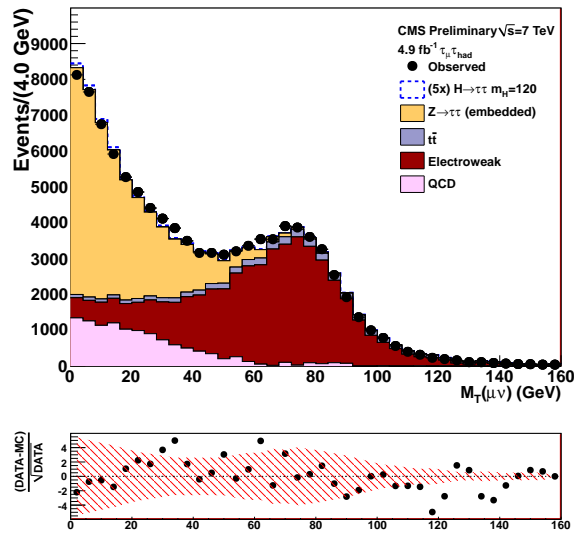
(b)

Figure A.4: Transverse mass $M_T^{\ell\nu}$.

214
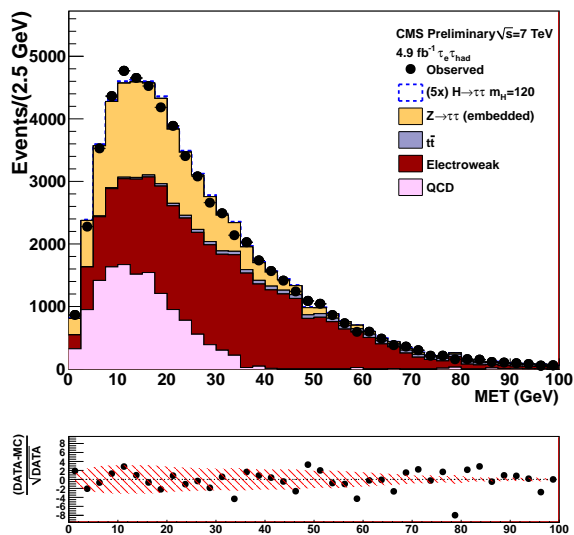
(a)
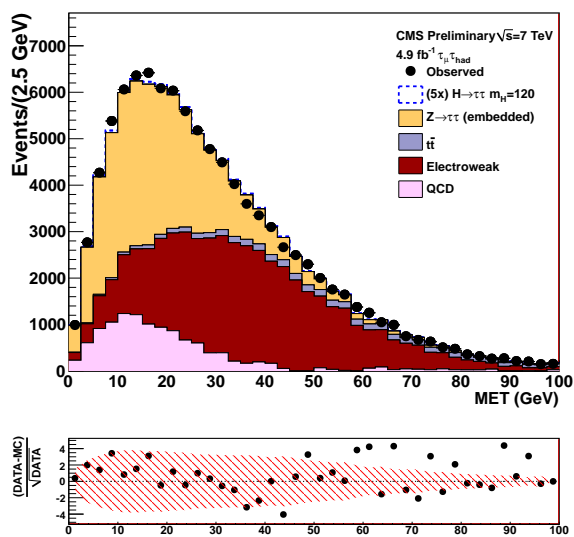
(b)

Figure A.5: E_T^{miss} before applying the $M_T^{\ell\nu}$ cut.
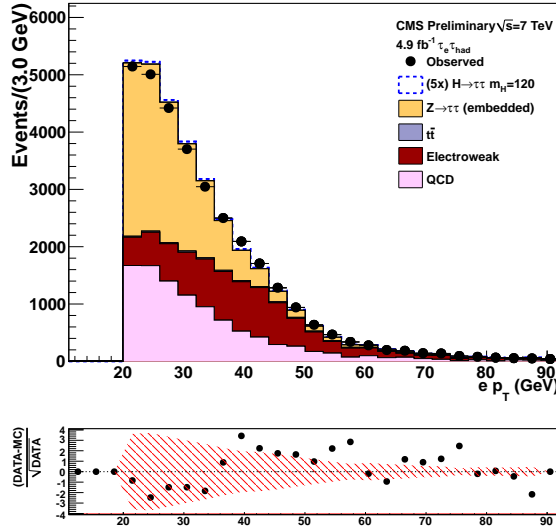
(a)
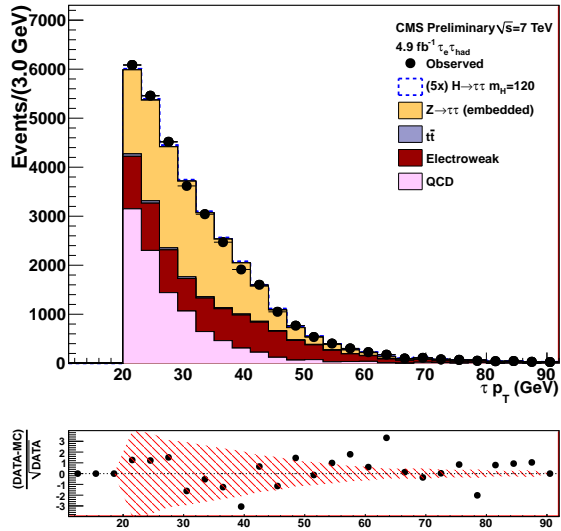
(b)

Figure A.6: p_T of the τ_e (a) and of the τ_h (b).

216

(a)

(b)

Figure A.7: η of the τ_e (a) and of the τ_h (b).

217
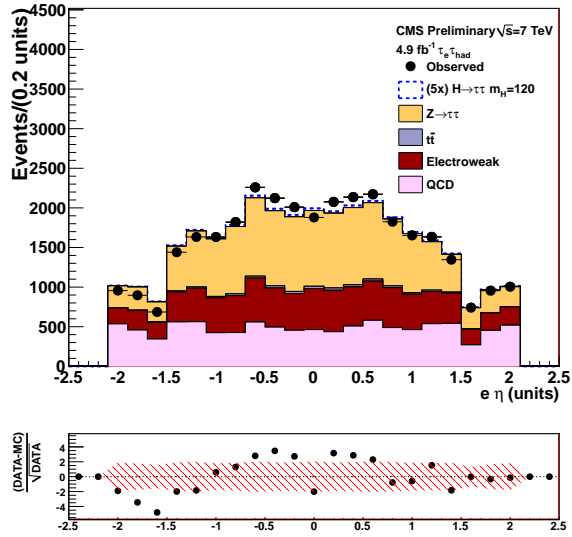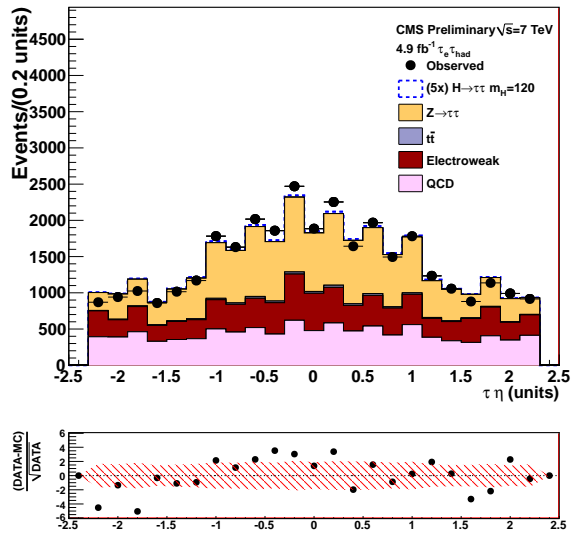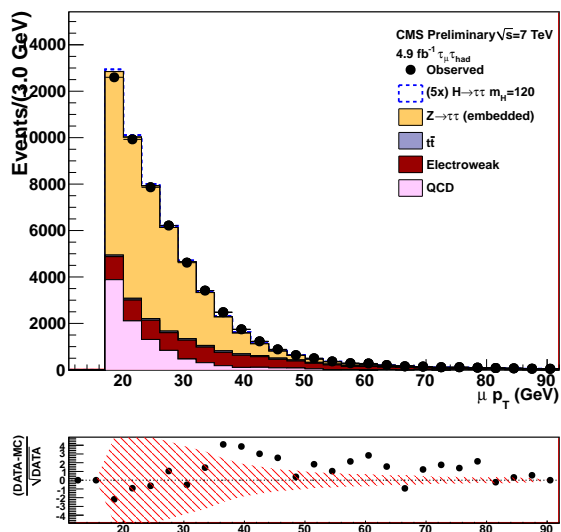
(a)
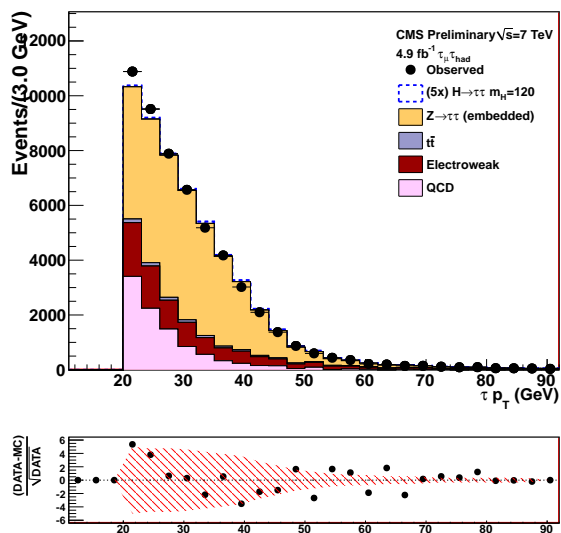
(b)

Figure A.8: p_T of the τ_μ (a) and of the τ_h (b).

(a)

(b)

Figure A.9: η of the τ_μ (a) and of the τ_h (b).

219
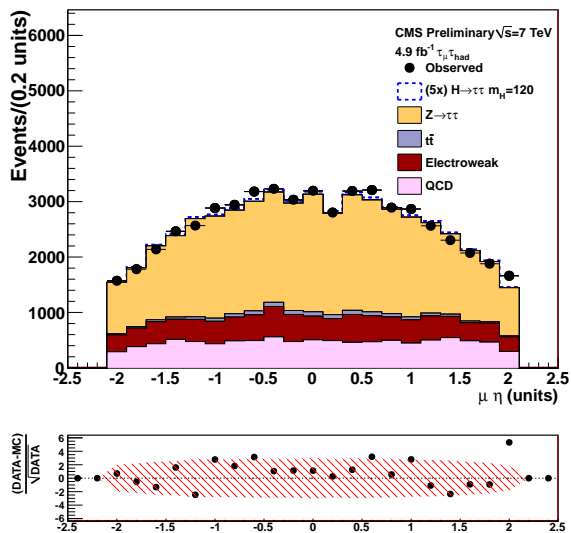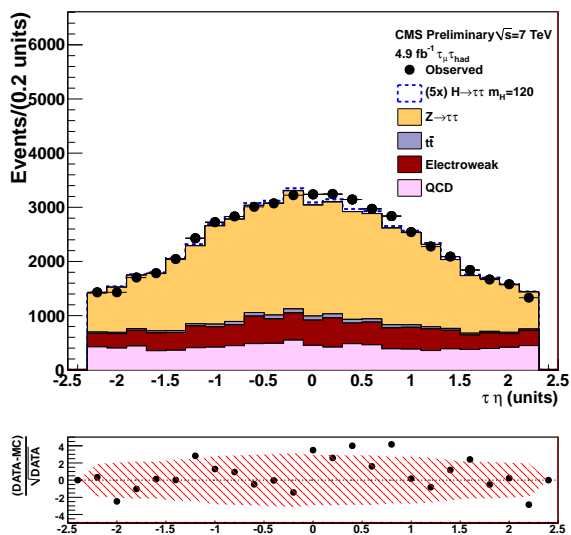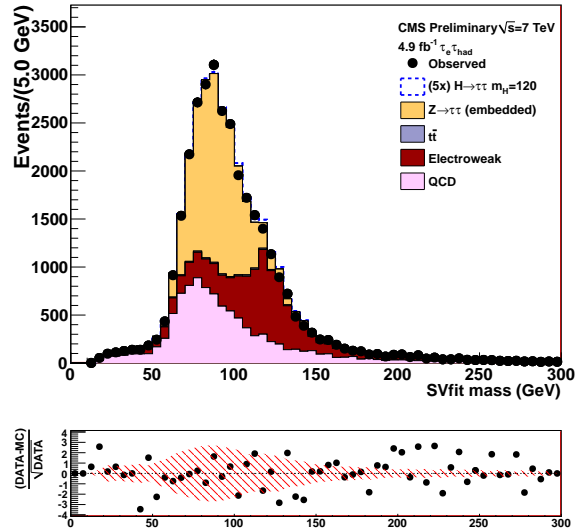
(a)
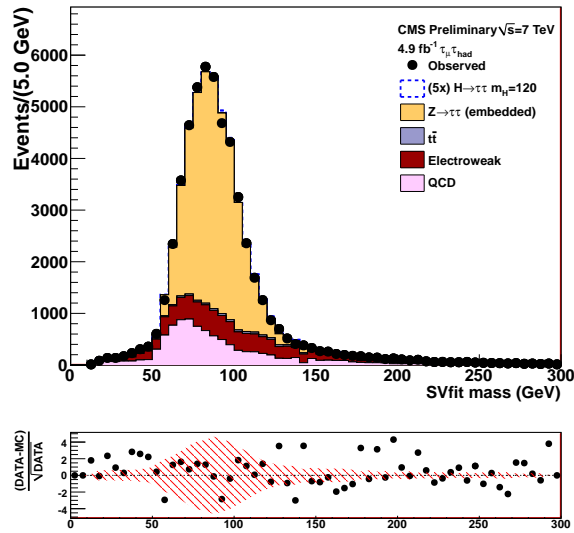
(b)

Figure A.10: SVfit di–tau mass.
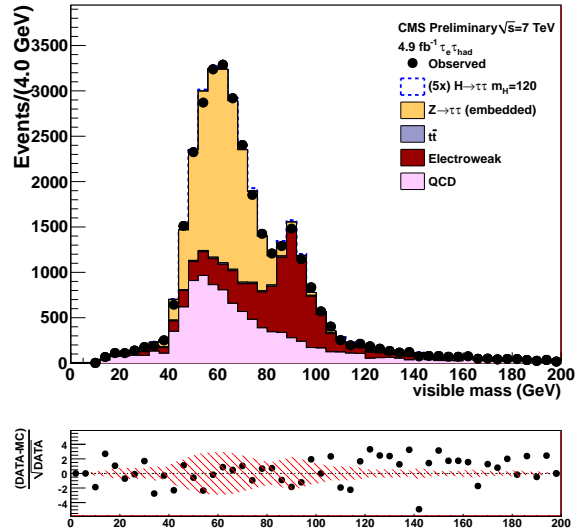
(a)
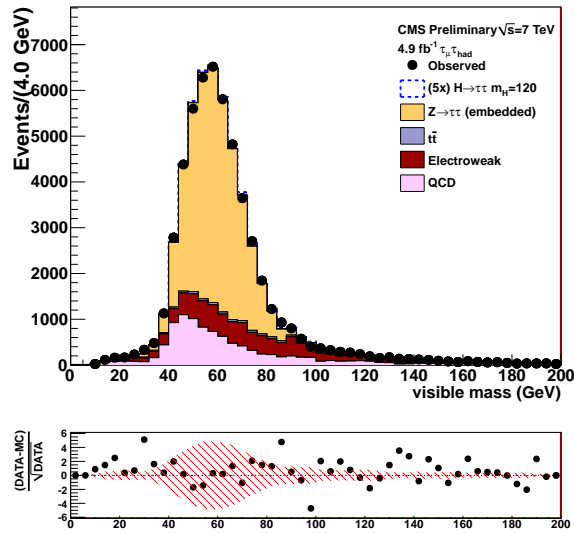
(b)

Figure A.11: Visible di–tau mass.

221
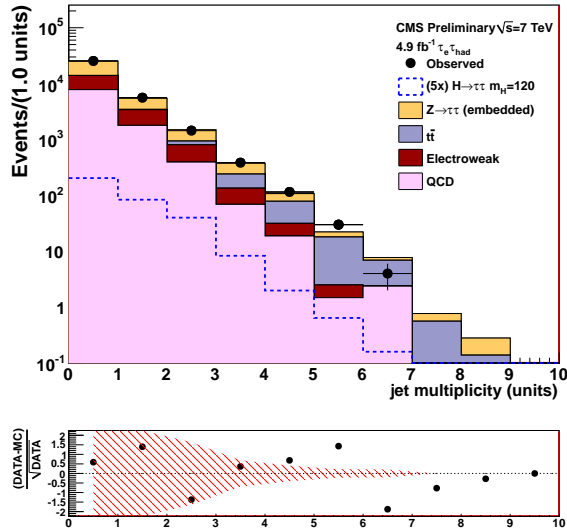
(a)
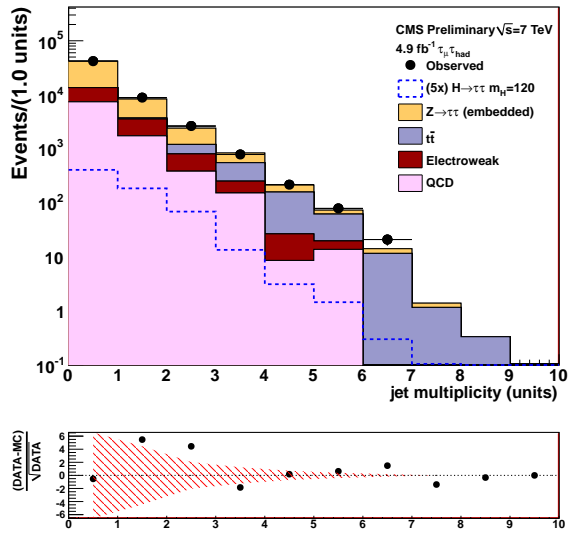
(b)

Figure A.12: Multiplicity of jets with p_T in excess of 30 GeV.
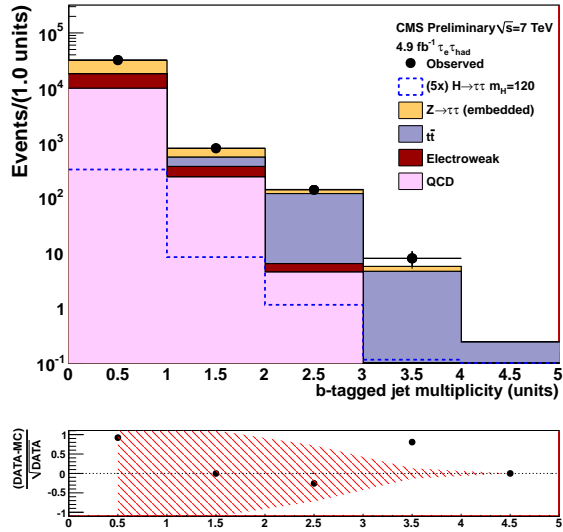
(a)
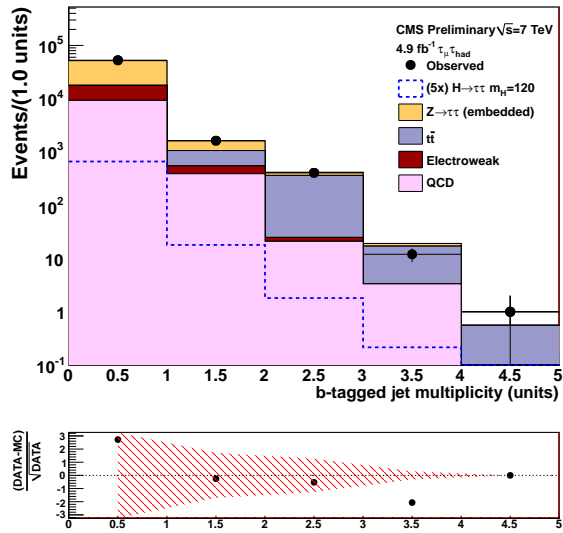
(b)

Figure A.13: Multiplicity of b–tagged jets with p_T in excess of 20 GeV.

223
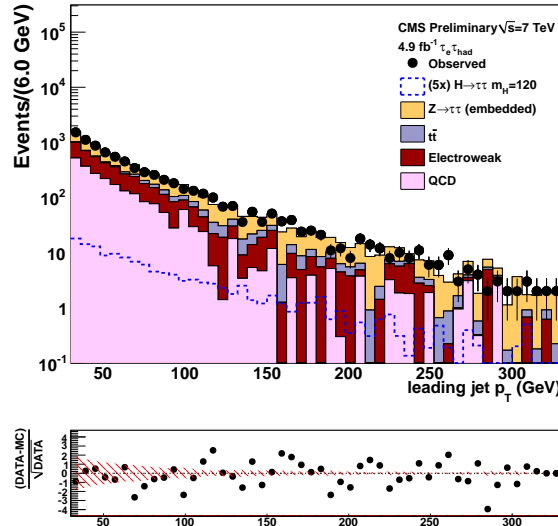
(a)
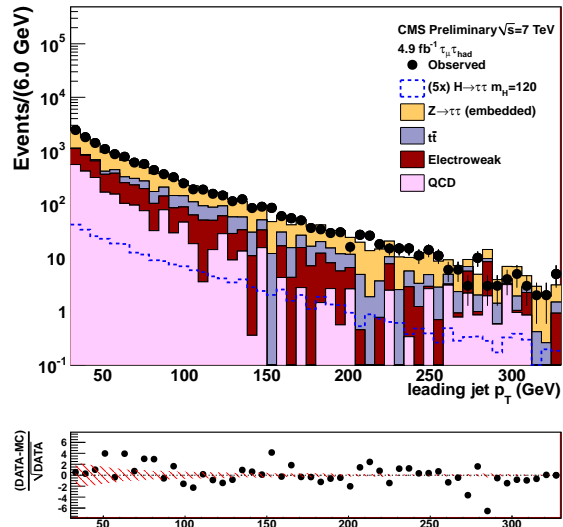
(b)

Figure A.14: p_T of the leading jet in events with at least one jet with p_T in excess of 30 GeV.
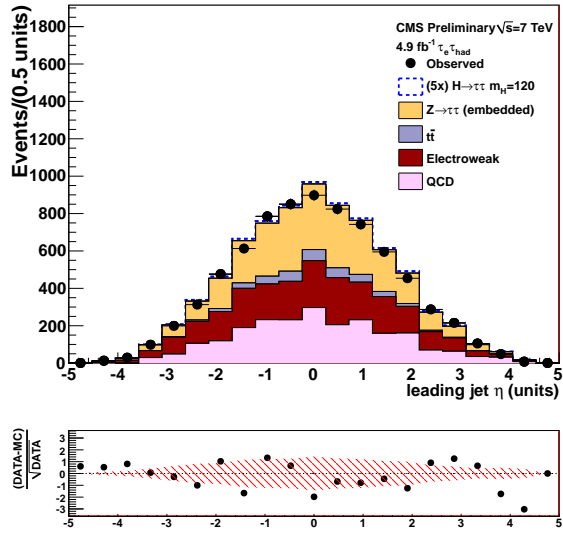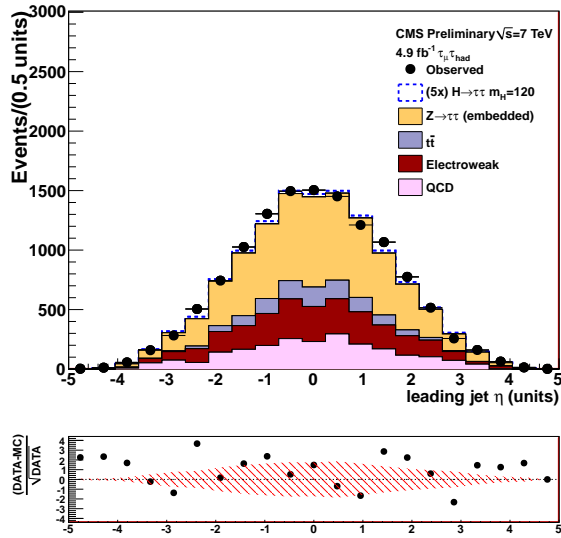
(a)

(b)

Figure A.15: η of the leading jet in events with at least one jet with p_T in excess of 30 GeV.
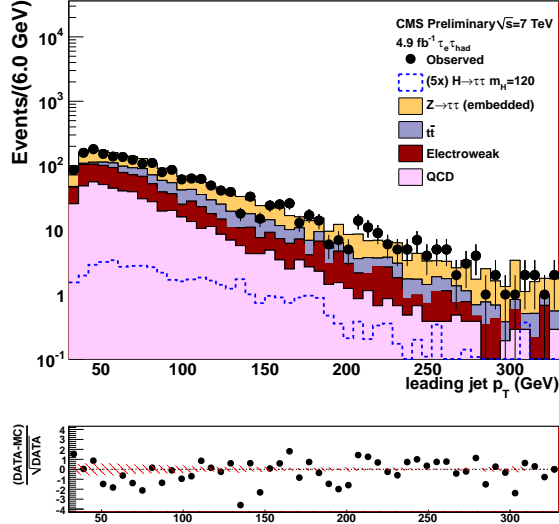
(a)
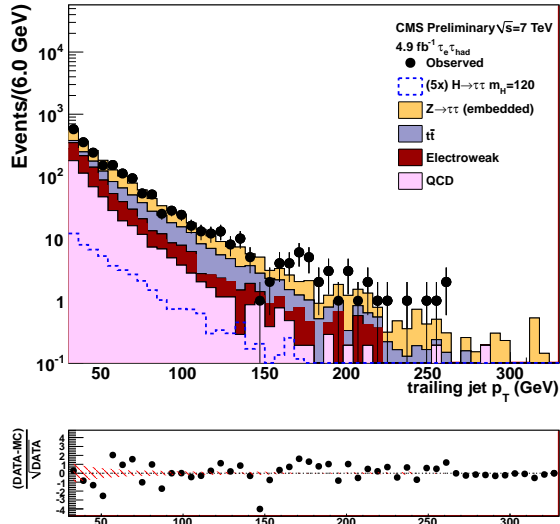
(b)

Figure A.16: p_T of the leading (a) and subleading (b) jets in events of the $\tau_e\tau_h$ channel with at least two jets with p_T in excess of 30 GeV.
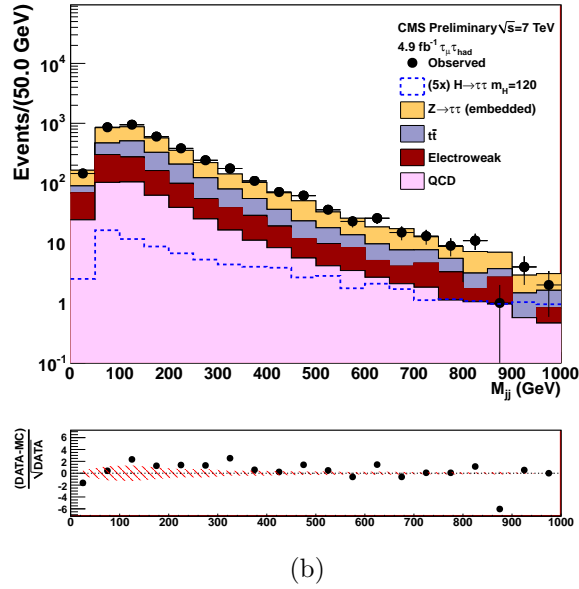
(a)

(b)
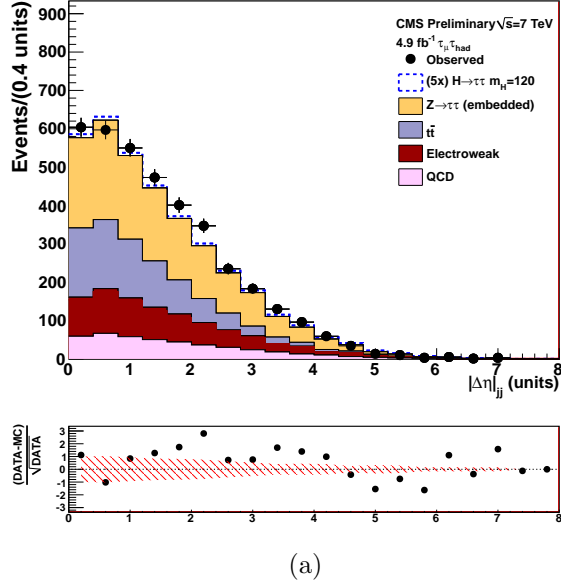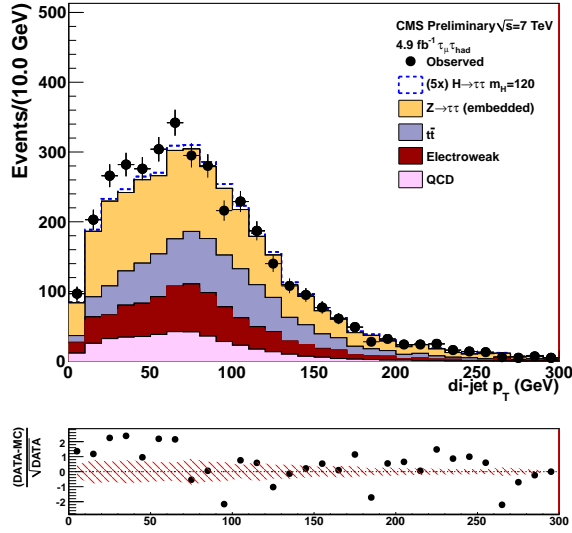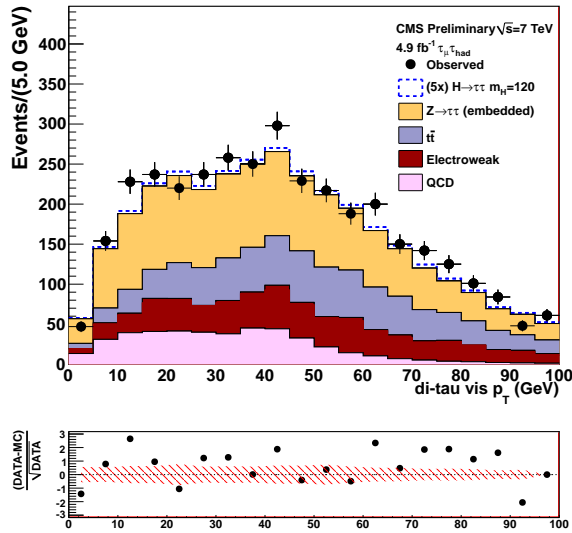
Figure A.17: η of the leading (a) and subleading (b) jets in events of the $\tau_e \tau_h$ channel with at least two jets with p_T in excess of 30 GeV.

(a)

(b)
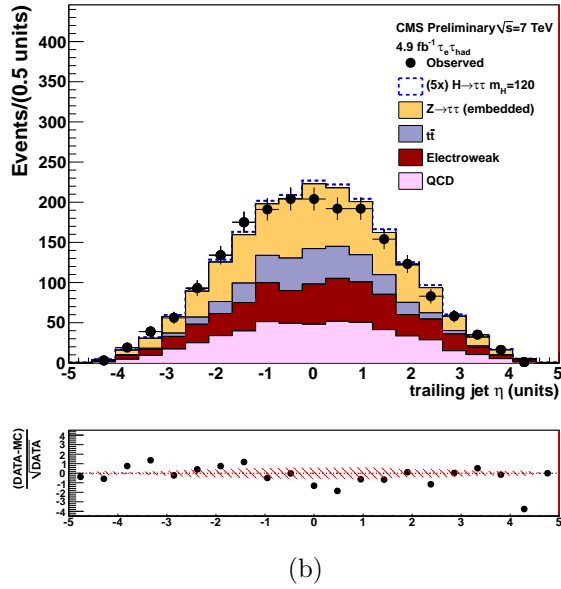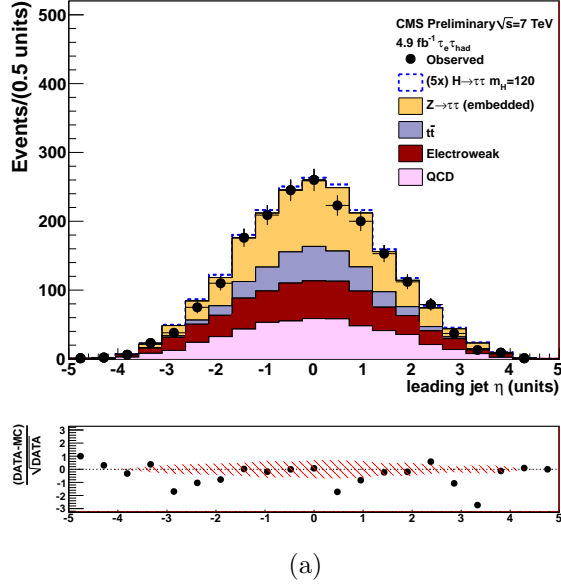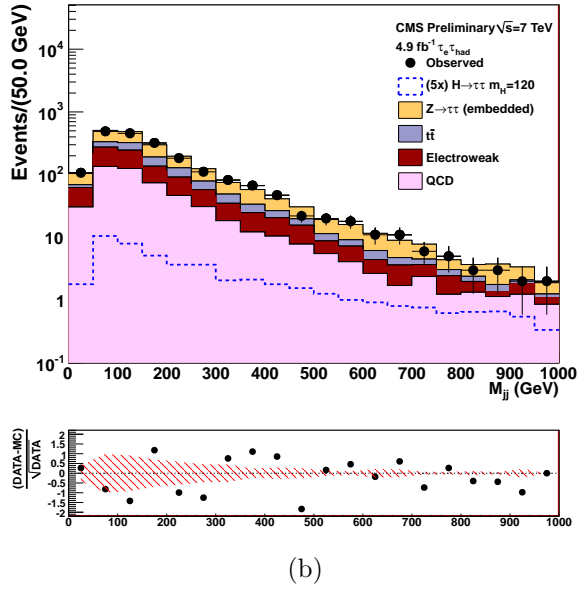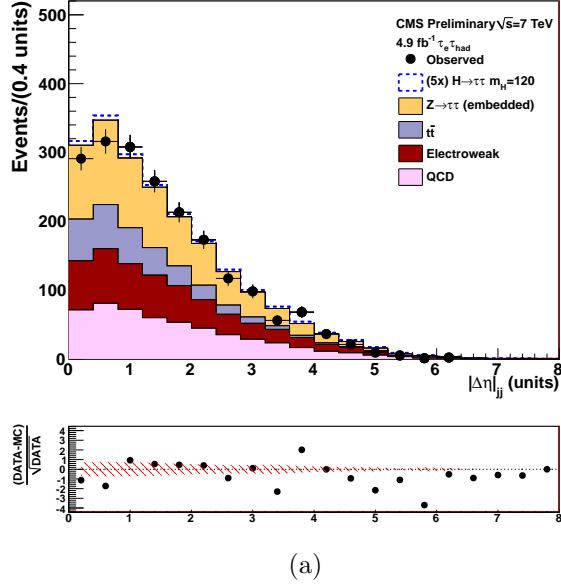
Figure A.18: Distribution of (a) $\Delta\eta_{jj}$ and (b) M_{jj} in events of the $\tau_e\tau_h$ channel with at least two jets with p_T in excess of 30 GeV.
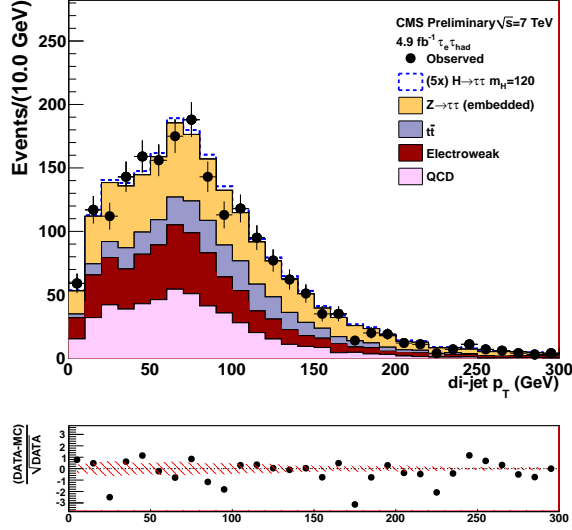
(a)
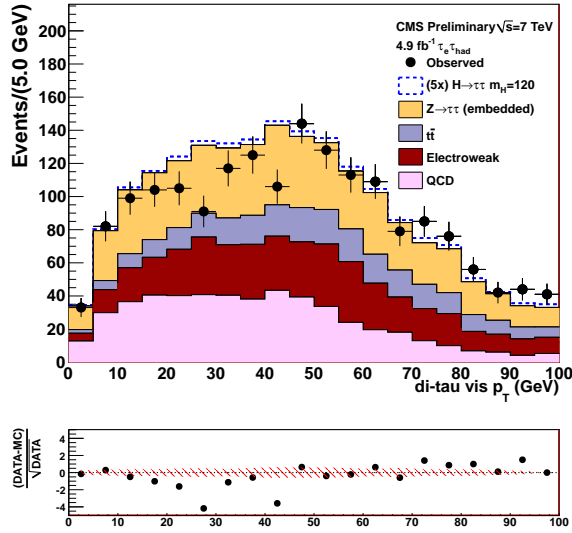
(b)

Figure A.19: Distribution of (a) p_T^{jj} and (b) $p_T^{\tau\tau}$ in events of the $\tau_e \tau_h$ channel with at least two jets with p_T in excess of 30 GeV.
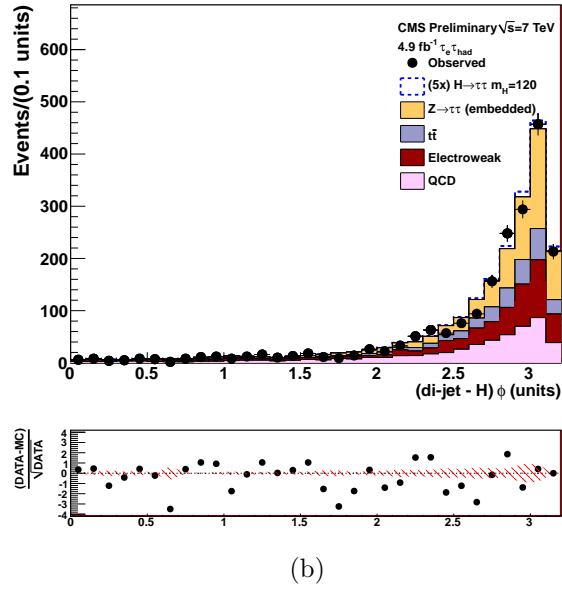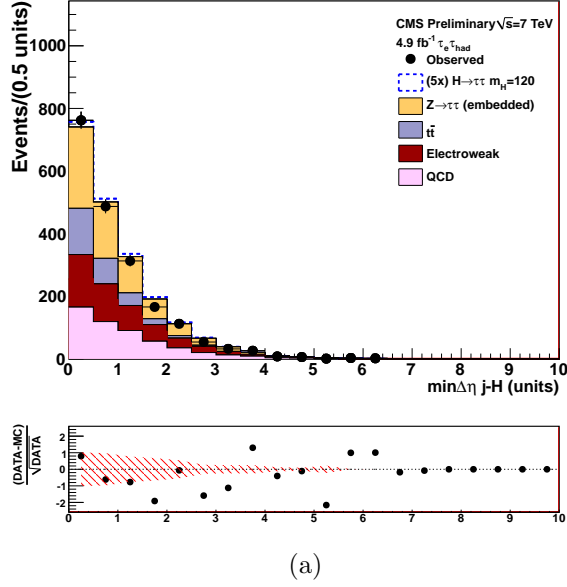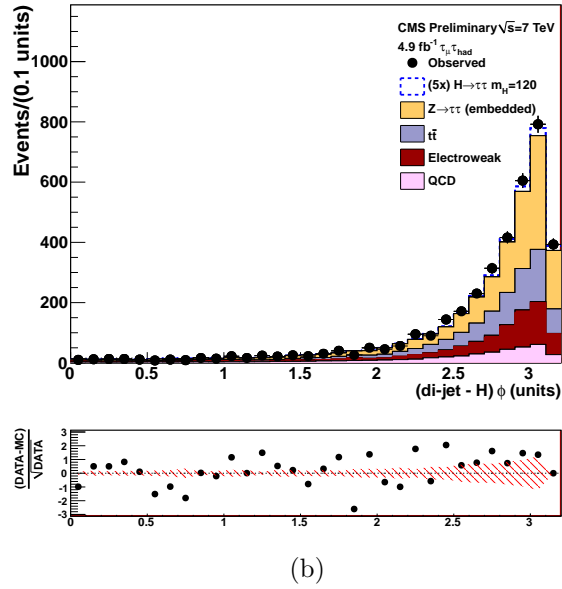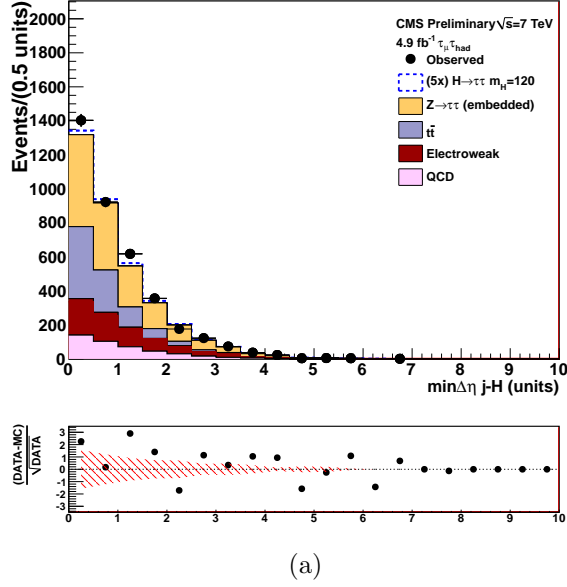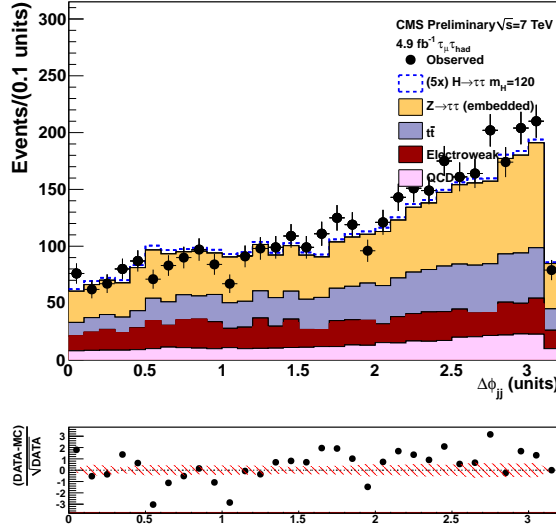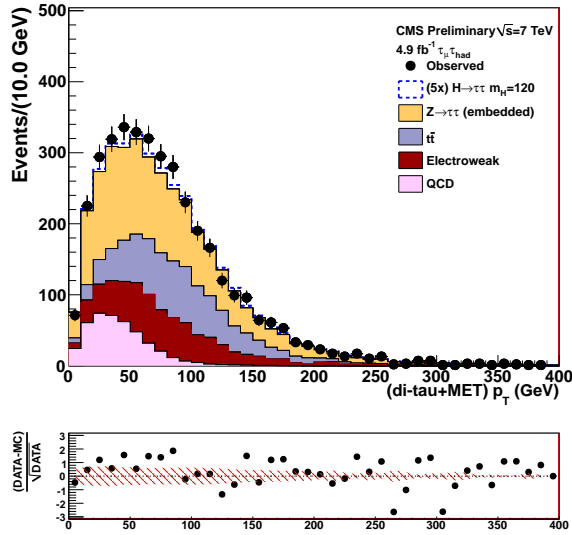
Figure A.20: Distribution of (a) $\Delta\eta_{min}$ and (b) $\Delta\phi_{Hjj}$ in events of the $\tau_e\tau_h$ channel with at least two jets with p_T in excess of 30 GeV.
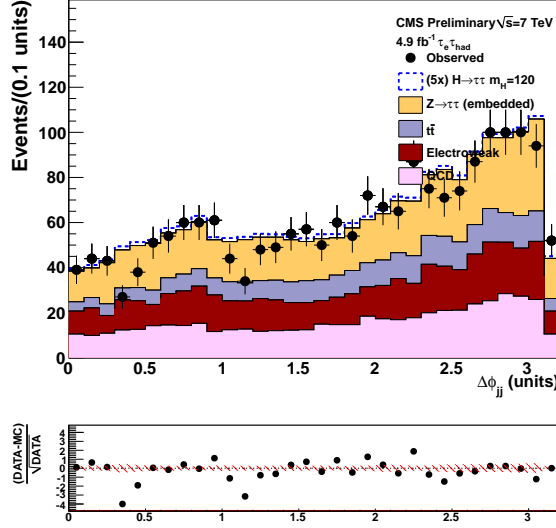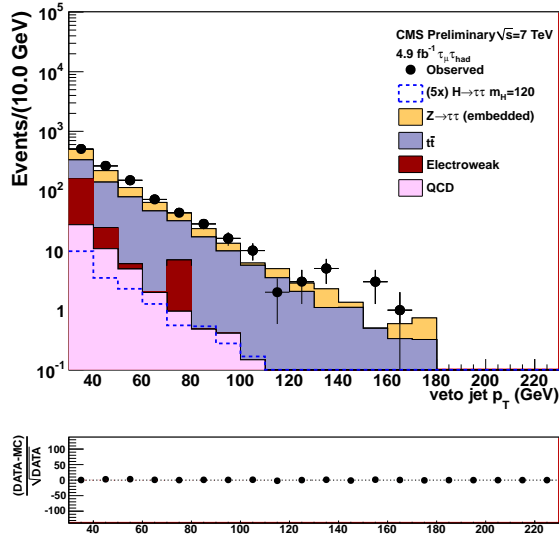
(a)
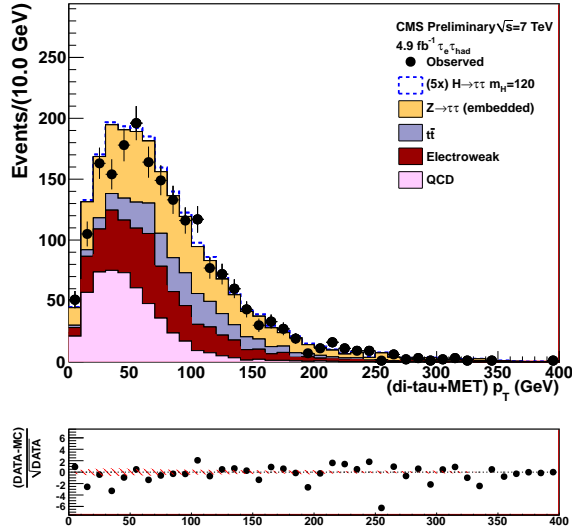
(b)

Figure A.21: Distribution of (a) $\Delta\phi_{jj}$ and (b) p_T^H in events of the $\tau_e\tau_h$ channel with at least two jets with p_T in excess of 30 GeV.
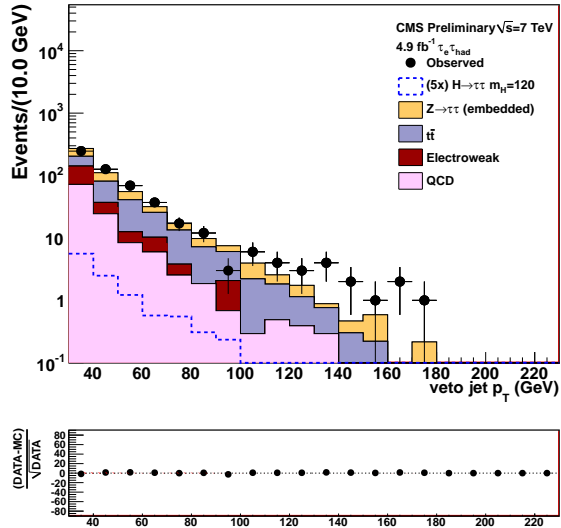
(a)
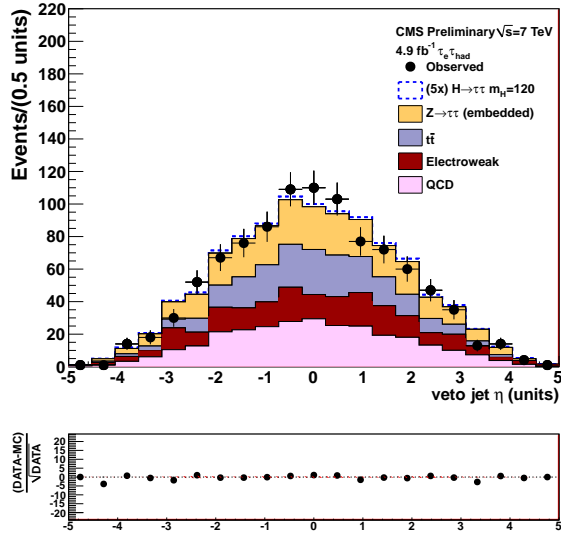
(b)

Figure A.22: Distribution of the (a) p_T and (b) η of the third highest–p_T jet in events of the $\tau_e \tau_h$ channel with at least two jets with p_T in excess of 30 GeV.

232
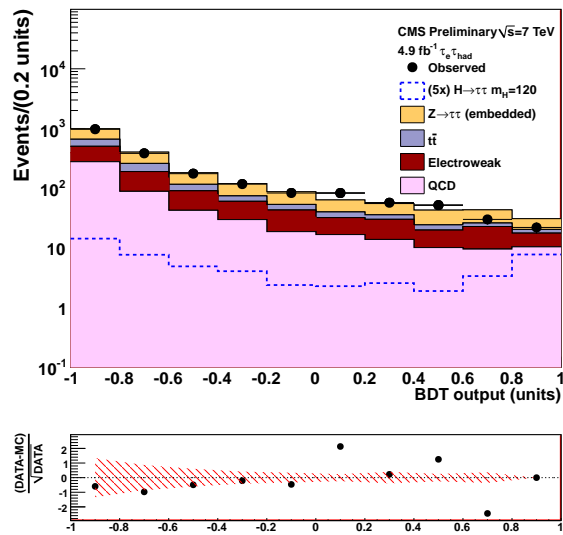
Figure A.23: Distribution of the VBF BDT output in events of the $\tau_e\tau_h$ channel with at least two jets with p_T in excess of 30 GeV.
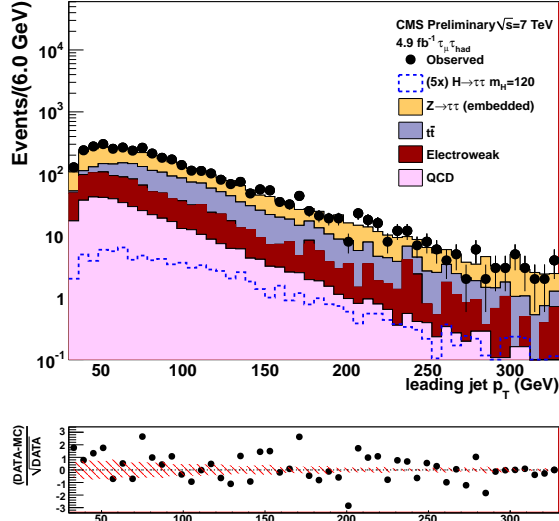
(a)
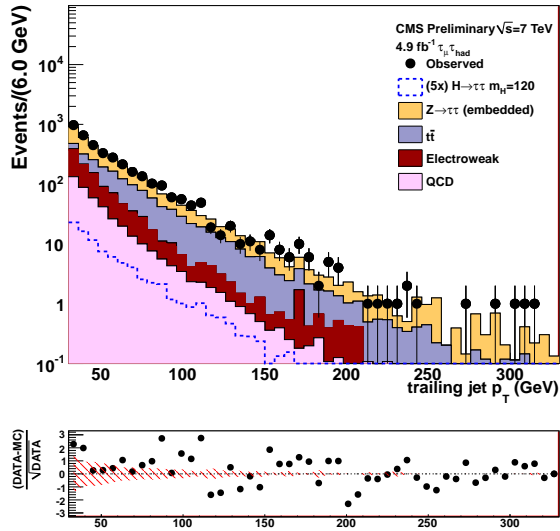
(b)

Figure A.24: p_T of the leading (a) and subleading (b) jets in events of the $\tau_\mu\tau_h$ channel with at least two jets with p_T in excess of 30 GeV.

234

(a)

(b)

Figure A.25: η of the leading (a) and subleading (b) jets in events of the $\tau_\mu\tau_h$ channel with at least two jets with p_T in excess of 30 GeV.

235

(a)

(b)
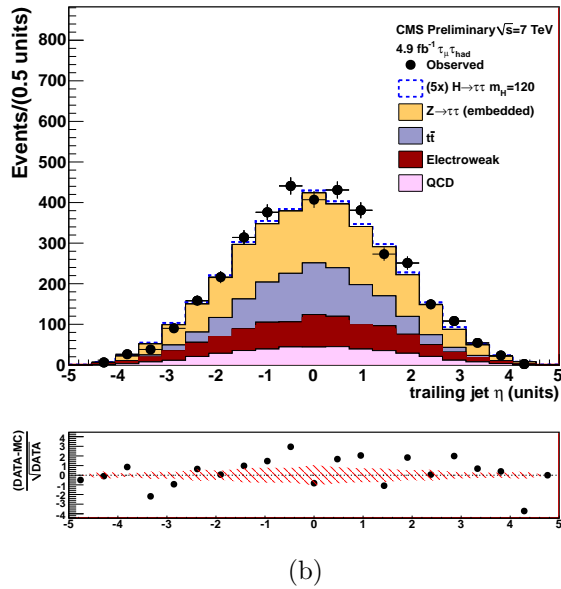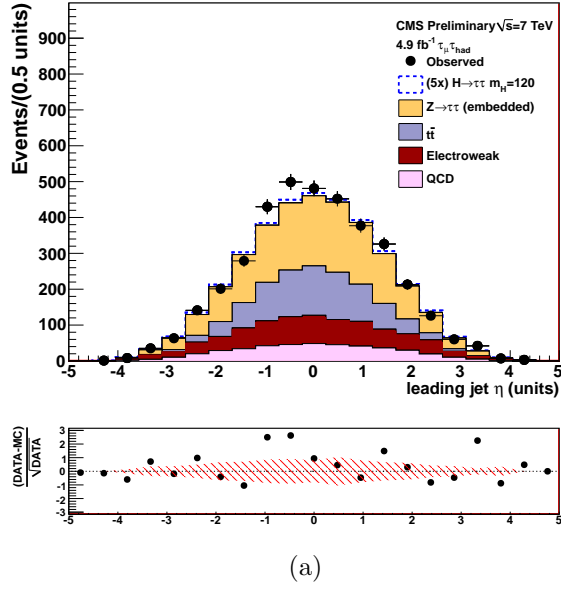
Figure A.26: Distribution of (a) $\Delta\eta_{jj}$ and (b) M_{jj} in events of the $\tau_\mu\tau_h$ channel with at least two jets with p_T in excess of 30 GeV.
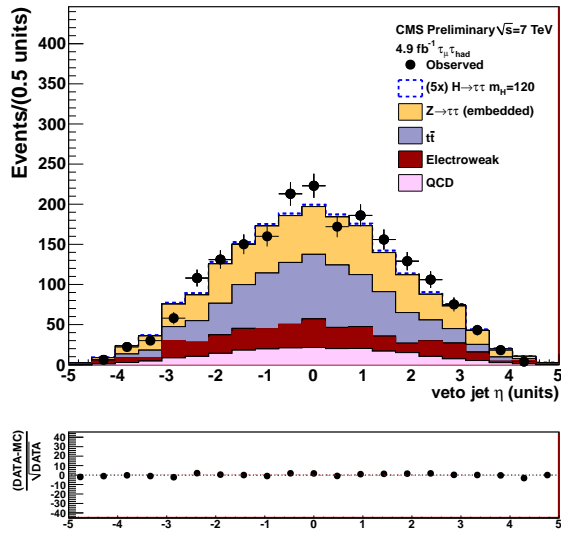
(a)

(b)

Figure A.27: Distribution of (a) p_T^{jj} and (b) $p_T^{\tau\tau}$ in events of the $\tau_\mu \tau_h$ channel with at least two jets with p_T in excess of 30 GeV.
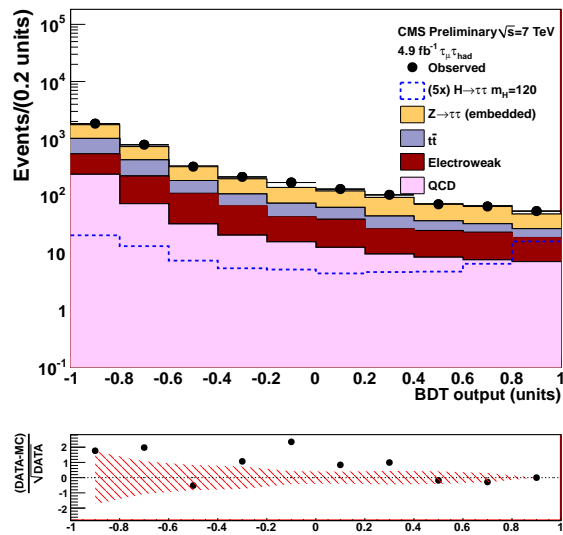
(a)

(b)

Figure A.28: Distribution of (a) $\Delta\eta_{min}$ and (b) $\Delta\phi_{Hjj}$ in events of the $\tau_\mu\tau_h$ channel with at least two jets with p_T in excess of 30 GeV.

(a)

(b)

Figure A.29: Distribution of (a) $\Delta\phi_{jj}$ and (b) p_T^H in events of the $\tau_\mu\tau_h$ channel with at least two jets with p_T in excess of 30 GeV.

(a)

(b)

Figure A.30: Distribution of the (a) p_T and (b) η of the third highest–p_T jet in events of the $\tau_\mu\tau_h$ channel with at least two jets with p_T in excess of 30 GeV.

Figure A.31: Distribution of the VBF BDT output in events of the $\tau_\mu\tau_h$ channel with at least two jets with p_T in excess of 30 GeV.

Appendix B

Study of mass templates

The observed mass distributions in W and $t\bar{t}$ enriched sidebands are compared to the Monte Carlo templates. Alternative templates obtained by varying the energy scale of the fake tau up and down by 3% are superimposed for comparison.
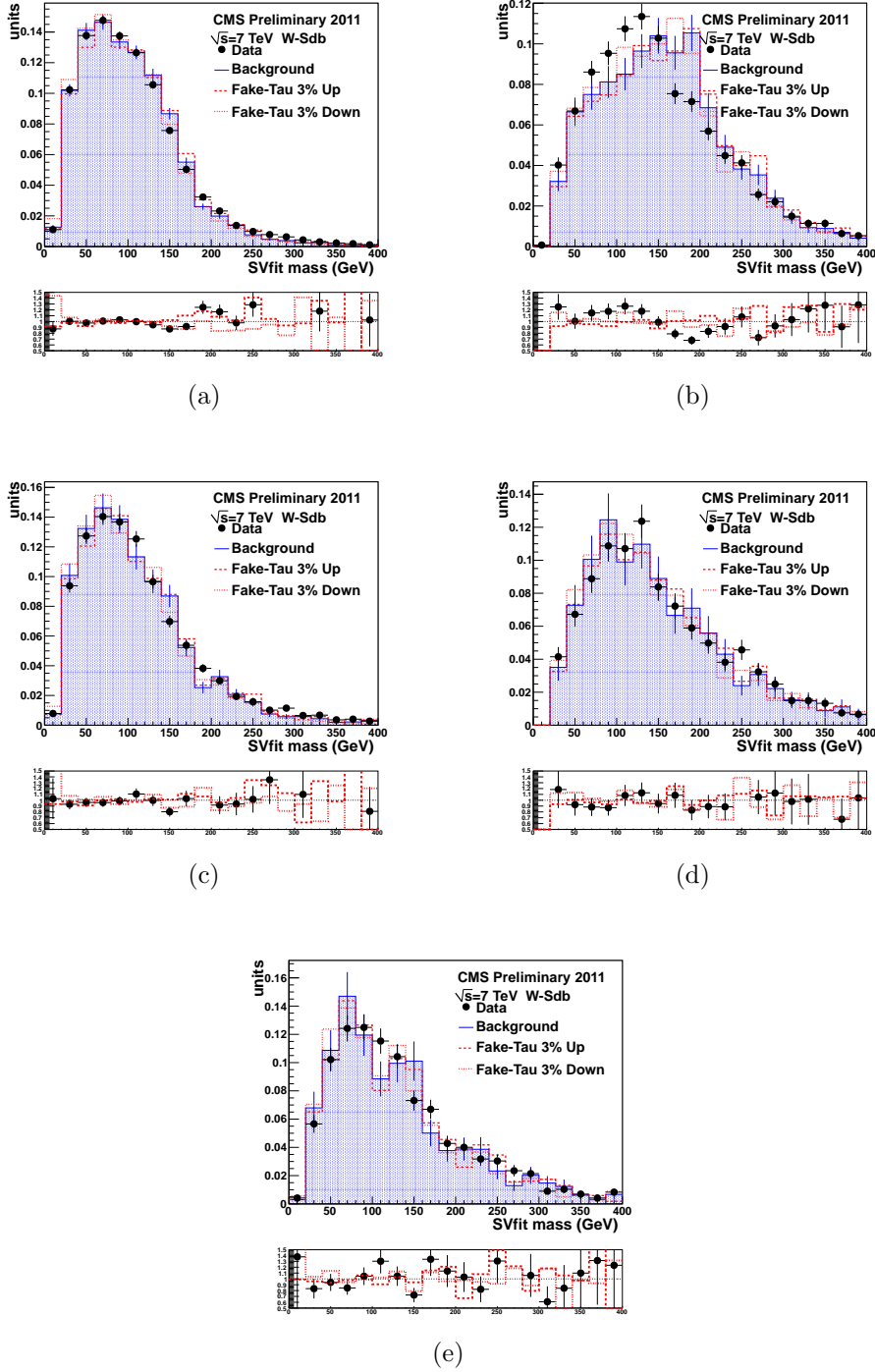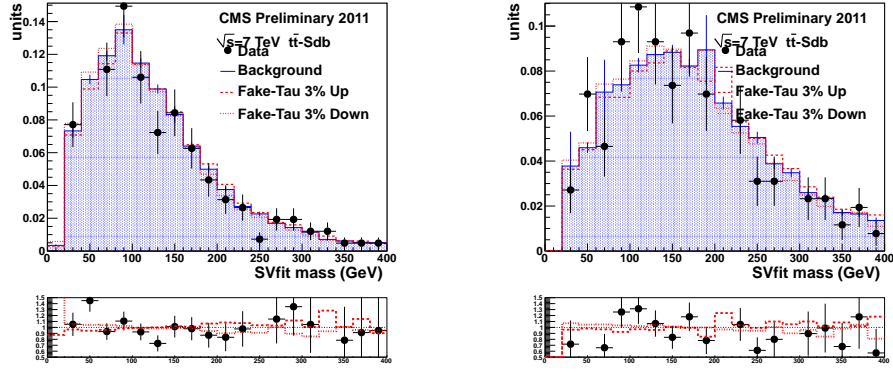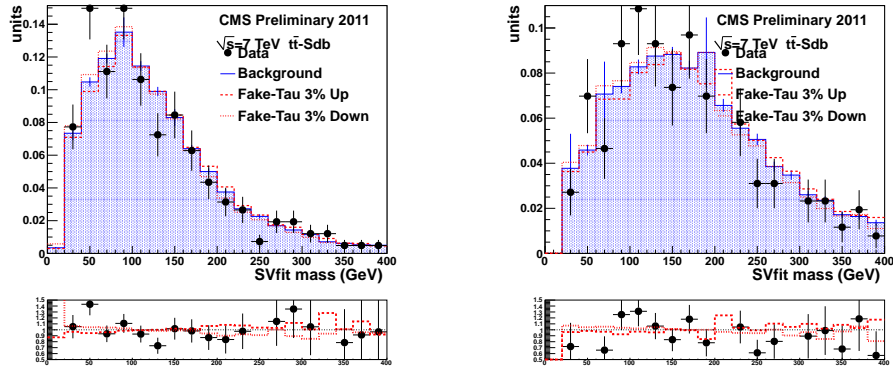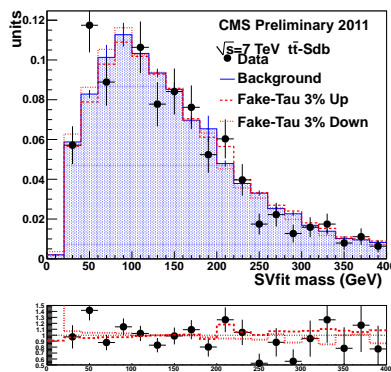
242

(a)

(b)

(c)

(d)

(e)

Figure B.1: Comparison between the observed and expected $\tau_\mu\tau_h$ mass distribution in W–enriched sidebands with ≥ 0 jets (top), ≥ 1 jets (middle) and ≥ 2 jets (bottom).
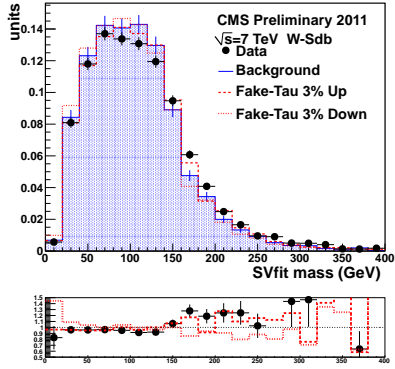
Figure B.2: Comparison between the observed and expected $\tau_\mu\tau_h$ mass distribution in $t\bar{t}$–enriched sidebands with ≥ 0 jets (top), ≥ 1 jets (middle) and ≥ 2 jets (bottom).

(a)

(b)

(c)

(d)

(e)

Figure B.3: Comparison between the observed and expected $\tau_e\tau_h$ mass distribution in W–enriched sidebands with ≥ 0 jets (top), ≥ 1 jets (middle) and ≥ 2 jets (bottom).
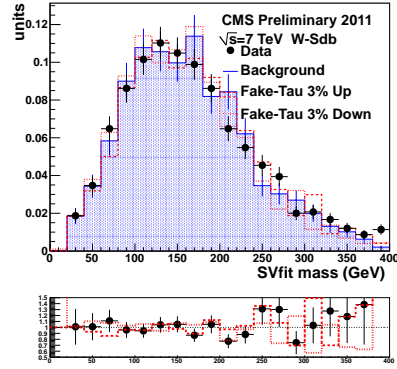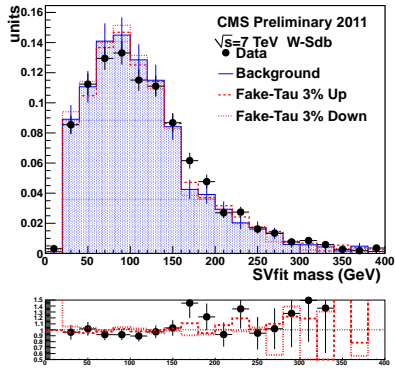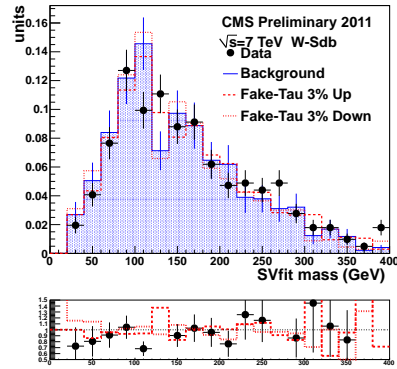
(a) (b)
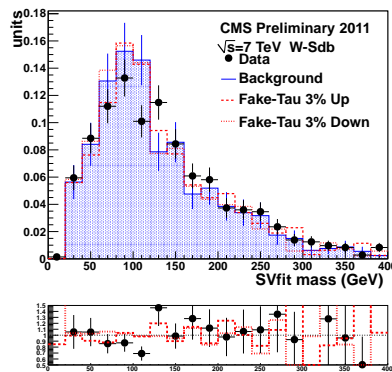
(c) (d)

(e)
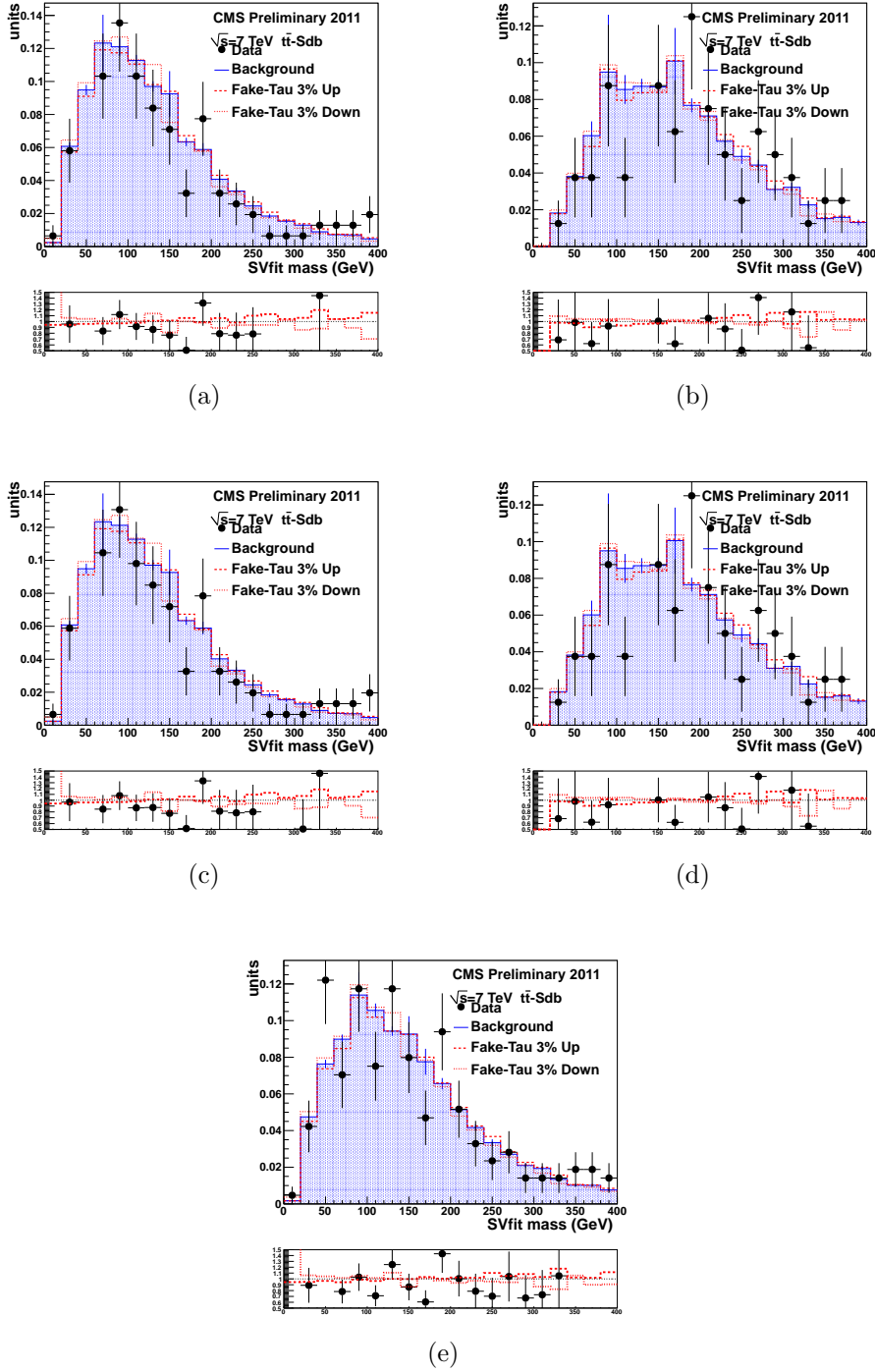
Figure B.4: Comparison between the observed and expected $\tau_e\tau_h$ mass distribution in $t\bar{t}$–enriched sidebands with ≥ 0 jets (top), ≥ 1 jets (middle) and ≥ 2 jets (bottom).

Appendix C

Limits per channel

The expected and observed 95% CL exclusion limits per channel are shown in Figure C.1(a) and C.1(b).

(a)   (b)
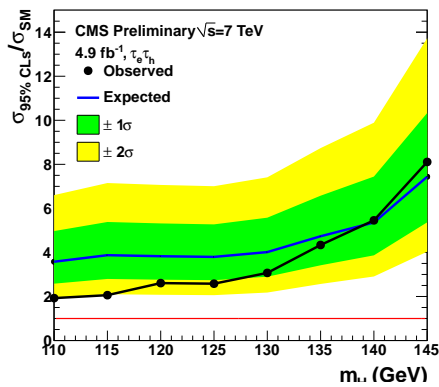
Figure C.1: Eexpected and observed 95% CLs exclusion limits on the SM signal strenght modifier for the $\tau_\mu\tau_h$ and $\tau_e\tau_h$ channels.

Bibliography

[1] S. L. Glashow, "Partial symmetries of weak interactions", *Nucl. Phys.*, 22:579–588, 1961.

[2] S. Weinberg, "A Model of Leptons", *Phys. Rev. Lett.*, 19:1264–1266, 1967.

[3] A. Salam and N. Svartholm, "Elementary particle physics", *Eighth Nobel Symposium*, Almquvist and Wiksell, 1968.

[4] F. Englert and R. Brout, "Broken symmetry and the mass of gauge vector mesons", *Phys. Rev. Lett.*, 13:321–323, 1964.
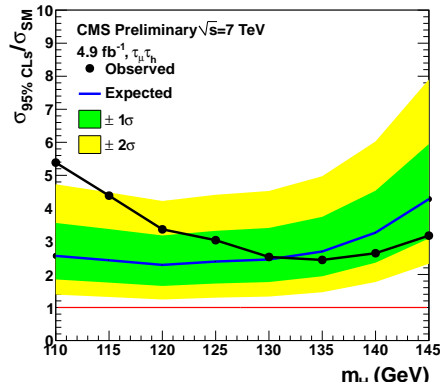
[5] P. W. Higgs, "Broken symmetries, massless particles and gauge fields", *Phys. Rev. Lett.*, 12:132–133, 1964.

[6] P. W. Higgs, "Broken symmetries and the masses of gauge bosons", *Phys. Rev. Lett.*, 13:508–509, 1964.

[7] G. S. Guralnik, C. R. Hagen, and T.W. B. Kibble, "Global conservation laws and massless particles", *Phys. Rev. Lett.*, 13:585, 1964.

[8] P. W. Higgs, "Spontaneous symmetry breakdown without massless bosons", *Phys. Rev. Lett.*, 145:1156, 1966.

[9] T.W. B. Kibble, "Symmetry breaking in non-Abelian gauge theories", *Phys. Rev. Lett.*, 155:1554, 1967.

[10] A. Djouadi, "The anatomy of electro-weak symmetry breaking", *Phys.Rept.*, 459:1-241, 2008.

[11] R. Barbieri, "Lectures on the electroweak interactions", *Edizioni della Normale*, 2007.

[12] Y. Nambu, *Phys. Rev. Lett. 4*, 380, 1960.

[13] Y. Nambu, G. Jona–Lasinio, *Phys. Rev. Lett. 122*, 345, 1961.

[14] J. Goldstone, *Nuov. Cim. 19*, 154, 1961.

[15] A. Salam J. Goldstone and S. Weinberg, *Phys. Rev. 127*, 965, 1962.

[16] N. Cabibbo, *Phys. Rev. 10*, 531, 1963.

[17] M. Kobayashi and T. Maskawa, *Prog. Theor. Phys. 49*, 652, 1973.

[18] M. S. Chanowitz, "Strong WW scattering at the end of the 90s: Theory and experimental prospects", *hep-ph/9812215*, p. 81.

[19] Michael E. Peskin, Dan V. Schroeder, "An Introduction To Quantum Field Theory", *Kindle Edition.*

[20] T. Hambaye and K. Riesselmann, *Phys. Rev*, D55, 1997.

[21] The LEP Collaborations, *Phys. Lett. B*, 565, 2003.

[22] The CDF, D0 Collaborations, "Combined CDF and D0 upper limits on standard model higgs boson production with up to 8.6 fb-1 of data", *arXiv:1107.5518v2*, 2011.

[23] The Atlas Collaboration, "Combined Standard Model Higgs Boson Searches in pp Collisions at $\sqrt{s} = 7$ TeV with the ATLAS Experiment at the LHC", *ATLAS–CONF–2011–112*, 2011.

[24] The CMS Collaboration, "Search for standard model Higgs boson in pp collisions at $\sqrt{s} = 7$ TeV", *CMS PAS*, HIG-11-011, 2012.

[25] G. Altarelli, R. Barbieri, F. Caravaglios, "Electroweak Precision Test: a Concise Review", *International Journal of Modern Physics A*, 13, 1998.

[26] H. Flacher, M. Goebel, J. Haller, A. Hocker, K. Monig, J. Stelzer, "Revisiting the global electroweak fit of the standard model and beyond with gfitter", *Eur. Phys. J. C*, 60, 2009.

[27] G–fitter Collaboration, http://gfitter.desy.de/Standard_ Model/.

[28] LHC Higgs Cross Section Working Group, "Handbook of LHC Higgs Cross Sections: 1. Inclusive Observables", *arXiv:1101.0593v3*, 2011.

[29] J. Kalinowski A. Djouadi and M. Spira, *Comput. Phys. Commun. 108*, 56, 1998.

[30] S. Dittmaier A. Mck A. Bredenstein, A. Denner and M. M. Weber, "A Monte Carlo generator for a proper description of the higgs decay into 4 fermions", http://omnibus.uni–freiburg.de/ sd565/programs/prophecy4f/prophecy4f.html, 2010.

[31] G. Altarelli et al., "Heavy Higgs Production at Future Colliders", *Nuclear Physics B*, 287, 1987.

[32] P. Bolzoni et al., "Higgs production via vector–boson fusion at NNLO in QCD", *Phys. Rev. Lett.*, 105, 2010.

[33] P. Fayet, *Nucl. Phys. B* 90:104, 1975.

[34] J.F. Gunion, H.E. Haber, G. Kane and S. Dawson, "The Higgs Hunter Guide", *Addison–Wesley Publishing Company, Reading, MA*, 1990.

[35] A. Belyaev et al., "Higgs boson phenomenology in $\tau^+ \tau^-$ final states at the LHC", *arXiv:hep–ph0912.2620v3*, 2009.

[36] S. P. Martin, "A supersymmetry primer", *arXiv:hep–ph/9709356v6*, 2011.

[37] H.E. Haber, "Higgs theory and phenomenology in the standard model and MSSM", *arXiv:hep–ph/0212136v2*, 2002.

[38] The ATLAS Collaboration, "The ATLAS Experiment at the CERN Large Hadron Collider", *JINST 3*, S08003, 2008.

[39] CMS Collaboration, "The CMS experiment at the CERN LHC", *JINST 3*, S08004, 2008.

[40] The LHCb Collaboration, "The LHCb Detector at the LHC", *JINST 3*, S08005, 2008.

[41] The Alice Collaboration, "The Alice Detector at the LHC", *JINST 3*, S08002, 2008.

[42] CMS Collaboration, "CMS technical design report, volume II: Physics performance", *J. Phys. G*, 34:995–1579, 2007.

[43] K. Nakamura et al. (Particle Data Group), *J. Phys. G 37*, 075021, 2010.

[44] CMS Collaboration, "CMS technical design report, volume II: The trigger and data acquisition project", *CERN LHCC*, 02–26, 2002.

[45] Henri Videau, "Energy flow or particle flow: the technique of particle flow for pedestrians", http://hal.in2p3.fr/in2p3-00069714, ICLC-LCWS04, Paris.

[46] CMS Collaboration, "Particle–flow event reconstruction in CMS and performance for jets, taus, and missing E_{T}", *CMS PAS*, PFT-09-001, 2009.

[47] CMS Collaboration, "Commissioning of the particle–flow event reconstruction with the first LHC collisions recorded in the CMS detector", *CMS PAS*, PFT-10-001, 2010. See also M. Bachtis et al., "Commissioning of the Particle–flow event reconstruction with the first LHC collisions recorded in the CMS detector", CMS Analysis Note AN–2010–031 (February 2010), 52 pp.

[48] CMS Collaboration, "Particle-flow commissioning with muons and electrons from J/Psi and W events at 7 TeV", *CMS PAS*, PFT-10-003, 2010. See also M. Bachtis et al., "Commissioning of the particle–flow event reconstruction with leptons from J/Psi and W decays at 7 TeV", CMS Analysis Note AN–2010–210 (July 2010), 20 pp.

[49] F. Gianotti C.W. Fabjan, "Calorimetry for particle physics", *Reviews of Modern Physics*, 75, 2003.

[50] C. Schwanenberger, "Calorimetery in particle physics", Ren-Yuan Zhu editor, 2002.

[51] Aleph Collaboration, "Performances of the Aleph detector at LEP", *Nucl. Instrum. Methods A*, 360, 1995.

[52] Jean–Claude Brient, "Improving the particle-flow method: an introduction", *arXiv:physics/0412149v1*.

[53] CMS Collaboration, "CMS tracking performance results from early LHC operation", *Eur. Phys. J. C*, 70, 2010.

[54] CMS Collaboration, "Performances of CMS muon reconstruction in pp collisions at $\sqrt{s} = 7$ TeV", *CMS PAS*, MUO-10-004, 2010.

[55] Byron P. Roe, Hai-Jun Yang, Ji Zhu, Yong Liu, Ion Stancu, Gordon McGregor, "Boosted Decision Trees as an Alternative to Artificial Neural Networks for Particle Identification", *arXiv:physics/0408124v2*, 2004.

[56] S. Baffioni et al., "Electron reconstruction in CMS", *The European Physical Journal C*, 49.

[57] W. Adam, R. Fruhwirth, A. Strandlie, T. Todorov, "Reconstruction of electrons with the Gaussian–Sum Filter in the CMS tracker at LHC",. *J.Phys. G31*, 2005.

[58] F. Beaudette , D. Benedetti , P. Janot , and M. Pioppi, "Electron Reconstruction within the Particle Flow Algorithm", CMS Analysis Note AN–2010–034 (February 2010).

[59] CMS Collaboration "Commissioning of the particle–flow reconstruction in minimum-bias and jet events from pp collisions at 7 TeV", *CMS PAS*, PFT-10-002, 2010.

[60] S. Agostinelli et al., "G4–a simulation toolkit", *Nucl. Instrum. Meth. A*, 506:250–303, 2003.

[61] CMS Collaboration, "MET performance in pp collisions at $\sqrt{s} = 7$ TeV", *CMS PAS*, JME-10-009, 2009.

[62] CMS Collaboration, "Determination of Jet Energy Calibration and Transverse Momentum Resolution in CMS", *JINST 6*, 11002, 2011.

[63] CMS Collaboration, "Performances of τ-lepton reconstruction and identification in CMS", *JINST 7*, P01001, 2012. See also M. Bachtis et al., "Performance of tau reconstruction algorithms in 2010 data collected with CMS", CMS PAS TAU–11–001 (March 2011), 10pp., and CMS Analysis Note AN–2011–045 (March 2011), 25pp.

[64] L. Bianchini, "Measurement of the $e \rightarrow \tau_{\mathrm{h}}$ fake rate with 33 pb^{-1} of pp collision data at $\sqrt{s} = 7$ TeV", CMS Analysis Note AN–2011–420 (February 2011), 18pp.

[65] A. Pich, "Tau physics", *arXiv:hep-ph/9912294v1*, 1999.

[66] K. Hagiwara B.K Bullok and A.D. Martin, "Tau polarization and its correlations as a probe of new physics", *Nucl. Phys.*, B395, 1993.

[67] CMS Collaboration, "Tau Reconstruction using the Particle Flow Technique", *CMS PAS* PFT-08-01, 2008.

[68] G. P. Salam M. Cacciari and G. Soyez, "The anti-kt jet clustering algorithm", *JHEP*, 04:063, 2008.

[69] courtesy of J. Swanson.

[70] CMS Collaboration, "Search for neutral MSSM higgs bosons decaying to tau pairs in pp collisions at $\sqrt{(s)} = 7$ TeV", *Phys.Rev.Lett.*, 106, 2011.

[71] http://tmva.sourceforge.net/

[72] CMS Collaboration, "Measurement of the inclusive Z cross section via decays to tau pairs in pp collisions at $\sqrt{s} = 7$ TeV", *JHEP*, 1108:117, 2011.

[73] R. Keith Ellis, W. James Stirling and Bryan R. Webber, "QCD and Collider Physics", *Cambridge monographs*, ISBN 0521 581893.

[74] CMS Collaboration, "Electron reconstruction and identification at $\sqrt{s} = 7$ TeV", *CMS PAS*, EGM-10-004, 2010.

[75] T. Sjostrand, S. Mrenna and P.Z. Skands, "PYTHIA 6.4 Physics and Manual", doi:10.1016/S0010-4655(00)00236–8, 2008.

[76] CMS Collaboration, "Search for neutral higgs bosons decaying to tau pairs in pp collisions at $\sqrt{s} = 7$ TeV", *Phys. Lett. B*, 713:68, 2012.

[77] F. James and M. Roos, "Minuit: A System for Function Minimization and Analysis of the Parameter Errors and Correlations" *Comput. Phys. Commun. 10*, 1975.

[78] D. Zeppenfeld et al., "Searching for $h \to \tau\tau$ in weak boson fusion at the cern LHC", *Physical Review D*, 59, 1998.

[79] L Bianchini, "Improved Collinear Approximation for VBF $H \to \tau\tau \to 3\nu + l + \tau_h$", CMS Analysis Note AN–2010–226 (July 2010), 14pp.

[80] J. Conway, E. K. Friis, C. Veelken, "Likelihood based Mass Reconstruction in Events containing Tau Leptons", CMS Analysis Note AN–2011–165 (June 2011), 29pp.

[81] A.J. Barr et al., "Speedy higgs boson discovery in decays to tau lepton pairs: $h \to \tau\tau$", *Physical Review D*, 59, 2011.

[82] D.J. Summers C.G. Lester, "Measuring masses of semi–invisibly decaying particles pair produced at hadron colliders", *Phys. Letters*, B463, 1999.

[83] A.J. Barr *et al.*, "Re–weighting the evidence for a light higgs boson in dileptonic W decays", *arXiv:1108.3468v2*, 2011.

[84] CDF Collaboration, "Search for Neutral MSSM Higgs Bosons Decaying to Tau Pairs with 1.8 fb of Data", *CDF note*, 9071, 2007.

[85] K. Kondo, "Dynamical likelihood method for reconstruction of events with missing momentum. 1: Method and toy models", *J. Phys. Soc. Jap. 57*, 1988.

[86] K. Kondo, "Dynamical likelihood method for reconstruction of events with missing momentum. 1: Mass spectra for 2 to 2 processes", *J. Phys. Soc. Jap. 60*, 1991.

[87] A. Ellangin, P. Murat, A. Pranko, A. Safanov, "A New Mass Reconstruction Technique for the Resonances Decaying to tau tau", *arXiv:1012:4686v1*, 2010.

[88] L. Bianchini, J. Conway, E. K. Friis, and C. Veelken, "Tau–Pair invariant Mass Reconstruction in High–Energy Hadron Collisions", in preparation, 2012.

[89] http://root.cern.ch/

[90] A. Rouge, "Polarization observables in he $3\pi\nu$ decay mode of the tau", *Z. Phys.*, C48, 1990.

[91] D. P. Roy S. Rayachadhuri, "Charged Higgs boson search at the TeVatron upgrade using Tau polarization", *arXiv:hep-ph/9503251v1*, 1995.

[92] S. Jadach, Z. Was, R. Decker, and J. H. Kuhn, "The tau decay library tauola: Version 2.4", *Comput. Phys. Commun.*, 76:361, 1993.

[93] L. Bianchini et al., "New SVfit developments", CMS Analysis Note AN–2012–124 (July 2012), 18pp.

[94] G. P. Lepage, "A New Algorithm for Adaptive Multidimensional Integration", *J. Comput. Phys. 27*, 1978.

[95] CMS Collaboration, "Search for the standard model Higgs boson decaying to tau pairs in pp collisions", *CMS PAS*, HIG-12-018, 2012. See also L. Bianchini et al., "Search for Higgs Bosons in Decay Channels with Tau Pairs in the Final state in pp Collisions at 7 TeV and 8 TeV", CMS Analysis Note AN–2012–150 (July 2012), 74 pp. See also https://twiki.cern.ch/twiki/bin/view/CMSPublic/Hig12018TWiki.

[96] CMS Collaboration, "Observation of a new boson with mass near 125 GeV", *CMS PAS*, HIG-12-028, 2012.

[97] S. Frixione, P. Nason, and C. Oleari, "Matching NLO QCD computations with parton shower simulations: the POWHEG method", *JHEP*, 0711:070, 2007.

[98] http://www.phys.ethz.ch/pheno/.

[99] F. Maltoni and T. Stelzer, "Madevent: Automatic event generation with madgraph", *JHEP*, 0302:027, 2003.

[100] K. Melnikov, F. Petriello, *Phys. Rev. D*, 74:114017, 2006.

[101] CMS Collaboration, "Measurement of the WW, WZ and ZZ cross sections at CMS", *CMS PAS*, EWK-11-010, 2010.

[102] M. Bachtis et al., "Search for Higgs Bosons Decaying to Tau Pairs in pp Collisions at $\sqrt{s} = 7$ TeV", CMS Analysis Note AN–2011–390 (December 2011).

[103] W. Erdmann, "Offline primary vertex reconstruction with deterministic annealing clustering", *CMS Internal Note*, 2011/014, 2011.

[104] http://fastjet.fr/

[105] M. Cacciari and G. P. Salam, "Pileup subtraction using jet areas", *Phys. Lett. B*, 659, 2008.

[106] https://cmsdoc.cern.ch/malberti/Hgg/JETID/efficiencyV00–02–06/44X_bkgSub/

[107] CMS Collaboration, "Commissioning of b–jet identification with pp collisions at $\sqrt{s} = 7$ TeV", *CMS PAS*, BTV-10-001, 2010.

[108] CMS Collaboration, "Measurement of b–tagging efficiency using $t\bar{t}$ events", *CMS PAS*, BTV-11-003, 2011.

[109] CMS Collaboration, "b-Jet Identification in the CMS Experiment", *CMS PAS*, BTV-11-004, 2011.

[110] ATLAS and CMS Collaborations, "Procedure for the LHC higgs boson search combination in Summer 2011", *ATL-PHYS-PUB-2011-11, CMS NOTE-2011/005*, 2011.

[111] A. L. Read, "Modified frequentist analysis of search results (the CLs method)", *CERN Yellow Report*, CERN-2000-005:81, 2000.

[112] G. Cowan et al., "Asymptotic formulae for likelihood–based test of new physics", *arXiv:hep–ph/10071727*, 2010.

[113] CMS Collaboration, "Search for Neutral Higgs Bosons Decaying into Tau Leptons in the Di-Muon Channel in pp Collisions at 7 TeV", *CMS PAS*, HIG-12-007, 2012.

[114] M. Carena, S. Heinemeyer, C.E.M. Wagner, G. Weiglein, "Suggestions for Benchmark Scenarios for MSSM Higgs Boson Searches at Hadron Colliders", *Eur. Phys. J.*, C26:601-607, 2003.

[115] CMS Collaboration, "Search for Neutral Higgs Bosons Decaying to Tau Pairs in pp Collisions at $\sqrt{s} = 7$ TeV", *Phys. Lett. B*, 106:231801, 2011.

[116] The D0 Collaboration, "Search for the Standard Model Higgs boson in tau lepton pair final states", *arXiv:1203.4443v2*, 2012.

[117] The CDF Collaboration, "Search for the Standard Model Higgs boson in tau lepton pair final states", *Phys. Rev. Lett.*, 108:181804, 2012.

[118] The ATLAS Collaboration, "Search for the Standard Model Higgs boson in the $H \rightarrow \tau^+ tau^-$ decay mode in $\sqrt{s} = 7$ TeV *pp* collisions with ATLAS", *arXiv:1206.5971v1*, 2012.

[119] C. N. Yang, "Selection Rules for the Dematerialization of a Particle into Two Photons", *Phys. Lett.*, 242, 1949.

[120] ATLAS Collaboration, "Observation of a new particle in the search for the Standard Model Higgs boson with the ATLAS detector at the LHC", *arXiv:1207.7214v1*, 2012.

[121] CDF Collaboration, D0 Collaboration, "Updated Combination of CDF and D0 Searches for Standard Model Higgs Boson Production with up to 10 fb^{-1} of Data", *arXiv:1207.0449v2*, 2012.

[122] CDF Collaboration, D0 Collaboration, "Evidence for a particle produced in association with weak bosons and decaying to a bottom–antibottom quark pair in Higgs boson searches at the Tevatron", *arXiv:1207.6436v1*, 2012.